

Terawatt-intensity few-cycle laser pulses

**Optical parametric chirped pulse amplification
and frequency comb spectroscopy**

VRIJE UNIVERSITEIT

Terawatt-intensity few-cycle laser pulses

Optical parametric chirped pulse amplification and frequency comb spectroscopy

ACADEMISCH PROEFSCHRIFT

ter verkrijging van de graad Doctor aan
de Vrije Universiteit Amsterdam,
op gezag van de rector magnificus
prof.dr. L.M. Bouter,
in het openbaar te verdedigen
ten overstaan van de promotiecommissie
van de faculteit der Exacte Wetenschappen
op woensdag 13 juni 2007 om 10.45 uur
in de aula van de universiteit,
De Boelelaan 1105

door

Stefan Michiel Witte

geboren te Alkmaar

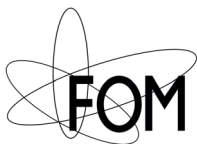
promotor: prof.dr. W. Hogervorst
copromotor: dr. K.S.E. Eikema

*Every morning in Africa, a gazelle wakes up.
It knows it must run faster than the fastest lion or it will be killed.*

*Every morning in Africa, a lion wakes up.
It knows it must outrun the slowest gazelle or it will starve to death.*

*It doesn't matter whether you are a lion or a gazelle.
When the sun comes up, you better start running.*

African proverb



vrije Universiteit *amsterdam*



The work described in this thesis was performed as part of the research program of the “Stichting voor Fundamenteel Onderzoek der Materie” (FOM) and was carried out at the Laser Centre of the Vrije Universiteit Amsterdam.

CONTENTS

CHAPTER 1: INTRODUCTION	1
1.1 Powerful laser systems	1
1.1.1 Development of the laser	1
1.1.2 Shorter pulses, higher intensity	2
1.1.3 Applications of high-intensity lasers	3
1.1.4 Optical parametric amplification	4
1.1.5 Optical parametric chirped pulse amplification	6
1.2 Precision spectroscopy and fundamental physics	7
1.2.1 Highly accurate tests of fundamental theories	7
1.2.2 The femtosecond frequency comb	8
1.3 High power meets precise control: The goal of this thesis	10
1.3.1 The motivation, the goals, the prospects	10
1.3.2 Outline of this thesis	11
CHAPTER 2: FREQUENCY COMB LASERS: ULTRASHORT PULSES AND PRECISION SPECTROSCOPY	13
2.1 Ultrashort pulse propagation	13
2.1.1 Propagation of electromagnetic waves	13
2.1.2 Electromagnetic wave-packets: Formation of pulses	15
2.1.3 Propagation equation for the pulse envelope	16
2.1.4 The pulse propagator	18
2.1.5 The carrier-envelope phase shift	19
2.1.6 Group-velocity dispersion	19
2.1.7 Propagation in a nonlinear medium	21
2.2 Principle and implementation of frequency combs	23
2.2.1 Pulse trains and their spectrum	23
2.2.2 The modelocked Ti:Sapphire oscillator	26
2.2.3 Repetition rate locking	27
2.2.4 The f -to- $2f$ technique	28
2.2.5 Spectral broadening to an optical octave	29
2.2.6 Carrier-envelope phase stabilization	30
2.2.7 Measuring the frequency of a continuous-wave laser	34
2.3 Quantum interference metrology	35
2.3.1 Coherent light-matter interaction	36
2.3.2 Excitation with a phase-coherent pulse pair	37
2.3.3 Intensity-induced phase shifts	40

CHAPTER 3: DEEP-ULTRAVIOLET QUANTUM INTERFERENCE METROLOGY	
WITH ULTRASHORT LASER PULSES	41
3.1 Introduction	41
3.2 Principle of quantum interference metrology	42
3.3 Setup for phase-coherent pulse-pair excitation	43
3.3.1 Amplification of pulse trains	44
3.3.2 Pulse-to-pulse phase shift measurements	45
3.3.3 Atomic beam generation and signal detection	46
3.4 Results and analysis	48
3.5 Conclusions	52
CHAPTER 4: NONCOLLINEAR OPTICAL PARAMETRIC CHIRPED PULSE	
AMPLIFICATION: THEORY AND SIMULATIONS	53
4.1 Theory of optical parametric amplification	53
4.1.1 The coupled-wave equations	53
4.1.2 Analytical solutions	55
4.1.3 Phase evolution during parametric amplification	58
4.1.4 Parametric amplification of ultra-broadband spectra	60
4.1.5 Parametric superfluorescence	63
4.2 Numerical modeling of NOPCPA	64
4.2.1 The split-step Fourier algorithm	65
4.2.2 Practical implementation of the numerical algorithm	66
4.2.3 Optimization of spectral bandwidth	67
4.2.4 Modeling an experimental NOPCPA system	69
4.2.5 Pulse contrast and amplified fluorescence	71
4.2.6 Wavelength-dependent gain saturation	72
4.2.7 Intensity-dependent phase shifts	75
4.2.8 Pump-seed synchronization	77
4.2.9 Conclusions	78
CHAPTER 5: EXPERIMENTAL ASPECTS OF FEW-CYCLE PULSE AMPLIFICATION	
USING NOPCPA	81
5.1 Stretching and compression of ultrashort laser pulses	81
5.1.1 Chirped pulse amplification	81
5.1.2 Grating-based pulse compressor	82
5.1.3 Grating-based pulse stretcher	84
5.1.4 Pulse compression through adaptive phase shaping	86
5.2 Design of a Nd:YAG pump laser system	87
5.2.1 Oscillator, pulse stretching and synchronization	87
5.2.2 Regenerative amplification	89
5.2.3 Pulse shortening in the regenerative amplifier	90
5.2.4 Diode-pumped post-amplifier	91
5.2.5 Flashlamp-pumped linear post-amplifier	93
5.2.6 Flashlamp-pumped post-amplifier in ring geometry	96
5.2.7 Relay-imaging and spatial filtering	98

5.3	NOPCPA amplifier geometry	99
5.4	Characterization of ultrafast laser pulses	102
5.4.1	Autocorrelation	102
5.4.2	SPIDER	103
5.4.3	Experimental implementation of SPIDER	104
5.4.4	SPIDER calibration	105
5.4.5	Reconstruction of the pulse shape	106
5.4.6	SPIDER design considerations	108
5.5	High-harmonic generation	110
5.5.1	XUV generation and detection setup	110
5.5.2	Measured spectra	111
CHAPTER 6: HIGH POWER PARAMETRIC AMPLIFICATION OF 11.8 FS LASER PULSES WITH CARRIER-ENVELOPE PHASE CONTROL		113
6.1	Introduction	113
6.2	Phase-stable ultra-broadband NOPCPA setup	114
6.3	Pulse characterization	116
6.4	Phase measurements	117
6.4.1	Single-shot f -to- $2f$ interferometry	117
6.4.2	Fourier-transform spectral interferometry	118
6.4.3	Results of FTSI phase measurements	120
6.5	Conclusions	122
CHAPTER 7: GENERATION OF FEW-CYCLE TERAWATT LIGHT PULSES USING OPTICAL PARAMETRIC CHIRPED PULSE AMPLIFICATION		123
7.1	Introduction	123
7.2	Optical parametric chirped pulse amplification	124
7.3	NOPCPA setup	124
7.4	Discussion and outlook	128
7.5	Conclusion	128
CHAPTER 8: A SOURCE OF 2 TERAWATT, 2.7 CYCLE LASER PULSES BASED ON NONCOLLINEAR OPTICAL PARAMETRIC CHIRPED PULSE AMPLIFICATION		129
8.1	Introduction	129
8.2	Ultra-broadband two terawatt NOPCPA system	130
8.3	Spectral phase shaping and few-cycle pulse compression	134
8.4	Pulse contrast measurements	136
8.5	Conclusions	142
CHAPTER 9: OUTLOOK		143
9.1	Optimization of the pump pulse shape for NOPCPA	143
9.2	Optical parametric tilted pulse amplification	145
9.3	Towards precision spectroscopy in the XUV	147
APPENDIX A: PROPAGATION IN ABSORBING MEDIA		149

APPENDIX B: PULSES IN TIME AND FREQUENCY	151
APPENDIX C: SOME MATHEMATICAL BACKGROUND TO THE OPA THEORY	153
C.1 Integration of the normalized coupled wave equations	153
C.2 Elliptic integral manipulations	154
BIBLIOGRAPHY	157
LIST OF PUBLICATIONS	173
SUMMARY	175
SAMENVATTING	179
DANKWOORD	183

CHAPTER 1

INTRODUCTION

1.1 Powerful laser systems

1.1.1 Development of the laser

The laser is arguably one of the most important inventions of the last century. Ever since the first demonstration of the Ruby laser in 1960 [1], a large community of researchers has continually designed and improved new types of laser systems. This evolution has continued to this day, and at present laser research may very well be a more active research field than it has ever been.

The development of the laser has its origin in the field of microwave spectroscopy. This was a field which became very popular during World War II because of its usefulness for the characterization of the absorption bands in water vapor, which is valuable data for the development of radar systems that could be used in the humid South Pacific region [2–4]. After WW II, this expertise in microwave spectroscopy was put to good use in molecular physics to characterize resonances and absorption bands in various molecules. The insight that more narrowband sources at shorter wavelengths would be a valuable tool for molecular spectroscopy eventually led to the development of the maser [5] (Microwave Amplification by Stimulated Emission of Radiation). The first maser was based on the inversion splitting in NH_3 (ammonia) [6]: A population inversion was generated by state-selective focusing of molecules in the upper state inside a waveguide, which served as the microwave oscillator. However, later maser systems were usually based on an improved maser design presented by Basov and Prokhorov [7] which used a population inversion created in a three-level system. This principle also formed the basis for the first working lasers. The maser provided a source of coherent, highly monochromatic microwaves, setting new standards for the resolution that can be achieved in molecular spectroscopy.

The success of the maser quickly sparked the interest of many spectroscopists to extend the technique to optical wavelengths. Within a few years, the first designs for such optical masers, which are presently known as lasers (light amplification by stimulated emission of radiation), were published [8–10], and the first working laser was demonstrated by Maiman in 1960 [1]. While Maiman used a flashlamp-pumped rod of Ruby ($\text{Cr}^{3+}:\text{Al}_2\text{O}_3$) that gave pulsed output at 694.3 nm, several other types of lasers were

quickly developed. Most notable are the first continuous-wave laser using a Helium-Neon gas cell by Javan et al. [11], and the first semiconductor laser by Hall et al. [12]. Other milestones in the development of laser technology are the demonstration of a four-level laser [13], and the first laser based on Nd^{3+} -doped glass [14], which forms the basis for present-day Nd:YAG lasers.

As lasers soon proved their worth for the study of light-matter interaction and of atomic and molecular structure, a continuing development towards new types of lasers started. This rapidly led to more efficient, more broadly tunable, and higher power lasers. Depending on the application, laser systems can be constructed with either ultra-narrow or ultra-broadband spectrum, continuous-wave or pulsed, and at an enormous range of possible output powers and repetition rates (for pulsed lasers). For spectroscopy, major steps forward have been the development of the dye laser [15–17] and later on the Ti:Sapphire laser [18–20], which are narrow-band, broadly tunable lasers that can cover most of the visible and near-infrared wavelength range.

1.1.2 Shorter pulses, higher intensity

Besides its usefulness for high-resolution spectroscopy, the laser has many applications as a source of high-intensity radiation. The high degree of spatial coherence allows focusing of a laser beam to a spot size with dimensions that are on the order of a wavelength, concentrating all its energy at this point in space. To maximize the peak intensity of a laser, it is beneficial to concentrate all its energy in a single pulse of as short a duration as possible. In addition, short-pulse lasers can be very useful in time-resolved spectroscopy, where the best time resolution that can be achieved is usually limited by the duration of the excitation pulse. While the first laser ever built was already operating in a pulsed mode due to the pulsed flashlamp pumping, more sophisticated techniques have been developed to shorten the pulse duration of lasers. Excellent overviews of the development of such techniques (e.g. Q-switching and modelocking) are given in several standard textbooks on laser physics [21, 22]. When it comes to generation of the shortest pulses directly from a laser cavity, present-day state-of-the-art lasers are usually Kerr-lens modelocked Ti:Sapphire oscillators. Such oscillators are capable of generating pulses with a duration down to about 5 fs. Although the pulse energy of such systems is usually limited to the nJ range (up to several hundred nJ has been demonstrated using chirped pulse oscillators [23] and cavity-dumping [24]), this still leads to a peak intensity of several MW.

When even higher intensities are needed, a single oscillator does not suffice anymore and external amplification is required to boost the power. However, at such high peak intensities the amplifier itself usually forms the limiting factor: For many experiments, an intensity is required that exceeds the damage threshold of even the strongest materials by orders of magnitude. A straightforward way of circumventing this problem is by simply increasing the transverse size of the amplifier, so that the power is spread out over a large area. Of course, this quickly leads to enormous amplifiers: An extreme example of such a system is the building-sized NOVA laser facility [25], which uses 10 separate beamlines with 46 cm diameter amplifier rods in each beam to generate >100 TW pulses of 0.1 ns duration.

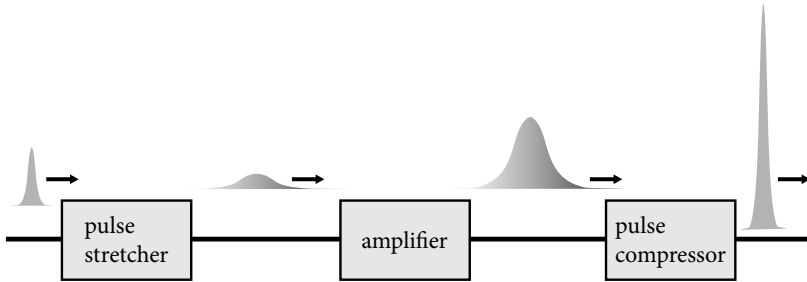


FIGURE 1.1: The principle of chirped pulse amplification: An ultrashort laser pulse is first stretched in time by a dispersive delay line, lowering the peak intensity. This stretched pulse is amplified, and recompressed to its original duration after amplification by a second delay line that cancels the dispersion introduced by the stretcher.

A more sophisticated technique, which makes use of the broad spectral bandwidth of ultrashort optical pulses, is called chirped pulse amplification [26], which is schematically depicted in Fig. 1.1. In this scheme, the initial laser pulse is stretched by imposing a large amount of group-velocity dispersion on it in a dispersive delay line. The peak intensity of this “chirped” pulse will then be lowered by a factor proportional to the amount of pulse stretching. The chirped pulse is amplified in the conventional way, and sent into another dispersive delay line which introduces exactly the opposite amount of group-velocity dispersion to the pulse. As a result the pulse will be recompressed to its original duration (provided that the spectrum has not been altered by the amplifier), with the accompanying increase in peak intensity. Since pulse compressors can in practice be constructed using only reflective optics, the damage threshold of such a compressor is much higher than that of a typical laser amplifier system. Chirped pulse amplification has led to a dramatic increase in the maximum achievable peak intensity, and in recent years several building-sized laser systems have been constructed that reach a peak power in the petawatt range [27–30].

1.1.3 Applications of high-intensity lasers

With the advent of powerful ultrashort pulse laser systems, several interesting applications in strong-field laser matter interaction have come within the reach of experimentalists. One particularly striking effect is the generation of high-order harmonics in atomic and molecular gases. In contrast to the perturbative regime of N^{th} harmonic generation that scales with $\sim I^N$, when a high-intensity ultrashort pulse is focused in a gas jet, many harmonic orders are generated which exhibit an extended plateau of constant intensity. This manifestly non-perturbative response of the atoms to the laser field can be explained qualitatively by a three-step model [31, 32]: In the first step, an electron tunnels out of the atomic Coulomb field, which is strongly distorted by the laser field. In the second step, the electron is accelerated away from the atom by the laser field, until the (oscillating) field changes sign and the electron trajectory is reversed. In the

third step, the accelerated electron collides with the atomic core and recombines back to the ground state, releasing the excess kinetic energy in the form of a high-frequency photon. This process of high-harmonic generation (HHG) provides a way of producing coherent radiation at XUV and soft X-ray wavelengths. By performing HHG with intense sub-10 fs pulses harmonic photons with an energy of 1 keV have been generated [33], and bright coherent radiation in the biologically interesting “water window” (at a wavelength of about 2-4 nm) can be produced [34].

When turning towards even higher intensity, the possibility of laser-assisted nuclear physics is starting to come within reach [35]. The most powerful laser systems can reach focused intensities of $\sim 10^{21}$ W/cm². Powerful lasers have already been employed in the acceleration of electron bunches to GeV energy [36], and for the production of multi-MeV protons [37]; especially the latter process may have promising applications in medical radiation therapy [38]. The possibilities for nuclear transmutation [39] and even radio-isotope production for positron emission tomography [40] are currently subjects under investigation.

Another major application for such extreme-intensity lasers is in the field of inertial confinement fusion (see e.g. [41, 42]). In this process, a capsule filled with a mixture of deuterium and tritium gas is compressed to very high pressures by heating it with a relatively long (\sim ns) high-energy laser pulse. If the resulting plasma is sufficiently dense, a high-intensity ultrashort pulse can be used to locally heat the plasma to temperatures exceeding a hundred million degrees. This heating can ignite a thermonuclear fusion reaction in the plasma sample: The laser is effectively used as a starter engine for a nuclear fusion reactor.

In a more everyday setting, lasers have found widespread use in applications such as precision cutting and welding, and especially micromachining of various materials. Focused laser beams can be employed to deposit energy very efficiently within a micron-sized spot. Therefore, lasers are ideally suited for cutting and welding of materials with high accuracy. The ability of lasers to engrave and slice material with such a high resolution is becoming increasingly important for (among others) the automotive, aeronautic and biomedical industries, where laser micromachining is used to obtain e.g. smaller sensors, miniature surgical devices, more efficient fuel injection systems, etc.

1.1.4 Optical parametric amplification

Immediately after the invention of the laser, it was realized that its high peak intensity in a small number of well-defined coherent electromagnetic field modes is well-suited for nonlinear optics in solids, i.e. the generation of new frequency components in a material through the nonlinear response of the electrons in this medium. The first demonstration of such an effect was given by Franken et al. [43], who performed frequency-doubling of a pulsed Ruby laser in a quartz crystal to generate coherent UV radiation. Soon after, the sum frequency of two different lasers was generated in a similar way [44]. The coherence properties of the nonlinear processes were investigated by Maker et al. [45] and Giordmaine [46], confirming the importance of phase matching for these processes: The refractive index of the nonlinear medium should be chosen

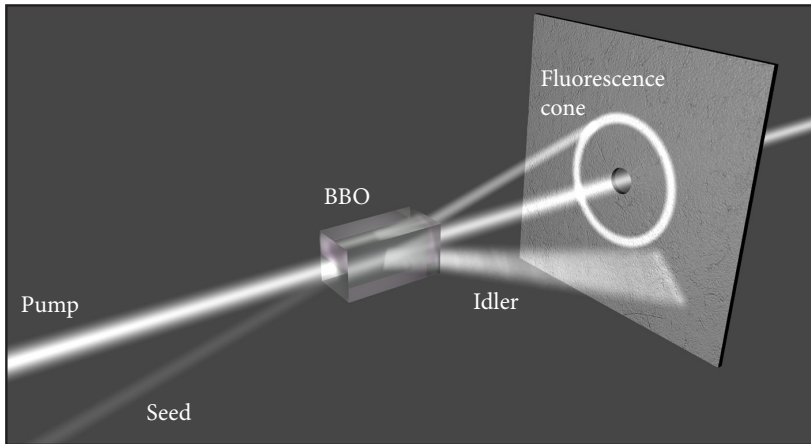


FIGURE 1.2: Illustration of optical parametric amplification: A weak seed beam is amplified by a strong pump beam inside a nonlinear medium. The difference in photon energy between pump and seed goes into a newly generated idler beam. A cone of spontaneous parametric fluorescence can be seen at high pump intensity.

such, that the fundamental and the generated harmonic wave remain in phase with each other, so that coherent addition of the generated amplitude occurs throughout the medium.

Aside from sum-frequency generation, the difference frequency between two optical waves can also be obtained through nonlinear interaction, effectively splitting a high-frequency photon into two photons at lower frequencies. It was soon realized that this process can work as an amplifier by seeding the nonlinear interaction with a laser beam at a suitable frequency (see Fig. 1.2). This interaction was named optical parametric amplification (OPA), where the term “parametric” highlights the role of the phase-matching parameter for the efficiency of the process. Even before the first experimental demonstration of parametric gain by Wang and Racette [47], theoretical studies of optical parametric amplification were already performed by several researchers [48–51]. Shortly after the demonstration of parametric amplification, the first optical parametric oscillator (OPO) was constructed [52]: This type of system places a parametric amplifier inside an optical cavity which is resonant for at least one of the generated low-frequency fields. An OPO generates tunable radiation with all the coherence properties of a laser, but its operation is based on a nonlinear interaction instead of a population inverted medium to provide the gain. Soon after the classical wave-theory of parametric amplification, quantum-mechanical descriptions were developed independently by a number of authors [53–56]. An interesting prediction from these quantum theories is the possibility of parametric fluorescence, i.e. the spontaneous generation of two low-frequency fields by a strong pump laser, even in the absence of seed light. The seeding in this case is done by zero-point fluctuations of the vacuum field, and parametric fluorescence was later observed experimentally [57–59].

As laser physics progressed, so did the production of new parametric amplifiers and oscillators. Especially in the field of ultrashort pulse generation, the development of the noncollinear optical parametric amplifier (NOPA) formed a large step forward [60–64], as these devices enabled the generation of ultrashort pulses that are tunable throughout the entire visible and near-infrared spectral range [62, 63, 65] and present state-of-the-art NOPAs are capable of generating visible pulses with a duration of only 4 fs [66, 67]. These systems are widely used for time-resolved spectroscopy on many types of physically interesting samples, ranging from photosynthetic light-harvesting complexes (see e.g. [68]) to carbon nanotubes [69].

1.1.5 Optical parametric chirped pulse amplification

Aside from the applications in ultrashort pulse generation, optical parametric amplification has also been employed for the generation of high intensity laser pulses. As was first realized by Dubietis et al. [70], the concept of chirped pulse amplification can be combined with optical parametric amplification to form a new amplification technique, which has been aptly named optical parametric chirped pulse amplification (OPCPA). In an OPCPA scheme, a chirped low intensity pulse is used to seed an OPA which is pumped by a high-energy pulse (usually from a separate laser system). Because the parametric amplification occurs instantaneously, the seed pulse should be chirped such that it matches the pump pulse duration, and the pulses should be accurately synchronized. After amplification, the pulse is recompressed to yield a high-intensity ultrashort pulse. As in conventional CPA, a high-energy long-pulse laser is used to supply energy to an initially low-power ultrashort seed pulse.

However, OPCPA has some very interesting properties compared to conventional amplifiers such Ti:Sapphire-based systems, which operate on the well-known laser principles of energy storage in a population-inverted medium. The most important advantages are:

- The huge single-pass gain. Typically, the small-signal gain in an OPA can be orders of magnitude larger than what can be reached with conventional amplifiers, so that only a few amplification passes are needed to obtain a high pulse intensity.
- The spectral gain bandwidth of an OPA can be significantly broader than any other known type of laser amplifier, allowing the amplification of shorter pulses.
- As parametric amplification is an instantaneous process, no energy is ever stored in the amplifier medium. This medium only plays the role of a passive host, providing the required nonlinear coupling between the waves. Therefore, the thermal effects that usually limit the performance of e.g. high-energy Ti:Sapphire amplifiers are virtually absent in OPCPA.
- While laser amplifiers usually suffer from amplified spontaneous emission (ASE), in an OPA this is less of a problem; although OPAs do emit spontaneous parametric fluorescence, this is only present during the pump pulse and its energy is usually much less than typical laser ASE.

- The phase of the seed pulse is preserved during amplification in an OPA, allowing the coherence and carrier-envelope phase stability (see later sections) of the initial pulse to be maintained throughout the entire system.

Especially Ross et al. pointed out the prospects of using OPCPA for the construction of high-intensity laser systems [71, 72], and his group was also the first to demonstrate a terawatt-intensity OPCPA system [73]. Several other OPCPA implementations followed quickly [74–77] and a 200 TW, 45 fs OPCPA system has recently been demonstrated [78].

Aside from these extremely high-power implementations, OPCPA can also be used for the amplification of extremely broadband spectra. Especially when a noncollinear geometry is used (i.e. introducing a noncollinear angle between pump and seed beam), favorable phase-matching conditions can be achieved over bandwidths spanning hundreds of nanometers [71]. In particular, such a noncollinear OPCPA (or rather NOPCPA) can be designed for the amplification of ~ 7 fs pulses from a Ti:Sapphire oscillator [71, 72]. The development of such an NOPCPA system that combines high intensity with few-cycle pulse durations is a major goal of the work presented in this thesis. Using this technique, we have been the first to produce sub-10 fs pulses with a peak intensity of one terawatt [79], and more recently 7.6 fs pulses with 2 TW peak intensity [80]. Our research efforts and results on NOPCPA are described in detail in chapters 4 to 8.

1.2 Precision spectroscopy and fundamental physics

1.2.1 Highly accurate tests of fundamental theories

With the development of narrowband light sources in the form of continuous-wave (cw) lasers, the field of atomic and molecular spectroscopy grew explosively due to the enormous increase in resolution that could be obtained. Excellent overviews of the techniques that have been developed, and the resulting increases in precision are given by e.g. Schawlow [81], and Hänsch and Walther [82].

While the measurement resolution increased, new physical phenomena could be observed. Initially, precision measurements of hyperfine structure and isotope shifts provided insight into models of the atomic nucleus, and an enormous amount of data could be obtained on the electronic structure of matter with unprecedented resolution. At even higher accuracy, laser spectroscopy was able to provide a sensitive test of quantum electrodynamics (QED), through the measurement of the Lamb shift in hydrogen [83, 84] and helium [85, 86]. Especially the hydrogen atom has been a test object for fundamental theories, since its properties can be calculated to high accuracy. Using the hydrogen atom and its isotope deuterium, and especially the 1S-2S two-photon transition at 2×243 nm, extremely accurate data has been obtained for e.g. the ground state Lamb shift and the Rydberg constant [87].

At present, new records in precision are being set continuously, and current state-of-the-art measurements approach and even exceed the 10^{-15} level (see e.g. [88–91]). By repeating such measurements on a yearly basis, stringent upper limits have been set on possible drifts of fundamental constants, such as the fine structure constant [92, 93].

The key to this success has been the development of the frequency comb, which is the subject of the next section.

1.2.2 The femtosecond frequency comb

While the methods for atomic spectroscopy grew in resolution, a limiting factor in the accuracy has been the measurement of the absolute frequency of the laser light. Since the definition of the S.I. second is given in terms of the cesium ground state hyperfine splitting at 9.193 GHz, a link is required to compare optical laser frequencies to this microwave frequency of an atomic cesium clock. Since visible light has a frequency on the order of hundreds of THz, there is a gap of four orders of magnitude that needs to be bridged.

In principle, the measurement of an absolute frequency of a wave comes down to simply counting the number of oscillation cycles per second. But while this is possible for RF frequencies of atomic clocks in the GHz range using fast electronics, optical waves oscillate much too fast to be able to count their frequencies using standard electronic counters (as an example, an infrared light wave with a wavelength of 750 nm has an oscillation period of only 2.5 femtoseconds = 2.5×10^{-15} s). One possible way of solving this problem is by upconversion of the atomic clock reference frequency to the desired optical transition frequency. In practice, this requires phase-locking a whole range of oscillators to each other using phase-locked loops, with each oscillator operating at a few times higher frequency than the previous one [94]. However, these “frequency chain” setups are large, costly and complicated to operate, while they can typically be used for the measurement of only one atomic transition frequency.

A much more elegant solution to this problem is the invention of the self-referenced optical frequency comb. Already in the 1970’s it was realized that a sequence of phase-coherent laser pulses can be used to perform spectroscopy with a resolution that is much better than the bandwidth of the individual pulses [95–97]. Using pairs of pulses, high-resolution spectroscopy has been demonstrated [98, 99] in a measurement scheme that is essentially a time-domain variation of Ramsey’s method of separated oscillatory fields [100]. The frequency spectrum of a phase-coherent pulse train consists of a “comb” of very narrow equidistant modes, spaced by the inverse of the time delay between the pulses (see Fig. 1.3). Typically, the output of a modelocked laser can be used to obtain the desired a pulse train. By stabilizing the inter-pulse time delay T (through stabilization of the modelocked laser cavity length), the spacing between the modes can be controlled to high accuracy [101]. Since the pulse repetition frequency $f_{\text{rep}} = 1/T$ (which is equal to the mode spacing) is typically in the RF domain, it can easily be measured using electronic counters. Due to the clear separation between the modes, a narrowband cw laser that is typically used for spectroscopy can be phase-locked to one of the comb modes. With this type of frequency comb referencing, large frequency differences could be bridged, allowing the measurement of e.g. atomic transition frequencies with respect to an accurately cw calibrated laser at a completely different frequency [102].

Apart from locking the repetition frequency, the phases of the pulses in the train must be accurately synchronized to each other in order to stabilize the absolute fre-

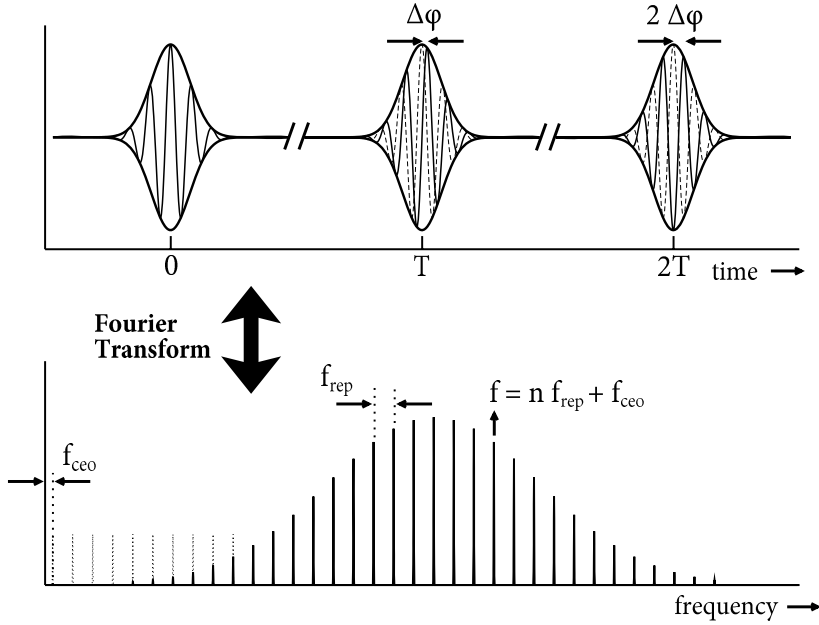


FIGURE 1.3: A train of ultrashort pulses and its frequency spectrum. The spectrum of such a frequency comb is characterized by the mode spacing f_{rep} and the offset frequency f_{ceo} , which are directly related to the inter-pulse time delay T and the carrier-envelope phase shift $\Delta\phi$ from pulse to pulse.

quencies of all the comb modes. In addition, any (constant) carrier-envelope phase shift (i.e. the relative phase between the carrier-wave and the pulse envelope) $\Delta\phi$ from pulse to pulse will have the effect of shifting all the comb lines by a carrier-envelope offset frequency $f_{ceo} = \Delta\phi/(2\pi)f_{rep}$ [103]. More precisely, the frequency of the n th comb mode is given by $f_n = n \times f_{rep} + f_{ceo}$. However, a measurement of f_{ceo} is not straightforward because a modelocked laser does not emit radiation at such low frequencies. For this reason, initial spectroscopic experiments using phase-locked pulse trains were limited to relative measurements. One solution that allows the measurement of absolute frequencies without knowledge of f_{ceo} is to produce various (sub-)harmonics of a cw laser, and to reference these harmonics to different modes of the frequency comb [104].

The real breakthrough that made the frequency comb self-referencing, i.e. a stand-alone absolute optical frequency calibration device, was the invention of the f -to- $2f$ interferometer [105, 106]. In this method, the second harmonic of a low-frequency comb mode with mode number n is compared to a comb mode at the high-frequency end of the spectrum, at a mode number $m = 2n$. The resulting beat signal is then given by $(m \times f_{rep} + 2 \times f_{ceo}) - (m \times f_{rep} + f_{ceo}) = f_{ceo}$, allowing the carrier-envelope frequency to be measured. For the f -to- $2f$ technique to work, however, an octave-wide spectrum is required. Such a spectrum can be obtained by broadening the output of a modelocked laser in a specially engineered photonic crystal fibre (PCF) [107], which has the prop-

erty that the zero-dispersion wavelength of the fibre coincides with the central laser frequency. Hence, the pulses remain short and intense throughout an extended interaction length, which strongly enhances the nonlinear effects inside the fibre that are responsible for spectral broadening and “supercontinuum generation”. It turns out that these nonlinear effects maintain the phase relationship between the pulses very well, so that the frequency comb structure is preserved after spectral broadening [108].

These self-referencing frequency combs have revolutionized frequency metrology. A typical frequency comb setup based on a Ti:Sapphire oscillator occupies less than 1 m^2 of table space, and can provide a direct link between an RF reference standard and an optical transition with an accuracy that has been verified to be better than 2×10^{-15} in 1 s [109] (basically limited by the RF reference source itself). When using optical reference standards instead of an RF source this accuracy can be even better, since the noise on the reference source is in this case not upconverted by a large integer [110]. For such optically referenced frequency combs, the stability has been verified down to the 10^{-19} level [111]. More recently, frequency combs based on fiber laser technology have been developed, which are even more compact while requiring very little maintenance [112].

1.3 High power meets precise control: The goal of this thesis

1.3.1 The motivation, the goals, the prospects

From the historic overview given in the previous sections, there is one particularly striking fact that seems to be very promising for a new direction in high-accuracy atomic physics: Up to the present day, there has been a segregation between the development of high-power pulsed lasers and of narrow-linewidth continuous-wave sources. However, the advent of the frequency comb seems to form a bridge, not only between the RF and optical frequency domains, but between the high-power and high-frequency-resolution domains as well. The fact that a frequency comb laser emits a train of pulses that are phase-coherent in the time domain, while having a spectrum that consists of many extremely narrow modes, opens up the possibility to use the best of both worlds: By using such powerful phase-locked laser pulses for frequency metrology, one can probe very weak (multiphoton) transitions, or produce higher harmonics of these pulses to perform high-precision measurements at short wavelengths (e.g. in the extreme-ultraviolet (XUV) or even the soft-X-ray regime). In the time-domain, one can envision high-resolution time-resolved spectroscopy with highly coherent laser pulses of which the electric field evolution can be controlled.

The goal of this thesis is to exploit the potential of phase-locked high-power laser pulses for precision studies of atomic systems, and to develop the measurement techniques and laser systems that allow the extension of such studies to shorter wavelength ranges and higher energies. To this end, we have constructed a frequency comb and various amplifier systems, to boost the power of these few-cycle laser pulses to unprecedented levels, while maintaining phase coherence. We have applied these pulses in frequency metrology experiments, to demonstrate the practical potential of pulsed spectroscopy at short wavelengths. As a means of amplifying few-cycle laser pulses to extreme peak intensity, we have investigated noncollinear optical parametric chirped

pulse amplification as an alternative to the more conventional Ti:Sapphire-based amplifiers. This has turned out to be a powerful approach to the generation of few-cycle laser pulses with a peak intensity in the terawatt range. Initial measurements on the phase stability of a parametric amplifier implementation that produces 0.1 mJ pulses are encouraging [113], making noncollinear optical parametric chirped pulse amplification a promising candidate for the production of phase-controlled electronic waveforms at extreme pulse intensities.

The prospects of this work are plentiful, and many possible applications of the developed laser systems can be envisioned. One important goal is to perform precision metrology on the helium atom with extreme-ultraviolet excitation wavelength radiation, to measure the ground state Lamb shift with sub-MHz accuracy. This would constitute an improvement of almost two orders of magnitude compared to the most accurate determination of this quantity to date [85, 86]. On a longer timescale, one can think of extending this type of spectroscopy to even shorter wavelengths, possibly even down to the soft X-ray region of the spectrum so that precision spectroscopy on hydrogen-like ions (He^+ , Li^{2+} , etc.) becomes feasible. Also, a whole range of coherent quantum control experiments with XUV radiation can be developed, exploiting the tight phase coherence between the various pulses that can be sustained over very long timescales (in the μs - to ms -range). On the high-power laser side, the achieved combination of terawatt peak intensity and sub-3-cycle pulse duration seems ideally suited for high-harmonic generation with high conversion efficiency at ultrashort wavelengths [114, 115]. In this way, a source of coherent X-ray radiation can be constructed, producing a large flux of photons in the biologically interesting water window spectral region (wavelength $\sim 2\text{-}4$ nm) [34], and even producing photons with keV energy [33]. In addition, the few-cycle pulse duration seems well suited for the production of attosecond XUV pulses, which may be promising for studying the extremely fast (sub-fs) dynamics of inner-shell electrons in atoms and molecules [116].

1.3.2 Outline of this thesis

This thesis is organized into two major parts: The first part discusses the properties of ultrashort pulses and their use in high-precision frequency measurements, while the second part deals with the generation and characterization of high-intensity few-cycle laser pulses using noncollinear optical parametric chirped pulse amplification (NOPCPA).

Part one consists of chapters 2 and 3. Chapter 2 provides an introduction to the properties and propagation characteristics of ultrashort pulses; in addition, it deals with practical aspects of frequency comb development and operation, and provides a theoretical description of quantum interference metrology. Chapter 3 describes a proof-of-principle experiment that we performed to demonstrate the practical applicability and the potential of quantum interference metrology: We have used this technique to calibrate a deep-ultraviolet two-photon transition in krypton, reaching an order of magnitude higher accuracy compared to conventional single-pulse excitation.

Chapters 4 to 8 form the second part of this thesis. In chapter 4, a theoretical description of NOPCPA is given, and numerical simulations are presented that provide

insight into the design parameters that are required for a practical NOPCPA system. Chapter 5 gives an overview of the most important experimental techniques that have been used for amplifier construction and pulse characterization, such as pulse stretching and compression, the pump laser design, and the SPIDER setup. Chapter 6 describes our first NOPCPA experiments, where we have constructed a kHz repetition rate amplifier producing 0.1 mJ pulses. Using Fourier-transform spectral interferometry, we could confirm that this NOPCPA system preserves the carrier-envelope phase of the pulses during amplification. In chapter 7, we report on the first laser system capable of generating sub-10 fs pulses with a peak power exceeding one terawatt (10 mJ per pulse). This system operates at a 30 Hz repetition rate, and displays good pulse characteristics. Chapter 8 concludes the second part with our latest NOPCPA system, that has been designed to test the limits of this amplification technique more closely: Using an ultra-broadband seed oscillator, we produce 7.6 fs pulses with a peak intensity of 2 terawatt. The spectrum corresponds well to the numerical simulations, and we have characterized the pulse compression, beam profiles, intensity stability and pulse contrast in detail.

Chapter 9 presents a further outlook and conclusions. The work presented in this thesis is of course by no means exhaustive: Many possible improvements and extensions to the present work can be implemented, and some interesting options will be discussed in this chapter.

CHAPTER 2

FREQUENCY COMB LASERS: ULTRASHORT PULSES AND PRECISION SPECTROSCOPY

In this chapter, a general introduction on the generation and propagation of ultrashort laser pulses is presented. The properties of such pulses are discussed, with special attention to the case of an extended train of mutually phase-coherent pulses acting together to form a frequency comb. Together with the principles of frequency combs, the design and operating characteristics of the frequency comb setup developed in the course of this thesis are presented. To demonstrate the potential of frequency combs for precision spectroscopy at very high frequencies, we introduce the concept of quantum interference metrology, of which a practical demonstration will be given in the next chapter.

2.1 Ultrashort pulse propagation

The generation and study of ultrashort laser pulses has been an active branch of physics for decades, and at present it still remains at the focus of attention for a large research community [117]. The reason for this is the enormous versatility of ultrashort pulses, both as a tool for time-resolved spectroscopy of matter and as a trigger for a large variety of nonlinear phenomena in light-matter interaction. To understand the physics of such processes, it is essential to have a theoretical framework of how ultrashort laser pulses propagate and interact with matter. This section provides an introduction to ultrashort pulse propagation in linear dispersive media, and it includes a discussion on how nonlinear interactions can be incorporated in the theory.

2.1.1 Propagation of electromagnetic waves

The propagation of an electromagnetic wave is described by a wave equation that can be derived from the Maxwell equations, which in its most basic form can be written as

(see e.g. [21, 118]):

$$\nabla^2 \mathbf{E}(\mathbf{r}, t) - \epsilon_0 \mu_0 \frac{\partial^2 \mathbf{E}(\mathbf{r}, t)}{\partial t^2} = 0 \quad (2.1a)$$

$$\nabla^2 \mathbf{B}(\mathbf{r}, t) - \epsilon_0 \mu_0 \frac{\partial^2 \mathbf{B}(\mathbf{r}, t)}{\partial t^2} = 0 \quad (2.1b)$$

$$(2.1c)$$

These equations describe the propagation of electromagnetic waves in vacuum. The waves travel with the speed of light c , which is given by $c = 1/\sqrt{\mu_0 \epsilon_0}$, where $\mu_0 = 4\pi \times 10^{-7}$ is the magnetic permeability of vacuum, and $\epsilon_0 = 8.854 \times 10^{-12}$ is the electric permittivity of vacuum. That the equation really describes waves is confirmed by checking its solutions, which are found to be of the form:

$$\mathbf{E}(\mathbf{r}, t) = E_0 e^{i(\mathbf{k} \cdot \mathbf{r} - \omega t)} + c.c. \quad (2.2)$$

where *c.c.* stands for complex conjugate. These solutions are traveling waves, with an angular frequency ω (which is related to the frequency f by $\omega = 2\pi f$), and with a wave-vector \mathbf{k} that points in the propagation direction of the wave; its magnitude is given by $|\mathbf{k}| = \omega/c$. From these solutions to Eq. (2.1a) it is found that in a time t the wave travels a distance z/c , confirming that the velocity of the wave is indeed c . In the following, we will limit the discussion to the electric field \mathbf{E} of the wave: Even though the magnetic field \mathbf{B} is of course always present, its magnitude B_0 equals E_0/c , and is therefore usually negligible compared to the electric field amplitude.

When the wave travels in a dielectric medium the situation becomes different, since the presence of the medium introduces a polarization \mathbf{P} to the wave equation (2.1a):

$$\nabla^2 \mathbf{E}(\mathbf{r}, t) - \epsilon_0 \mu_0 \frac{\partial^2 \mathbf{E}(\mathbf{r}, t)}{\partial t^2} = \mu_0 \frac{\partial^2 \mathbf{P}(\mathbf{r}, t)}{\partial t^2} \quad (2.3)$$

The properties of any possible solution to this equation now of course depend on the form of the polarization term. When the medium is assumed to be linear and the medium response to the electric field is assumed to be instantaneous, the polarization can be written as [119]:

$$\mathbf{P}(\mathbf{r}, t) = \epsilon_0 \int_{-\infty}^{\infty} \chi_e(t - t') \mathbf{E}(\mathbf{r}, t') dt' \quad (2.4)$$

where χ_e is the electric susceptibility of the medium. Note that in general χ_e is both frequency-dependent and complex. In the frequency-domain, this convolution can simply be described as a product $\mathbf{P}(\mathbf{r}, \omega) = \epsilon_0 \chi_e(\omega) \mathbf{E}(\mathbf{r}, \omega)$. Therefore, the wave equation (2.3) can be written in a much simpler form in the frequency domain:

$$\nabla^2 \mathbf{E}(\mathbf{r}, \omega) + [1 + \chi_e(\omega)] \frac{\omega^2}{c^2} \mathbf{E}(\mathbf{r}, \omega) = 0 \quad (2.5)$$

The wave equation in a medium remains similar to its vacuum counterpart, with the added factor χ_e being the only difference; the solutions to equation (2.5) are still plane

waves, but with some modifications compared to (2.2). In the time-domain, they are found to be:

$$\mathbf{E}(\mathbf{r}, t) = E_0 e^{-\alpha z} e^{i(\mathbf{k}\cdot\mathbf{r}-\omega t)} + c.c. \quad (2.6)$$

where the wave-vector $\mathbf{k} = n(\omega)\omega/c \hat{\mathbf{k}}$ now contains the refractive index, defined as $n = \text{Re}\sqrt{1 + \chi_e}$, and the velocity of the wave has changed to $v = c/n$. Since n is frequency-dependent, the velocity of a wave now also depends on its frequency: this phenomenon is well-known as dispersion. In addition, the wave (2.6) contains a real-valued exponential part that describes attenuation or amplification of the electric field amplitude, depending on the sign of α . The factor α in this real-valued part is defined as $(c/\omega)\text{Im}\sqrt{1 + \chi_e}$.

2.1.2 Electromagnetic wave-packets: Formation of pulses

Now consider a wave-packet, consisting of multiple frequency components:

$$\mathbf{E}(\mathbf{r}, t) = \int_{-\infty}^{\infty} A(\omega - \omega_0) e^{i(\mathbf{k}\cdot\mathbf{r}-\omega t)} d\omega \quad (2.7)$$

where $A(\omega - \omega_0)$ gives the amplitude of each frequency component in the wave-packet, and ω_0 is the central frequency (note that the *c.c.*-term has been left out for compactness). This equation has the form of a Fourier integral, and it is easy to see that the frequency-domain representation of the field is then given by:

$$\mathcal{FT}[\mathbf{E}(\mathbf{r}, t)] = \frac{1}{2\pi} \tilde{\mathbf{E}}(\mathbf{r}, \omega) = \frac{1}{2\pi} A(\omega - \omega_0) e^{i\mathbf{k}\cdot\mathbf{r}} \quad (2.8)$$

Using this information, the wave-packet can also be written in terms of its Fourier-transform:

$$\mathbf{E}(\mathbf{r}, t) = \int_{-\infty}^{\infty} \tilde{\mathbf{E}}(\mathbf{r}, \omega) e^{-i\omega t} d\omega = \int_{-\infty}^{\infty} A(\omega - \omega_0) e^{i\mathbf{k}\cdot\mathbf{r}} e^{-i\omega t} d\omega \quad (2.9)$$

This last relation can be turned into a more convenient form by writing $A(\omega - \omega_0)$ in terms of a carrier-frequency and an envelope function $A(\omega - \omega_0) = A(\omega) e^{-i\omega_0 t}$, and by expanding the wave-vector \mathbf{k} around the same carrier-frequency as $\mathbf{k} = \mathbf{k}_0 + \delta\mathbf{k}$. Equation (2.9) then turns into:

$$\begin{aligned} \mathbf{E}(\mathbf{r}, t) &= e^{i(\mathbf{k}_0\cdot\mathbf{r}-\omega_0 t)} \int_{-\infty}^{\infty} A(\omega) e^{i\delta\mathbf{k}\cdot\mathbf{r}} e^{-i\omega t} d\omega \\ &= A(\mathbf{r}, t) e^{i(\mathbf{k}_0\cdot\mathbf{r}-\omega_0 t)} \end{aligned} \quad (2.10)$$

The wave-packet can thus be written in terms of a carrier wave at a certain central frequency ω_0 , and an envelope function that contains all the information on the shape of the wave-packet in space and time. Note that when the electric field contains only one single frequency $A(\omega) = A_0 \delta(\omega - \omega_0)$ the envelope function will be a constant, i.e. $A(\mathbf{r}, t) = A_0$. However, as soon as the wave-packet consists of more frequency components, $A(\mathbf{r}, t)$ turns into a (possibly complex) function of both space and time:

the various waves with different frequencies can add up coherently to form a pulse. The exact shape of such a pulse depends on the amplitudes and phases of the various frequency components as described by equation (2.10). The situation can still be made clearer by writing the last term in this equation as $A(\mathbf{r}, \omega) = A(\omega)e^{i\delta\mathbf{k}\cdot\mathbf{r}}$, describing a complex pulse envelope in the frequency domain. In this notation the pulse envelopes in the time- and frequency-domain are simply each others Fourier-transform:

$$A(\mathbf{r}, t) = \int_{-\infty}^{\infty} A(\mathbf{r}, \omega)e^{-i\omega t} d\omega \quad (2.11)$$

This last equation demonstrates the intimate connection between the time and frequency domain of an electric pulse: if one has full knowledge of such a pulse in one domain, then all the pulse characteristics in the other domain can be calculated by a single Fourier-transform.

2.1.3 Propagation equation for the pulse envelope

Describing electromagnetic wave-packets in terms of a carrier-wave and a pulse envelope can have significant advantages when calculating the propagation of optical pulses through a medium [21, 119, 120]. Especially when the pulse envelope is a slowly varying function of \mathbf{r} and t compared to the carrier-wave, many simplifications to equation (2.5) can be made. A good starting point is obtained by inserting an optical pulse into equation (2.5). For simplicity, we restrict ourselves to propagation in only one dimension (the $+z$ -direction):

$$\left(\frac{\partial^2}{\partial z^2} + (1 + \chi_e) \frac{\omega^2}{c^2} \right) A(z, \omega) e^{-i(k_0 z - \omega_0 t)} = 0 \quad (2.12)$$

Writing out all the partial derivatives and dividing out the carrier-wave results in an equation for the pulse envelope:

$$\frac{\partial^2 A(z, \omega)}{\partial z^2} - 2ik_0 \frac{\partial A(z, \omega)}{\partial z} - k_0^2 A(z, \omega) + (1 + \chi_e) \frac{\omega^2}{c^2} A(z, \omega) = 0 \quad (2.13)$$

If χ_e is independent of frequency, this equation can directly be Fourier-transformed to the time-domain, leading to an equation identical to (2.1a), apart from an additional (constant) refractive index. In other words, in the absence of dispersion the pulse envelope will propagate in exactly the same way as the carrier-wave, with the same velocity, maintaining its original pulse shape. In general, due to the frequency-dependence of χ_e such a straightforward time-domain equation can not be obtained without making some simplifying approximations to (2.13).

One major simplification that can be made to equation (2.13) is based on the assumption that the pulse envelope is a slowly varying function of z compared to the carrier-wave, i.e:

$$\frac{\partial^2 A(z, \omega)}{\partial z^2} \ll 2ik_0 \frac{\partial A(z, \omega)}{\partial z}$$

which allows the second-order derivative of $A(z, \omega)$ with respect to z to be neglected, turning equation (2.13) into a first-order differential equation in z .

Another issue about equation (2.13) is the frequency-dependence of χ_e : note that if we assume a medium without absorption, then $k^2 = (1 + \chi_e)\omega^2/c^2$. Equation (2.13) can now be written as:

$$\frac{\partial A(z, \omega)}{\partial z} + \frac{i}{2k_0}(k^2 - k_0^2)A(z, \omega) = 0 \quad (2.14)$$

To be able to transform (2.14) into a time-domain equation, the frequency-dependent $(k^2 - k_0^2)$ -term still needs to be turned into a more suitable form. To this end, we approximate that $k + k_0 \approx 2k_0$ and perform a Taylor-expansion of k around ω_0 :

$$\begin{aligned} (k^2 - k_0^2) &\approx 2k_0(k - k_0) \\ &= 2k_0 \left(k_0 + \left. \frac{\partial k}{\partial \omega} \right|_{\omega_0} (\omega - \omega_0) + \frac{1}{2} \left. \frac{\partial^2 k}{\partial \omega^2} \right|_{\omega_0} (\omega - \omega_0)^2 + \dots - k_0 \right) \end{aligned}$$

Inserting this expansion into equation (2.14) then leads to:

$$\frac{\partial A(z, \omega)}{\partial z} + i \sum_{n=1}^{\infty} \frac{1}{n!} k^{(n)} (\omega - \omega_0)^n A(z, \omega) = 0 \quad (2.15)$$

where we have used the abbreviated notation $k^{(n)} = \left. \frac{\partial^n k}{\partial \omega^n} \right|_{\omega_0}$. Transformation of this equation to the time-domain can now be performed by Fourier-transformation of all the separate terms in the sum. These terms yield integrals of the form[‡]:

$$\begin{aligned} &\int_{-\infty}^{\infty} A(z, \omega) \frac{1}{n!} k^{(n)} (\omega - \omega_0)^n e^{-i\omega t} d\omega \\ &= \frac{1}{n!} k^{(n)} \int_{-\infty}^{\infty} A(z, \omega - \omega_0) (\omega - \omega_0)^n e^{-i(\omega - \omega_0)t} d\omega \\ &= \frac{i^n}{n!} k^{(n)} \frac{\partial^n A(z, t)}{\partial t^n} \end{aligned}$$

so that we finally arrive at a time-domain differential equation for the slowly-varying pulse envelope:

$$\frac{\partial A(z, t)}{\partial z} - \sum_{n=1}^{\infty} \frac{(-i)^{n+1}}{n!} k^{(n)} \frac{\partial^n A(z, t)}{\partial t^n} = 0 \quad (2.16)$$

Although some approximations have been used in its derivation, equation (2.16) is exact in the sense that it incorporates the linear dispersion of the medium completely. In many cases, especially if the spectral bandwidth of the pulse is much smaller than the carrier-wave frequency ω_0 , it is not necessary to keep all the terms of the infinite

[‡]Using the identity for the Fourier transform of a derivative:

$$\mathcal{FT} \left[\frac{\partial^n A(z, t)}{\partial t^n} \right] = (-i\omega)^n \mathcal{FT} [A(z, t)]$$

sum in (2.16). The propagation of such a pulse can already be described accurately by keeping only the first two terms, which simplifies the equation to:

$$\frac{\partial A(z, t)}{\partial z} + k^{(1)} \frac{\partial A(z, t)}{\partial t} - \frac{ik^{(2)}}{2} \frac{\partial^2 A(z, t)}{\partial t^2} = 0 \quad (2.17)$$

This equation is often encountered in the literature, and is known as the *parabolic equation for the pulse envelope* [21, 121]. It is suitable for optical pulses with a duration down to a few hundred femtoseconds. When the pulse duration decreases, consecutive higher-order terms in the dispersion expansion in Eq. (2.16) need to be taken into account. Equation (2.17) can be modified to include the effects of absorption on the pulse propagation. Since absorption is only of limited concern for the work described in this thesis, it will only be discussed in Appendix A.

2.1.4 The pulse propagator

When we have an initial solution to the wave equation (2.3) in the form $E(z, t)$, it is very desirable to follow the evolution of the pulse shape in space and time as it propagates through a medium. This can be achieved quite conveniently in the following way [120]: First decompose the pulse in its various frequency components:

$$E(z, t) = \int_{-\infty}^{\infty} E(z, \omega) e^{-i\omega t} d\omega \quad (2.18)$$

Recalling that the z -dependence of $E(z, t)$ is given by $e^{ik(\omega)z}$, equation (2.18) can be rewritten as:

$$E(z, t) = \int_{-\infty}^{\infty} E(\omega) e^{ik(\omega)z} e^{-i\omega t} d\omega \quad (2.19)$$

Transforming $E(\omega)$ back to the time domain, we obtain:

$$\begin{aligned} E(z, t) &= \int_{-\infty}^{\infty} \frac{1}{2\pi} \int_{-\infty}^{\infty} E(\tau) e^{i\omega\tau} d\tau e^{ik(\omega)z} e^{-i\omega t} d\omega \\ &= \frac{1}{2\pi} \int_{-\infty}^{\infty} E(\tau) \int_{-\infty}^{\infty} e^{ik(\omega)z} e^{-i\omega(t-\tau)} d\omega d\tau \\ &= \int_{-\infty}^{\infty} E(\tau) G(t-\tau) d\tau \end{aligned} \quad (2.20)$$

$$\text{where } G(t-\tau) = \frac{1}{2\pi} \int_{-\infty}^{\infty} e^{i[k(\omega)z - \omega(t-\tau)]} d\omega \quad (2.21)$$

This last relation is convenient for calculation of the electric field $E(z, t)$ at a given point in space and time, starting out from an initial field $E(\tau)$ at $z = 0$ and $t = \tau$. The function $G(t - \tau)$ plays the role of a propagator.

2.1.5 The carrier-envelope phase shift

The integral equation (2.21) derived in the previous section is especially useful to demonstrate the effects of dispersion on the propagation of ultrashort pulses [120, 121]. Consider for instance a pulse with an initial electric field $E(\tau)$, which propagates through a dispersive medium. The wave-vector k can be expanded in a Taylor series as:

$$k(\omega) = k_0 + k^{(1)}(\omega - \omega_0) + \frac{1}{2}k^{(2)}(\omega - \omega_0)^2 + \frac{1}{6}k^{(3)}(\omega - \omega_0)^3 + \dots \quad (2.22)$$

For the moment, we will approximate $k(\omega)$ by taking only the first-order expansion term into account. After propagation over a distance z , the electric field is given by:

$$\begin{aligned} E(z, t) &= \frac{1}{2\pi} \int_{-\infty}^{\infty} E(\tau) \int_{-\infty}^{\infty} e^{i[k_0 + k^{(1)}(\omega - \omega_0)]z - \omega(t - \tau)} d\omega d\tau \\ &= e^{i(k_0 z - k^{(1)} \omega_0 z)} \int_{-\infty}^{\infty} E(\tau) \delta(\tau - t + k^{(1)} z) d\tau \\ &= e^{i(k_0 z - k^{(1)} \omega_0 z)} E(t - k^{(1)} z) \end{aligned} \quad (2.23)$$

This final result shows that, aside from a phase factor, in this first-order dispersion approximation the pulse shape remains constant during propagation. Note that the pulse moves with a group velocity $v_g = 1/k^{(1)}$, and not simply with the phase velocity $v_\varphi = c/n\omega_0 = \omega_0/k_0$. Using these definitions for group and phase velocity, we can rewrite equation (2.23) in a more insightful way:

$$E(z, t) = e^{i\left(\frac{1}{v_\varphi} - \frac{1}{v_g}\right)\omega_0 z} E_0\left(t - \frac{z}{v_g}\right) \quad (2.24)$$

This relation clarifies the meaning of the phase that is accumulated by the electric field during propagation: due to the dispersion-induced difference between v_φ and v_g , a phase shift is introduced between the center of the pulse envelope and the carrier wave underneath it. This effect is known as the *carrier-envelope phase shift*, and it is of particular importance in pulse trains emitted by modelocked lasers, as will be discussed in section 2.2 on frequency combs.

2.1.6 Group-velocity dispersion

When only the first-order term in the dispersion expansion is taken into account, we find that the pulse shape remains constant during propagation. However, the situation becomes more complex when a more accurate description of the dispersion is employed [120–122]. When the second-order term in the wave-vector expansion (2.22) is also incorporated, the shape of the pulse will change during propagation. As an example, consider a Gaussian initial pulse shape $E(\tau) = e^{-\tau^2/2\tau_0^2}$. Inserting this into the propagation integral leads to:

$$E(z, t) = \frac{1}{2\pi} \int_{-\infty}^{\infty} e^{-\frac{1}{2}\left(\frac{\tau}{\tau_0}\right)^2} \int_{-\infty}^{\infty} e^{i\left(k_0 + \frac{1}{2}k^{(2)}(\omega - \omega_0)^2\right)z - \omega(t - \tau)} d\omega d\tau \quad (2.25)$$

where the first-order (group velocity) term is left out for convenience (its effect has already been discussed in the previous section). This integral can be solved analytically:

$$\begin{aligned}
 E(z, t) &= \frac{1}{2\pi} \int_{-\infty}^{\infty} e^{-\frac{1}{2}(\tau/\tau_0)^2} \int_{-\infty}^{\infty} e^{i\left[\frac{1}{2}k^{(2)}z\omega^2 + (\tau-t-k^{(2)}z\omega_0)\omega\right]} d\omega d\tau \\
 &= \frac{1}{\sqrt{2\pi i k^{(2)}z}} \int_{-\infty}^{\infty} e^{-\frac{1}{2}(\tau/\tau_0)^2} e^{i(1/2k^{(2)}z)(\tau-t)^2} d\tau \\
 &= \frac{\tau_0}{\sqrt{\tau_0^2 + i k^{(2)}z}} e^{-\frac{1}{2}(t/\tau_c)^2 + i\varphi(t)} \tag{2.26}
 \end{aligned}$$

The resulting pulse after propagation still has a Gaussian shape, but the pulse duration has changed and a time-dependent phase pattern has been added to the initially Fourier-limited pulse. Note that we have neglected all constant phase terms that appeared during the derivation of (2.26). The pulse duration and phase are found to be:

$$\tau_c = \tau_0 \sqrt{1 + \left(\frac{k^{(2)}z}{\tau_0^2}\right)^2} \quad \text{and} \quad \varphi(t) = \frac{1}{2k^{(2)}z} \frac{\tau_0^2}{\tau_c^2} t^2 \tag{2.27}$$

From this phase factor, we can derive that the group-velocity dispersion causes the various spectral components to arrive at different times; defining the instantaneous frequency of the pulse as $\omega_i = \frac{\partial\varphi}{\partial t}$, we find that this corresponds to:

$$\omega_i = \frac{\partial\varphi}{\partial t} = \frac{1}{k^{(2)}z} \frac{\tau_0^2}{\tau_c^2} t \tag{2.28}$$

In other words, the frequency of the pulse has become linearly time-dependent, and the pulse is said to have a *linear chirp*. From Eq. (2.27) it can be seen that the amount of linear chirp after a propagation distance z is determined by the Fourier-limited pulse duration and the material parameter $k^{(2)}$. The constant $k^{(2)}$ is therefore known as the *group-velocity dispersion parameter*. A similar analysis as the one presented in this section can be performed for the higher-order terms in the k -expansion (2.22). All these terms lead to a distortion of the pulse shape in time, and introduce various forms of nonlinear chirp to the pulse.

For large amounts of dispersion (i.e. $k^{(2)}z \gg \tau_0^2$), the expression for the chirped pulse duration (2.27) can be approximated as:

$$\tau_c \approx \frac{k^{(2)}z}{\tau_0} \tag{2.29}$$

The duration of the chirped pulse for a given amount of dispersion relates inversely proportional to the initial Fourier-limited pulse duration. This is explained by the fact that shorter pulses have a larger spectral bandwidth, which will be spread out over a longer time span by a given group-velocity dispersion $k^{(2)}z$ compared to a more narrow-band pulse (with a longer Fourier-limited pulse duration). To give an estimate of how severe the effects of group velocity dispersion can be, consider the case of a 10 fs pulse (intensity FWHM pulse duration) with a center wavelength of 800 nm, traversing a block of

fused silica (for which $k^{(2)} = 36.2 \text{ fs}^2/\text{mm}$). From equation (2.27) we can calculate that the pulse will have stretched to 20 fs after passing through only 1.73 mm of material.

The group-velocity dispersion described in this section is caused by the second-order term in the dispersion expansion (2.22). Of course, the higher-order terms in this expansion will also influence the pulse shape. During pulse propagation, these higher-order chirps lead to a chirp which is nonlinear in time. As a result, the pulse will not only broaden, but it will also change its shape. For example, the third-order dispersion term in Eq. (2.22) causes the formation of pre- or postpulses, and leads to steepening of the pulse edges. These higher-order dispersion terms become more important with an increasing spectral width of the pulse: Proper compression of sub-10 fs pulses therefore requires dispersion control up to the fourth order or better.

2.1.7 Propagation in a nonlinear medium

So far we have only considered pulse propagation in materials that are perfectly linear, i.e. with a polarization \mathbf{P} that is proportional to \mathbf{E} . Now consider the possibility of an additional nonlinear polarization term that depends on a higher-order of the electric field: $\mathbf{P} = \mathbf{P}_L + \mathbf{P}_{NL}$ [119, 123]. Such a nonlinear polarization modifies the wave equation (2.3) to:

$$\nabla^2 \mathbf{E}(\mathbf{r}, t) - \epsilon_0 \mu_0 \frac{\partial^2 \mathbf{E}(\mathbf{r}, t)}{\partial t^2} = \mu_0 \frac{\partial^2 \mathbf{P}_L(\mathbf{r}, t)}{\partial t^2} + \mu_0 \frac{\partial^2 \mathbf{P}_{NL}(\mathbf{r}, t)}{\partial t^2} \quad (2.30)$$

This equation forms the basis for the entire field of nonlinear optics; depending on the exact form of \mathbf{P}_{NL} , an enormous range of nonlinear light-matter interaction phenomena can be studied using equation (2.30). However, in many cases the presence of the nonlinearity also makes the differential equation extremely difficult to solve, and approximations need to be made.

Depending on the exact interaction between the light pulse and the material, many different functional forms for \mathbf{P}_{NL} can occur. We discuss only a few basic ones, which describe phenomena that are encountered in the course of the experiments described in this work. Such nonlinear interactions form the basis for e.g. sum-frequency generation, frequency doubling, optical parametric amplification, and for the existence of an intensity-dependent nonlinear refractive index n_2 . The most straightforward expression for the nonlinear polarization has a second-order field dependence:

$$\mathbf{P}_{NL}(t) = \epsilon_0 \int_{-\infty}^{\infty} \int_{-\infty}^{\infty} \chi^{(2)}(t - t_1, t - t_2) \mathbf{E}(t - t_1) \mathbf{E}(t - t_2) dt_1 dt_2 \quad (2.31)$$

This type of second-order nonlinear response initiates a wave at frequency 2ω in the propagation medium, and describes the process of second-harmonic generation [43]. In an isotropic medium, however, such a second-order nonlinearity is not possible, as it violates inversion symmetry. This type of $\chi^{(2)}$ -processes are only possible in anisotropic media, such as birefringent crystals. The lowest-order nonlinear effects that can occur in isotropic materials are third-order processes [119, 123]:

$$\mathbf{P}_{NL}(t) = \epsilon_0 \int_{-\infty}^{\infty} \int_{-\infty}^{\infty} \int_{-\infty}^{\infty} \chi^{(3)}(t - t_1, t - t_2, t - t_3) \mathbf{E}(t - t_1) \mathbf{E}(t - t_2) \mathbf{E}(t - t_3) dt_1 dt_2 dt_3 \quad (2.32)$$

Note that any higher-order susceptibility $\chi^{(n)}$ is a tensor of rank n . This third-order nonlinear polarization can lead to the generation of a medium polarization with a frequency 3ω through a tensor component $\chi^{(3)}(\omega, \omega, \omega, 3\omega)$. However, it can also generate an additional polarization at frequency ω , through a $2\omega - \omega = \omega$ four-wave-mixing process governed by $\chi^{(3)}(\omega, \omega, -\omega, \omega)$. This last process is of special interest, since it leads to an intensity-dependent polarization at the frequency of the original electric field. If for the moment we only consider this component of \mathbf{P}_{NL} and insert it in the wave equation (2.5), we find:

$$\nabla^2 \mathbf{E}(\mathbf{r}, \omega) + [1 + \chi_e(\omega) + \chi^{(3)}(\omega)|\mathbf{E}(\mathbf{r}, \omega)|^2] \frac{\omega^2}{c^2} \mathbf{E}(\mathbf{r}, \omega) = 0 \quad (2.33)$$

where we have assumed that the $\chi^{(3)}$ -process is instantaneous, so that the convolution (2.32) can simply be written as a product (which also means that we neglect any possible frequency-dependence of $\chi^{(3)}$ [119]). Since the carrier-wave of this polarization term is identical to that of the incident field \mathbf{E} , we can extract an equation for the pulse envelope from (2.33) in a similar way as was done to arrive at equation (2.17). If once again we neglect absorption, we can write [119]:

$$1 + \chi_e(\omega) + \chi^{(3)}(\omega)|\mathbf{E}(\mathbf{r}, \omega)|^2 \approx n + n_2|E|^2 \quad (2.34)$$

Here n_2 is known as the *nonlinear refractive index*. This name comes from the fact that the propagating wave now feels an effective refractive index $n + n_2|E|^2$ that depends on the pulse intensity. By inserting this term into equation (2.33), approximating $|\mathbf{E}(\mathbf{r}, \omega)|^2 = |A|^2$ to be constant and Fourier-transforming to the time-domain, a nonlinear propagation equation is obtained:

$$\frac{\partial A(z, t)}{\partial z} + k^{(1)} \frac{\partial A(z, t)}{\partial t} - \frac{ik^{(2)}}{2} \frac{\partial^2 A(z, t)}{\partial t^2} = i \frac{n_2 \omega_0}{c} |A|^2 A(z, t) \quad (2.35)$$

Even though a few rather crude approximations have been made in its derivation, equation (2.35) is suitable for modeling the propagation of high-energy pulses in transparent bulk materials. It is often referred to as the *nonlinear Schrödinger equation*, and has been used extensively in the theory of ultrashort pulse propagation in optical fibers. An interesting property of this equation is that it can actually be solved exactly, and that solutions can be found corresponding to optical solitons. But even without such an extensive analysis, some of the implications of the nonlinearity in equation (2.35) can already be seen directly from (2.34), which states that the refractive index of the medium depends on the field intensity. The effect of such an intensity-dependent refractive index is that the high-intensity peak of a pulse will travel slower (provided that $n_2 > 0$) than the low-intensity wings, leading to an intensity-dependent phase shift across the pulse. This phenomenon is known as self-phase-modulation, and has the remarkable effect of broadening the pulse spectrum during propagation: Due to the difference in velocity between the various parts of the pulse local phase-modulation occurs, generating additional spectral components at the edges of the input pulse spectrum. Besides such temporal effects, the nonlinear refractive index n_2 can also have

an impact on the spatial properties of a pulse: a beam with a Gaussian transverse profile for instance, will also experience a Gaussian refractive index modulation across the beam. Since optical beams refract towards regions of higher refractive index, the beam will start to focus spontaneously as a result of the nonlinearity, an effect that is known as self-focusing. Excellent overviews of the effects caused by the nonlinear refractive index are given by e.g. Agrawal [119], Boyd [123] and Shen [124].

It should be remembered that the assumptions that have been made to arrive at equation (2.35) limit its usefulness to pulses with a duration down to ~ 1 ps. For shorter pulses, a more accurate description of P_{NL} is required. Also, to properly describe stimulated inelastic scattering a complex-valued $\chi^{(3)}$ is required, while Raman effects can only be incorporated through a time delayed response in (2.32). When very short pulses or materials with complicated dispersion are involved, the equation can be augmented by higher-order terms in the dispersion expansion [119, 120] as written in equation (2.16).

2.2 Principle and implementation of frequency combs

2.2.1 Pulse trains and their spectrum

The previous section described the propagation of single ultrashort laser pulses. Now consider the case of a train consisting of multiple ultrashort pulses, spaced by a time delay T . The electric field of this pulse train can be written as (see e.g. [125]):

$$E_{\text{train}}(t) = \sum_{n=0}^{N-1} E(t - nT) e^{-in\Delta\varphi} \quad (2.36)$$

where $E(t)$ is the electric field of a single pulse and N is the total number of pulses. Also, the possibility of a pulse-to-pulse carrier-envelope phase shift $\Delta\varphi$ needs to be taken into account due to a possible difference between the group- and phase velocity of the pulses (see section 2.1.5). The intensity and shape of the pulses are assumed to be constant throughout the entire pulse train, and therefore the Fourier transforms of the individual pulses will be identical up to a phase factor:

$$\mathcal{FT}[E(t - nT)] = e^{-in(\omega T + \Delta\varphi)} \mathcal{FT}[E(t)] \quad (2.37)$$

With this in mind Eq. (2.36) can be Fourier transformed to the frequency domain, and the summation can be solved[‡]:

$$\begin{aligned} E_{\text{train}}(\omega) &= E(\omega) \sum_{n=0}^{N-1} e^{-in(\omega T + \Delta\varphi)} \\ &= E(\omega) \frac{1 - e^{-iN(\omega T + \Delta\varphi)}}{1 - e^{-i(\omega T + \Delta\varphi)}} \end{aligned} \quad (2.38)$$

[‡]Using the solution of a standard series:

$$\sum_{n=0}^{N-1} x^n = \frac{1 - x^N}{1 - x}.$$

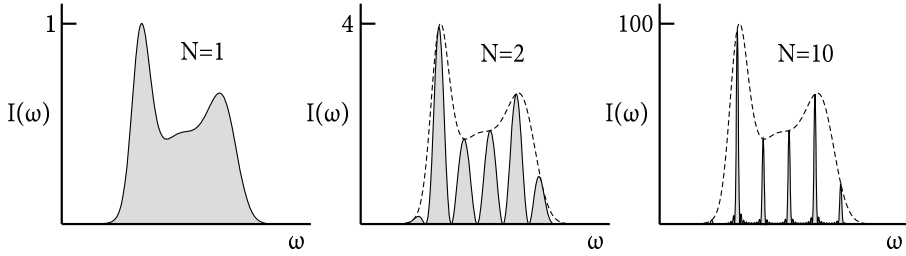


FIGURE 2.1: Spectrum of a train of N pulses. While the single-pulse spectrum determines the intensity of the respective modes, the position and width of the modes is completely determined by the time delay, the pulse-to-pulse phase shift, and the number of pulses.

From this expression for the electric field of the pulse train, we can calculate the intensity as a function of frequency $I(\omega)$:

$$I(\omega) = |E(\omega)|^2 = \frac{\sin^2 [N(\omega T + \Delta\varphi)/2]}{\sin^2 [(\omega T + \Delta\varphi)/2]} I_0(\omega) \quad (2.39)$$

We find that the spectrum of a train of identical pulses that are regularly spaced in the time domain consists of an equally spaced fringe pattern in the frequency domain. Equation (2.39) describes the formation of fringes with a repetition frequency $1/T$, which become increasingly narrow as more pulses contribute. The effect of the pulse-to-pulse carrier-envelope phase shift is that it causes a shift of the fringe maxima in the interference pattern by an amount $\Delta\varphi/2\pi T$. For $N = 1$, the spectrum is simply the single-pulse spectrum $I_0(\omega)$. When a second pulse is added, Eq. (2.39) still consists of the single-pulse spectrum, but with a cosine-shaped amplitude modulation imprinted on it:

$$I(\omega) = 4I_0(\omega) \cos^2 \frac{\omega T + \Delta\varphi}{2} \quad (2.40)$$

A graphical representation of Eq. (2.39) for the cases of $N=1, 2$ and 10 is given in Fig. 2.1: the cosine-modulation of Eq. (2.40) and the rapid narrowing of the fringes for $N \gg 1$ are clearly visible.

In the limit of $N \rightarrow \infty$, the fringe pattern behaves in an interesting way. When $\omega T + \Delta\varphi \rightarrow n2\pi$, both the numerator and the denominator in relation (2.39) tend to zero. A proper evaluation of this limit leads to:

$$\lim_{\omega T + \Delta\varphi \rightarrow n2\pi} \frac{\sin^2 [N(\omega T + \Delta\varphi)/2]}{\sin^2 [(\omega T + \Delta\varphi)/2]} I_0(\omega) = N^2 I_0(\omega) \quad (2.41)$$

showing that the intensities of the fringe maxima scale quadratically with N . However, when $\omega T \neq n2\pi$, the intensity tends to zero due to destructive interference between the pulses. In general, the limit of Eq. (2.39) for $N \rightarrow \infty$ can be expressed as:

$$\lim_{N \rightarrow \infty} \frac{\sin^2 [N(\omega T + \Delta\varphi)/2]}{\sin^2 [(\omega T + \Delta\varphi)/2]} I_0(\omega) = I_0(\omega) \sum_{n=0}^{\infty} \delta(\omega T + \Delta\varphi - n2\pi) \quad (2.42)$$

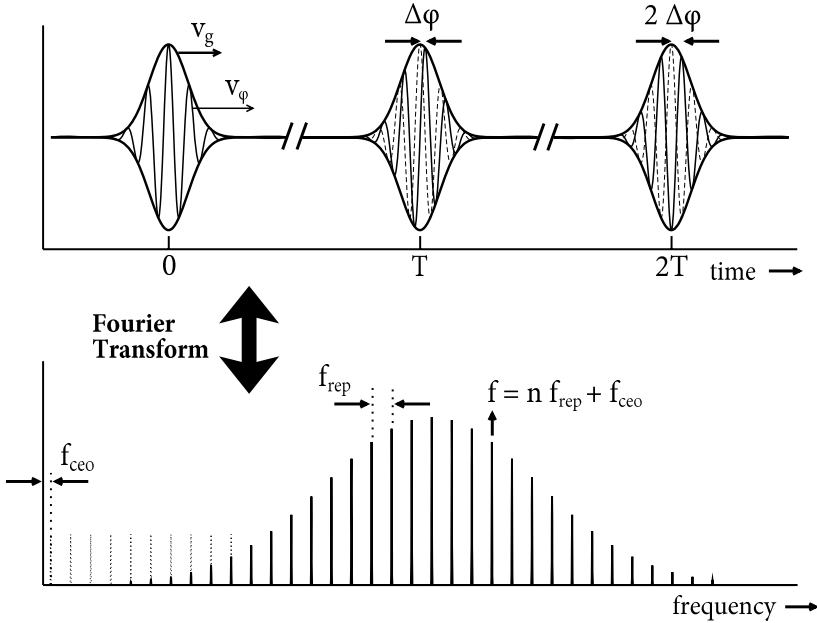


FIGURE 2.2: The relation between time and frequency domain. A train of ultrashort pulses equally spaced by a time T corresponds to a comb of equidistant narrow lines in the frequency domain. These comb lines are separated by the repetition frequency $f_{\text{rep}} = 1/T$. Note that due to the difference between phase and group velocity ($v_{\phi} \neq v_g$) a carrier-envelope phase shift appears between consecutive pulses. This results in a shift of all comb lines by $f_{\text{ceo}} = (\Delta\phi/2\pi)f_{\text{rep}}$.

The spectrum of an infinitely long train of identical pulses is found to consist of a comb of extremely narrow frequency spikes, provided that the time delay T and the carrier-envelope phase shift $\Delta\phi$ remain constant from pulse to pulse [103, 126]. In reality, the comb modes will of course not be infinitely narrow: Similar to every realistic light source, the laser that emits the pulse train will have a certain stability, which leads to a finite linewidth of the comb modes. But with proper laser stabilization, this linewidth can be kept extremely small, and Hz-level linewidths have been demonstrated for the modes of such a frequency comb [127].

From the preceding analysis, we obtain a remarkable result: The absolute frequencies of the frequency comb modes are given by the simple relation $f_n = \Delta\phi/2\pi T + n/T$ (note that from here on we will use the “true” frequency $f = \omega/2\pi$ instead of the angular frequency ω , as this is more convenient to describe experimental observations). We can make this relation more insightful by defining the pulse repetition frequency $f_{\text{rep}} = 1/T$ and the carrier-envelope frequency $f_{\text{ceo}} = (\Delta\phi/2\pi)f_{\text{rep}}$. Using these terms, we can write the expression for the n^{th} mode of the frequency comb as:

$$f_n = n f_{\text{rep}} + f_{\text{ceo}} \quad (2.43)$$

which states that the absolute frequency of every comb mode is completely determined

by the two frequencies f_{rep} and f_{ceo} . But f_{rep} and f_{ceo} are in the radio-frequency (RF) domain (typically $f_{\text{rep}} \sim 10 \text{ MHz} - 1 \text{ GHz}$), while the frequency comb operates at optical frequencies (hundreds of THz). Thus, a frequency comb provides a phase-coherent link between the optical and RF frequency domains: If we can stabilize f_{rep} and f_{ceo} to an absolute RF frequency reference such as an atomic clock, we can use the frequency comb to measure the absolute frequency of light with an accuracy that can approach the noise limit of the RF reference. In addition, since the frequencies of all the comb modes are defined by the simple relation (2.43), the stabilization of the RF frequencies f_{rep} and f_{ceo} can provide an array of precisely known optical frequencies across a large spectrum ($\sim 10^6$ modes for a train of pulses with 10 fs duration), making the frequency comb an extremely powerful tool for optical metrology. A schematic drawing of the relation between time- and frequency domains for such a frequency comb laser pulse train is shown in Fig. 2.2. With the principles described here as a starting point, the next paragraphs discuss how to construct such a frequency comb in practice.

2.2.2 The modelocked Ti:Sapphire oscillator

A natural starting point for the generation of a frequency comb is the use of a modelocked laser, which emits the required train of ultrashort pulses [97]. The laser oscillator that forms the basis for our frequency comb is the Femtosource Scientific Pro from FemtoLaser GmbH, pumped by 5.5 W of 532 nm light from a single-mode continuous-wave Nd:YVO₄ laser (Coherent Verdi X). It is a Kerr-lens modelocked Ti:Sapphire laser with a linear cavity design, as shown in Fig. 2.3. Dispersion compensation is implemented using chirped mirrors, allowing pulses with a bandwidth from 680 to 950 nm to form. The pulses emitted by this laser have a duration of 11 fs and an energy of 7 nJ. The cavity is 2 metres long, leading to a 75 MHz pulse repetition rate. The repetition rate can be varied roughly between 60 MHz and 85 MHz by changing the cavity length. Outside this range, stable modelocked operation becomes difficult to maintain.

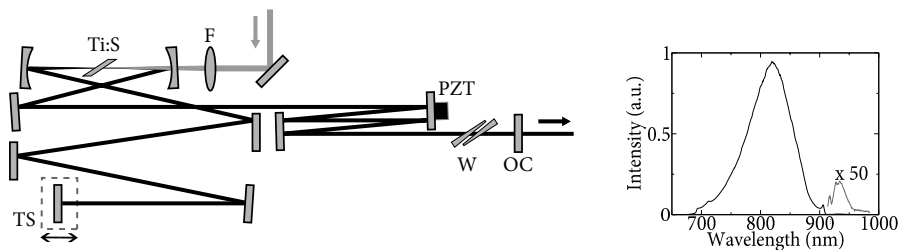


FIGURE 2.3: Schematic of the Femtosource Scientific Pro. The pump beam is focused in a Ti:Sapphire crystal (Ti:S), and modelocking is induced by providing a rapid disturbance to the translation stage (TS). The cavity length is stabilized by a mirror mounted on a piezo-transducer (PZT). A pair of fused silica wedges (W) is used for rough tuning of the pulse-to-pulse carrier-envelope phase slip. The pulses are coupled out by a 90% output coupler (OC). The graph on the right shows a typical output spectrum of the laser, where the long wavelength side has been magnified for clarity (grey trace).

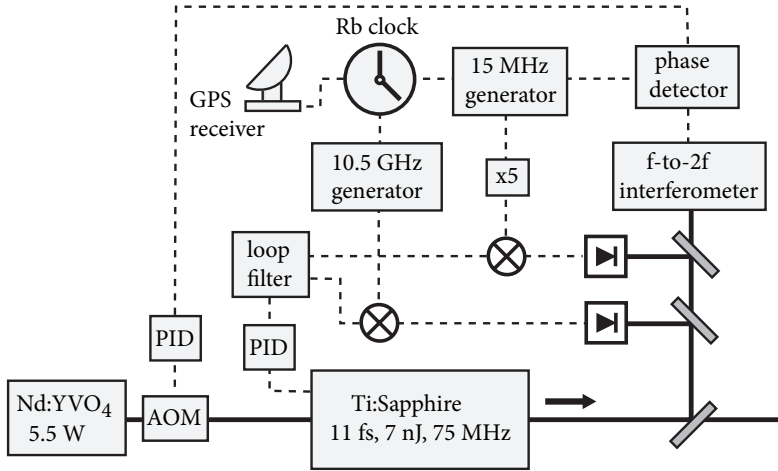


FIGURE 2.4: Schematic layout of the frequency comb setup. Details are given in the text.

In addition to this commercial laser system, a home-built Ti:Sapphire oscillator has been developed which employs more broadband dispersion compensation than the Femtsource. The output spectrum of this laser extends from 670 to 1100 nm, and Fourier transforming leads to a pulse duration of 6.2 fs. The repetition rate of this laser can be varied from 70 MHz to 330 MHz, and the pulse energy is typically 5 nJ at 75 MHz. In most experiments described in this thesis, the commercial Femtsource has been used; the home-built ultra-broadband oscillator has only been developed recently, and this laser was used for the experiments described in chapter 8.

2.2.3 Repetition rate locking

To operate the modelocked laser as a frequency comb, the repetition rate and carrier-envelope phase of the emitted pulse train need to be stabilized [103]. A schematic overview of the stabilization scheme for the frequency comb laser is depicted in Fig. 2.4. The repetition rate is controlled by stabilizing the oscillator cavity length using a piezoelectric transducer. As the RMS timing jitter of the synchronization scales with the inverse of the locking frequency, we have implemented the stabilization circuitry for both the 75 MHz fundamental frequency and for the 140th harmonic at 10.5 GHz. This 140th harmonic of the repetition rate is detected using a fast photodiode (EOT ET-4000), and mixed with the output of a highly stable RF generator (Agilent E8241 PSG-L) which is phase-locked to a Rubidium atomic clock (Stanford Research Systems PRS-10, 10 s Allan variance $< 1 \times 10^{-11}$). The mixer output is sent to a PID controller, which provides the appropriate feedback signal to the piezo-driver. In addition, the feedback signal also controls the laser-baseplate temperature by switching heating resistors on the baseplate on and off. This temperature stabilization provides additional (albeit coarse) control over the cavity length at longer timescales. To obtain an absolute

frequency reference, the Rb clock is continuously disciplined to the Global Positioning System, using the one-pulse-per-second output signal of a GPS receiver (Trimble Acutime 2000) mounted on the roof of the building.

The system allows switching from one loop to the other while keeping the laser in lock, a feature that is very useful for controlling the relative pulse timing between two separate lasers locked to the same 10.5 GHz oscillator, as will be discussed later in section 5.2.1.

2.2.4 The f -to- $2f$ technique

While stabilization of the repetition frequency is relatively straightforward, getting control over the carrier-envelope frequency f_{ceo} is more involved. Since the laser spectrum does not contain any power at frequencies close to zero, f_{ceo} can not be measured directly. This problem has been solved by the development of the f -to- $2f$ technique [105, 106], which is schematically depicted in Fig. 2.5. In the f -to- $2f$ scheme, a low-frequency comb mode is frequency-doubled using second harmonic generation, resulting in a frequency component:

$$f = 2 \times (n f_{\text{rep}} + f_{\text{ceo}}) = m f_{\text{rep}} + 2 f_{\text{ceo}}$$

where $m = 2n$. If the spectrum of the frequency comb spans a full octave, such a doubled low-frequency mode can be compared to a high-frequency comb mode with mode number m that is also present in the spectrum, but at the frequency:

$$f = m f_{\text{rep}} + f_{\text{ceo}}$$

These modes can be overlapped in an interferometer, and the resulting signal will then contain the beat (difference) frequency:

$$\Delta f = 2 \times (n f_{\text{rep}} + f_{\text{ceo}}) - (m f_{\text{rep}} + f_{\text{ceo}}) = f_{\text{ceo}}$$

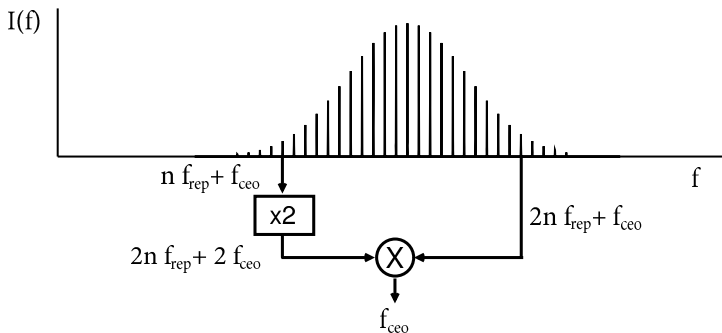


FIGURE 2.5: The f -to- $2f$ principle of carrier-envelope phase measurement. A low-frequency comb mode is frequency-doubled and compared to a high-frequency mode in a beat experiment. The generated beat signal then contains the carrier-envelope frequency f_{ceo} , which can be isolated by low-pass filtering. This measurement principle is only applicable if the spectrum of the frequency comb spans a full octave.

which is simply the carrier-envelope frequency f_{ceo} . In practice, the beat signal will contain additional frequencies due to interference between various additional modes such as e.g. the frequency-doubled n^{th} mode and the $2n + 1^{\text{st}}$ mode, leading to a set of frequencies:

$$f_{\text{ceo}}, f_{\text{rep}} - f_{\text{ceo}}, f_{\text{rep}} + f_{\text{ceo}}, 2f_{\text{rep}} - f_{\text{ceo}}, \dots$$

therefore the desired f_{ceo} -signal must be isolated using appropriate low-pass and/or band-pass filtering.

Using this f -to- $2f$ scheme, f_{ceo} can be measured and compared to an RF reference signal. However, stabilization of the frequency comb requires a certain degree of external control over f_{ceo} . Since f_{ceo} is related to the pulse-to-pulse phase shift through $f_{\text{ceo}} = (\Delta\varphi/2\pi)f_{\text{rep}}$, stabilization of f_{ceo} can be achieved by controlling both f_{rep} and $\Delta\varphi$. As already mentioned earlier, the pulse-to-pulse phase shift $\Delta\varphi$ is caused by the difference between the phase velocity and the group velocity of the pulses. Therefore, $\Delta\varphi$ can be stabilized by controlling the ratio v_φ/v_g inside the laser cavity. Several ways of achieving this have been demonstrated, e.g. by tilting the end mirror in a prism-dispersion-compensated modelocked laser [105], or by modulating the pump intensity inside the gain medium of a Kerr-lens modelocked laser with an acousto-optic modulator (AOM) in the pump beam [106]. As such a laser depends on the Kerr-effect for stable modelocking, the pump intensity inside the laser crystal needs to be sufficiently high to induce a significant nonlinear refractive index. A modulation of the pump intensity will then also lead to a variation of the refractive index of the laser crystal, which changes v_φ and v_g by different amounts and thus provides the required control knob on $\Delta\varphi$. It has been shown that since v_φ and v_g have a different intensity dependence, it is possible to find a set of operating parameters of an oscillator at which the ratio v_φ/v_g becomes independent of the intensity to first order [128]. At this point, φ_{ce} displays a high passive stability (i.e. without locking). An additional coarse control over $\Delta\varphi$ can be implemented by placing a pair of quartz wedges in the laser. Moving one of the wedges changes the amount of dispersive material in the cavity, leading to a variation of the ratio between v_φ and v_g .

2.2.5 Spectral broadening to an optical octave

The f -to- $2f$ technique provides the means to measure f_{ceo} , enabling the construction of a fully-stabilized optical frequency comb. But in order for the f -to- $2f$ scheme to work, the width of the comb spectrum needs to span (or rather exceed) a full octave, i.e. the spectrum should contain both a frequency component f on the low-frequency side, as well as a frequency component $2f$ on the high-frequency side. Typical modelocked lasers do not emit such ultra-broadband spectra, although some octave-spanning Ti:Sapphire oscillators have recently been demonstrated [129–131]. In general, the output of the modelocked lasers needs to be spectrally broadened.

Spectral broadening of the laser output is possible because of the high peak intensity of ultrashort pulses, which can reach the MW range even for the low-energy pulses from a modelocked oscillator. These pulses can be broadened through their nonlinear interaction with materials as described in section 2.1.7, leading to effects such as

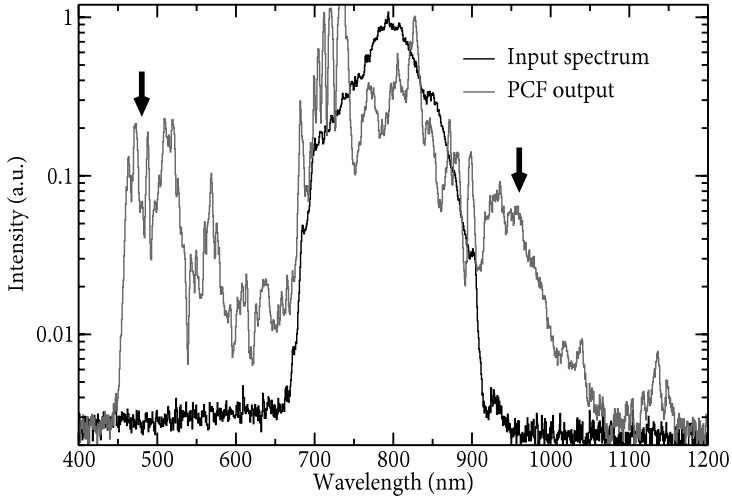


FIGURE 2.6: Broadening of the laser spectrum using a photonic crystal fiber (logarithmic intensity scale). The grey curve is the output from a 6 cm long, $1.7 \mu\text{m}$ core diameter PCF. The arrows indicate the spectral components used in the f -to- $2f$ stabilization scheme.

self-phase-modulation (SPM), four-wave mixing, etc. However, when using oscillator pulses sufficient broadening is usually only achieved after interaction of a tightly focused beam with several centimetres of material. As any bulk material introduces group-velocity dispersion, ultrashort pulses broaden rapidly in duration, leading to an equally rapid decrease in peak intensity which hampers the nonlinear interaction. A solution to this problem has been the development of photonic crystal fibers (PCF's), which are optical fibers with a lattice of airholes around the core [107]. The structure of these PCF's can be engineered such that the group-velocity dispersion is zero around the carrier wavelength of an optical pulse, allowing the pulse to retain its peak intensity over many centimeters of propagation inside the fiber.

Coupling the pulse train from a modelocked oscillator into a PCF leads to large amounts of nonlinear spectral broadening, generating supercontinuum output spectra that easily span a full octave [132]. Figure 2.6 shows the broadening of 10 fs, $\sim\text{nJ}$ pulses in a 6 cm long PCF with a core diameter of $1.7 \mu\text{m}$. The spectrum at the fiber output extends from 450 to 1050 nm, exceeding the octave width required for the f -to- $2f$ technique. The arrows drawn in the figure at 480 and 960 nm indicate the spectral components used in our implementation of the f -to- $2f$ scheme, which is described in detail in the next section.

2.2.6 Carrier-envelope phase stabilization

The first implementation of the f -to- $2f$ scheme was based on a Mach-Zehnder interferometer [105, 106]. Following this design, we initially also constructed a Mach-Zehnder-type f -to- $2f$ interferometer, which is shown in Fig. 2.7. The advantages of such a setup

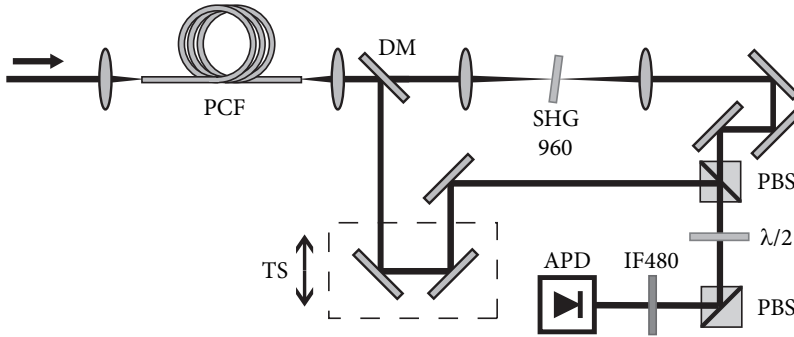


FIGURE 2.7: The Mach-Zehnder f -to- $2f$ interferometer. PCF: Photonic crystal fiber, SHG: BBO crystal for second harmonic generation, PBS: Polarizing beamsplitter, $\lambda/2$: half-wave plate, IF480: Interference filter for 480 nm, APD: Avalanche photodiode, TS: Translation stage.

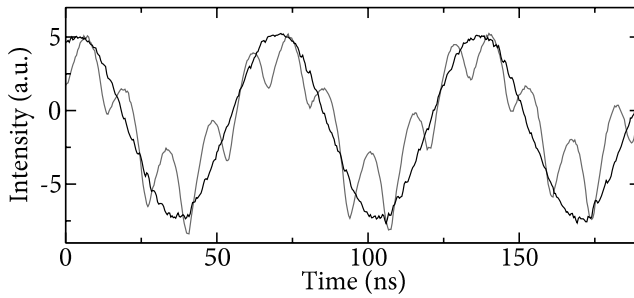


FIGURE 2.8: The f -to- $2f$ output signal in time (grey curve). The two frequency components at f_{ceo} and f_{rep} are clearly visible. The black curve is the isolated f_{ceo} signal after bandpass filtering.

are the straightforward alignment, and the option to incorporate an AOM in one of the interferometer arms to lock the carrier-envelope offset frequency f_{ceo} to zero. The spectrum of the Ti:Sapphire oscillator pulses is broadened to more than one octave in a 6 cm photonic crystal fiber (PCF, Crystal Fiber A/S) with $1.7 \mu\text{m}$ core diameter. A dichroic mirror separates the infrared and blue spectral components, each passing through one interferometer arm. The infrared spectrum around 960 nm is frequency doubled in a 1 mm thick type I BBO crystal, and the resulting 480 nm radiation is recombined with the blue spectral components from the PCF using a polarizing beamsplitter. The delay in the interferometer is adjusted to temporally overlap the pulses from both arms, and the relative pulse intensity is controlled with a $\lambda/2$ -plate and a polarizing beamsplitter. The relevant spectrum around 480 nm is selected by an interference filter, and the light is focused onto an avalanche photodiode (APD, Analog Modules Inc. 712A-4). Besides frequency components at integer times the oscillator repetition rate, the APD output signal contains a beat signal corresponding to f_{ceo} (see Figs. 2.8 and 2.9).

This beat signal is isolated using bandpass filters, and the output signal from the

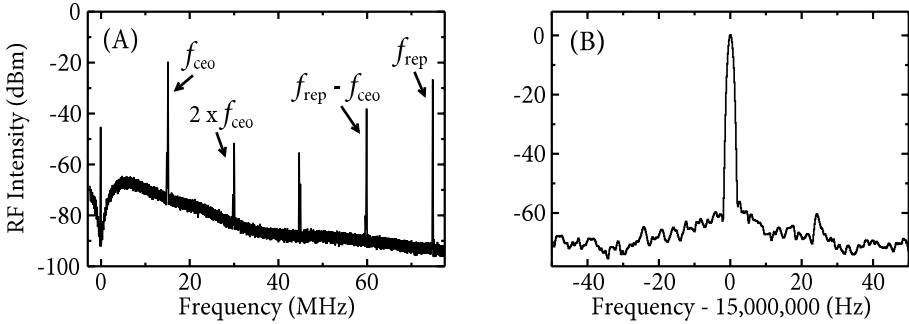


FIGURE 2.9: Measuring f_{ceo} with the f -to- $2f$ scheme. **(A)** Besides the laser repetition frequency f_{rep} , the output of the avalanche photodiode shows a strong signal at f_{ceo} , as well as higher-order and difference frequency signals. The non-flat background is due to the APD response. The resolution bandwidth in this scan is 10 kHz, and the video bandwidth is 1 kHz. **(B)** A high-resolution scan of the (stabilized) f_{ceo} peak reveals a 60 dB signal-to-noise ratio in a 1 Hz resolution bandwidth (with 1 Hz video bandwidth). The peak has a 3 dB width of 1 Hz, limited by the spectrum analyzer resolution.

APD before and after bandpass filtering is shown in Fig. 2.8. After filtering, a clean sinusoidal signal remains, which allows phase-locking to an RF reference waveform generator (Agilent 33120A) with high fidelity. Stabilization of f_{ceo} is achieved using a phase detector and a PID controller that modulates the intensity of the pump laser power to the oscillator through an AOM. The degree of stabilization can be verified in both time and frequency domain: Fig. 2.9B shows a high-resolution scan from a spectrum analyzer (Agilent E4440A). The locked beat signal is 1 Hz wide at -3 dB below the peak, which is limited by the resolution of the spectrum analyzer.

When characterizing the stability of the f_{ceo} , it should be realized that beatnote spectra as shown in Fig. 2.9 are measured inside the feedback loop, i.e. the same interferometer is used for both measurement and locking. Such in-loop measurements can be unreliable if the feedback-electronics or the f -to- $2f$ interferometer introduces phase noise on f_{ceo} , as this noise signal is then written onto the laser output. A particularly important question is whether the highly nonlinear processes involved in continuum generation in the PCF will retain the structure of the input pulse train, or that unwanted effects such as amplitude-to-phase coupling cause large amounts of phase noise on f_{ceo} .

We verified the degree of phase stability by constructing a second, similar f -to- $2f$ interferometer to measure the f_{ceo} beat signal independently, outside of the feedback loop. Since any possible amplitude-to-phase coupling would influence both f -to- $2f$ measurements in a similar way, we coupled twice as much pulse energy into this second interferometer to avoid common-mode effects in the measurement analysis. In addition to the spectral measurements as shown in Fig. 2.9, we obtained data on the phase shift between the detected f_{ceo} signal and the RF reference oscillator directly in the time domain, by recording both signals with a 4 GHz sampling oscilloscope (Tektronix TDS7404). The difference between these two measured signals then yields the

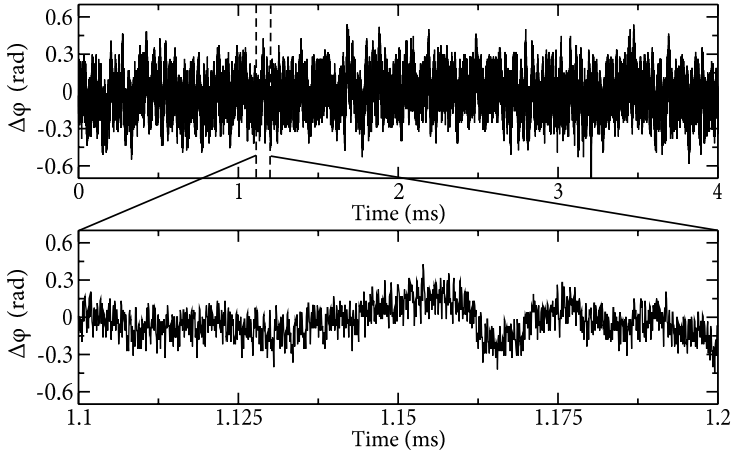


FIGURE 2.10: Measurement of the carrier-envelope phase deviations using a second f -to- $2f$ interferometer outside of the stabilization loop. The RMS phase stability is 152 mrad.

instantaneous deviations of the pulse-to-pulse carrier-envelope phase shift $\Delta\phi$, and a typical scan is displayed in Fig. 2.10. The root-mean-square phase deviations of $\Delta\phi$ are found to be 152 mrad, which is less than $1/40^{\text{th}}$ of an optical cycle of the pulse carrier wave. Therefore, we can conclude that the continuum generation and the feedback electronics combined introduce less than 152 mrad of RMS phase noise on f_{ceo} , and that the f -to- $2f$ technique is a reliable method for f_{ceo} -stabilization.

Although the Mach-Zehnder type f -to- $2f$ setup works properly and is employed by most groups working with frequency combs, we developed an alternative setup based on a Michelson interferometer that exhibits substantial advantages compared to the Mach-Zehnder system. The setup is depicted in Fig. 2.11. Instead of separating the various spectral components behind the PCF, we focus the entire beam through the SHG crystal, which is only phase-matched for wavelengths around 960 nm. The generated second harmonic is separated from the 480 nm light directly from the PCF us-

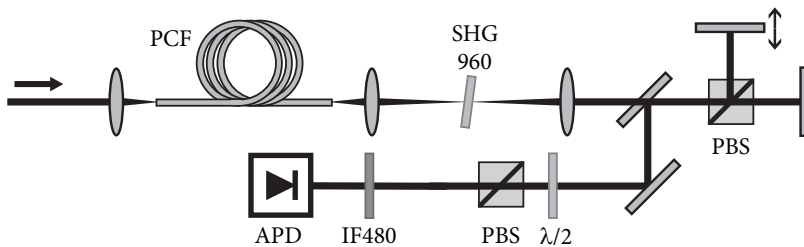


FIGURE 2.11: The Michelson f -to- $2f$ interferometer. See Fig. 2.7 for the abbreviations.

ing a polarizing beamsplitter. The relative delay between both beams is minimized in a Michelson-type setup. Both beams are recombined, their relative intensities are set equal, filtered and detected in the same way as in the Mach-Zehnder setup. The main advantages of the Michelson over the Mach-Zehnder f -to- $2f$ system are the reduced size and the robustness against misalignment, but most notably the fact that the beams are only separated for about 1 cm inside the actual interferometer, leading to a much reduced sensitivity to ambient noise. We have been able to robustly lock the carrier-envelope phase without shielding this interferometer against air flow and acoustic noise, which was not possible with our previous setup using a Mach-Zehnder interferometer.

2.2.7 Measuring the frequency of a continuous-wave laser

When both the repetition rate and the carrier-envelope phase have been stabilized, the absolute frequencies of all the comb modes are known. The absolute frequency of a narrow-band, continuous-wave (cw) laser can then be measured by generating a beat signal between the cw laser and the nearest mode of the frequency comb. A typical setup for such measurements is shown in Fig. 2.12. In this scheme, a grating-based $4f$ -spectrometer is employed to spatially disperse the comb modes, so that ideally only the cw laser beam and the comb mode that is closest in frequency fall onto the detector (in practice usually a few tens of modes reach the detector, depending on the spectrometer, the size of the slit and the repetition rate of the frequency comb laser). The frequency difference f_{beat} between the cw laser and this comb mode results in a beat signal, which is measured using an avalanche photodiode. The frequency of the narrow-band laser can then simply be determined as $f_{\text{cw}} = n f_{\text{rep}} + f_{\text{ceo}} + f_{\text{beat}}$, with an accuracy that is only limited by the bandwidths of the cw laser and the comb mode, and ultimately by the stability of the RF reference standard.

We employed this technique to calibrate a single-mode cw Ti:Sapphire laser (Coherent 899), operating at a wavelength of around 800 nm [133, 134]. In these measurements, the width of the beat signal f_{beat} is determined by the bandwidth and fast

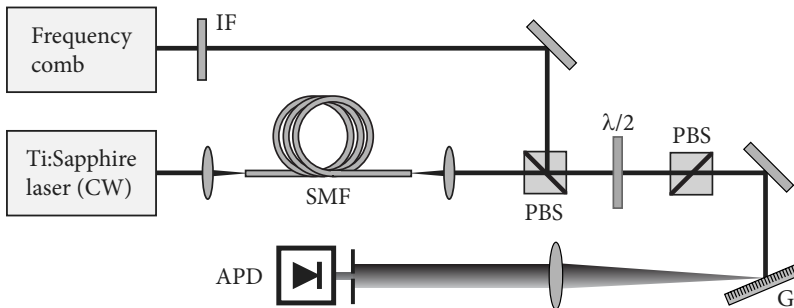


FIGURE 2.12: Setup for measurement of the frequency of a cw laser using the frequency comb. The notation is identical to Fig. 2.7, G: Grating, SMF: Single-mode fiber.

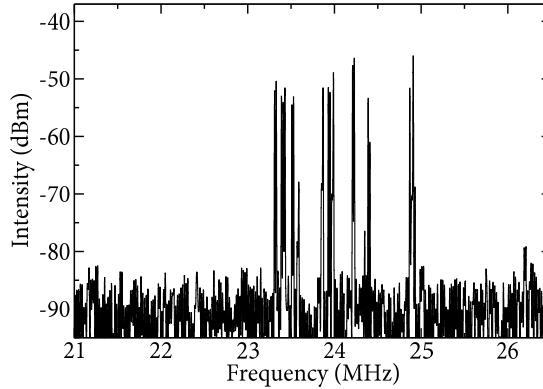


FIGURE 2.13: Measured beat signal between a cw Ti:Sapphire laser and a frequency comb mode. By monitoring the exact frequency of this beat signal, the absolute frequency of the cw laser can be obtained. This particular trace has been taken with a 12 kHz resolution bandwidth and 50 ms sweep time. Within this sweep time, the cw Ti:Sapphire experiences frequency fluctuations on a timescale much faster than the sweep time, leading to the multiple peak structure in the scan.

frequency jitter of the cw laser, and has an estimated contribution of about 1 MHz from the linewidth of the frequency comb tooth. A typical beatnote signal is shown in Fig. 2.13. The width of the f_{beat} beat signal is determined by the bandwidth and fast frequency jitter of the cw laser, and has an estimated contribution of about 1 MHz from the linewidth of the frequency comb tooth. The frequency of this signal is then monitored using a counter (Agilent 53132A). With sufficient averaging, both f_{rep} and f_{ceo} can be measured with 11-digit accuracy, leading to a calibration of the cw laser with \sim kHz precision. The accuracy can be increased further by reducing the linewidth of the cw laser, which can be achieved by locking the laser to a high-finesse reference cavity. When a cesium fountain clock is used as an RF reference, a frequency accuracy at the 10^{-15} level has been demonstrated by several groups [88–91].

2.3 Quantum interference metrology

The techniques that were discussed in the previous section have turned the frequency comb into an indispensable tool for the measurement of absolute optical frequencies of narrow-band continuous-wave lasers that are used to perform high-resolution spectroscopy. In this section, a method for high-resolution spectroscopy is presented that employs the frequency comb pulses directly for excitation of the transition under study. With this technique, high-precision frequency measurements can be performed without the need for narrow-band lasers.

The technique is based on the principle of coherent atomic excitation with a train of phase-controlled laser pulses. Therefore, the next paragraph provides the general formalism describing the coherent interaction of light with an ideal two-level system. In the rest of the section, the results of this first paragraph are then applied to the specific

case of excitation with a train of ultrashort laser pulses, with which the desired method for high-resolution spectroscopy can be explained.

2.3.1 Coherent light-matter interaction

Consider a two-level atom, with a ground state $|g\rangle$ and an excited state $|e\rangle$. When the amplitudes of these states are given by c_g and c_e , respectively, we can write the wave-function of the two-level atom as:

$$|\psi\rangle = \begin{pmatrix} c_e \\ c_g \end{pmatrix} \quad (2.44)$$

When such an atom is excited by an approximately resonant laser field $\mathbf{E}(t) = E_0(e^{i\omega_L t} + e^{-i\omega_L t})$, then the Schrödinger equation of the system can be written in the dipole approximation as [135]:

$$\begin{aligned} i\hbar \frac{\partial |\psi\rangle}{\partial t} &= H_0 |\psi\rangle - \mathbf{d} \cdot \mathbf{E} |\psi\rangle \\ &= \hbar \begin{pmatrix} \omega_0/2 & -\Omega(e^{i\omega_L t} - e^{-i\omega_L t}) \\ -\Omega^*(e^{i\omega_L t} - e^{-i\omega_L t}) & -\omega_0/2 \end{pmatrix} |\psi\rangle \end{aligned} \quad (2.45)$$

where $\Omega = \mathbf{d} \cdot \mathbf{E}_0/\hbar$ is the Rabi frequency, $\omega_0 = (E_e - E_g)/\hbar$ is the angular transition frequency between $|g\rangle$ and $|e\rangle$, and \mathbf{d} is the dipole operator. This equation can be simplified considerably by transforming to a frame rotating with the laser frequency, using the unitary transformation:

$$|\psi\rangle \rightarrow U|\psi\rangle \quad \text{and} \quad H \rightarrow -i\hbar U^\dagger \dot{U} + U^\dagger H U \quad (2.46)$$

in which:

$$U = \begin{pmatrix} e^{-i\omega_L t/2} & 0 \\ 0 & e^{i\omega_L t/2} \end{pmatrix} \quad (2.47)$$

This transformation leads to the equation:

$$\begin{aligned} i\hbar \frac{\partial |\psi\rangle}{\partial t} &= \hbar \begin{pmatrix} -\frac{1}{2}(\omega_L - \omega_0) & -i\Omega(1 + e^{2i\omega_L t}) \\ i\Omega^*(1 + e^{-2i\omega_L t}) & \frac{1}{2}(\omega_L - \omega_0) \end{pmatrix} |\psi\rangle \\ &\approx \hbar \begin{pmatrix} -\frac{\Delta}{2} & -\Omega \\ -\Omega^* & \frac{\Delta}{2} \end{pmatrix} |\psi\rangle \end{aligned} \quad (2.48)$$

In this last step we introduce the detuning $\Delta = \omega_L - \omega_0$, and the rotating-wave approximation has been used: Since $\omega_0 \approx \omega_L$, the rapidly oscillating $\pm 2\omega_L t$ phase terms are assumed to average out very quickly, and can therefore be neglected. As a result, equation (2.48) is now time-independent, allowing direct integration. The formal solution for the wave-function at a time t is then:

$$\begin{pmatrix} c_e(t) \\ c_g(t) \end{pmatrix} = e^{-iHt/\hbar} \begin{pmatrix} c_e(0) \\ c_g(0) \end{pmatrix} \quad (2.49)$$

The exponentiated operator $e^{-iHt/\hbar}$ is only defined through its series expansion [135]:

$$e^{-iHt/\hbar} = e^{it\mathbf{a}\cdot\boldsymbol{\sigma}} = \sum_{n=0}^{\infty} \frac{1}{n!} (it\mathbf{a}\cdot\boldsymbol{\sigma})^n \quad (2.50)$$

where we have expanded the Hamiltonian as $H = \hbar\mathbf{a}\cdot\boldsymbol{\sigma}$, with:

$$\mathbf{a} = \begin{pmatrix} \text{Re}\Omega \\ -\text{Im}\Omega \\ \frac{\Delta}{2} \end{pmatrix} \text{ and } \boldsymbol{\sigma} = \begin{pmatrix} \sigma_x \\ \sigma_y \\ \sigma_z \end{pmatrix}, \quad (2.51)$$

in which $\boldsymbol{\sigma}$ is the vector of the Pauli matrices:

$$\sigma_x = \begin{pmatrix} 0 & 1 \\ 1 & 0 \end{pmatrix}, \quad \sigma_y = \begin{pmatrix} 0 & -i \\ i & 0 \end{pmatrix}, \quad \sigma_z = \begin{pmatrix} 1 & 0 \\ 0 & -1 \end{pmatrix} \quad (2.52)$$

Using this expansion, we arrive at the final form of the time evolution operator (2.50):

$$e^{-iHt/\hbar} = \mathbf{1} \cos at + i \frac{\mathbf{a}\cdot\boldsymbol{\sigma}}{a} \sin at \quad (2.53)$$

where the unit matrix is denoted as $\mathbf{1}$, and $a = |\mathbf{a}| = \sqrt{\left(\frac{\Delta}{2}\right)^2 + |\Omega|^2}$ is known as the Rabi flopping frequency. Using this time evolution operator, the final state of the two-level system can be calculated as a function of time, provided the initial wave-function and the laser parameters Δ and Ω are known.

2.3.2 Excitation with a phase-coherent pulse pair

Using the time-evolution operator (2.53), we can calculate the final state wave-function after excitation with a square pulse of duration τ , assuming the atoms are initially in the ground state. Straightforward application of equation (2.49) leads to:

$$\begin{pmatrix} c_e(\tau) \\ c_g(\tau) \end{pmatrix} = \begin{pmatrix} i \frac{\Omega}{a} \sin a\tau \\ \cos a\tau - i \frac{\Delta}{2a} \sin a\tau \end{pmatrix} \quad (2.54)$$

The amplitudes of both levels undergo Rabi oscillations as a function of time, with an amplitude and period determined by the Rabi flopping frequency a . The amplitude of the excited state for small times τ is mostly determined by the electric field strength through the Rabi frequency Ω .

Now consider excitation of the atom by a pair of time-delayed laser pulses with a well-defined phase relationship. The pulse shape is again approximated as a square to neglect any possible time dependence of Ω (this approximation only holds when the pulses are relatively weak, $\Omega\tau \ll 1$). The wave-function after the first pulse has just been calculated to be (2.54). The field-free period in between the pulses is also described by the evolution operator (2.53), with Ω set to zero. The electric field of the second pulse is taken identical to the first pulse, aside from a time delay T and a phase shift φ , leading to $\mathbf{E}(t) = \mathbf{E}_0(e^{i\omega_L(t-T)-i\varphi} + e^{-i\omega_L(t-T)-i\varphi})$. To accommodate for this phase shift of

$\omega_L T + \varphi$, a different unitary transformation is required to make the Hamiltonian time-independent as required for using equation (2.49). This also means that $|\psi\rangle$ needs to be transformed to this new reference frame before applying the second pulse, using the transformation matrix:

$$U = \begin{pmatrix} e^{-i(\omega_L T + \varphi)/2} & 0 \\ 0 & e^{i(\omega_L T + \varphi)/2} \end{pmatrix} \quad (2.55)$$

The second pulse can then be modeled using again the evolution operator (2.53). After the pulse sequence, the resulting excited state amplitude is found to be:

$$\begin{aligned} c_{e2} &= \frac{2\Omega \sin a\tau}{a^2} \left(a \cos a\tau \cos \frac{1}{2}(\tau\Delta - \omega_0 T - \varphi) + \frac{\Delta}{2} \sin a\tau \sin \frac{1}{2}(\tau\Delta - \omega_0 T - \varphi) \right) \\ &= -\frac{2c_{e1}}{a} \left(\cos \frac{\omega_0 T + \varphi}{2} \left(a \cos a\tau \cos \frac{\tau\Delta}{2} + \frac{\Delta}{2} \sin a\tau \sin \frac{\tau\Delta}{2} \right) \right. \\ &\quad \left. + \sin \frac{\omega_0 T + \varphi}{2} \left(a \cos a\tau \sin \frac{\tau\Delta}{2} - \frac{\Delta}{2} \sin a\tau \cos \frac{\tau\Delta}{2} \right) \right) \end{aligned} \quad (2.56)$$

This complicated expression can be simplified considerably if we assume that $\Omega \ll \Delta$ so that $a \approx \Delta/2$, resulting in a final excited state population [99]:

$$|c_{e2}|^2 = 4|c_{e1}|^2 \cos^2 \left(\frac{\omega_0 T + \varphi}{2} \right) \quad (2.57)$$

In this approximation, the excited state population does not depend on the detuning and Rabi frequency, but only on the transition frequency ω_0 , and the time delay T and phase shift φ between the pulses. These are exactly the parameters that are controlled to a high degree in a frequency comb. Therefore, by taking a pair of pulses emitted by a frequency comb laser, the transition frequency of the system can be derived with an accuracy that is only limited by the frequency comb.

This analysis can be extended to longer pulse trains consisting of N pulses. Although the expressions become longer, it is still possible to derive a formula analogous to equation (2.57), which has the form:

$$|c_{eN}|^2 = N^2 |c_{e1}|^2 \left| \sum_{n=0}^{N-1} e^{in(\omega_0 T + \varphi)} \right|^2 \quad (2.58)$$

This expression is very similar to the formulas that describe the formation of a frequency comb from a finite number of phase-locked pulses. As a result, a measurement of the excited state population as a function of either T or φ will result in a spectrum that consists of a regularly spaced comb of increasingly narrow spikes separated by $1/T$. In particular, note the striking similarity between equations (2.40) and (2.57): Interaction of a two-level system with a pair of consecutive frequency comb pulses leads to an excitation probability that mimicks the frequency comb structure. Figure 2.14 shows the excited state population as predicted by equation (2.58) for trains of up to four laser pulses. The parameters are $T = 13$ ns, $\varphi = 0$ and $\omega_0 = 2821$ THz. This

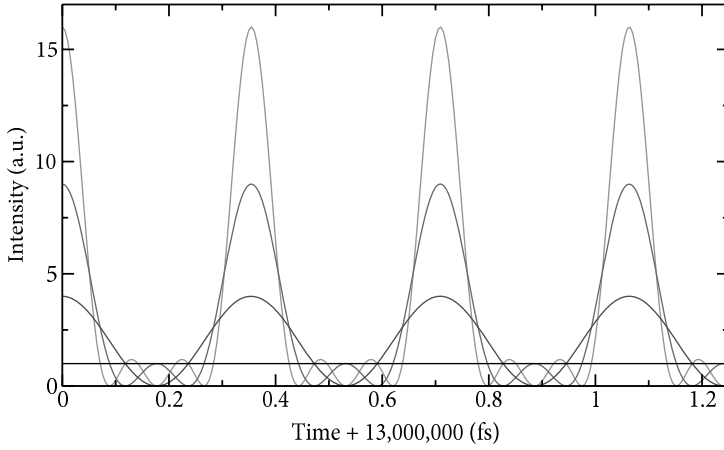


FIGURE 2.14: Excited state population as a function of the time delay T using trains of 1, 2, 3 and 4 phase-locked pulses, respectively. The pulse-to-pulse phase shift φ is kept constant.

figure shows the expected narrowing of the fringes for an increasing number of pulses, and the maximum intensities of the fringes scale with N^2 . It should be noted that although in practice the theory presented in this section forms a very good approximation (which will be confirmed in the next section), a more detailed analysis using real experimental parameters and including e.g. pulse envelopes, Doppler broadening, etc., requires numerical integration of a set of Bloch equations for the density matrix of the system [136].

An interesting aspect of the analysis presented here is that Eqs. (2.57) and (2.58) do not contain the bandwidth of the individual laser pulses. Of course, the pulse spectrum is encoded in Ω through the pulse envelope E_0 , but this only influences the general amplitude of the signal and not its phase. In contrast to traditional spectroscopy, the accuracy is not limited by the spectral characteristics of the individual pulses, but only by the reproducibility of the pulses, which can be extremely good when a frequency comb is employed. Therefore, direct excitation with phase-coherent pulse trains provides a good alternative to high-precision metrology with narrow-band continuous-wave lasers. Such an alternative based on pulsed excitation is especially promising for measurements in wavelength ranges where the construction of narrow-band continuous-wave lasers is extremely challenging (if not impossible). Since the high peak intensity of typical ultrashort pulsed lasers can exceed a terawatt, frequency conversion of such pulses using nonlinear optics and high-harmonic generation can be performed much more efficiently. As a result, quantum interference metrology is very promising for the measurement of atomic and molecular transition frequencies in the extreme ultraviolet and soft-X-ray spectral regions.

In the next chapter, an experimental demonstration of this type of quantum interference metrology is given using amplified and frequency-upconverted pulse pairs

from a frequency comb laser system [79]. The studied transition is the $4p^6 \rightarrow 4p^5 5p[1/2]_0$ two-photon transition in krypton at a frequency of 2821 THz (i.e. 2×212.55 nm).

2.3.3 Intensity-induced phase shifts

From the previous section, we find that the transition frequency of a two-level system can be measured using a sequence of two time-delayed phase-locked pulses. However, the expression (2.57) that describes the excited state population as a function of time delay T and phase shift φ is only an approximation of the more general solution (2.56) for the case where $a \approx \Delta/2$, or rather that both $\tau\Delta \ll 1$ and $\Omega\tau \ll 1$. This approximation basically states that the excited state population remains negligible compared to that of the ground state, and that coherent accumulation effects such as Rabi oscillations are not significant. To get a better estimate of the accuracy of these approximations, we can rewrite the various terms in equation (2.56) using the Taylor expansions $\sin x = x + \dots$ and $\cos x = 1 - \frac{1}{2}x^2 + \dots$, which leads to:

$$c_{e2} \approx -2c_{e1} \left[\left(1 - \frac{1}{2}|\Omega|^2\tau^2\right) \cos \frac{\omega_0 T + \varphi}{2} - \frac{1}{2} \frac{\Delta}{2} |\Omega|^2\tau^3 \sin \frac{\omega_0 T + \varphi}{2} \right] \quad (2.59)$$

where we have neglected any terms of order τ^4 and higher. Some interesting conclusions can be drawn from this expression, most notably that the only assumption that needs to be made for equation (2.57) to be valid is that $\Omega\tau \ll 1$. Even if for example $\Omega\tau = 0.2$, a detuning of $\Delta/2 = 1/\tau$ is required to induce a phase shift of about 42 mrad ($= 1/150^{\text{th}}$ of a cycle). But since $1/\tau$ is on the order of the spectral bandwidth of the pulses, the excitation probability will go down rapidly for such a large detuning.

Another conclusion that can be drawn from equation (2.59) is that the approximations improve for decreasing pulse duration. Obviously, when τ decreases a higher Rabi frequency Ω is required for efficient population transfer to the excited state. For $\tau = 1$ ps and a typical dipole moment of $d = 10^{-30}$, already a very large electric field strength of 10^8 V/m is needed to achieve $\Omega\tau = 1$, and this number scales inversely proportional with the pulse duration.

From this analysis we conclude that equation (2.57) describes the experimentally observed signals very well for any reasonable set of parameters Δ , Ω and τ . Any phase shifts due to the detuning and Rabi frequency can easily be kept within ~ 0.1 mrad ($\sim 10^{-5}$ th of a cycle), which is usually far below the experimental accuracy with which a measured fringe pattern can be fitted. Therefore, precision spectroscopy using trains of phase-locked laser pulses can be performed reliably according to the theory presented here.

CHAPTER 3

DEEP-ULTRAVIOLET QUANTUM INTERFERENCE METROLOGY WITH ULTRASHORT LASER PULSES

Precision spectroscopy at ultraviolet and shorter wavelengths has been hindered by poor accessibility of narrowband lasers to that spectral region. We demonstrate high-accuracy quantum interference metrology on atomic transitions with the use of an amplified train of phase-controlled pulses from a femtosecond frequency comb laser. The peak power of these pulses allows for efficient harmonic upconversion, paving the way for extension of frequency comb metrology in atoms and ions to the extreme ultraviolet and soft X-ray spectral regions. A proof-of-principle experiment was performed on a deep-ultraviolet (2×212.55 nanometers) two-photon transition in krypton; relative to measurement with single nanosecond laser pulses, the accuracy of the absolute transition frequency and isotope shifts has been improved by more than an order of magnitude.

3.1 Introduction

In recent years, the invention of the femtosecond frequency comb laser [105, 106, 126] has brought about a revolution in metrology. A frequency comb acts as a bridge between the radio frequency (RF) domain (typically tens of MHz) and the optical frequency domain (typically hundreds of THz). Thus in precision spectroscopy, the optical cycles of a continuous wave (CW), ultra-stable laser can be phase-locked and counted directly with respect to an absolute frequency standard such as an atomic clock [91, 104]. The resultant frequency measurements approach a precision of 1 part in 10^{15} in certain cases, potentially enabling the detection of possible drift in the fundamental constants [92, 137], among other quantum mechanical applications.

Here we perform precision metrology without the use of a CW laser. Instead, an atomic transition is excited directly with amplified and frequency-upconverted pulses from a femtosecond frequency comb laser. As a result of quantum interference effects in the atomic excitation process, we can achieve an accuracy that is about six orders of magnitude higher than the optical bandwidth of the individual laser pulses.

The method used is related to Ramsey's principle of separated oscillatory fields [100], which probes the phase evolution of an atom in spatially separated interaction zones. This technique is widely used in the RF domain for atomic fountain clocks [138]. By extension, in the optical domain excitation can be performed by pulses separated in time (rather than in space) to maintain phase coherence between the excitation contributions. Several experiments have been performed to investigate Ramsey-type quantum interference fringes in the optical domain [96, 98, 99, 139, 140] and phase-stable amplification of single pulses [141]. Actual quantitative spectroscopy with phase-coherent oscillator pulses has been limited to a few relative frequency measurements on fine and hyperfine structure of atoms [97, 139, 140] and relative and absolute measurements on rubidium [142]; absolute frequency measurements with amplified pulses have been frustrated by an unknown phase difference between the pulses or by limited resolution.

We generate powerful laser pulses with a precise phase relationship by amplifying a selected pulse train from a frequency comb laser. This amplified frequency comb can be used to measure absolute optical frequencies directly. The advantage of amplified laser pulses is that the high peak power allows for efficient frequency upconversion in crystals and gases. It has been shown that harmonic generation in gases can preserve the coherence properties of the driving laser pulse [143, 144]. Therefore the present experiment paves the way for precision metrology with frequency combs at optical frequencies that are very difficult or almost impossible to reach with CW lasers, such as vacuum-ultraviolet and even shorter wavelengths (e.g. X-rays). Possible applications are precision spectroscopy of hydrogen-like ions and helium to test quantum electrodynamics and nuclear size effects. The technique may also lead to more accurate atomic clocks that operate on resonances with ultrahigh frequencies.

3.2 Principle of quantum interference metrology

The principle of quantum interference metrology (Fig. 3.1) has already been introduced in the previous chapter. Briefly, an atom is excited by a train of N phase-locked laser pulses separated by a time T . Assuming a two-level system, the resulting excited state population after the pulse train can be written as

$$|b_N|^2 = \left| \sum_{n=1}^N a_n e^{i(n-1)(\omega_0 T + \varphi)} \right|^2, \quad (3.1)$$

where φ is the phase difference between subsequent laser pulses, and a_n is the excitation amplitude for the n^{th} pulse. Thus $|b_N|^2$ is a periodic function of both the pulse delay T and the phase difference φ . The resonance frequency ω_0 is encoded not just in the amplitude a_n , as with conventional spectroscopy, but also in the phase of the oscillating population signal. The first pulse creates an atomic superposition with a well-defined initial phase. The maxima of the excited state population occur when subsequent laser pulses arrive in phase with this superposition. If the time delay and the pulse-to-pulse phase shift are known, the exact transition frequency can be derived from the position of these maxima. The more pulses are used, the narrower the resulting interference

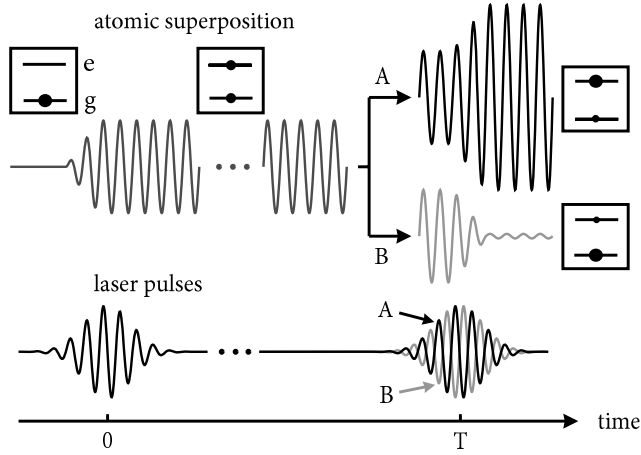


FIGURE 3.1: The principle of quantum interference metrology. An atom in the ground state $|g\rangle$ is resonantly excited by a broadband laser pulse. This pulse creates a coherent superposition of the ground state and the excited state, with an initial phase difference between the states determined by the laser pulse. After the initial excitation, the superposition will evolve freely with a phase velocity $\omega_0 = (E_e - E_g)/\hbar$, where $E_e - E_g$ is the energy difference between the states. After a time T , a second pulse with a controlled phase illuminates the atom, interfering with the atomic superposition. Depending on the phase and the time delay T , the total $|g\rangle \rightarrow |e\rangle$ excitation probability can be either enhanced (case A, black pulse) or suppressed (case B, grey pulse). By measuring the amplitude of the superposition (i.e. the population of the excited state) after the second pulse (with, e.g., an ionizing laser pulse), the energy difference between the states can be deduced.

fringes. Therefore, multiple-level contributions can be resolved by the use of a sufficient number of pulses.

This method to measure the transition frequency is largely insensitive to the laser pulse spectral shape, which only influences the global signal amplitude. Therefore spectral distortions of the laser pulses due to amplification or harmonic generation have little influence on the measurement, provided the distortion is identical from pulse to pulse. In contrast, traditional single pulse spectroscopy is strongly affected by chirp [85, 86]. However, the periodicity of the signal with respect to T leads to an inherent ambiguity in the determination of the transition frequency. This ambiguity can be resolved if a previous measurement with an accuracy much better than the repetition frequency exists; otherwise the measurement can be repeated with different repetition rates, as shown below.

3.3 Setup for phase-coherent pulse-pair excitation

For efficient harmonic generation and excitation of weak (multiphoton) transitions, a high peak intensity of the incident laser pulses is indispensable. Usually, the intensity of

pulses from a modelocked oscillator is not yet sufficient, and additional amplification is required. In this section, the experimental setup that we constructed to demonstrate quantum interference metrology is presented: The main components are a frequency comb oscillator, a multipass Ti:Sapphire pulse-train amplifier, the pulse-to-pulse phase measurement interferometer, and an atomic beam apparatus for excitation and detection.

3.3.1 Amplification of pulse trains

The frequency comb used in our experiment is based on the modelocked 11 fs Ti:sapphire oscillator described in the previous chapter (section 2.2.2). It emits 7 nJ pulses with a bandwidth (full width at half maximum) of ~ 90 nm, centered at 800 nm, and with an adjustable repetition rate between 60.9 and 79 MHz. For frequency accuracy, both the repetition rate and the phase of the pulses are locked to a Global Positioning System-disciplined Rb atomic clock [105, 106, 145, 146].

An electro-optic modulator (EOM) is used to select up to three consecutive pulses from the modelocked pulse train. These pulses are sent into a Ti:sapphire multipass amplifier, where they make a total of six roundtrips (see Fig. 3.2). The pulses are coupled in through a Faraday isolator (which also stretches the pulses in duration), and make three roundtrips through the amplifier with a small-signal gain of about 30 per pass. The gain medium is a 10 mm long Ti:Sapphire crystal, pumped by 7 mJ pulses from a frequency doubled Nd:YAG laser at 1 kHz rep. rate (Coherent Corona). After these first three passes, the pulses are sent into a $2f$ -setup consisting of a grating and a curved mirror to spatially spread out the spectrum. Close to the end mirror, a slit is placed to select the spectral bandwidth that is needed for the experiment: For these krypton measurements, a ~ 0.5 nm wide spectrum centered at 850.2 nm is transmitted. The filtering reduces the complexity of the signal, as only a single transition will be excited (see below). This remaining portion of the pulses is reflected back through the amplifier for an additional three passes before being coupled out by the Faraday isolator. Typical output powers of the amplified pulse pair at 850 nm are $\sim 30 \mu\text{J}$ per pulse.

The amplifier operates in the non-saturating regime, i.e. only a small fraction of the stored pump energy is extracted by the seed pulses. This allows the amplification of multiple pulses, since the energy extraction by the first pulse does not alter the gain for the later pulses significantly. It does, however, lead to a decreased intensity stability ($\sim 10\%$) compared to a saturated amplifier system, although such fluctuations will be largely identical within the pulse train since they are mostly caused by variations of the pump intensity. Therefore, the relative intensity stability between the pulses is much better. To limit pulse intensity fluctuations, we actively stabilize the pump energy to the crystal by rotating a $\lambda/2$ -plate in the pump beam using a servo motor. This changes the polarization of the pump light, which introduces tunable losses when pumping the Brewster-angled Ti:Sapphire crystal. The relative strength of the pulses can be controlled by changing their timing with respect to the pump pulse. In contrast, standard amplifiers operate in saturated mode to reduce output power fluctuations, and can therefore amplify only one pulse. In the present experiment, the number of pulses that can be amplified is limited to three by the EOM, which must be switched off before

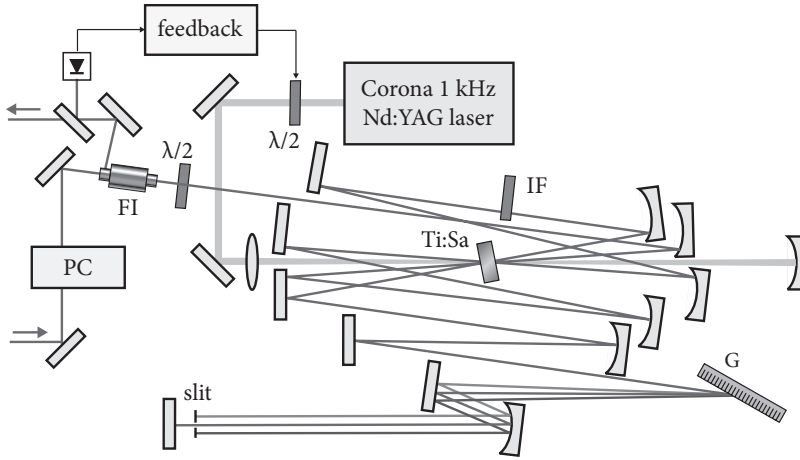


FIGURE 3.2: Schematic of the multipass amplifier for pulse pairs. PC: Pockels cell, Ti:Sa: Ti:Sapphire amplifier crystal, FI: Faraday isolator, G: 1200 lines/mm grating.

any backreflections from the amplifier lead to uncontrolled extra pulses (an additional Faraday isolator in the setup would lift this limitation).

3.3.2 Pulse-to-pulse phase shift measurements

The amplification process gives rise to a small phase shift (~ 100 to 200 mrad) between the pulses, which is measured with a 1σ accuracy of 25 mrad ($< 1/250^{\text{th}}$ of an optical cycle). These measurements are performed by placing the amplifier in one arm of a Mach-Zehnder interferometer and recording spatial interferograms on a charge-coupled device (CCD) camera, from which this phase shift can be extracted. A schematic of the setup is shown in Fig. 3.3.

The pulses are split in two before the amplifier (but behind the Pockels cell), after which one of the replica pulse pairs is sent into the amplifier, while the other passes through a reference arm of the same length. In this reference arm, the pulses are spectrally clipped and given a beam size and divergence that matches the amplifier output. After recombination, an EOM and polarizing optics are used to project the interference patterns for two consecutive pulses simultaneously and vertically displaced from one another on a CCD camera.

In practice, the determination of the pulse-to-pulse phase shift is somewhat more involved, since any slight misalignment of the relative positions of the interferograms will also lead to an apparent shift between the patterns. To identify a position misalignment the Pockels cell timing is switched periodically, such that it rotates the polarization of the either the first or the second pulse. In this way, the paths taken by the respective pulses are periodically interchanged, and any position-dependent phase shift can be identified. An example of such a measurement is shown in Fig. 3.4. Fig-

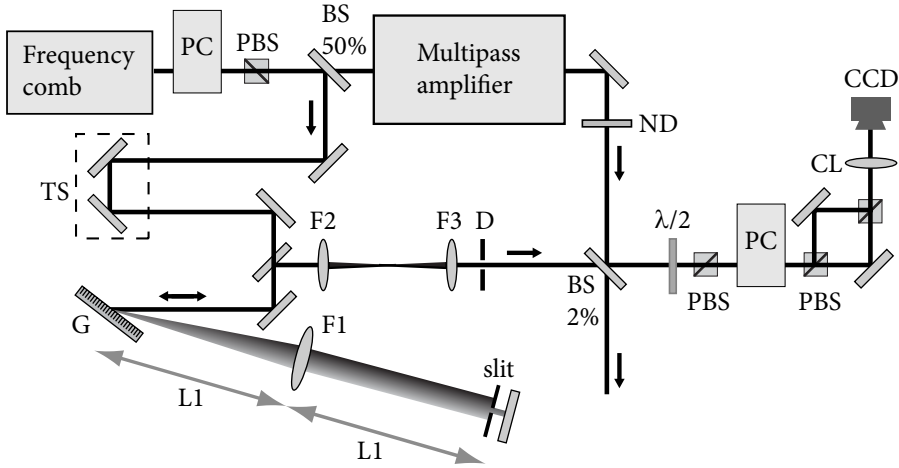


FIGURE 3.3: Mach-Zehnder interferometer for measurement of amplifier-induced phase shifts. PC: Pockels cell, PBS: Polarizing beamsplitter, TS: Translation stage, BS: Beamsplitter, ND: Neutral density filters, D: Diaphragm, G: 1200 lines/mm grating, CL: $f = 15$ cm cylindrical lens. $F1 = L1 = 50$ cm, $F2 = 20$ cm, and $F3 = 10$ cm. See text for details.

ure 3.4A shows the extracted phase of both interferograms as a function of time. Although drifts due to acoustic and thermal ambient noise are present, these are almost completely identical for both pulses. The difference between these phase traces is displayed in Fig. 3.4B, where the effect of the Pockels cell time-switching is clearly visible: While any alignment-induced phase shift would not cause any changes, a real phase shift between the pulses leads to a sudden jump in this phase difference when the Pockels cell timing is switched. Using this technique, amplifier-induced phase shifts can be measured with an accuracy of 25 mrad, while the reproducibility is better than 15 mrad.

3.3.3 Atomic beam generation and signal detection

To investigate the krypton transition, we used the setup shown in Fig. 3.6. The vacuum apparatus consists of a source chamber and a detection chamber, each having a turbomolecular pump backed by oil-free pre-pumps to keep the pressure around 10^{-7} mbar in the absence of an atomic beam. Krypton gas enters the vacuum chamber through a discharge cell, which is not turned on during the actual measurements, but allows the generation of ions, metastable atoms and a bright white glow that are helpful in aligning the system. A collimated atomic beam is created using two skimmers: One circular skimmer with a 0.29 mm aperture, and a 0.24 mm wide slit skimmer. Assuming an adiabatic expansion, we estimate a most probable velocity of 381 m/s for the krypton atoms in the atomic beam. With the present skimmer arrangement, the residual Doppler width of the transition under study is estimated to be around 10 MHz. This

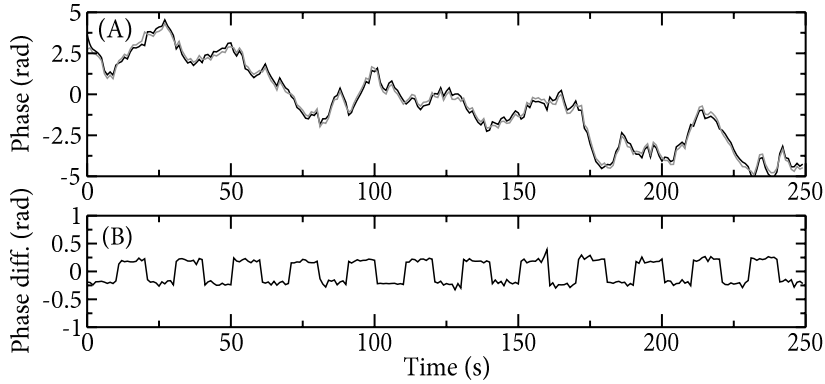


FIGURE 3.4: (A) Measurement of the phases of the individual pulses. (B) The difference between these phase traces. Due to the periodic position switching (see text), any misalignment effect is filtered out, and the actual amplifier-induced phase shift is half the size of the jumps.

estimate has been obtained by comparing model calculations on the expected fringe contrast with experimental data [136].

In the interaction region, the atoms are perpendicularly intersected by the focused 212.55 nm laser pulse pair which excites the $4p^6 \rightarrow 4p^5 5p[1/2]_0$ transition. After a fixed delay (between 10 and 90 ns), a 1.5 mJ, 100 ps pulse from a frequency-doubled Nd:YAG laser-amplifier is focused in the interaction region (collinear with the UV pulse pair) to ionize atoms that are in the excited state. The produced ions are then detected using a time-of-flight system: first, they are pulled away from the interaction region by an electric field generated with a pair of extraction plates at +300 V (bottom plate) and +250 V (top plate), separated by 1.7 cm. The ions are accelerated further towards a third plate at 0 V, again 1.7 cm above the previous plate. Above this plate, the ions travel through a field-free 65 cm flight tube before hitting a channel-electron multiplier detector. In front of the detector, two perpendicular slits have been placed to select only ions from the center of the interaction region. To steer the ions towards the detector, small compensation fields can be applied in both transverse directions using additional pairs of plates at the entrance of the flight tube. The resulting time-of-flight signals show clearly separated peaks for the various krypton isotopes, as displayed in Fig. 3.5.

The signal from a single isotope is selected by mixing the time-of-flight detector output with a square 100 ns gate-pulse from an arbitrary waveform generator. The resulting mixing product is then sent to a discriminator, of which the output is connected to a counter. The counter counts the number of ions detected in a 10 s gate time and sends this data to a computer. The computer then scans the delay between the UV pulses by adjusting the cavity length of the frequency comb oscillator, while keeping the carrier-envelope phase fixed. The quantum interference signal is then recorded by monitoring the ion signal as a function of pulse separation. The oscillator cavity length is adjusted by scanning the frequency of the 10.5 GHz waveform generator that is used to stabilize the 140th harmonic of the repetition rate. A typical scan changes

this 10.5 GHz frequency by 1 kHz in 100 steps of 10 Hz. Every step corresponds to a timing difference of 12.6 attoseconds between the pulses. As the oscillation period of the excited state is $2\pi/\omega = 355$ attoseconds, about 3.5 oscillations are observed within a scan.

3.4 Results and analysis

To demonstrate the potential of high-frequency quantum interference metrology we selected the $4p^6 \rightarrow 4p^5 5p[1/2]_0$ two-photon transition in krypton at a frequency of $\omega_0/2\pi = 2821$ THz. Because both the ground state and the excited state of this transition are $J=0$ states, this atom can be considered to be a two-level system. The required wavelength of 212.55 nm for the two-photon krypton resonance was obtained by fourth-harmonic generation of the amplifier output at 850.2 nm through sequential frequency doubling in two beta-barium borate (BBO) crystals. The resultant 212.55 nm pulses ($1.6 \mu\text{J}$) were focused in a highly collimated atomic beam of krypton (Fig. 3.6). The excited-state population was probed by a delayed 532 nm ionization pulse (1.5 mJ, 100 ps) from a Nd:YAG laser-amplifier system, and the experiment was repeated at 1 kHz.

The isotope shift and the absolute transition measurements described below can be influenced by a possible systematic Doppler shift as a result of non-perpendicular excitation. Therefore all measurements were performed from two opposite sides, with the average taken to determine the Doppler-free signal. The Doppler shift can in principle be reduced on a two-photon transition by measuring with colliding pulses from opposite sides. This arrangement also enhances the signal, as was seen experimentally. However, contrary to CW spectroscopy, Doppler-free signal (photons absorbed from opposite sides) and Doppler-shifted signal (two photons from one side) cannot be dis-

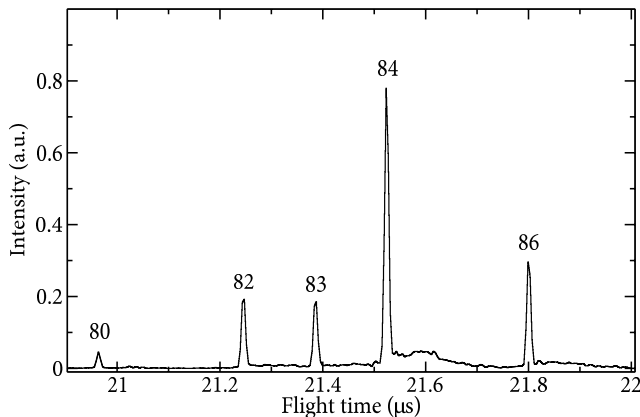


FIGURE 3.5: Mass spectrum of krypton measured with a time-of-flight detector. The various isotopes are well separated in time.

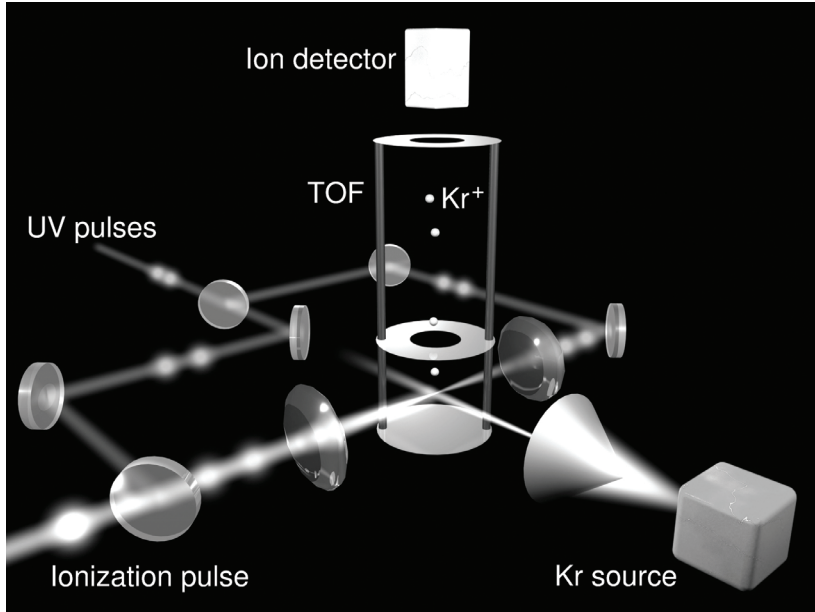


FIGURE 3.6: Schematic of the experimental setup. The ultraviolet pulses (beam diameter 1 mm) are focused with an $f = 30$ cm lens in a collimated 0.3 mm wide krypton beam (double skimmer arrangement, Doppler width <10 MHz) from both sides, crossing the beam perpendicularly. Measurements are performed with light from one side at a time. After the ultraviolet excitation, a delayed 532 nm pulse is used for ionization, and the resulting krypton ions are accelerated into a 60-cm time-of-flight mass spectrometer (TOF) by a pulsed electric field. Here the isotopes are separated in time (see inset) and counted with a channeltron detector.

tinguished properly in the case of excitation with two ultrashort pulses, because the large bandwidth always contains a resonant frequency. This situation might lead to a calibration error when there is an imbalance in signal strength from opposite sides. Another aspect is that the total Doppler shift has an ambiguity due to the periodicity of the signal. The difference in Doppler shift between neighbouring isotopes, which is on the order of a few hundred kHz, therefore provides a valuable initial estimate of about 25 MHz for this shift. From the measurement of the absolute positions, one can then determine the Doppler shift to be 29 MHz for each of the counter-propagating beams.

The data depend on the number of phase-locked pulses used to excite the transition (Fig. 3.7A). The pulse delay T was scanned by changing the comb laser repetition frequency, which is near 75 MHz. With a single pulse the excitation probability is constant. With two pulses a clear cosine oscillation is observed, with a contrast reaching 93%. Three pulse excitation gives the pulse-like structure predicted by Eq. 3.1 ($N = 3$) as well as an expected narrowing by $3/2$ relative to two-pulse excitation. The solid lines are fits using Eq. 3.1, including an additional amplitude scaling factor to account for signal strength variations between the traces. In the three-pulse case, we took into account

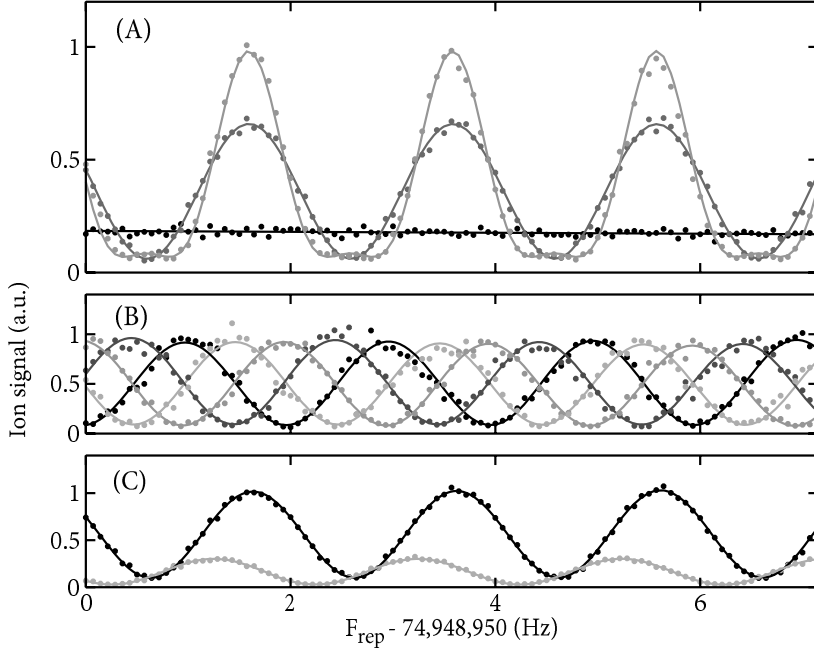


FIGURE 3.7: Demonstration of quantum interference metrology. **(A)** ^{84}Kr signal as a function of the repetition rate of the comb laser for one (black), two (dark grey), and three (light grey) pulses 13.3 ns apart. The solid lines are fits to the theory (see text). **(B)** Measurement of the quantum interference signal for various phase differences between two excitation pulses, with the pulse-to-pulse phase shift (as seen by the atom) set to 0 (black trace), $\pi/2$, π and $3\pi/2$ (lightest trace), respectively. **(C)** Measurement of the isotope shift between ^{84}Kr (black) and ^{86}Kr (light grey). The isotope shift can be determined from the phase shift between these two simultaneously recorded scans. The counter gate time is 10 s for each data point.

that the amplitude contribution of the pulses is not exactly equal because of spontaneous emission of the 5p state (lifetime 23 ns) and differences in energy between the three pulses. The energy ratio of pulses 1, 2 and 3 is 1.0 : 0.91 : 0.6 (in all measurements with two pulses, the pulse energies have been kept equal to within about 5%). For all other measurements, we used two-pulse excitation, as this minimizes the complexity of the experiment without sacrificing accuracy in this two-level case. The first of these measurements concerns the dependence on the pulse-to-pulse (carrier-envelope) phase shift φ_{ce} (Fig. 3.7B), which is in complete agreement with expectations: The interference signal moves by one fringe when φ_{ce} of the comb laser is scanned through one-eighth of a cycle (due to the frequency conversion and two-photon transition).

Isotope shifts can be measured straightforwardly. The broad spectrum of the pulses places a frequency ruler on all isotopes simultaneously, so that spectra of ^{80}Kr through ^{86}Kr could be acquired at the same time (Fig. 3.7C). The measurements of Kaufman [147] were used for identification of the proper comb line for each isotope.

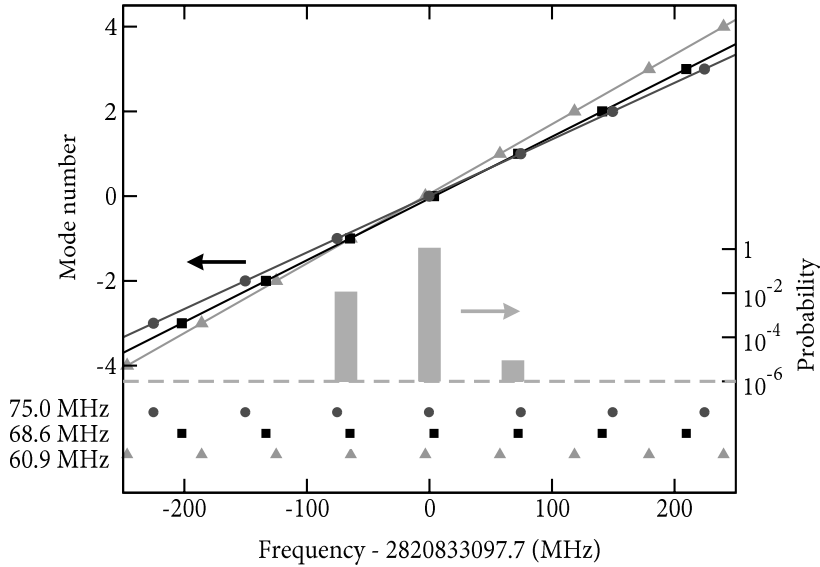


FIGURE 3.8: Absolute calibration of the $4p^6 \rightarrow 4p^5 5p[1/2]_0$ transition in krypton is performed by finding the coincidence of three separate measurement series with repetition rates of 60.9 MHz (light grey line and triangles), 68.6 MHz (dark grey line and squares) and 75.0 MHz (black line and circles). The light grey bars (logarithmic scale) show the normalized statistical probability per mode for each measured mode position, revealing the location of the most probable coincidence.

The resulting shifts ($^{84}\text{Kr} - ^X\text{Kr}$), based on at least six measurements per isotope, are 302.02 ± 0.28 MHz (^{80}Kr), 152.41 ± 0.15 MHz (^{82}Kr), 98.54 ± 0.17 MHz (^{83}Kr), and -135.99 ± 0.17 MHz (^{86}Kr). The stated uncertainties (1σ) are smaller than the 6 MHz uncertainty reported by Kaufman [147] by a factor of 20 to 40.

In the measurement of the absolute transition frequency, an additional issue is the determination of the mode that corresponds to the true position of the resonance. The most accurate measurement to date [148] has an uncertainty of 45 MHz, which is not sufficient to assign the mode with confidence. Therefore measurements were repeated at repetition rates near 60.9 MHz, 68.6 MHz and 75.0 MHz to find the point at which the measurements coincide (four to nine measurements were performed at each repetition rate). Two systematic effects dominate the determination of the resonance frequency: the phase shifts induced by the amplifier (100 to 200 mrad in the infrared), and the residual Doppler shift (2 MHz) due to possible misalignment of the counter-propagating beams. Other effects include light-shifts (0.47 ± 0.44 MHz), static field effects ($\ll 100$ kHz), the second-order Doppler shift (~ 1 kHz), and a recoil shift (209 kHz). The phase shift due to the pulse-picker EOM is negligible (< 5 mrad) when it is aligned such that it acts as a pure polarization rotator, as verified experimentally. The phase shift due to frequency doubling is negligible as well, on the order of 1 mrad in the ultraviolet, as estimated from the model of DeSalvo et al. [149]. After correction of the data

for the phase shifts and systematic effects, there were three sets of possible positions for the 5p resonance transition (Fig. 3.8). The measurements have one clear coincidence (with an estimated probability of 98%, based on a statistical uncertainty of 2.5 MHz for each data point) near the literature value. Combining the three sets leads to an absolute frequency of 2,820,833,097.7 MHz with a 1σ uncertainty of 3.5 MHz (statistical and systematic errors combined). This is an order of magnitude better than the previous determination by Brandi et al [148], who obtained a value of $2,820,833,076 \pm 40$ MHz using single nanosecond laser pulses.

3.5 Conclusions

We envision several extensions of the above technique. One possibility is the use of a regenerative amplifier to amplify pulses to the μJ level at a repetition rate of 100 kHz. For high frequency metrology, the resolution is ultimately limited by the comb laser and the interaction time of the atom with the pulses. This interaction time can be increased almost indefinitely if cooled ions in a trap are used in place of an atomic beam, opening the prospect of atomic optical clocks operating at vacuum-ultraviolet or extreme-ultraviolet frequencies. Outside frequency metrology, amplified frequency combs could be used to perform quantum-control experiments on a time scale much longer than is currently possible, because phase coherence can be maintained for many consecutive laser pulses.

CHAPTER 4

NONCOLLINEAR OPTICAL PARAMETRIC CHIRPED PULSE AMPLIFICATION: THEORY AND SIMULATIONS

Chapter 2 gave a description of nonlinear pulse propagation and discussed the basics of how to deal with nonlinear polarization in very general terms. In contrast, this chapter is devoted entirely to one particular nonlinear process: Optical parametric amplification. This process is of special interest for the development of high-power amplifier systems for few-cycle laser pulses, as will become clear from the analysis in this chapter and from the experimental work that is described in later chapters. In section 4.1 the general theory of optical parametric amplification is presented, using analytical expressions whenever possible. This section discusses the coupled-wave equations and their solutions, as well as the possibilities for amplification of ultra-broadband spectra, and the generation of parametric superfluorescence. In section 4.2 a numerical approach is taken to simulate an NOPCPA system without the approximations of the analytical treatment. Results of numerical simulations are presented for the case of a multi-stage, high-power ultra-broadband NOPCPA system similar to the experimental system described in chapter 8.

4.1 Theory of optical parametric amplification

The theory of optical parametric amplification is basically a special case of the nonlinear pulse propagation theory developed in chapter 2: It can be described by a three-wave mixing process, involving a set of nonlinear propagation equations that are coupled through a χ^2 -polarization. Behind this seemingly simple set of equations lies a wealth of possible interaction geometries and applications. This section provides a theoretical framework of optical parametric amplification, focused especially on the amplification of ultrashort (and therefore ultra-broadband) laser pulses.

4.1.1 The coupled-wave equations

In chapter 2 the possibility of a polarization with a nonlinear dependence on the electric field was discussed. Consider now the case of two separate laser pulses with frequencies

ω_p and ω_s . When these pulses overlap in a birefringent medium (to allow a nonzero $\chi^{(2)}$), this gives rise to a nonlinear polarization of the form (see e.g. [124]):

$$\mathbf{P}_{NL} = \epsilon_0 \int_{-\infty}^{\infty} \int_{-\infty}^{\infty} \chi^{(2)}(t-t_1, t-t_2) \mathbf{E}_p(t-t_1) \mathbf{E}_s^*(t-t_2) dt_1 dt_2 \quad (4.1)$$

This particular \mathbf{P}_{NL} source term describes the generation of a new pulse with a carrier frequency $\omega_i = \omega_p - \omega_s$ from the interaction between the two input fields. If we assume that this nonlinear process is instantaneous, we can write Eq. (4.1) as (limiting ourselves to one spatial dimension):

$$\begin{aligned} P_{NL}(z, t) &= \epsilon_0 \chi^{(2)} E_p(z, t) E_s^*(z, t) \\ &= \epsilon_0 \chi^{(2)} A_p(t) A_s^*(t) e^{-i[(k_p - k_s)z - (\omega_p - \omega_s)t]} \end{aligned} \quad (4.2)$$

When such a wave is generated, this effectively means that a photon from the pump beam is split into a photon at the signal frequency, and a residual idler photon at the difference frequency: $\omega_p \rightarrow \omega_s + \omega_i$. In effect, energy is transferred from the pump pulse to the signal and idler pulses. The entire process now involves three waves, each having its own nonlinear propagation equation. This leads to the following set of *coupled-wave equations* (see e.g. [22, 64, 124]):

$$\frac{\partial A_s}{\partial z} + k^{(1)} \frac{\partial A_s}{\partial t} - \frac{ik^{(2)}}{2} \frac{\partial^2 A_s}{\partial t^2} = -i\chi^{(2)} \left(\frac{\omega_s}{2n_s c} \right) A_p A_i^* e^{-i\Delta k \cdot z} \quad (4.3a)$$

$$\frac{\partial A_i}{\partial z} + k^{(1)} \frac{\partial A_i}{\partial t} - \frac{ik^{(2)}}{2} \frac{\partial^2 A_i}{\partial t^2} = -i\chi^{(2)} \left(\frac{\omega_i}{2n_i c} \right) A_p A_s^* e^{-i\Delta k \cdot z} \quad (4.3b)$$

$$\frac{\partial A_p}{\partial z} + k^{(1)} \frac{\partial A_p}{\partial t} - \frac{ik^{(2)}}{2} \frac{\partial^2 A_p}{\partial t^2} = -i\chi^{(2)} \left(\frac{\omega_p}{2n_p c} \right) A_s A_i e^{i\Delta k \cdot z} \quad (4.3c)$$

where $\Delta \mathbf{k} = \mathbf{k}_p - \mathbf{k}_s - \mathbf{k}_i$ is the wave-vector mismatch. These equations can be solved numerically, but analytical solutions exist for certain limiting cases, which will be discussed in more detail in the next section. However, even without solving the set of equations a number of conclusions can be drawn from (4.3). For instance, the efficiency of the energy transfer between the interacting pulses depends strongly on their respective intensities. Another parameter that has a major influence on the coupling efficiency is the aforementioned wave-vector mismatch, which should ideally fulfill the phase-matching condition $\mathbf{k}_p = \mathbf{k}_s + \mathbf{k}_i$ (note that in general this is a vector-relation, since the respective waves can travel in different directions). This condition is a statement of momentum conservation, as the momentum of a single photon is given by $\mathbf{p} = \hbar \mathbf{k}$. In terms of traveling electromagnetic waves, it means that the interacting waves remain in phase during propagation, so that any light generated at ω_s through the nonlinear process will add up coherently with the wave that is already present at this frequency.

The presence of the $\partial^n / \partial t^n$ -terms on the left-hand side of the equations incorporates the effects of linear dispersion on the propagation of the three pulses inside the nonlinear medium. Ideally, the propagation should be identical for the pulses to remain

in phase. But even when the phase-matching condition is satisfied, the group velocities of the pulses can still be different, as well as the higher-order dispersion; these effects can limit the efficiency of the nonlinear process, especially if they are large enough to limit the distance over which the pulses can be temporally overlapped before they are separated by the difference in group velocity.

The coupled-wave equations given in this section form the starting point for an analysis of optical parametric amplification in the context of classical electrodynamics. Full quantum theories of optical parametric amplification have been developed [53–56], and the classical treatment presented here is of course only a special case of this quantum approach for the case of large photon numbers. However, for the practical situations that are discussed in later chapters the classical theory is adequate, and therefore the calculations presented in this chapter will be based on this classical treatment using Eqs. (4.3). The only phenomenon that can not be explained without resorting to a quantum description is the production of parametric superfluorescence in the absence of an input pulse at the signal frequency [57–59]. This process will be discussed in section 4.1.5, using the required quantum Hamiltonian to explain the mechanism that drives the spontaneous generation of parametric superfluorescence.

4.1.2 Analytical solutions

Although a generally valid analytical solution to the coupled wave equations (4.3) does not exist, good approximate solutions can be found for certain limiting cases [51, 150]. The main approximation that needs to be made in order for these equations to become analytically tractable is that the effects of linear dispersion are neglected. As a result, all the $\partial^n/\partial t^n$ -terms are removed from (4.3), and a coupled set of first-order differential equations in one variable remains.

To simplify the notation and to write the equations in a more general form, we introduce some abbreviations: The total intensity (power per unit area) of all pulses combined can be written as:

$$I_{\text{tot}} = \frac{1}{2} \epsilon_0 c \left(n_s |E_s(0)|^2 + n_i |E_i(0)|^2 + n_p |E_p(0)|^2 \right) \quad (4.4)$$

which is a constant, since the nonlinear coupling through P_{NL} is instantaneous. The respective pulse envelopes can be decomposed into a time-dependent amplitude and phase according to $A_m(z, t) = \rho_m(z, t) e^{-i\varphi_m(z, t)}$ (with $m = s, i, p$), so that the coupled-wave equations are converted into six coupled differential equations for the (real-valued) amplitudes and phases. Using expression (4.4) for the total intensity, a set of normalized amplitudes can be introduced:

$$u_m = \sqrt{\frac{\epsilon_0 n_m c}{2\omega_m I_{\text{tot}}}} \rho_m = \sqrt{\frac{I_m}{\omega_m I_{\text{tot}}}} \quad (4.5)$$

In addition, we can define a combined phase $\theta = \Delta k z + \varphi_p - \varphi_s - \varphi_i$ which includes the accumulated phase mismatch $\Delta k z$. With these normalized pulse amplitudes (4.5), the coupled-wave equations for the amplitudes can be rewritten in a normalized form

as [51, 150]:

$$\frac{\partial u_s}{\partial \xi} = -u_i u_p \sin \theta \quad (4.6a)$$

$$\frac{\partial u_i}{\partial \xi} = -u_s u_p \sin \theta \quad (4.6b)$$

$$\frac{\partial u_p}{\partial \xi} = +u_s u_i \sin \theta \quad (4.6c)$$

$$\frac{\partial \theta}{\partial \xi} = \frac{\Delta k z}{\xi} + \left(\frac{u_s u_i}{u_p} - \frac{u_i u_p}{u_s} - \frac{u_s u_p}{u_i} \right) \cos \theta \quad (4.6d)$$

where the normalized length variable ξ is given by:

$$\xi = \chi^{(2)} \left(\frac{\omega_s \omega_i \omega_p}{2\epsilon_0 n_s n_i n_p c^3} I_{\text{tot}} \right)^{1/2} z \quad (4.7)$$

Since all three equations for the phase only depend on θ , they can be combined into a single differential equation (4.6d). This equation can be directly integrated, which yields:

$$\cos \theta = \frac{\Gamma - \frac{1}{2} \frac{\Delta k z}{\xi} u_p^2}{u_s u_i u_p} \quad (4.8)$$

where the integration constant Γ is given by the initial conditions:

$$\Gamma = u_s(0)u_i(0)u_p(0) \cos \theta(0) + \frac{1}{2} \frac{\Delta k z}{\xi} u_p^2(0) \quad (4.9)$$

The full derivation of the solution to this differential equation (4.6d) is in fact rather lengthy, and is therefore only given in Appendix C.1. At this point it is convenient to remember that photon energy conservation implies for the three-wave mixing process that $\omega_s + \omega_i = \omega_p$, while according to Eq. (4.4) the conservation of total power can be written as $\omega_s u_s^2 + \omega_i u_i^2 + \omega_p u_p^2 = 1$. Combining these two relations leads to the Manley-Rowe relations [51, 124, 150]:

$$m_s = u_s^2 + u_p^2 \quad (4.10a)$$

$$m_i = u_i^2 + u_p^2 \quad (4.10b)$$

$$m_p = u_s^2 - u_i^2 \quad (4.10c)$$

where m_s , m_i and m_p are constants. The Manley-Rowe relations are basically an expression of photon number conservation, stating that the annihilation of one pump photon at frequency ω_p must lead to the creation of one signal photon and one idler photon at frequencies ω_s and ω_i , respectively.

To find a solution to the normalized coupled-wave equations (4.6) we use the phase expression (4.8) to eliminate the $\sin \theta$ -term from the differential equation for u_p (4.6c). After some manipulation and the use of the Manley-Rowe relations (4.10), we arrive

at an integral equation for the normalized length ξ in terms of the normalized pump intensity u_p^2 [51]:

$$\xi = \frac{1}{2} \int_{u_p^2(0)}^{u_p^2(\xi)} \frac{d(u_p^2)}{(u_p^2(m_i - u_p^2)(m_s - u_p^2) - (\Gamma - \frac{1}{2} \frac{\Delta kz}{\xi} u_p^2)^2)^{1/2}} \quad (4.11)$$

Although it may seem unnatural from an experimental point of view to write the interaction length as a function of pump intensity, Eq. (4.11) is convenient because it has the form of a Jacobi elliptic integral, for which analytical solutions are known [151]. We can now find such a solution, and from it we immediately obtain the inverse function that defines the desired expression for $u_p^2(\xi)$, which will then be given in terms of the Jacobi elliptic sn-function.

To solve Eq. (4.11) we need to determine the roots of the denominator. At this point it becomes more insightful if we restrict ourselves to the special case of optical parametric amplification of an initially weak signal beam by a much stronger pump, meaning that $u_s^2(0) \ll u_p^2(0)$ and $u_i^2(0) = 0$. The roots of Eq. (4.11) are now found to be (in order of increasing magnitude):

$$u_p^2 = \left(\frac{\Delta kz}{2\xi} \right)^2, \quad u_p^2(0), \quad u_p^2(0) + u_s^2(0) \quad (4.12)$$

Using this information, the solution to Eq. (4.11) is found to be [51, 150]:

$$u_p^2(\xi) = \left(\frac{\Delta kz}{2\xi} \right)^2 + (u_p^2(0) - \left(\frac{\Delta kz}{2\xi} \right)^2) \text{sn}^2 \left[\sqrt{u_p^2(0) + u_s^2(0) - \left(\frac{\Delta kz}{2\xi} \right)^2} \xi + K(\gamma^2), \gamma^2 \right] \quad (4.13a)$$

$$u_s^2(\xi) = u_s^2(0) + u_p^2(0) - u_p^2(\xi) \quad (4.13b)$$

$$u_i^2(\xi) = u_i^2(0) + u_p^2(0) - u_p^2(\xi) \quad (4.13c)$$

where the solutions for the signal and idler intensities are derived from the solution for the pump intensity using the Manley-Rowe relations. The function $K(\gamma^2)$ is a complete elliptic integral of the first kind [151]: It corresponds to a quarter-wave period of the sn-function, and its presence simply introduces a phase shift such that $\text{sn}^2 = 1$ at $\xi = 0$. In addition, we have introduced the constant γ :

$$\gamma^2 = \frac{u_p^2(0) - \left(\frac{\Delta kz}{2\xi} \right)^2}{u_p^2(0) + u_s^2(0) - \left(\frac{\Delta kz}{2\xi} \right)^2} \quad (4.14)$$

which is completely determined by the phase mismatch and the initial pump and seed intensities. Although the general form of these expressions is still rather complicated, it does provide a solution for the intensities of pump, seed and idler waves as a function of propagation distance ξ .

With Eqs. (4.13) at hand, it is interesting to take a closer look at the initial stages of amplification where the pump depletion is still negligible. Even without any approximations, we can focus our attention on the equation for the signal intensity and rewrite it as [151]:

$$u_s^2(\xi) = u_s^2(0) \left(1 + \frac{\gamma^2}{1-\gamma^2} (1 - \text{sn}^2[\sqrt{u_p^2(0) + u_s^2(0) - \left(\frac{\Delta kz}{2\xi}\right)^2} \xi + K(\gamma^2), \gamma^2]) \right) \quad (4.15)$$

When the initial seed intensity is very small (i.e. $u_s(0) \ll u_p(0)$), we can approximate $\gamma \approx 1$. In this case Eq. (4.15) takes the form of a hyperbolic sine-function \sinh , and the initial solutions (4.13) can be considerably simplified. Details of this approximation can be found in Appendix C.2. Transforming back from the normalized amplitudes u_m to the intensities I_m , the no-pump-depletion solutions are written as:

$$I_s(z) = I_s(0) \cosh^2 gz \quad (4.16a)$$

$$I_i(z) = \frac{\omega_i}{\omega_s} I_s(0) \sinh^2 gz \quad (4.16b)$$

$$I_p(z) = I_p(0) \quad (4.16c)$$

where the parametric gain coefficient g is defined as:

$$g = \sqrt{u_p^2(0) - \left(\frac{\Delta kz}{2\xi}\right)^2} \frac{\xi}{z} = \sqrt{\chi^{(2)2} \frac{\omega_s \omega_i I_p(0)}{2\epsilon_0 n_s n_i n_p c^3} - \left(\frac{\Delta k}{2}\right)^2} \quad (4.17)$$

When the gain is large ($gz \gg 1$), the cosh-function can be approximated as $\cosh x \approx \frac{1}{2}e^x$, and consequently the signal intensity becomes:

$$I_s(z) \approx I_s(0) \frac{1}{4} e^{2gz} \quad (4.18)$$

The small-signal gain is found to depend exponentially on the pump intensity. From this last expression, we can estimate that when using a pump wavelength of 532 nm, a signal wavelength of 800 nm, and BBO as the nonlinear medium (which implies that $n \approx 1.65$ and $\chi^{(2)} \approx 4 \times 10^{-12}$ m/V) that a gain of 10^4 can be achieved in only 5 mm of material if the pump intensity is 4 GW/cm².

4.1.3 Phase evolution during parametric amplification

By writing the coupled wave equations in the form (4.6), the influence of the respective phases on the amplification process becomes more explicit. Maximum amplification is achieved when $\sin \theta = -1$, meaning $\theta = -\pi/2$. Usually there is no idler present at the start of the amplification, and the phase of the idler that is generated by the interaction of pump and seed will automatically obtain a phase $\varphi_i(0) = \varphi_p(0) - \varphi_s(0) + \pi/2$ that maximizes the gain.

In the presence of a phase mismatch Δk , the phases of the waves must change to maintain the $\sin \theta = -1$ condition, since the phase mismatch Δkz accumulates with

distance. This phase evolution can be followed by explicitly writing out the phase terms in the coupled wave equations instead of lumping them into one single expression for θ as was done in (4.6). This gives [72]:

$$\frac{\partial \varphi_s}{\partial z} = -\chi^{(2)} \left(\frac{\omega_s}{2n_s c} \right) \frac{\rho_i \rho_p}{\rho_s} \cos \theta \quad (4.19a)$$

$$\frac{\partial \varphi_i}{\partial z} = -\chi^{(2)} \left(\frac{\omega_i}{2n_i c} \right) \frac{\rho_s \rho_p}{\rho_i} \cos \theta \quad (4.19b)$$

$$\frac{\partial \varphi_p}{\partial z} = -\chi^{(2)} \left(\frac{\omega_p}{2n_p c} \right) \frac{\rho_s \rho_i}{\rho_p} \cos \theta \quad (4.19c)$$

If we use expression (4.8) and the Manley-Rowe relations, and consider the situation where the idler intensity is initially zero, these equations reduce to:

$$\frac{\partial \varphi_s}{\partial z} = -\frac{\Delta k}{2} \frac{f}{f + \gamma_s^2} \quad (4.20a)$$

$$\frac{\partial \varphi_i}{\partial z} = -\frac{\Delta k}{2} \quad (4.20b)$$

$$\frac{\partial \varphi_p}{\partial z} = -\frac{\Delta k}{2} \frac{f}{1-f} \quad (4.20c)$$

where $\gamma_s^2 = \frac{\omega_p I_s(0)}{\omega_s I_p(0)}$, and $f = 1 - \frac{I_p(z)}{I_p(0)}$ is the fractional pump depletion. These equations can be integrated to yield [72]:

$$\varphi_s(z) = \varphi_s(0) - \frac{\Delta k}{2} \int_0^z \frac{f}{f + \gamma_s^2} dz' \quad (4.21a)$$

$$\varphi_i(z) = \varphi_p(0) - \varphi_s(0) + \frac{\pi}{2} - \frac{\Delta k z}{2} \quad (4.21b)$$

$$\varphi_p(z) = \varphi_p(0) - \frac{\Delta k}{2} \int_0^z \frac{f}{1-f} dz' \quad (4.21c)$$

These phase solutions have some interesting properties. One particularly noteworthy result is that the phase of the signal is independent of the coherence of the pump [55]: The pump pulse phase only influences the generated idler. However, while the phase of the pump pulse is of no importance, the pump intensity can influence the phase of the amplified signal pulse. From the last term in Eq. (4.21a), we can see that such an intensity dependence will influence the signal phase through the fractional pump depletion f : An additional phase will be imprinted onto the signal pulse, with a spectral shape corresponding to the phase mismatch Δk , and with a maximum magnitude of $\Delta k z / 2$. In the time domain, this may lead to intensity-dependent variations of the carrier-envelope phase. Numerical simulations are needed to estimate the magnitude of these phase shifts; such simulations are the subject of section 4.2, and the magnitude of these intensity-dependent phase shifts will be discussed in more detail in section 4.2.7.

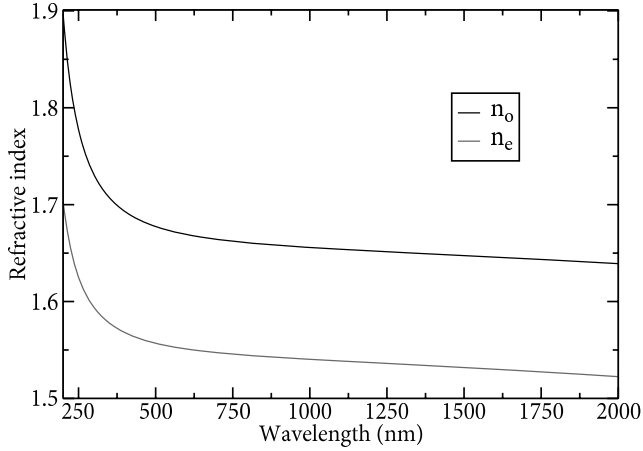


FIGURE 4.1: Refractive index of BBO as a function of wavelength, for ordinary and extraordinary waves. By tuning the phase-matching angle θ between the optical axis and the polarization of an incoming extraordinary wave, the refractive index for this wave can be set to any value in between these curves. The data in this graph is calculated using the Sellmeier equations for BBO given by Zhang et al. [152].

4.1.4 Parametric amplification of ultra-broadband spectra

The main factor that determines the gain in an OPA is the phase mismatch Δk , which can be written as:

$$\Delta k = k_p - k_s - k_i = \frac{n_p \omega_p}{c} - \frac{n_s \omega_s}{c} - \frac{n_i \omega_i}{c} \quad (4.22)$$

As energy conservation requires that $\omega_p = \omega_s + \omega_i$, Eq. (4.22) places strict demands on the refractive indices of the pump, signal and idler beams in the amplifier crystal. As the refractive index of practically all materials that are transparent to visible light is a monotonously increasing function of frequency (in the optical wavelength range), this condition is impossible to fulfill with normal crystals. A solution is the use of birefringent materials (which are required anyway to allow that $\chi^{(2)} \neq 0$), which have different refractive indices for different polarizations of the incoming light. Wave propagation in such materials is governed by the optical axes of the crystal, which determine the refractive index that a given polarization state experiences (see e.g. [22]). Depending on the symmetry, a birefringent crystal can have one or two optical axes. In the case of a uniaxial crystal the situation is considerably simplified due to symmetry considerations. In this case, an incoming light wave with a polarization perpendicular to the plane in which the optical axis lies is called an ordinary wave, and experiences a refractive index n_o . A light wave polarized parallel to this plane is called an extraordinary wave, and sees a refractive index n_e . As an example, the refractive indices n_o and n_e of the negative (i.e. $n_e < n_o$) uniaxial crystal β -BaB₂O₄ are shown in Fig. 4.1 as a function

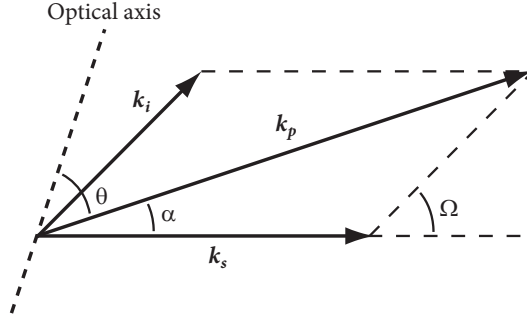


FIGURE 4.2: Phase-matching geometry for noncollinear optical parametric amplification.

of wavelength. This material, also known as BBO, is a popular amplifier material for OPA's, for reasons that will be discussed later on.

By changing the angle θ between the polarization of the incoming light wave and the optical axis, the refractive index can be tuned continuously between the values of n_o and n_e . In this way, the phase-matching condition (4.22) can be fulfilled by using an extraordinary pump wave and ordinary signal and idler waves ($e \rightarrow o + o$, or type-I phase matching). Alternatively, either the signal or idler can also be an extraordinary wave ($e \rightarrow o + e$, type-II phase matching).

Due to the shape of the dispersion curves in Fig. 4.1, the spectral bandwidth over which phase matching is achieved is limited. The phase mismatch can be expanded as a function of the signal frequency:

$$\Delta k = \Delta k_0 + \frac{\partial \Delta k}{\partial \omega_s} \Delta \omega_s + \frac{1}{2} \frac{\partial^2 \Delta k}{\partial \omega_s^2} (\Delta \omega_s)^2 + \dots \quad (4.23)$$

To acquire a large phase-matching bandwidth, the first-order term $\frac{\partial \Delta k}{\partial \omega_s}$ should be set to zero, while maintaining $\Delta k_0 = 0$ [62, 65]. This requires an additional control parameter in the phase-matching process, which can be obtained by introducing a noncollinear angle α between the pump and signal beams, as illustrated in Fig. 4.2. The phase-matching conditions should hold for both vector components parallel and perpendicular to the signal beam:

$$\Delta k_{\parallel} = k_p \cos \alpha - k_i \cos \Omega - k_s \quad (4.24a)$$

$$\Delta k_{\perp} = k_p \sin \alpha - k_i \sin \Omega \quad (4.24b)$$

which reduces to the collinear phase-matching equation (4.22) when α is set to zero. Note that there is no unique solution for α : Phase matching of three given frequencies ω_s , ω_p and ω_i can in general be achieved for many different noncollinear angles, by adjusting the phase-matching angle θ . The first order frequency dependence of the phase mismatch in the expansion (4.23) can now also be decomposed into these vector

components, by differentiating (4.24) with respect to ω_s :

$$\frac{\partial \Delta k_{\parallel}}{\partial \omega_s} = -\cos \Omega \frac{\partial k_i}{\partial \omega_s} + k_i \sin \Omega \frac{\partial \Omega}{\partial \omega_s} - \frac{\partial k_s}{\partial \omega_s} \quad (4.25a)$$

$$\frac{\partial \Delta k_{\perp}}{\partial \omega_s} = -\sin \Omega \frac{\partial k_i}{\partial \omega_s} - k_i \cos \Omega \frac{\partial \Omega}{\partial \omega_s} \quad (4.25b)$$

where a narrow-band pump beam and no angular dispersion are assumed (i.e. $\frac{\partial k_p}{\partial \omega_s} = \frac{\partial \alpha}{\partial \omega_s} = 0$). Both components can be made to vanish simultaneously by a proper choice of Ω [60], which in turn is determined by the value that is taken for α through (4.24). Multiplication of (4.25a) by $\cos \Omega$ and (4.25b) by $\sin \Omega$, and subsequent addition yields a simple expression:

$$\frac{\partial k_s}{\partial \omega_s} \cos \Omega + \frac{\partial k_i}{\partial \omega_s} = 0 \quad (4.26)$$

which, since the group velocity $v_g = \left(\frac{\partial k}{\partial \omega}\right)^{-1}$, can be written as:

$$v_{gs} = v_{gi} \cos \Omega \quad (4.27)$$

This relation states that broadband phase matching can be achieved by *group-velocity matching*, i.e. adjusting the group velocity components of signal and idler along the signal propagation direction to be equal [61, 62, 65, 71].

When group-velocity matching is realized, the residual phase mismatch is determined by the higher-order terms in expansion (4.23), most notably by the second-order term $\frac{\partial^2 \Delta k}{\partial \omega_s^2}$. Writing out the vector components of this second-order yields:

$$\frac{\partial^2 \Delta k_{\parallel}}{\partial \omega_s^2} = -\cos \Omega \frac{\partial^2 k_i}{\partial \omega_s^2} + 2 \sin \Omega \frac{\partial k_i}{\partial \omega_s} \frac{\partial \Omega}{\partial \omega_s} + k_i (\sin \Omega + \cos \Omega) \frac{\partial^2 \Omega}{\partial \omega_s^2} - \frac{\partial^2 k_s}{\partial \omega_s^2} \quad (4.28a)$$

$$\frac{\partial^2 \Delta k_{\perp}}{\partial \omega_s^2} = -\sin \Omega \frac{\partial^2 k_i}{\partial \omega_s^2} - 2 \cos \Omega \frac{\partial k_i}{\partial \omega_s} \frac{\partial \Omega}{\partial \omega_s} + k_i (\sin \Omega - \cos \Omega) \frac{\partial^2 \Omega}{\partial \omega_s^2} \quad (4.28b)$$

These equations can be simplified in the same way as (4.25). Assuming that group-velocity matching is satisfied, we obtain:

$$-\sin \Omega \frac{\partial k_s}{\partial \omega_s} \frac{\partial \Omega}{\partial \omega_s} + k_i (\sin 2\Omega + \cos 2\Omega) \frac{\partial^2 \Omega}{\partial \omega_s^2} = 0 \quad (4.29)$$

This expression states that the magnitude of the second-order term in (4.23) is determined by the angular dispersion between signal and idler beams. In general, this relation can not be satisfied just by tuning the noncollinear angle α . Again, an additional control parameter is required, which can be provided by introducing a frequency-dependent noncollinear angle $\alpha = \alpha(\omega)$. Such a frequency dependence can be produced by e.g. using multiple pump beams with different noncollinear angles [153, 154], or by using an angularly dispersed signal beam [155–157]. The use of multiple pump beams results in a discrete set of different values for α , each with its own relations for

phase- and group-velocity matching (4.25) and (4.28). The proper choice of a set of α 's can then lead to a compensation of the phase mismatch over a broader spectral range compared to the case of a single pump beam. Seeding the OPA with an angularly dispersed signal beam results in $\frac{\partial \alpha}{\partial \omega_s} \neq 0$, leading to additional terms in the phase-matching relations (4.25) and (4.28). These terms can be used to minimize the phase mismatch over a larger bandwidth by tailoring the angular dispersion, provided that the initial phase mismatch is not too large. However, from an experimental point of view the use of an angularly dispersed seed beam is not very attractive, because the generation of controlled angular dispersion requires a precisely aligned combination of dispersive and focusing optics, both for the generation of the angular chirp as well as for its compensation after amplification. Although various design studies have been published of ultra-broadband NOPCPA schemes using angularly dispersed seed beams [155, 156], such systems have – to the best of our knowledge – never been demonstrated experimentally. A more practical variation on this concept is the use of an angularly dispersed broadband pump pulse [63, 66, 67], which has the advantage that recollimation of the amplified seed spectrum after the amplifier is not required.

4.1.5 Parametric superfluorescence

Although the classical wave theory given in the previous sections is sufficient for a good understanding of optical parametric amplification, it can not explain the generation of parametric superfluorescence: Even in the complete absence of seed light, photons are generated spontaneously at the signal and idler frequencies [57, 58]. This is a purely quantum phenomenon, which is caused by seeding of the parametric amplifier by the zero-point modes of the vacuum field [54–56, 158].

To describe this effect properly, a quantum-mechanical model of optical parametric amplification is required. Such a model can be constructed by considering two modes of the electromagnetic field A and B , which are coupled by a driving field that oscillates harmonically at a frequency $\omega_p = \omega_A + \omega_B$ [22, 53, 54]. The Hamiltonian of this system is given by:

$$H(t) = \hbar\omega_A a^\dagger a + \hbar\omega_B b^\dagger b - \hbar\kappa[a^\dagger b^\dagger e^{-i\omega_p t} + abe^{i\omega_p t}] \quad (4.30)$$

where κ is the coupling strength, and a , a^\dagger , b and b^\dagger are the time-dependent photon creation and annihilation operators for the modes A and B . The coupling strength κ can be shown to have a form similar to Eq. (4.17), and it plays the role of a small-signal gain factor [53]. From this Hamiltonian, the Heisenberg equations of motion for the a - and b -operators can be derived:

$$\frac{\partial a(t)}{\partial t} = -i\omega_A a + i\kappa b^\dagger e^{-i\omega_p t} \quad (4.31)$$

$$\frac{\partial b^\dagger(t)}{\partial t} = i\omega_B b^\dagger - i\kappa a e^{-i\omega_p t} \quad (4.32)$$

and similar equations exist for their Hermitian conjugates a^\dagger and b . The solutions to

these equations are found to be:

$$a(t) = e^{-i\omega_A t} [\cosh(\kappa t) a + i \sinh(\kappa t) b^\dagger] \quad (4.33)$$

$$b^\dagger(t) = e^{i\omega_B t} [\cosh(\kappa t) b^\dagger - i \sinh(\kappa t) a] \quad (4.34)$$

In quantum mechanics, the number operator $N_A(t) = a^\dagger a$ gives the number of photons in a state $|n_A\rangle$. We can construct these number operators using the expressions (4.34). After some rearranging this yields:

$$N_A(t) = \cosh^2(\kappa t) a^\dagger a + [1 + \sinh^2(\kappa t)] b^\dagger b + \frac{i}{2} \sinh(2\kappa t) [a^\dagger b^\dagger - ab] \quad (4.35)$$

along with a similar expression for $N_B(t)$.

Now consider the case where initially at $t = 0$ the system is in the vacuum state $|0, 0\rangle$, so that there are no photons in mode A or mode B to seed the parametric amplifier. Nevertheless, when we calculate the expectation value for the photon number operator N_A at a given time t using equation (4.35), we find:

$$\langle 0, 0 | N_A(t) | 0, 0 \rangle = \sinh^2 \kappa t \quad (4.36)$$

This result states that, even in the absence of seed photons, the optical parametric amplifier will spontaneously produce output photons at the signal and idler frequencies. These photons are observable as parametric superfluorescence, and their number depends on the coupling strength κ which is proportional to the intensity of the driving field at frequency ω_p . Note that expression (4.36) is very similar to the classical gain in the absence of pump depletion (4.16), especially in the limit where the gain is high ($\kappa t \gg 1$). From Eq. (4.36) we find that parametric superfluorescence at the signal frequency ω_A behaves as if it was seeded by one photon at the idler frequency ω_B [22]. By summing over all possible input frequencies and taking phase matching into account, an estimate for the output power of the generated parametric superfluorescence in a particular system can be obtained [22, 55, 56, 59].

A quantum-mechanical description is very useful for the investigation of coherence effects and photon number statistics in optical parametric amplification. Such studies have been undertaken by a number of researchers, and many interesting results have been obtained [53–56, 158]. However, since all the experimental work in this thesis has been directed towards high-power amplifiers using highly coherent laser pulses with large photon numbers, the classical wave theory presented in the previous sections is an excellent approximation when performing simulations of our experimental system. Therefore, a rigorous quantum treatment of optical parametric amplification will not be given here.

4.2 Numerical modeling of NOPCPA

While the previous section showed that the coupled wave equations can be solved analytically using certain approximations, it is difficult to obtain a complete picture of how

a realistic NOPCPA system works from such a collection of formulas. The normal operating conditions of our NOPCPA system involve significant pump depletion, multiple amplification stages with different sets of parameters, chirped ultra-broadband seed spectra, and amplifier crystals with a frequency-dependent refractive index. For such a complicated system, analytical calculations become intractable, and computer-based numerical algorithms are required for proper modeling of the amplification process.

We have developed a numerical algorithm that is capable of solving the coupled wave equations for the pulse envelope (4.3). The simulation program can handle ultra-broadband input seed spectra, and takes full account of the material dispersion. In addition, multiple amplification stages with different sets of parameters can be modeled. This algorithm allows realistic modeling of a high-power multi-stage NOPCPA system for few-cycle laser pulses, similar to the amplifier systems that we have demonstrated experimentally (see chapters 6-8). In this section, we discuss the working principles and details of the numerical algorithm, and present a systematic study of the influence of several important experimental parameters on the NOPCPA process.

4.2.1 The split-step Fourier algorithm

The algorithm is based on the split-step Fourier scheme [119, 159]: It takes a modular approach, dividing the total interaction length into a number of slices. For each slice, the nonlinear parametric interaction and the linear dispersive pulse propagation are calculated in turns. In essence, the amplification and dispersion operators are assumed to be independent from each other. This approach can have a good degree of accuracy, provided that the slices are chosen sufficiently thin. More formally, the differential equations governing the interaction (which are the coupled-wave equations (4.3)) can be written as [119]:

$$\frac{\partial A_m}{\partial z} = (\hat{D} + \hat{N})A_m \quad (m = s, i, p) \quad (4.37)$$

where \hat{D} is the operator that describes pulse propagation in a linear dispersive medium, and \hat{N} is the operator for the nonlinear parametric interaction. The general solution to this equation for propagation from z to $z + h$ is then given by:

$$A(z + h, t) = e^{h(\hat{D} + \hat{N})} A(z, t) \quad (4.38)$$

Taking this step twice is then of course described by applying the exponential operator twice. In the split-step scheme, this solution is approximated by:

$$A(z + h, t) = e^{h\hat{D}} e^{h\hat{N}} A(z, t) \quad (4.39)$$

which is equivalent to taking a step with only nonlinearity present (i.e. $\hat{D} = 0$), and then taking a step with only dispersion ($\hat{N} = 0$). The accuracy of this approximation can be estimated by expanding the split-step operator in Eq. (4.39) using the Baker-Campbell-Hausdorff formula:

$$e^{h\hat{D}} e^{h\hat{N}} = e^{h\hat{D} + h\hat{N} + (h^2/2)[\hat{D}, \hat{N}] + \dots} \quad (4.40)$$

This expansion shows that the main deviation from the exact solution (4.38) is due to the noncommutating nature of the two operators, and the magnitude of the error is of the order h^2 .

4.2.2 Practical implementation of the numerical algorithm

One reason that makes the split-step approach appealing is that the dispersion can be modeled very accurately in the absence of nonlinear interactions. In the time domain, the operator \hat{D} is written as:

$$\hat{D}(t) = \sum_{n=1}^{\infty} \frac{(-i)^{n+1}}{n!} k^{(n)} \frac{\partial^n}{\partial t^n} \quad (4.41)$$

Although the operator is complicated to apply in this form, a Fourier transformation to the frequency domain makes it relatively simple. As was already discussed in chapter 2, in the frequency domain the dispersion operator can simply be expressed as:

$$\hat{D}(\omega) = n(\omega) \frac{\omega}{c} \quad (4.42)$$

The dispersion operator introduces a phase shift to every frequency component in the pulse. Therefore, a propagation step of length h can be calculated by taking the Fourier transform of the pulse, applying the phase shift by multiplication with a complex exponential, and inverse Fourier transformation back to the time domain:

$$A(z+h, t) = \mathcal{FT}^{-1} \left[e^{in\omega h/c} \mathcal{FT} [A(z, t)] \right] \quad (4.43)$$

Since this step only requires two Fourier transforms and some multiplication, it is computationally fast. In addition, it can be very accurate as the Sellmeier equations that describe the frequency-dependence of the refractive index are well-known [152] and can be used directly, without the need to use polynomial expansions for the dispersion. This propagation step can be implemented for pump, seed and idler pulses independently from each other.

While the dispersion operator is relatively easy to implement, the nonlinear interaction operator \hat{N} is much more complex, since it contains nonlinear coupling of pump, seed and idler waves. For instance, the operator for the seed pulse has the form (see Eqs. (4.3)):

$$\hat{N}_s = -i \frac{\omega \chi^{(2)}}{2n_s c} A_p A_i^* \quad (4.44)$$

and similar operators exist for the pump and idler pulses. These operators depend explicitly on the product of two different pulse envelopes in the space-time domain. Therefore, calculating the effect of a nonlinear interaction step requires the simultaneous integration of the full set of coupled differential equations. This can be done using the Jacobi elliptic integrals introduced in subsection 4.1.2 [72], but since this requires some approximations we chose to perform the integration numerically. To this end, we employ a fourth-order Runge-Kutta integration routine with adaptive stepsize control [160]. Such an algorithm is usually not capable of handling complex numbers, so

the three initial differential equations are split up into real and imaginary parts leading to a set of six coupled equations with only real data as input. The pulses are defined on a time axis of length N , and the integration is performed for every point on this time axis.

The numerical algorithm requires the electric field of a pump and a seed pulse in the time domain as input data. It starts out by solving the six coupled-wave equations for all real and imaginary parts of pump, seed and idler pulses. In this integration, the phase-mismatch term for the carrier frequencies $e^{i\Delta k z}$ in Eqs. (4.3) has been incorporated into the pulse envelopes $A_m(z, t)$; in this way, the phase mismatch between the waves is introduced in a natural way through the dispersive propagation step. The integration step is performed first over one crystal slice, and when the solution is found the effects of pulse propagation are incorporated by taking a step over the same slice again, using only the dispersion operator [159].

The number of slices that the crystal needs to be divided into to achieve sufficient accuracy is determined by repeating a simulation using typical input data with an increasing number of slices, until the solution converges (typically at 20-30 slices per crystal). The propagation step is calculated in the reference frame of the pump pulse. This is done for convenience, as the time axis can be kept smaller in this frame.

The numerical model describes a three-stage amplifier, similar to the experimental system presented in chapters 7 and 8. In this amplifier, the first two passes are pumped by 10 mJ pulses at a wavelength of 532 nm. After this pre-amplifier stage, the amplified signal beam is expanded from 2 to 10 mm diameter by a telescope, and sent to a third amplification pass pumped by 150 mJ pulses. Typically, the simulations are performed using pump intensities 7.5 GW/cm² in the first two passes and 6 GW/cm² in the last pass, and an input pulse energy of ~ 1 nJ. These model pump intensities have been used because they lead to the best match between the calculated spectra and the experimental observations presented in chapter eight. While the intensity of the first two passes corresponds well to the estimated experimental value, the intensity of the last pass is about 20-50% higher than expected. This is probably due to uncertainties in the exact pump pulse shape and duration, and to several other experimental parameters that influence the interaction in the last crystal.

4.2.3 Optimization of spectral bandwidth

Both the gain and bandwidth of the amplifier system depend sensitively on the phase matching conditions. The strong effect of the phase mismatch on the parametric amplification process is explained by the different frequency-dependent nonlinear propagation characteristics of the various pulses. This can be seen explicitly from the complex $e^{i\Delta k z}$ -term in the nonlinear polarization of the coupled-wave Eqs. (4.3), which splits into an imaginary part that causes a phase shift between waves, and a real part that directly influences the gain. Therefore, many characteristics of an NOPCPA system can already be predicted by the shape and size of the phase-mismatch curve as a function of wavelength. Examples of such graphs for the case of a type I parametric amplification process in BBO using a pump wavelength of 532 nm are shown in Fig. 4.3. A rotation of the phase-matching angle θ (the angle between the pump beam k -vector and the optic

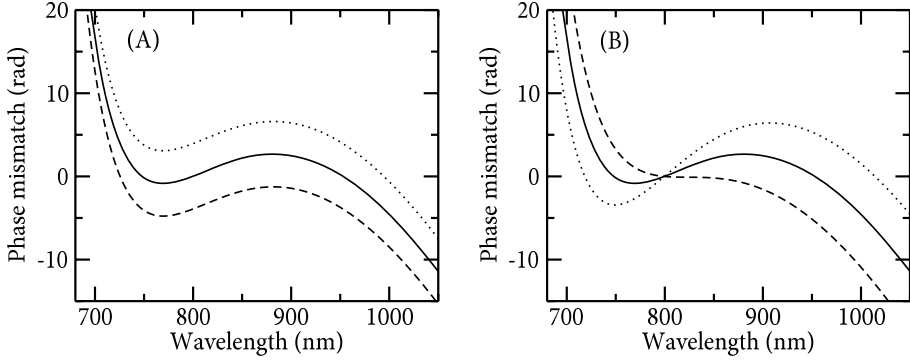


FIGURE 4.3: Wavelength-dependent phase mismatch for type I parametric amplification in a 5 mm BBO crystal using a 532 nm pump beam. **(A)** Variation of the phase-matching angle θ : the depicted angles are 23.89° (solid), 23.85° (dotted) and 23.93° (dashed) respectively. **(B)** Variation of the noncollinear angle α , while keeping the phase matching optimized for a signal wavelength of 800 nm. The curves shown are for angles of 2.30° (dotted), 2.40° (solid) and 2.50° (dashed).

axis of the crystal) leads to a shift in phase mismatch which is constant across the entire spectrum as shown in Fig. 4.3A, whereas a change of the noncollinear angle α (the angle between pump and seed beams) introduces an additional, frequency-dependent phase shift that rotates the entire phase-matching curve (Fig. 4.3B). Note that for this particular case of a 532 nm pump wavelength and BBO as the nonlinear medium, the phase mismatch can be kept small enough for efficient amplification of a very broadband infrared spectrum. The shape and structure of this spectrum then depend on the exact angles in the interaction.

The major influence that these angles have on the parametric amplification process is demonstrated by performing simulations using different values for these angles, as shown in Fig. 4.4. The central values for the angles in this simulation are $\theta = 23.829^\circ$ and $\alpha = 2.36^\circ$, which are close to the optimum values for broadband phase matching [72, 161], as is also confirmed by the present calculations. The effect of adding slight variations $\Delta\theta$ (where in this case $\Delta\theta = \pm 0.06^\circ$) to θ is shown in the left panels of Fig. 4.4: Changing θ has the effect of shifting the phase-mismatch curve up or down in a wavelength-independent way, and consequently the gain is seen to be highest in the regions where the phase-mismatch is minimized. Figure 4.4B demonstrates the effect of changing α , which is to tilt the phase-mismatch curve, allowing it to be minimized over a large spectral bandwidth. In these simulations, θ was adjusted such that the phase-mismatch at 800 nm is zero, so that the phase mismatch curve is effectively tilted around this center wavelength. While an angle $\alpha = 2.36^\circ$ leads to a very broad amplified spectrum with some modulation, the amplified bandwidth can be made even broader by tuning α to slightly smaller values. However, this is only achieved at the cost of stronger spectral intensity modulations. The reason for this is immediately apparent from the phase-mismatch curves, which are tilted from a monotonously decreasing function at large α to a shape with local maxima and minima at smaller α . This phase-

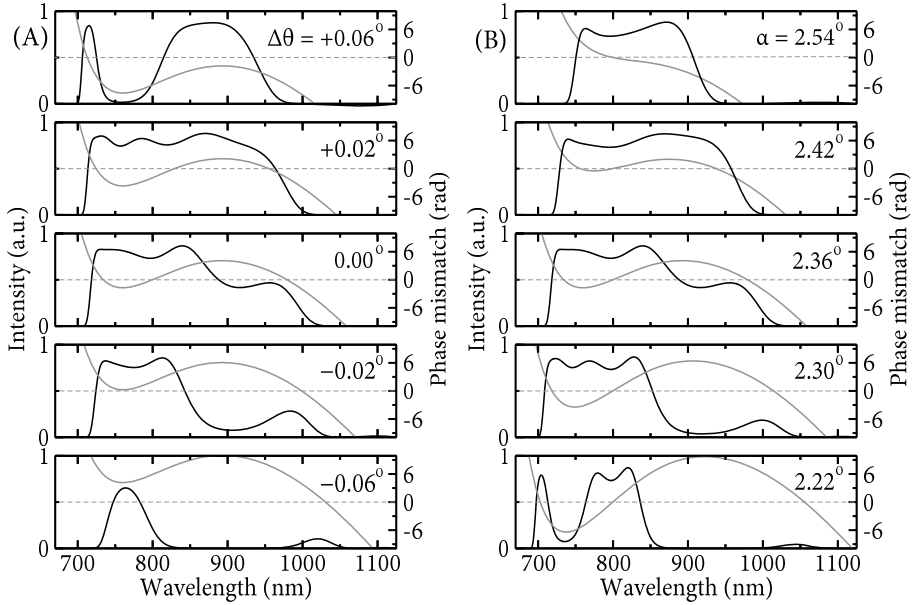


FIGURE 4.4: Numerical simulations of the wavelength-dependent output of a three-stage NOPCPA system. **(A)** using various phase-matching angles $\theta = 23.829^\circ + \Delta\theta$, while keeping $\alpha = 2.36^\circ$. **(B)** using various noncollinear angles α , while adjusting θ to optimize phase matching at a wavelength of 800 nm. The black lines represent the amplified signal spectra, while the grey lines are the corresponding wavelength-dependent phase mismatches. The dashed grey lines indicate zero phase mismatch.

mismatch curve at small α contains three zero-crossings, leading to the three-peak structure of the spectrum. Between these zero-crossings the phase excursions become quite substantial, causing a strong suppression of the gain at these wavelengths. From an experimental point of view, Fig. 4.4 demonstrates the high accuracy with which θ and α need to be set, as changes on the order of 0.01° already have a significant effect on the amplification process.

4.2.4 Modeling an experimental NOPCPA system

The usefulness of a numerical model is of course determined by its ability to simulate the behaviour of a realistic experimental system. Therefore, we initially tested the ability of the numerical algorithm to reproduce the output characteristics of our experimental NOPCPA system from its input parameters. For all the simulations described in this paper, we used pump and seed pulse durations that correspond to our experimental situation [80]. However, in the experiment the angles θ and α in each pass are optimized for optimal broadband amplification, but their exact values are not known to the required level of accuracy to simply insert them into the model. The same problem arises for the exact pump-seed timing delay for each pass. Therefore, to find a spectrum

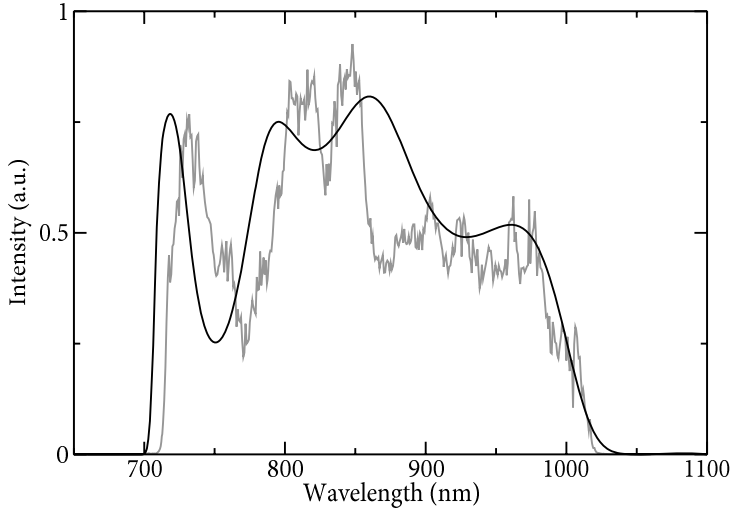


FIGURE 4.5: Comparison of a measured output spectrum from our NOPCPA system (grey trace) with a numerical simulation (black trace). A relatively straightforward calculation already reproduces the main features of the spectrum, although the exact wavelengths at which they occur are shifted slightly. See text for details.

that matches the experimental data we performed a series of simulations for varying sets of noncollinear angles and phase mismatches. Due to the large parameter space and to save computation time, we restricted the search by using the same noncollinear angle and phase mismatch in all three amplification passes.

A comparison between the measured spectrum and a model calculation is shown in Fig. 4.5. This simulation is performed using a noncollinear angle α of 2.31° and a phase-matching angle θ of 23.783° in all crystals. The shape of the simulated spectrum corresponds very well to the experiment, and all the general features are reproduced. Some discrepancies are visible, such as the shift in the position of the peak structure around 730 nm to shorter wavelengths, and the relatively sharp edge around 860 nm which is smoother in the simulation than in the experimental spectrum. These details are most likely caused by slight variations in angles and pulse timings between amplification passes. However, aside from these small differences, a good agreement is found between numerical simulation and experimental observation, which gives confidence that the model is capable of making realistic predictions of the output characteristics of our NOPCPA system.

A convenient feature of the split-step algorithm is that the pulse shapes and spectra of all three involved waves are calculated in small steps through each crystal, and the data from each of these steps can be saved individually. The amplification process is thus automatically monitored at various positions inside the crystal, as shown in Fig. 4.6. In Fig. 4.6A the temporal pulse profile of the signal is plotted as it travels through the first crystal, while Fig. 4.6B displays the signal spectrum as the pulse prop-

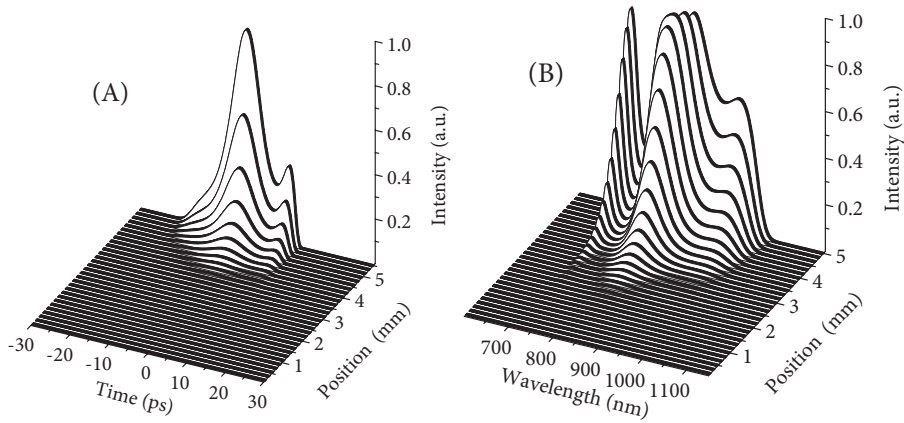


FIGURE 4.6: (A) Evolution of the temporal profile of the signal pulse during amplification in the first pass. (B) Spectral intensity of the signal pulse in the last amplification pass.

agates through the last crystal. From these pictures, the pulse evolution in the entire amplifier can be studied in both frequency- and time domain.

4.2.5 Pulse contrast and amplified fluorescence

An important aspect of high-intensity NOPCPA systems is the achievable pulse contrast, which is limited by the incoherent background caused by parametric superfluorescence. The first passes in a practical NOPCPA system have a high gain (on the order of several GW/cm^2), which can lead to the generation of a significant amount of parametric superfluorescence, through the mechanism described in section 4.1.5. This fluorescence from the first stage can then be amplified efficiently in later passes, leading to an incoherent background added to the final NOPCPA output pulse.

To limit the amount of fluorescence, three key points should be taken into account in the design of an NOPCPA system. First, the gain per pass should not be too high, to limit the amount of fluorescence that is produced. Second, the intensity of the seed pulse should be as high as possible, since parametric amplification and fluorescence generation are competing processes: A higher seed intensity will therefore lower the gain for the production of fluorescence. Third, deep saturation of the amplification process should be avoided, as this will lead to a reduced contrast between the amplified pulse and the (initially much weaker) fluorescence background). Especially when the seed pulse is significantly shorter than the pump pulse, there will be points in space and time where there is significant gain without any seed light present. At these points, the parametric fluorescence can reach significant intensity if the considerations mentioned above are not fulfilled.

A quantitative estimate of the amount of parametric superfluorescence that will be generated by an NOPCPA system is difficult to calculate. To check whether fluorescence will be a serious problem in our NOPCPA system, we performed calculations

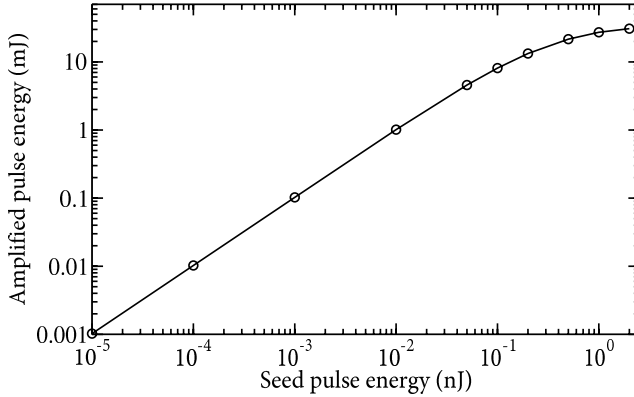


FIGURE 4.7: Calculated amplified output pulse energy as a function of input seed pulse energy for a three-stage NOPCPA system, for typical pump intensities and crystal lengths as used in our experiments (see text, section 4.2.2). The circles indicate calculated points, the straight line is a guide to the eye.

for various initial seed intensities. All the pump intensities, crystal lengths, angles, etc. that have been used in this calculation correspond to our experimental parameters (see sections 4.2.2 and 4.2.4). The resulting amplified pulse energy as a function of the seed pulse energy is depicted in Fig. 4.7. These calculations confirm that at the present pump intensities saturation is not excessive, and only sets in at a seed pulse energy of ~ 1 nJ seed pulses (comparable to the experimental situation). As a result, any fluorescence produced in the first pass will remain much weaker than the amplified seed pulse, even after subsequent amplification in the last two passes. This result is confirmed by experimental observations, as described in detail in chapters 7 and 8.

4.2.6 Wavelength-dependent gain saturation

An interesting feature of NOPCPA is depicted in Fig. 4.8, which consists of cuts through the data of Fig. 4.6B taken at various wavelengths. This graph reveals the wavelength-dependent gain dynamics as the amplification process saturates in the last crystal. While the wavelengths with the highest gain (i.e. the lowest phase mismatch) already saturate and even exhibit energy back-conversion, wavelengths with a lower gain still show a small-signal exponential gain behaviour. This effect does not occur in conventional (e.g. Ti:Sapphire) amplifiers, and is directly related to the instantaneous nature of parametric amplification: Since the seed pulse is chirped, its frequency components are separated in time and overlap with different parts of the pump pulse. Each wavelength therefore has its own “slice” of pump light available for amplification, without competition from the other wavelengths. The interaction length that is required for gain saturation then depends only on the phase mismatch for this particular wavelength, leading to the behaviour that is observed in Fig. 4.8. The small dip around 820 nm in the amplified spectrum shown in Fig. 4.5 may be explained by such spectrally depen-

dent amplification dynamics, as the simulation indicates some energy back-conversion to occur at this wavelength. In a configuration where the gain is even higher this effect can lead to an increasingly complicated spectral structure, with various peaks and dips depending on the saturation regime experienced by each spectral component. From an experimentalist's point of view, the occurrence of wavelength-dependent gain saturation calls for a high pump pulse intensity stability, because a change in pump power affects all the spectral components of the signal pulse in a different way. For example, by analyzing the saturation curves shown in Fig. 4.8 it can be seen that a decrease in pump intensity leads to a stronger signal intensity decrease at 950 nm than at 855 nm, while at the same time the intensity at 820 nm would increase. Such spectral variations directly translate into changes of the temporal pulse shape, causing undesirable intensity-dependent changes of the pulse duration. To assess the magnitude of this effect, we have repeated the simulations that resulted in Fig. 4.8 using different pump intensities. For a pump intensity variation of 4%, the transform-limited amplified seed pulse duration is found to change by $\sim 5\%$. In addition, we have measured the output spectrum of our NOPCPA system [80] at various power levels, and found similar results. Such a coupling between pump intensity fluctuations and the shape of the final spectrum will become more pronounced when the total gain of the amplifier increases. As a result, a high intensity stability of the pump laser is essential for reliable NOPCPA operation.

Another important consequence of wavelength-dependent gain saturation is that the beam profile of the pump laser system must be very homogeneous. From the discussion above, it is clear that any pump intensity variation will lead to a different am-

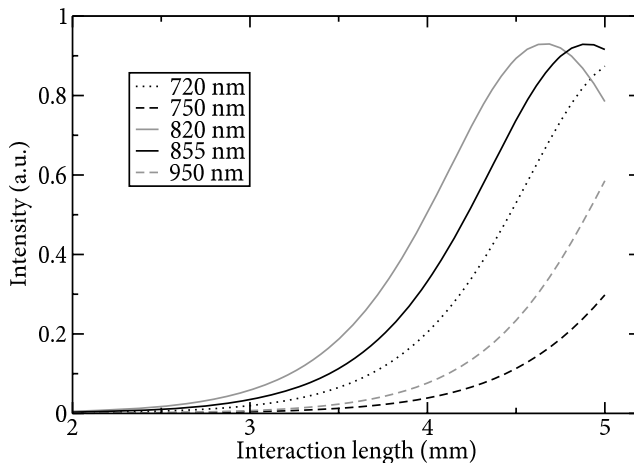


FIGURE 4.8: Wavelength-dependent gain saturation: Due to the differences in phase mismatch, the NOPCPA gain is frequency-dependent. Since all the frequencies are temporally separated in the chirped seed pulse, gain saturation and even backconversion occurs for every wavelength independently.

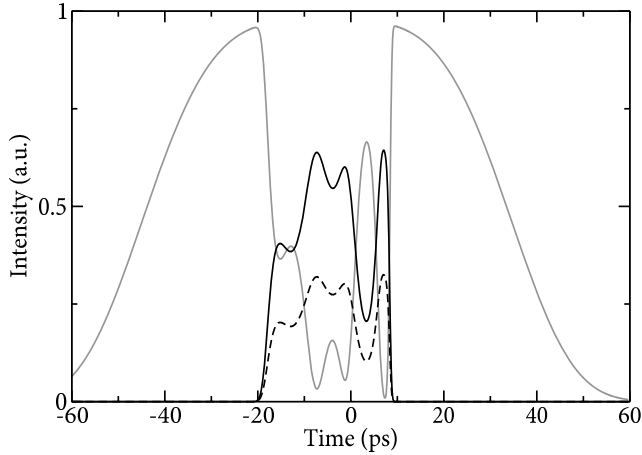


FIGURE 4.9: Temporal profile of pump, (grey curve), signal (black curve) and idler (dashed curve) after amplification. The total pump-to-signal energy conversion is about 17%, although local pump depletion exceeds 90%.

plified spectrum, and therefore to a different amplified pulse duration. Therefore, any spatial intensity variations across the pump beam profile will also translate into spatial variations of the amplified spectrum and the pulse duration. A direct consequence is that the pump pulse of a few-cycle NOPCPA system needs to be top-hat shaped, to prevent a spatially dependent pulse duration after amplification. In addition, temporal fluctuations of the pump beam profile should be avoided.

An estimate of the total pump-to-signal conversion efficiency for a specific set of parameters can be obtained by looking at the pulses in the time domain, as shown in Fig. 4.9. This figure demonstrates that the present NOPCPA configuration already operates with strong local pump depletion. From calculations by Ross et al. [72] it is known that in principle 100% conversion efficiency is possible when the phase-mismatch Δk is zero and group velocity effects are absent. The presence of a nonzero Δk , and the occurrence of a small group velocity mismatch therefore place a limit on the maximum efficiency. In addition, the interaction length needed to achieve maximum conversion becomes longer when $\Delta k \neq 0$. Our simulations show that with the present experimental parameters we can achieve $> 90\%$ conversion at wavelengths where the phase mismatch is minimized. However, since the signal pulse has been chosen shorter than the pump pulse to efficiently amplify all spectral components, the total conversion efficiency is much lower. For the amplified pulses shown in Fig. 4.9, the pump-to-signal energy conversion efficiency is 17%, while the idler then takes another 8.5% of the initial pump energy. This number is quite close to the experimentally achieved pump-to-signal conversion efficiency of about 19%.

From Fig. 4.9 it can be seen that during amplification, the shape of the signal pulse has changed from a Gaussian input pulse to a strongly modulated square-like structure. This is also the result of the instantaneous, wavelength-dependent amplification

process, which leads to a temporal pulse shape that mimicks the shape of the amplified spectrum. Note that for a positively chirped pulse the shortest wavelengths are at the trailing edge of the pulse, which is confirmed by comparing the structure of the signal pulse in the time-domain picture in Fig. 4.9 with the corresponding frequency spectrum in Fig. 4.5. This behaviour can already be seen before saturation sets in, as is shown in Fig. 4.6A, where the wavelength-dependent differences in gain lead to a re-shaping of the amplified seed pulse. Again, this is a feature specific to NOPCPA which is not encountered in amplifier systems that use energy storage in a medium, such as Ti:Sapphire. This feature opens up the possibility of spectral amplitude shaping by using a temporally modulated pump pulse, which also makes it possible to control the shape of the Fourier-limited pulse shape of the final amplified output pulse in the time domain. However, it also causes the transfer of noise which may be present on the pump pulse profile (due to e.g. mode-beating in a system based on a multimode pump laser) to the spectral shape of the amplified signal pulse [162].

4.2.7 Intensity-dependent phase shifts

As already discussed in section 4.1.3, pump intensity variations can lead to a phase shift of the amplified signal pulse. To estimate the magnitude of these phase shifts, we performed simulations of this effect using normal experimental NOPCPA operating conditions. From these simulations, we obtained values for the fractional pump depletion and γ_s^2 (see section 4.1.3) as a function of interaction length z in all crystals. Using this data, we are able to perform the integration in Eq. (4.21a), so that the phase shift caused by the parametric interaction can be calculated. By repeating this procedure for various pump intensities, the phase shifts that result from pump intensity fluctuations can be estimated.

Since the fractional pump depletion in NOPCPA depends on wavelength (see previous section), the integral in Eq. (4.21a) will be wavelength-dependent as well. For our typical experimental situation, we find that the last amplification pass introduces a significant signal phase shift that varies across the pulse spectrum, reaching values of e.g. $0.2 \Delta kz$ at a wavelength of 820 nm, and $0.1 \Delta kz$ at 750 nm. This phase shift should be taken into account when designing a compressor for the amplified output pulses. However, the phase shifts caused by intensity variations when the amplifier is operating at full power are found to be much smaller. This is explained by Fig. 4.10A, where the integrand of Eq. (4.21a) is plotted as a function of z for full pump intensity (black trace) and for 5% lower power (grey trace). The magnitude of the phase shift caused by such a 5% intensity variation is determined by the difference between the integrals of both traces, given by the grey shaded area. This area is only a fraction of the total integral: We find that the 5% intensity variation leads to a phase shift of only $0.035 \Delta kz$. Because the last NOPCPA pass operates in the regime of significant pump depletion ($f \gg \gamma_s^2$), the magnitude of this difference between the integrals is found to vary only a few percent across the pulse spectrum. Therefore, the resulting phase shift as a function of wavelength mimicks the spectral shape of the phase mismatch Δk (see Fig. 4.10B). For a 5% change in intensity, the size of this phase shift remains smaller than 0.2 rad

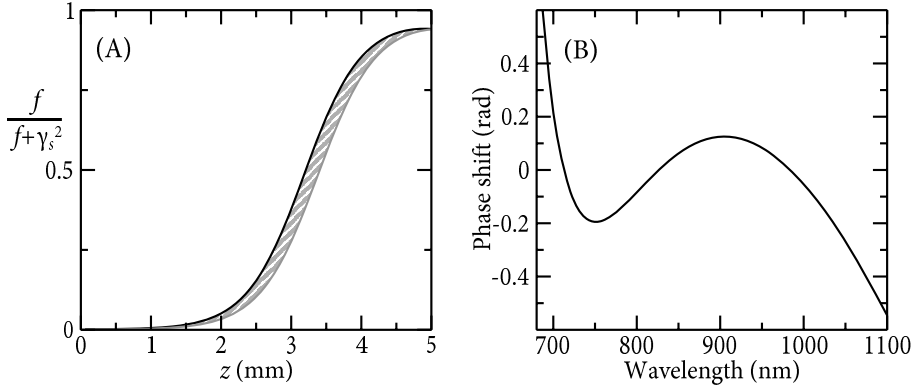


FIGURE 4.10: (A) Argument of the integral in Eq. (4.21a) at a wavelength of 855 nm. The black and grey curves correspond to a 5% difference in the initial pump intensity. The grey shaded area illustrates the difference between the integrals of these two cases, which gives rise to an intensity-dependent phase shift. (B) The added spectral phase shift according to Eq. (4.21a), for a 5% intensity decrease in our experimental situation (see text for details).

across the entire pulse spectrum, and is much lower on average. Such a spectral phase will only lead to minor variations of the pulse shape.

To estimate the effect of such a spectral phase shift on the carrier-envelope phase, we studied the influence of this spectral phase on an initially Fourier-limited 7.3 fs pulse in the time domain. For a pump intensity variation of 5%, we find a carrier-envelope phase shift below $1/40^{\text{th}}$ of a cycle in the last amplification pass. Repeating this calculation for the first two passes yields even smaller values. It should be noted, however, that the added spectral phase does give rise to a small change in the temporal pulse shape: In this example, the 5% intensity variation leads to the broadening of an initially Fourier-limited 7.3 fs pulse by about 3%. Similar to the wavelength-dependent gain saturation discussed in the previous section, we find a small coupling between the pump intensity and the amplified pulse duration. This coupling then also leads to some additional intensity fluctuations of the amplified signal pulses through the variation of the pulse duration. However, this effect is small compared to the direct changes in the amplified pulse energy caused by a decrease in pump intensity. Although the pump-induced phase shifts may be observable in a well-controlled experimental situation, they are sufficiently small to allow phase-stable amplification in a multi-stage amplifier system with realistic requirements for the pump intensity stability.

Another consequence of this parametric phase shift is the possibility of a spatial phase variation when the pump pulse is not exactly top-hat shaped. In the case of a pump pulse with a Gaussian transverse beam profile, the amplified pulse would obtain a wavelength-dependent phase variation across the beam profile. As the pump power smoothly tends to zero at the beam edges, the saturation of the amplification process and the fractional pump depletion f become less. Depending on the exact pump beam profile and the ratio between pump and seed beam diameters, this local pump intensity

variation can be significantly larger than the 5% that was used in the calculations discussed above. Therefore, the phase shift that this effect induces can be substantial, and care should be taken to ensure that the pump beam has a top-hat shape with minimal intensity variations across the beam profile.

4.2.8 Pump-seed synchronization

The duration of pump and seed pulses and the timing between them can have a significant influence on the parametric amplification process, because of the instantaneous nature of the interaction. Intuitively it is to be expected that timing fluctuations on the order of the pump pulse duration will cause significant changes in the amplified spectrum. Also, the ratio between pump and seed pulse durations is expected to be an important parameter in the case of Gaussian pump pulses: For instance, when the seed pulse is much shorter than the pump pulse the amplification will be inefficient. But if the seed pulse is chirped too strongly only its central part will be amplified, leading to a narrowed spectrum. When also the exact pulse shape of the pump pulse is taken into account it is clear that the final output spectrum depends heavily on the pulse overlap, and there is a tradeoff between bandwidth and efficiency, especially for ultra-broadband few-cycle seed pulses.

To determine the influence of the pump-seed timing, we measured the spectrum from our NOPCPA system at various pump-seed delays using a translation stage to introduce a controlled delay of the seed pulse. In our experimental situation, the pump-seed timing can be stabilized with a residual jitter well below 1 ps [113]. The results of these measurements are shown in Fig. 4.11. In general, a good agreement between the numerical simulations and the experiment is obtained, although the measurements have been carried out with a spectral gain bandwidth which was not fully optimized. The measured spectra show the same timing dependence as predicted by the model, but the exact shape of the spectra differs somewhat from the model calculations. This is mostly due to some residual timing differences between the various amplification passes, leading to a slightly different influence on each pass. The exact shape of the pump pulse is also of considerable influence, especially at larger delays where saturation is less prominent.

To find the optimum value for the ratio between the durations of the pump and chirped seed pulses, simulations have been performed using various amounts of group velocity dispersion for the input seed pulse. The results are shown in Fig. 4.12. As expected, a small group velocity dispersion (i.e. a short pulse) leads to a broad amplified spectrum with a relatively low intensity. When the chirp increases the pump-seed overlap improves, resulting in a rapid increase in efficiency. However, the spectrum is also observed to narrow down as the chirp increases, since the spectral wings (which are on the edges of the chirped pulse) now overlap with a lower-intensity part of the pump pulse. For the highest chirp values, even the total efficiency goes down: The reason for this is that the large stretching ratio lowers the input seed intensity to a point where the amplifier does not saturate properly anymore. From the simulations shown in Fig. 4.12 we can conclude that the seed pulse should be stretched to about 0.2-0.3 times the pump pulse duration for a good balance between spectral bandwidth and conversion

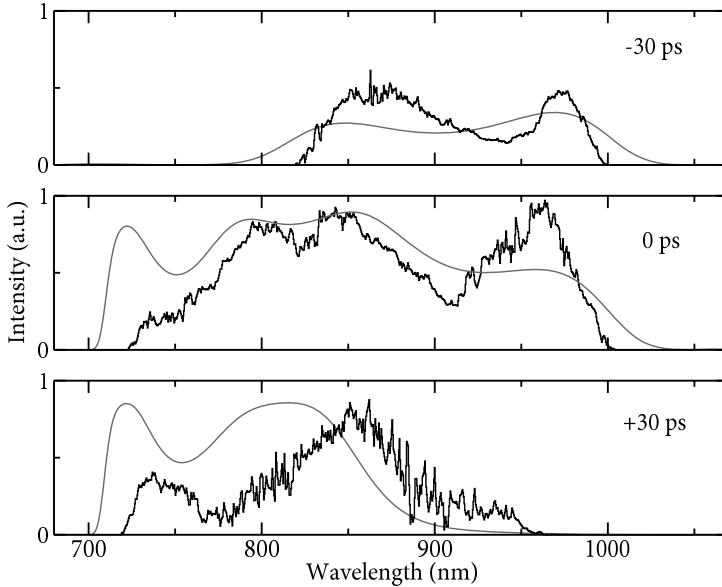


FIGURE 4.11: Comparison between simulations (grey traces) and experiment (black traces) of the influence of the pump-seed timing delay on the amplification process: A reasonably good agreement is obtained, although the shape of the spectrum at a given delay depends on the exact pump pulse shape and the relative delays between different amplification passes.

efficiency. A higher conversion efficiency can be achieved, but only at the expense of the amplified bandwidth. Note that a maximum efficiency can be obtained if the pump pulse has a square temporal shape, because all the spectral components in the chirped seed pulse then experience the same gain, and the ratio between the pulse durations can in principle be set to one [77]. The generation of such a square pulse shape, however, is not trivial for the case of picosecond pump pulses.

4.2.9 Conclusions

In conclusion, we have performed numerical simulations of a terawatt-class few-cycle NOPCPA system consisting of three amplification stages. The results show good agreement with experimental data from the 2 TW, 7.6 fs NOPCPA system that we developed recently in our laboratory [80]. As a result, we can take advantage of this model to predict the behaviour of our NOPCPA system under various operating conditions, and to analyze the influence of important parameters on the amplification process.

By following the evolution of the amplified seed pulse intensity in both time and frequency domains, we observe and analyze wavelength-dependent gain saturation, which is a phenomenon that is caused by the instantaneous nature of the amplification process and is therefore specific to NOPCPA. This effect places stringent requirements on the pump intensity stability, to prevent intensity-dependent fluctuations of the am-

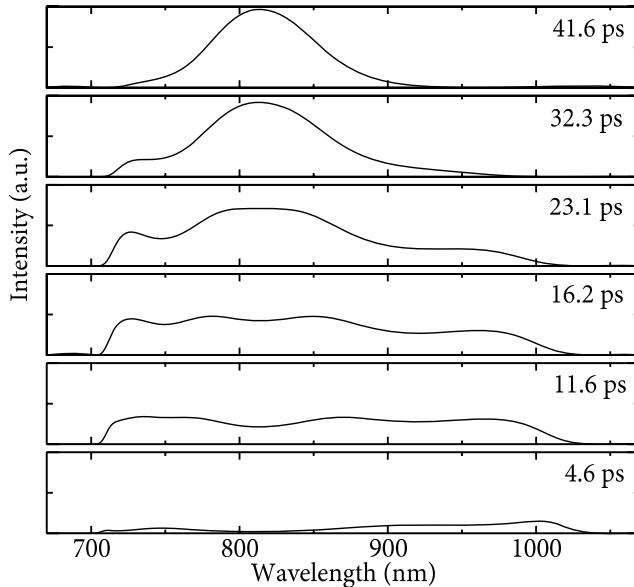


FIGURE 4.12: Simulation of a three-stage NOPCPA system for different amounts of group velocity dispersion on the input seed pulse: Pulses with a larger chirp amplify more efficiently, but only at the cost of a reduced spectral bandwidth. The pump pulse FWHM duration is 60 ps; the FWHM pulse duration of the stretched seed pulse is given in each graph.

plified pulse duration. From our calculations, we find that a 4% pump intensity jitter translates into a 5% variation of the Fourier-limited amplified pulse duration.

We have used the numerical model to find optimized values for the phase-matching- and noncollinear angles, and to study the effects of timing jitter between the pump and seed pulses. Also, we investigated the influence of the stretching factor of the seed pulse on the amplification process, and find a good compromise between amplified bandwidth and efficiency when the seed pulse is stretched to a value around 0.2-0.3 times the pump pulse duration (in the case of Gaussian temporal profiles). The model calculations presented here provide a realistic picture of the operating conditions of our experimental NOPCPA system. Therefore, this numerical approach can be used to design future implementations of more advanced amplifier systems with a more complicated geometry, and it can aid in the design of future few-cycle NOPCPA systems operating at the 100 TW level and beyond.

CHAPTER 5

EXPERIMENTAL ASPECTS OF FEW-CYCLE PULSE AMPLIFICATION USING NOPCPA

In the previous chapter, the principles and theory of optical parametric amplification have been introduced. From the simulations presented there, the required operating parameters for a realistic, high-intensity, few-cycle NOPCPA laser system can be estimated. With this knowledge in mind, several experimental NOPCPA setups have been designed and constructed. Besides the actual amplifier, several other devices need to be developed, such as the pump laser, pulse stretcher and compressor, and diagnostic tools for few-cycle pulse characterization. This chapter presents these various critical parts of the setup in detail, along with their design considerations, their capabilities, and their limitations.

5.1 Stretching and compression of ultrashort laser pulses

5.1.1 Chirped pulse amplification

As was already described in chapter 2, dispersion can dramatically change the shape of a laser pulse in time. This can be put to good use in the amplification of ultrashort pulses to extreme intensities. A fundamental limitation to the intensity that a laser pulse can reach inside an amplifier system is given by the damage threshold of the materials in the beam path. To generate pulses with higher intensity, this limitation needs to be circumvented. A technique that has become the standard in this field is chirped pulse amplification (CPA) [26]: The initially ultrashort pulse is passed through a system with a strong (positive) group velocity dispersion before amplification, stretching the pulse in time duration by several orders of magnitude. As a result, the peak intensity will decrease proportionally with the amount of stretching. This chirped pulse is then amplified in the usual way, and is sent into a system with the opposite (negative) group velocity dispersion to recompress the pulse to its original duration. In this way, ultrashort pulses can be produced with a peak intensity that exceeds the damage threshold of most materials by orders of magnitude. Of course, this is only true if the pulse compression system can sustain such intensities. As will be discussed in detail later, pulse

compressors can be designed using only reflective optics, using large beam diameters to lower the energy fluence to acceptable levels.

Although stretching an ultrashort pulse is relatively easy and can be achieved by simply putting some dispersive bulk material in the beam path, designing a complete chirped pulse amplification system requires more careful attention. Ideally, the stretcher and compressor should be each others exact mirror image in terms of dispersion, so that an initially transform-limited pulse that traverses the entire system will be stretched by 3-6 orders of magnitude in duration after the stretcher, and return to its transform-limited pulse duration after the compression stage. Of course, any additional dispersion introduced by the amplifier system also needs to be compensated.

For not-so-ultrashort pulses (>100 fs), compensation of the group velocity dispersion usually suffices for decent compression close to the Fourier limit of the input pulse. However, as the duration of a pulse decreases, its spectral bandwidth increases, and for proper pulse compression the spectral phase needs to be controlled over this entire bandwidth. The influence of higher-order spectral phase deviations therefore increases for shorter pulses, and these higher-order dispersion contributions need to be taken into account in the design of the chirped pulse amplification system.

A commonly used option for the construction of such a matched stretcher-compressor system to compensate dispersion up to higher orders, is the use of grating pairs, as will be explained in the following sections. Another possibility is to employ bulk material as a stretcher, in combination with a prism compressor. But since the amount of group-velocity dispersion that can be compensated by such a system is small, we will limit the present discussion to the grating-based setup mentioned above. The compressor system will be introduced first, as the design of the grating-based pulse stretcher is an extension of the concept on which the pulse compressor is based.

5.1.2 Grating-based pulse compressor

A typical system for pulse compression is displayed in Fig. 5.1, and was first described by Treacy [163]. It consists of a pair of gratings aligned parallel to each other, separated by a distance L . The spectrum of a pulse incident on the first grating will be spatially dispersed into the -1^{st} grating order according to the grating equation:

$$\sin \gamma + \sin \theta = \frac{2\pi c}{\omega d} \quad (5.1)$$

where γ is the incidence angle of the pulse on the first grating with respect to the grating normal vector, $\theta = \theta(\omega)$ is the angle at which a frequency ω is diffracted, and d is the groove spacing of the grating. When the 1^{st} order of the grating is used instead, the plus sign in front of the $\sin \theta$ -term changes into a minus. The optical path length P through the system in Fig. 5.1 can be calculated from this equation using simple geometrical optics, and is found to be:

$$P = \frac{L}{\cos \theta} [1 + \cos(\gamma - \theta)] \quad (5.2)$$

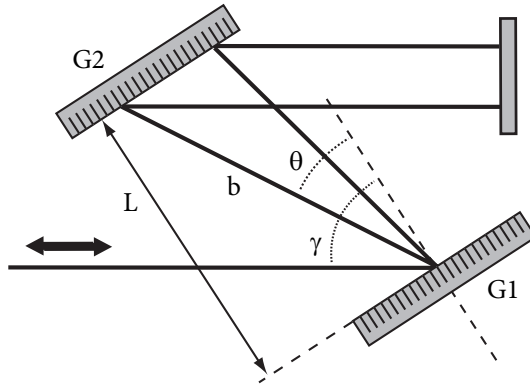


FIGURE 5.1: Schematic drawing of a pulse compressor.

The group delay τ of a pulse traversing the system can then simply be written as [163–165]:

$$\tau = \frac{\partial \varphi}{\partial \omega_s} = \frac{P}{c} \quad (5.3)$$

That the group delay can indeed be written as P/c is not obvious, since the optical path length is frequency-dependent, i.e. $P = P(\omega)$. By naively inserting this into the definition of the group delay $\tau = \frac{\partial \varphi}{\partial \omega_s}$, one would obtain $\tau = \frac{P}{c} + \frac{\omega}{c} \frac{\partial P}{\partial \omega_s}$. However, when looking at Fig. 5.1 the light is seen to travel completely in vacuum (neglecting air dispersion), only affected by reflections from the gratings. Therefore, according to Fermat's principle the group velocity should be equal to the speed of light c , which directly results in Eq. (5.3). This apparent inconsistency is caused by the origin of the frequency-dependent optical path length: A grating compressor uses angular dispersion instead of the more familiar material dispersion, for which the expression $P = n(\omega)L$ does not lead to such a paradox. In a grating compressor, the frequency dependence of P is entirely due to the grating diffraction, leading to a frequency-dependent diffraction angle $\theta(\omega)$ according to the grating equation (5.1).

Brorson and Haus [164] showed that by properly incorporating the geometrical effects of grating diffraction into the theory of the compressor, the inconsistency is removed and Eq. (5.3) is valid. A more direct and intuitive treatment of this problem is given by Ware et al. [165], who explicitly take the vectorial nature of both P and the wave-vector k into account to calculate the group delay along the propagation direction of a given $k(\omega)$. They find that Eq. (5.3) holds, regardless of the functional form of $\theta(\omega)$.

To make the connection between the phase delay $\varphi = \frac{\omega}{c}P$ and the group delay τ , Treacy [163] originally used the fact that two parallel waves incident on neighbouring grooves of a grating will have a relative phase difference of 2π after diffraction into the $\pm 1^{\text{st}}$ order. By calculating the number of grooves between two waves of different frequency incident on the second grating and adding the resulting phase shift to φ ,

$\frac{\partial \varphi}{\partial \omega_s} = P/c$ is obtained. Of course, this 2π -per-groove phase shift is not physically meaningful, since it originates from the grating equation (5.1): Any deviations from 2π are not possible, since this would simply lead to destructive interference and consequently zero intensity behind the grating. Therefore, any point behind the second grating necessarily has a phase shift of exactly 2π -per-groove to get a nonzero intensity in the first diffraction order. Unfortunately, this artificial phase shift has been the cause of much confusion, as several authors concluded that this phase shift would lead to a strong coupling between beam pointing and the carrier-envelope phase of a pulse [166]. That no such effect exists in reality has been confirmed by the development of carrier-envelope phase-stable grating-based CPA systems [167–169]; we have also measured the dependence of beam pointing on the phase using Fourier-transform spectral interferometry, and found a null result (see section 6.4.3 for more details).

The total group velocity dispersion (GVD) that is introduced by the system is given by $\frac{\partial^2 \tau}{\partial \omega_s^2}$. Using Eqs. (5.1)–(5.3), we can calculate the group velocity dispersion to be:

$$\begin{aligned} \frac{\partial^2 \varphi}{\partial \omega^2} &= -\frac{8\pi^2 c}{\omega^3 d^2} \frac{b}{\cos^2 \theta} \\ &= -\frac{8\pi^2 c}{\omega^3 d^2} \frac{L}{\left[1 - \left(\frac{\lambda}{d} - \sin \gamma\right)^2\right]^{3/2}} \end{aligned} \quad (5.4)$$

where we have used the grating equation (5.1) and the fact that $L = b/\cos \theta$. Note that this relation holds for a complete pass back and forth through the compressor, which introduces an additional factor of 2 because the grating pair is traversed twice. The group velocity introduced by the grating pair is found to be negative, and it can be controlled by the grating separation L and the angle of incidence γ . Such a system can therefore act as a compressor for positively chirped pulses, which is convenient since virtually all bulk materials introduce positive GVD onto a pulse.

It should be mentioned, however, that the dispersion introduced by such a grating pair compressor is not strictly quadratic: Higher-order dispersion terms are present as well, and can be deduced by additional differentiation of the spectral phase. The first of these higher-order terms is the third-order dispersion, which is found to be:

$$\frac{\partial^3 \varphi}{\partial \omega^3} = -\frac{3}{\omega} \frac{1 + \frac{2\pi c}{\omega d} \sin \gamma - \sin^2 \gamma}{1 - \left(\frac{2\pi c}{\omega d} - \sin \gamma\right)^2} \times \frac{\partial^2 \varphi}{\partial \omega^2} \quad (5.5)$$

The third-order dispersion (TOD) is found to be positive, as it is proportional to -1 times the group velocity dispersion. The ratio between TOD and GVD is immediately clear from Eq. (5.5). Clearly, this ratio depends on the input angle and the groove spacing; these parameters can thus be employed to (partly) compensate higher-order dispersion terms as well.

5.1.3 Grating-based pulse stretcher

As mentioned before, an ultrashort laser pulse can easily be stretched in duration by passing it through a slab of dispersive material. However, to compensate the higher-order dispersion terms as well, a more controlled stretcher system is utilized, again

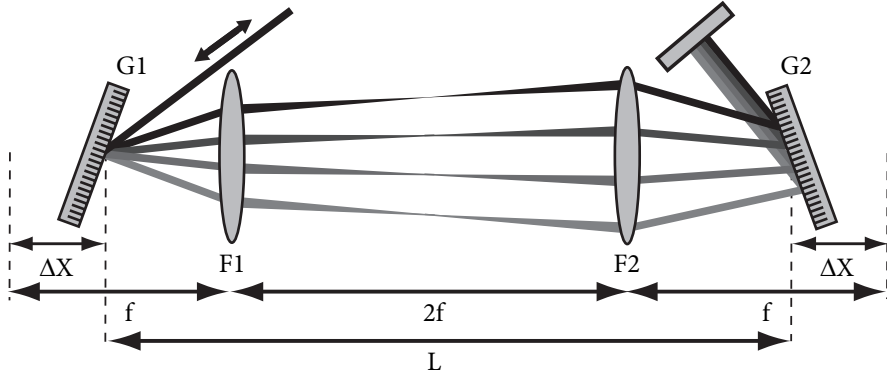


FIGURE 5.2: Schematic drawing of a pulse stretcher. The telescope controls the angular dispersion between the gratings G1 and G2. By adjusting ΔX and L , the magnitude and sign of the group velocity dispersion can be controlled.

based on a pair of gratings [170]. A schematic of such a pulse compressor is shown in Fig. 5.2, and basically consists of a grating compressor as described in the previous section with a telescope between the gratings. Since the GVD of a grating compressor has its origin in the angular dispersion introduced by the gratings, the magnitude and the sign of this GVD can be controlled by using the imaging properties and angular magnification provided by a telescope [171]. In the most general case, a telescope consisting of two lenses (or curved mirrors) with different focal lengths f_1 and f_2 will change the GVD of a grating pair into:

$$\frac{\partial^2 \varphi}{\partial \omega^2} = -\frac{8\pi^2 c}{\omega^3 d^2} \frac{1}{\cos^3 \theta} [L - 2(f_1 + f_2)] \left(\frac{f_1}{f_2}\right)^2 \quad (5.6)$$

(note that we have neglected any possible GVD introduced by the lenses). Although the angular magnification f_1/f_2 is found to have a strong (quadratic) influence on the GVD, in practice this term is set to 1 (i.e. $f_1 = f_2$) since any other value would also require the use of gratings with different groove spacings to recollimate the beam after the telescope. An interesting result obtained from Eq. (5.6) is that the effective path length $L - 4f$ (again taking $f_1 = f_2$ for simplicity) does not need to be positive. By making the distance between the gratings and the lenses smaller than f , then $L - 4f$ becomes negative and the overall sign of the GVD in Eq. (5.6) becomes positive. In the configuration shown in Fig. 5.2 this is also the case. The GVD introduced by this particular system is:

$$\frac{\partial^2 \varphi}{\partial \omega^2} = \frac{8\pi^2 c}{\omega^3 d^2} \frac{2\Delta X}{\cos^3 \theta} \quad (5.7)$$

With this in mind, the setups from Figs. 5.1 and 5.2 can be combined to realize an implementation of the CPA principle: Typically, a positive GVD is used to stretch the pulse while a negative GVD is used for compression. Therefore a setup as drawn in

Fig. 5.2 is usually called a pulse stretcher, while the setup in Fig. 5.1 is known as a pulse compressor. The reason for using positive GVD to stretch a pulse before amplification is that almost all materials also introduce positive GVD. Negative dispersion stretching could therefore lead to partial pulse compression during amplification due to material dispersion in the amplifier. Negative dispersion stretching has been employed in CPA systems, but typically for low-dispersion amplifiers that produce low peak intensity but high average power [172].

Note that, since the expressions (5.4) and (5.7) for the compressor and stretcher can be made equal and opposite in sign, the dispersion can be matched for all higher orders as well. Therefore, an ultrashort pulse can in principle be stretched and recompressed to its original form without residual phase deviations. In practice the compression is limited by aberrations introduced mostly in the stretcher telescope. By using an all-reflective telescope system based on a low-aberration, all-reflective Öffner-type telescope design [173], dispersion compensation up to the fourth order has been achieved [174–176]. However, these systems do not take into account any dispersion which is added by e.g. an amplifier placed between the stretcher and compressor. A solution to deal with this added dispersion is to design the stretcher and compressor with different grating groove spacings d , incidence angles γ and spacings L and ΔX , to balance the total system dispersion [177].

5.1.4 Pulse compression through adaptive phase shaping

Aside from the possibilities for stretching and compression, a system as shown in Fig. 5.2 can also be adjusted to give exactly zero dispersion, by setting $b = 4f$. While not directly influencing the pulse shape, such a $4f$ -system can be useful, as all the frequencies that are present in the pulse will be spatially separated by the first grating. After pass-

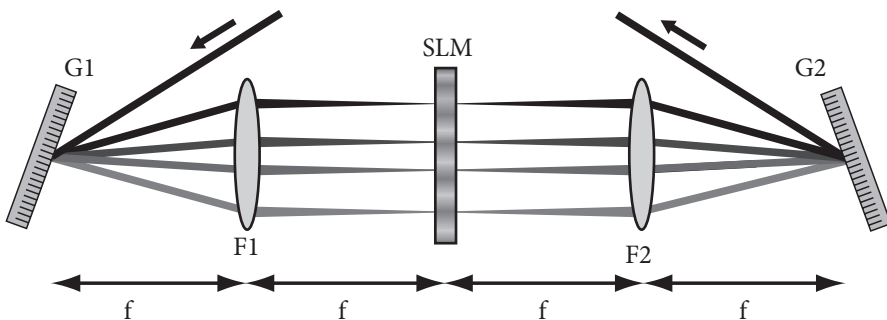


FIGURE 5.3: Schematic setup for spectral phase manipulation. A programmable phase pattern is applied to the spatial light modulator (SLM) placed in the Fourier-plane of a $4f$ -setup. The combined effect of the gratings (G1 and G2) and the telescope (L1 and L2) is that the various frequencies focus on a line in the Fourier-plane, allowing the phase and amplitude of each frequency component to be addressed individually.

ing through the first lens, the pulse as a whole will be collimated, but with the various frequencies propagating side-by-side. In the Fourier-plane (see section 5.2.7 on relay-imaging) at a distance f behind the lens, the individual frequencies all focus next to each other on a line. By placing a phase and/or amplitude mask in this plane, the spectral properties of the pulse can be manipulated directly in the frequency domain.

Consider now the schematic setup drawn in Fig. 5.3, where a spatial light modulator (SLM) is placed in the Fourier-plane of a $4f$ -system. Such an SLM consists of an array of typically 640 cells filled with nematic liquid crystals, and to each of these LCD “pixels” a voltage can be applied. This applied electric field orients the molecules in the liquid crystal structure, which changes the refractive index. By applying a different voltage to each pixel, the various frequencies in the pulse will experience different phase shifts depending on the refractive index of the respective pixels. In this way the spectral phase of the pulse can be tailored with high resolution, and the SLM can be exploited to compensate any residual phase errors caused by imperfect stretching and compression.

Since a pulse stretcher also contains a Fourier-plane, an SLM can be incorporated conveniently in a chirped pulse amplification system. In our setup, we have incorporated a Jenoptik SLM-S 640/12 phase shaper in this way. However, it should be noted that this is not true for the Öffner-type stretcher configuration, because such a stretcher only has a virtual Fourier-plane as it employs a convex-concave mirror arrangement instead of two concave mirrors.

5.2 Design of a Nd:YAG pump laser system

In this section we discuss the various implementations of high power Nd:YAG laser systems that we have developed as a pump source for our terawatt few-cycle non-collinear optical parametric chirped pulse amplifier. The laser system always consists of a modelocked Nd:YVO₄ oscillator and a diode-pumped Nd:YAG regenerative amplifier, while various types of post-amplifiers have been constructed using both diode-pumped and flashlamp-pumped Nd:YAG amplifier modules. Using these different implementations, we can pump the NOPCPA either with 2.5 mJ pulses at 1 kHz repetition rate, or with 160 mJ pulses at 30 Hz.

5.2.1 Oscillator, pulse stretching and synchronization

The initial light source for the laser system is a Nd:YVO₄ oscillator (High-Q Laser GmbH), passively modelocked using a semiconductor saturable absorber (SESAM) mirror. The oscillator emits ~ 40 nJ, 7 ps pulses at a repetition rate of 70 MHz. To be useful as a pump source for NOPCPA, these laser pulses must be synchronized to the Ti:Sapphire seed laser with an accuracy of better than 1 ps. Therefore, one of the cavity mirrors is mounted on a piezo-transducer, and we detect the 150th harmonic of the laser repetition rate on a 10 GHz photodiode (EOT, ET-3500). This signal is mixed with the output of a highly stable 10.5 GHz RF generator, which is referenced to a Rubidium atomic clock. The resulting mixing product contains the difference frequency between the generator signal and the detected harmonic, which is isolated by low-pass

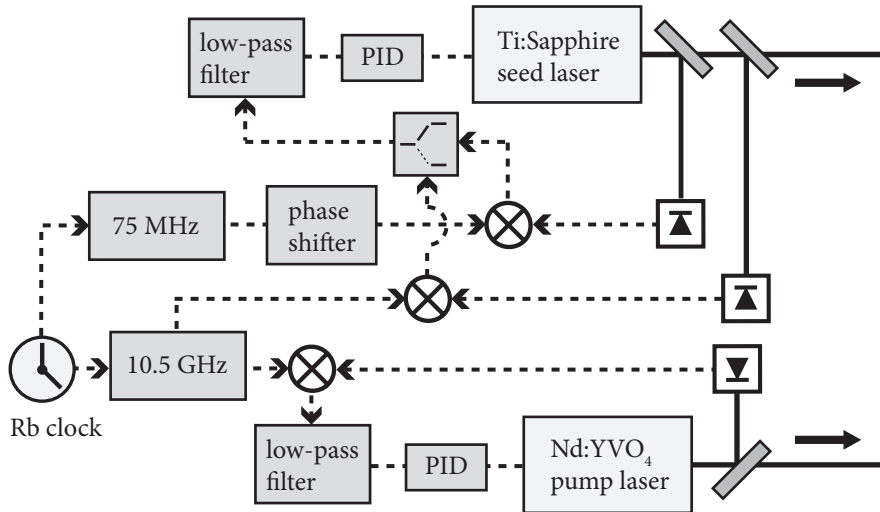


FIGURE 5.4: Schematic of the electronic circuits for synchronization of the NOPCPA pump and seed oscillators. Solid lines represent laser beams, while dashed lines are electronic connections.

filtering and used as a feedback signal for a PID loop that controls the voltage on the piezo-transducer.

The synchronization between the Ti:Sapphire seed oscillator and the Nd:YVO₄ pump source is still somewhat more involved, since it not only requires the lasers to have fixed repetition rates, but also that the pulses overlap inside the OPA crystal. When both lasers are simply stabilized to the same RF generator the repetition rates will be locked, but the absolute timing between the pulses is still randomly set every time the locking system is activated. In other words, not only the frequency of the pulse trains needs to be synchronized, but the relative phase should be adjustable as well. In principle this can be achieved by incorporating a phase shifter into one of the feedback loops, but in practice this is not possible, since typical 10.5 GHz phase shifters do not have the required tuning range: A 2π phase shift at 10.5 GHz corresponds to a time delay of only 95 ps, while the time delay should be tunable over $(f_{\text{rep}}/2)^{-1} = 6.7$ ns. This would require either a $70 \times 2\pi$ phase shifter or a delay line adjustable over 2 metres, which are both extremely difficult to make.

As an alternative, we implemented a dual-frequency locking scheme [178], as depicted in Fig. 5.4. In this scheme, only the pump oscillator is locked directly to the 10.5 GHz generator, while the seed oscillator is stabilized at its fundamental frequency to an independent 75 MHz RF source running at exactly $1/140^{\text{th}}$ of the 10.5 GHz frequency. Although this low-frequency loop does not provide the required timing stability, a simple 2π phase shifter suffices to adjust the time delay between the pulses over 13.3 ns. Such a low-frequency phase shifter is a much more standard device, and is in fact already integrated into the 75 MHz RF generator. This phase shifter is then used to

adjust the time delay between the pulses to approximately zero inside the OPA crystal. To achieve the required timing stability, the seed oscillator is also equipped with feedback circuitry to lock this laser to the 10.5 GHz generator. By gradually decreasing the gain of the low-frequency loop while simultaneously increasing the gain of the high-frequency loop, we can make the transition from one loop to the other while the laser remains locked. Any residual time delay is now in principle limited to one cycle of the 10.5 GHz signal, and is adjusted to zero using a translation stage in the seed beam path (which has to be tunable over only $c/10.5 \text{ GHz} = 2.9 \text{ cm}$).

Another point worth mentioning is that the Ti:Sapphire and Nd:YVO₄ oscillators run at different repetition rates, which are 75 MHz and 70 MHz, respectively. Although at first glance this may seem problematic, it is of no concern for our application: By locking the 140th harmonic of the Ti:Sapphire seed laser and the 150th harmonic of the Nd:YVO₄ pump oscillator to the same 10.5 GHz RF source, we ensure that every 15th seed pulse coincides with every 14th pump pulse. In this way, we have overlap between pulses once every 200 ns. This is sufficient, since the NOPCPA system runs at much lower repetition rate. We use repetition rates of either 1 kHz or 30 Hz, which requires pulses to overlap only once per 1 ms or 33.3 ms, respectively.

To reach terawatt-scale peak intensity with the NOPCPA system, the required pump pulse energy (at 532 nm) is about 150 mJ. However, the present 7 ps pulse duration is too short to readily amplify the pulses to such high power, as the peak power would exceed the damage threshold of most materials in the beam path (including YAG). We stretch the pump pulses in time by sending them through a spectral filter. This spectral filter is a $4f$ -system, consisting of a 1680 lines/mm grating which disperses the pulse spectrum, an $f = 50 \text{ cm}$ lens that collimates the beam, but focuses the separate colors on a mirror, which reflects the beam back through the lens to the grating. In front of this mirror a slit is placed, cutting away part of the pulse spectrum, and hence stretching the pump pulse in time to about 100 ps.

5.2.2 Regenerative amplification

The stretched pump pulses, with an energy of $\sim 0.2 \text{ nJ}$, are injected into a regenerative amplifier (reg. amp.) through an optical isolator, consisting of a Faraday rotator and thin film polarizers. The gain medium in this amplifier is a diode-pumped 10 cm long, 5 mm diameter Nd:YAG rod (Cutting Edge Optonics RD-50 module) with a single-pass gain of about 1.5. A schematic of the entire reg. amp. is shown in Fig. 5.5.

Pulses are captured inside the reg. amp. by switching on the electro-optic Pockels cell (PC), which then acts as a $\lambda/4$ -plate. When the PC is off, each pulse is coupled out after one complete roundtrip through the cavity due to polarization rotation by the $\lambda/4$ -plate inside the reg amp. Turning on the PC (to 5.4 kV) eliminates this polarization change, trapping any pulse already present in the reg amp, thus allowing this selected pulse to be amplified in many consecutive roundtrips. The total length of the reg. amp. is 1 m, leading to a roundtrip time of 7 ns. The reg. amp. is capable of amplifying pulses to 2 mJ at 1 kHz rep. rate, when the gain saturates after ~ 40 roundtrips. At this stage, the amplified pulse is coupled out of the reg. amp. by switching the PC voltage off again. The reg. amp. cavity is a stable resonator with a TEM₀₀ output beam profile.

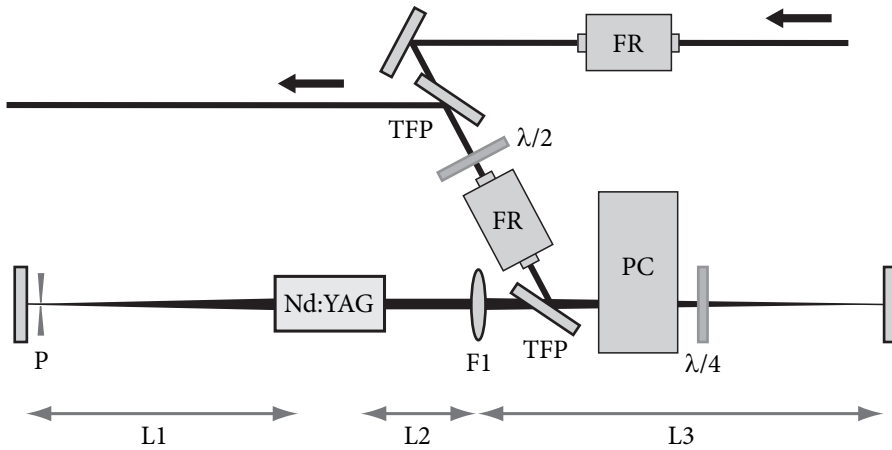


FIGURE 5.5: The regenerative amplifier. FR: Faraday rotator, TFP: thin film polarizer, PC: Pockels cell, P: 0.9 mm pinhole, Nd:YAG: diode-pumped Nd:YAG rod, F1: $f = 50$ cm lens, $L_1 = 48$ cm, $L_2 = 20$ cm and $L_3 = 44$ cm.

In developing this cavity, we have followed the design principles given by Magni et al. [179–181] for high-power laser resonators with significant thermal lensing in the amplifier medium. The beam diameter in the Nd:YAG rod is chosen to be 3 mm, and the shortest possible thermal lens focal length $f_{\min} = 38$ cm. Taking flat end mirrors, the arm lengths of the cavity then follow: $L_1 = 48$ cm, $L_2 = 20$ cm and $L_3 = 44$ cm. To keep the reg. amp. compact, a lens ($f = 50$ cm) is inserted in one arm, to shorten the length of this arm while preserving the cavity stability and the beam diameter inside the Nd:YAG rod [182].

5.2.3 Pulse shortening in the regenerative amplifier

One particularly unattractive feature of the regenerative amplification process is that a significant shortening of the pulse duration can occur during amplification. The effect can be quite dramatic, as output pulses as short as ~ 25 ps (a factor of 4 shorter than the input pulse) have been observed in the regime of full gain saturation at an output energy of 2 mJ per pulse. Using an autocorrelator suitable for picosecond pulses, we measured the pulse duration after the reg. amp. while varying the number of roundtrips, and the results are displayed in Fig. 5.6. In the saturation regime (starting around 40 roundtrips) an almost linear decrease in pulse duration is observed, while during the pulse-buildup phase the pulse duration remains relatively constant (note that the initial pulse duration for these measurements was set around 55 ps). This pulse shortening effect is caused by a combination of gain and self-phase-modulation in the Nd:YAG rod [183–185]: With sufficient amplification, the pulse intensity can become high enough to induce significant self-phase-modulation, leading to nonlinear broadening of the amplified spectrum, accompanied by a chirp. This broadened spectrum is

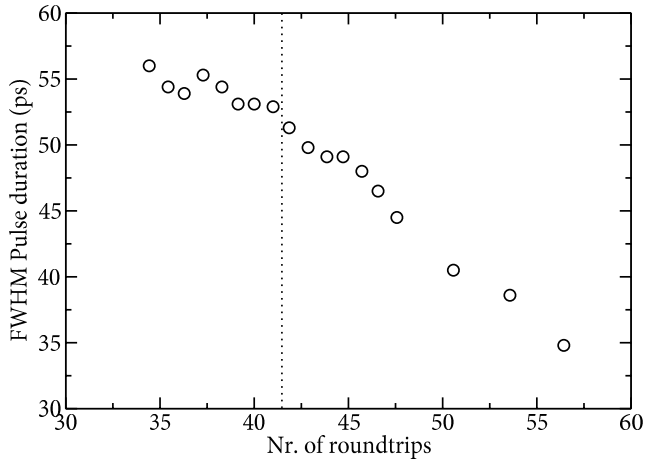


FIGURE 5.6: Measured pulse duration of the regenerative amplifier output as a function of the number of roundtrips that the pulse has taken inside the cavity. The dotted line indicates the saturation regime at which the reg. amp. is normally operated.

then amplified in the Nd:YAG rod. However, if the width of the broadened pulse spectrum exceeds the amplifier gain bandwidth, significant spectral narrowing will occur, which dispenses with part of the newly generated spectral components. Since these components are mostly at the leading and trailing edge of the pulse, this will result in a shortening of the pulse duration. The final pulse duration that can in principle result from this process is mainly limited by the gain bandwidth of Nd:YAG, and is on the order of 20 ps.

That the reg. amp. indeed operates at an intensity where self-phase-modulation starts to become significant is illustrated in Fig. 5.7. In this case, the duration of the input seed pulse coming from the stretcher was varied, while keeping the energy of this seed pulse constant. While the output energy did not vary significantly for these various measurements, the amplified spectrum changed dramatically. The observed spectra with two peaks on the edges and a relatively low plateau in between are a clear signature of self-phase-modulation.

The effects of pulse shortening can be kept small if the reg. amp. is not operated at full saturation. Although this reduces the pulse-to-pulse stability and limits the output power to ~ 1 mJ per pulse, it ensures a sufficiently long pulse duration of about ~ 60 ps, which allows further amplification in a flashlamp-pumped post-amplifier as will be discussed in sections 5.2.5 and 5.2.6.

5.2.4 Diode-pumped post-amplifier

After the regenerative amplifier, the pulses can be further amplified in a double-pass post-amplifier. The gain medium in this post-amp is a diode-pumped Nd:YAG module

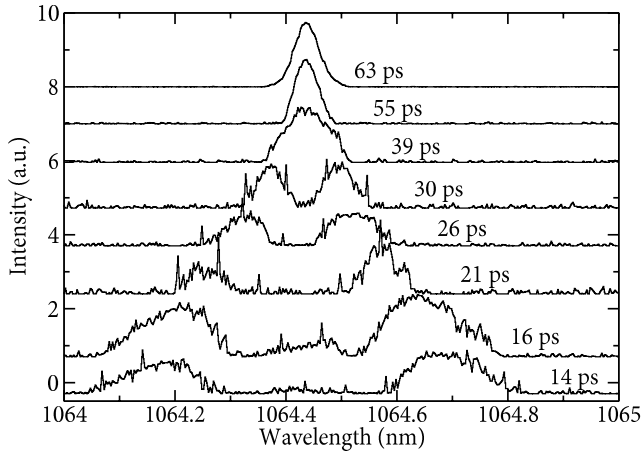


FIGURE 5.7: Measured spectrum of the regenerative amplifier output pulses for various input pulse durations. The amplifier output pulse energy is similar in all measurements (~ 1 mJ). The numbers indicate the measured pulse duration of the input seed pulse corresponding to each output spectrum.

identical to the one in the reg. amp. (Cutting Edge Optronics RD-50), which is operated with a single-pass gain of 1.6.

A schematic of the diode-pumped post-amplifier is shown in Fig. 5.8. The beam diameter of the pulses emitted by the reg. amp. is increased to ~ 4.5 mm by a telescope, to efficiently fill the gain medium. The pulses are reflected by a thin film polarizer (TFP), and make a first pass through the Nd:YAG rod. Behind this rod, the pulses are relay-imaged onto the end mirror by a $1.5\times$ magnifying telescope, which is setup up slightly too short to compensate for thermal lensing in the amplifier rod. In front of the end mirror, a Faraday rotator is placed. After backreflection through this rotator, the polarization has been rotated by 90° . The beam then passes the Nd:YAG rod once more, and is transmitted by the TFP. This post-amp increases the pulse energy by a factor of 2, to 3.8 mJ per pulse at 1 kHz rep. rate. It should be noted that we operate the reg. amp. at full saturation in this system, so that the post-amp is seeded by about 2 mJ pulses. The effects of pulse shortening become a problem only at higher powers, i.e. when using a flashlamp-pumped post-amp as will be discussed in the next section.

The use of a Faraday rotator for the polarization rotation is essential in keeping a good quality output beam. As the amplifier is operated at high diode pumping power, thermal effects become quite severe. At full pumping power, the thermal lens of the loaded Nd:YAG rod has a focal length of about 30 cm, and the single-pass depolarization due to thermally induced birefringence approaches 30%. Especially this thermal birefringence causes substantial power loss, and severely distorts the beam profile as it introduces a position-dependent polarization rotation across the beam profile. The combination of relay-imaging and the Faraday rotator ensures an exact 90° rotation independent of the input polarization, therefore exchanging the fast and slow axes of the

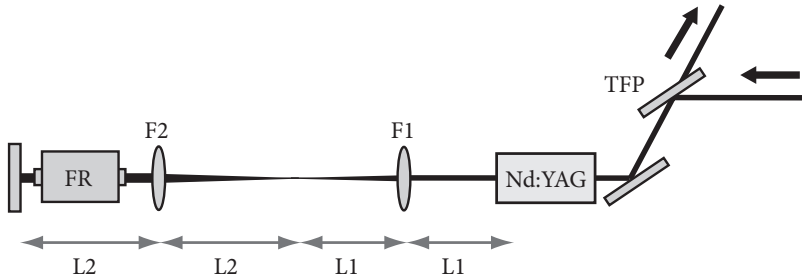


FIGURE 5.8: Diode-pumped double-pass post-amplifier. F1 and F2 are lenses with $f_1 = 15$ cm and $f_2 = 10$ cm, respectively. Distances are approximately $L_1 = f_2$ and $L_2 = f_1$, in fact they are slightly shorter to compensate for thermal lensing effects.

birefringent Nd:YAG rod between the first and second pass at every point in the beam profile [186–188]. The use of a $\lambda/4$ -plate instead of a Faraday rotator leads to incomplete compensation; it can be beneficial in low-power systems [189], where the depolarization is only a few percent to begin with. In the present high-power system however, a $\lambda/4$ -plate does not improve compensation, and can even increase the depolarization losses [187]. The relay-imaging telescope is required because the presence of both thermal lensing and thermal birefringence results in bifocusing, i.e. a different focal length of the thermal lens for the radial and azimuthal polarization components. Because the input beam fills the amplifier rod almost completely, the output beam profile resembles a top-hat. As a result, the rod end-face should be relay-imaged onto the target location to ensure a good beam profile at this position.

5.2.5 Flashlamp-pumped linear post-amplifier

To produce higher energy pulses, another double-pass post-amplifier has been constructed using two amplifier modules with flashlamp-pumped Nd:YAG rods. The rods are 10 cm in length and 12 mm in diameter, and these modules are operated with a small-signal gain of about 6 per rod. A schematic of this post-amp is depicted in Fig. 5.9. The beam emitted by the reg. amp. is passed through a Faraday isolator, and magnified to 11 mm diameter using a telescope. This beam is transmitted through a TFP into the amplifier.

As thermal lensing and birefringence are also present in these amplifier modules (although less severe than in the case of the diode-pumped post-amp; the thermal lens focal length of one module is about 2 metres), compensation for these effects is required. A well-established technique for double-rod amplifiers is the use of a 90° active quartz rotator, and relay-imaging of the rod principal planes onto each other [188, 190, 191]. The relay-imaging telescope consists of two $f = 20$ cm lenses, which are placed slightly closer to each other than $2f$ to compensate for the thermal lensing. One of the telescope lenses is mounted on a two-dimensional translation stage, to allow minimization of the residual depolarization after the second module by fine-tuning the

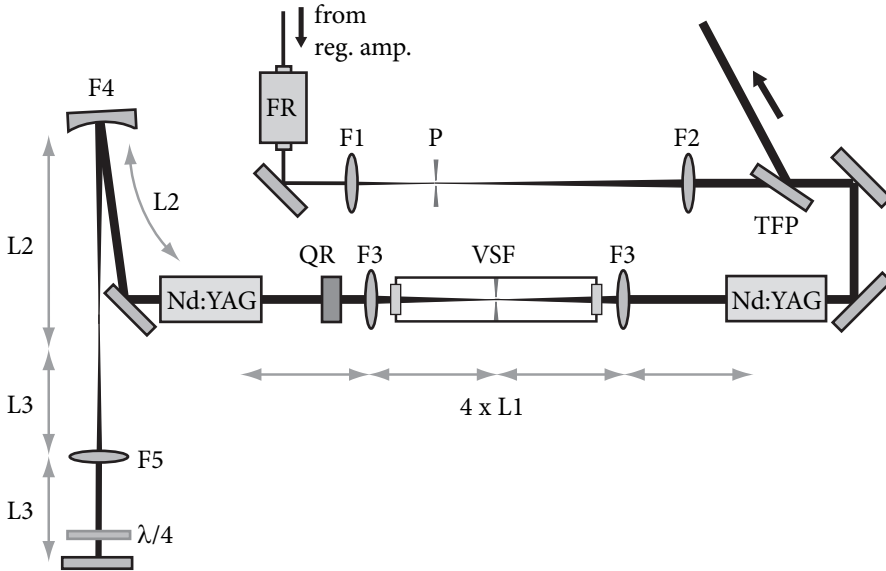


FIGURE 5.9: Flashlamp-pumped post-amplifier. FR: Faraday rotator, TFP: thin film polarizer, P: ceramic pinhole, Nd:YAG: flashlamp-pumped Nd:YAG rod, VSF: vacuum spatial filter, QR: 90° quartz rotator. F1=10 cm, F2=50 cm, F3=20 cm, F4=30 cm, F5=10 cm, L1=20 cm, L2=30 cm, L3=10 cm.

transverse lens position [192]. A vacuum spatial filter with a 1 mm ceramic pinhole is placed in between the lenses, to filter out the diffraction rings that are present in the beam after passing through the first module. The pressure inside the tube is kept at about 10^{-1} mbar, to prevent optical breakdown in air in the focus on the return pass. That proper compensation of thermal effects is crucial for such high energy laser systems becomes clear from Fig. 5.10, which shows the fraction of energy that ends up in the wrong polarization state due to thermally induced birefringence. While a single uncompensated amplifier module can already cause a 30% energy loss, our double-module setup combined with polarization rotation and relay-imaging ensures that the losses are limited to about 2%. In addition, the beam profile strongly improves when applying the birefringence compensation scheme, which can be seen in Fig. 5.11. From Figs. 5.11A and 5.11B, the induced birefringence is found to be spatially dependent: it is almost absent on-axis, while leading to an almost 90° rotation in the corners of the beam profile, as is expected from theory [187, 188, 190]. With the compensation measures in place, a round homogeneous beam profile is recovered.

After the first pass through both modules, another telescope consisting of an $f = 30$ cm mirror and a $f = 10$ cm lens relay-images the last principal plane of the second rod onto the end mirror. The reason for taking a $f = 30$ cm lens is that shorter focal lengths lead to optical breakdown in the focus of this lens. A $\lambda/4$ -plate is placed close

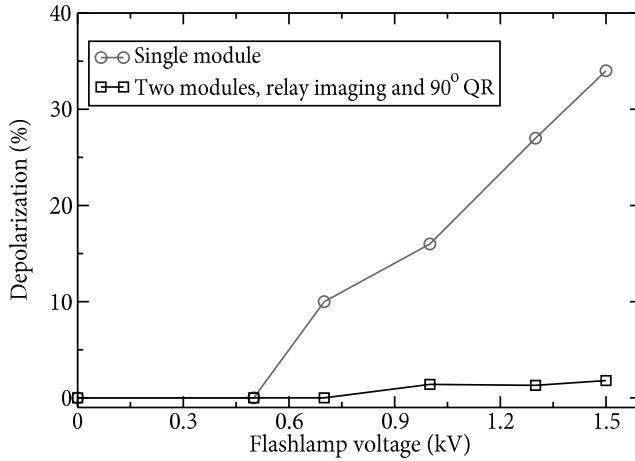


FIGURE 5.10: Measured thermally induced depolarization for a single flashlamp-pumped Nd:YAG amplifier module, and for two identical modules with full birefringence compensation in between (see text for details).

to the end mirror, to rotate the polarization by 90° . Note that, in contrast to the case of the diode-pumped post-amp, a Faraday rotator is not required here. This is because the birefringence compensation is already performed between the rods, so that a simple polarization rotation will suffice to provide a properly polarized pulse after double-passing the post-amp. Further minimization of the depolarization can be achieved by tuning the flashlamp voltages such that both rods are identically pumped, although in practice these voltages can be kept at the same value for both modules. Since the polarization has been rotated between passes, the amplified beam after the second pass is reflected by the TFP.

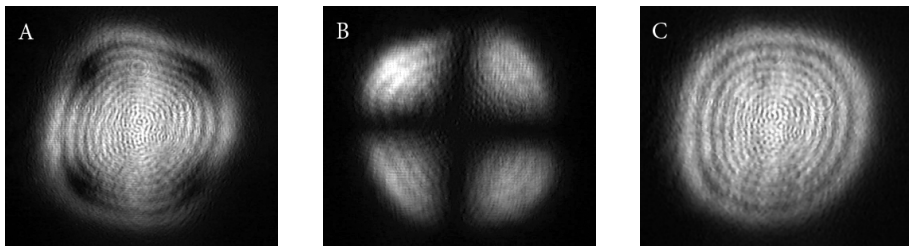


FIGURE 5.11: Effect of thermal birefringence on the beam profile. (A) and (B) are the beam profiles in the original and the orthogonal polarization after one pass through a single flashlamp-pumped amplifier module, respectively. (C) shows the beam profile after one pass through two modules with birefringence compensation in place. The diffraction rings are due to the Nd:YAG rods, and are largely removed by spatial filtering (see Fig. 5.14).

The amplifier gain is at an optimum when the input pulse arrives 540 μs after the flashlamps have been triggered. The fully operational post-amp amplifies the pulses to about 15 mJ after the first pass, and to 210 mJ after the second pass. Similar to the diode-pumped system, the output beam profile is top-hat shaped, and therefore requires relay-imaging to ensure a proper beam profile on target. The amplified pulses are relay-imaged onto a 3 mm long, 14 mm diameter type-I BBO crystal for second harmonic generation. The pulses are upconverted to 532 nm with an efficiency of 67%, yielding 140 mJ pulses of about 60 ps duration.

5.2.6 Flashlamp-pumped post-amplifier in ring geometry

Although the flashlamp-pumped post-amplifier from the previous section works properly and has been employed to obtain the results described in chapter 7, it suffers from several drawbacks. The main source of problems in this linear design is the direct back-reflection through the amplifier in combination with the imperfect birefringence compensation. As a result of this, any residual light in the wrong polarization state will not be coupled out by the TFP, but transmitted back towards the regenerative amplifier. Although the Faraday isolator at the amplifier entrance prevents this light from reaching the regenerative amplifier, the pulses can have a significant intensity. Even though the percentage of residual birefringence is only 2% for a properly aligned system, the energy of this fraction can still reach several mJ per pulse. Combined with the highly structured beam profile that usually accompanies depolarization, such a backreflection can cause considerable damage to the optics between the TFP and the Faraday rotator. This can be partially prevented by putting a pinhole in the focus of the telescope that is in front of the amplifier, and slightly misaligning the second pass such that it (partly) hits the pinhole. What remains of the spatially separated backreflection can also be picked off by a mirror before it reaches the Faraday rotator. However, this approach makes the entire amplifier system very sensitive to alignment, since it requires a spatial separation between the passes while the beam size almost equals the Nd:YAG rod diameters. Any misalignment can therefore lead to either a clipped beam profile or a detrimental backreflection towards the Faraday rotator. Another possible source of problems is the focus in the relay-imaging system after the first amplification pass (see Fig. 5.9), which has not been placed inside a vacuum tube, while the pulse intensity might already be sufficient for self-phase-modulation to occur.

To deal with these problems we changed the design of the post-amplifier to a ring geometry, as depicted in Fig. 5.12. The diameter of the initial injected beam is kept relatively small (about 6.5 mm), which decreases the influence of thermal lensing and birefringence in the first pass. Instead of direct backreflection after this first amplification pass, the beam goes through a TFP and is guided around the amplifier for a second pass in the same direction. In between the passes, the polarization is rotated 90° by a $\lambda/2$ -plate so that the beam now reflects off the first TFP and overlaps with the light from the first pass. To maintain beam quality, relay-imaging is employed between passes using an $f = 30$ cm and an $f = 50$ cm lens to image the beam profile from one Nd:YAG rod to the next. In addition, this telescope expands the beam to 11 mm diameter, to efficiently fill the amplifier rods on the second pass. To prevent self-phase-modulation

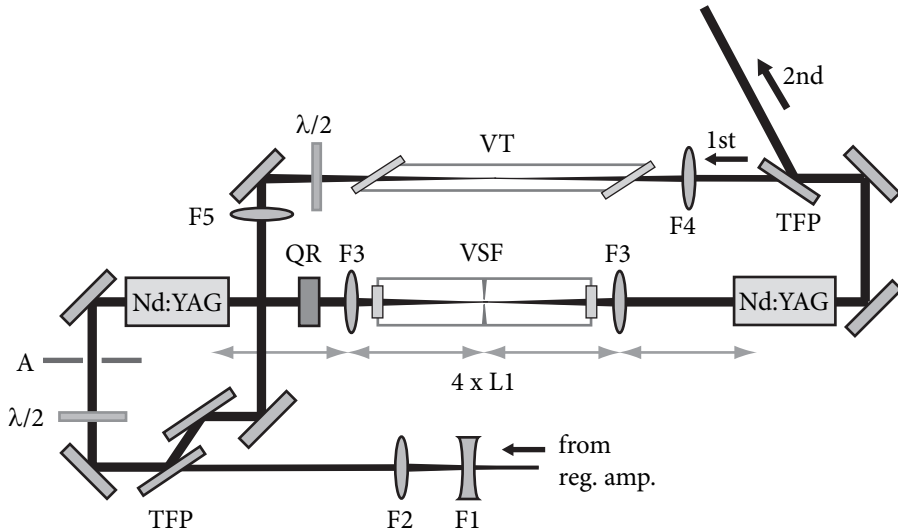


FIGURE 5.12: Flashlamp-pumped post-amplifier in ring geometry. Abbreviations identical as in Fig 5.9, and A: 11 mm aperture, VT: vacuum tube. F1=-5 cm, F2=15 cm, F3=20 cm, F4=30 cm, F5=50 cm, L1=20 cm. 1st and 2nd indicate the paths taken by the first and second amplification passes, respectively.

and breakdown in air, the focus of the telescope is placed inside a vacuum tube. After the second pass, the amplified pulses are reflected off the TFP towards the experiment.

In this amplifier geometry, any uncompensated depolarization will not be reflected back in the direction of the input, but will make an additional roundtrip through the system while maintaining a large beam diameter. Even more so, this residual beam will be expanded by the telescope to 18 mm diameter. An 11 mm aperture is placed in front of the first amplifier module to prevent this beam from hitting the edge of the first Nd:YAG rod. The gain for this beam will be relatively low, since the second pass has already extracted a significant fraction of the stored energy from the amplifier. In combination with this large beam diameter and the low seed power due to the aperture clipping, this residual beam is not intense enough to cause any problems. Instead, it leads to a small post-pulse accompanying the pump pulse on its path towards the frequency-doubling crystal.

With the backreflection issues out of the way, this amplifier geometry allows amplification to higher energy, and up to 250 mJ per pulse has been generated at 30 Hz repetition rate. In addition, this ring-amplifier geometry is less difficult to align than the linear post-amplifier. This is partly due to the decreased backreflection, but also because the respective passes are decoupled; the first pass can be coupled out towards the frequency doubling crystal with the TFP by simply rotating the $\lambda/2$ -plate in front of the first amplifier module. The produced visible light is very convenient for opti-

mization of gain, beam profile and birefringence compensation in the first pass. With the first pass optimized, the polarization is rotated back to allow the second amplifier pass, which now only needs to be overlapped with the beam from the first pass for proper amplification. Fine-tuning of the birefringence compensation is done by placing a CCD camera in front of the vacuum tube between the passes, where the beam is just small enough to fit on the camera. The camera image provides a more detailed view of the beam profile which can be used to minimize the transmission through the TFP by tuning the lens in the relay-imaging system between the amplifier modules.

5.2.7 Relay-imaging and spatial filtering

To maximize energy extraction efficiency of the post-amplifier, the beam diameter in the last pass is set almost equal to the size of the Nd:YAG rods. In combination with saturation effects, the output beam profile will have a top-hat spatial distribution. However, such a spatial distribution will not stay constant with propagation distance. The far-field beam profile is determined by Fraunhofer diffraction, and the spatial frequency spectrum of this far-field distribution is the Fourier transform of the initial beam profile [193]:

$$\tilde{E}(k_x, k_y) = \iint E(x, y) e^{i(k_x x + k_y y)} dx dy \quad (5.8)$$

where x and y are the transverse beam coordinates, and $k_{x,y}$ are the transverse spatial frequencies, which are the projections of the wave-vector \mathbf{k} in the x and y directions. From this relation it can be seen that a Gaussian beam profile will retain its shape in the far-field. In contrast, a top-hat shaped beam profile will transform into a sinc(r)-function (where $r = x^2 + y^2$) after propagation over large distances. In the intermediate regime between the amplifier output and the far-field, the beam profile will therefore change continuously. In addition, any subtle deviations of the amplifier beam profile from a perfect top-hat shape can cause hot-spots and strong intensity variations across the beam at certain points in the beam path, which may be capable of damaging optics.

To ensure a good-quality beam profile at crucial points in the system (e.g. at amplifier modules or frequency-doubling crystals), the technique of relay-imaging is used. A relay-imaging system typically consists of two lenses in a $4f$ -configuration, as shown in Fig. 5.13. The first lens focuses the initial $z = 0$ beam profile at $z = 2f$, where the spatial distribution will be the aforementioned Fraunhofer diffraction pattern. The second lens then performs an inverse Fourier transformation and images the produced diffraction pattern from the first lens at $z = 4f$, and the initial beam profile is regained. In this way, the top-hat beam profile can be reconstructed at any distance from the amplifier output by using the appropriate lens system.

Such a relay-imaging setup can also be used to modify the beam profile, by placing an aperture in the Fourier-plane of the $4f$ -system. Since the various spatial frequency components of the initial beam are separated in this plane, a sufficiently small aperture can serve as a low-pass filter for spatial frequencies. The resulting beam at the output of the $4f$ -system will have a smoother profile, since the high spatial frequencies are

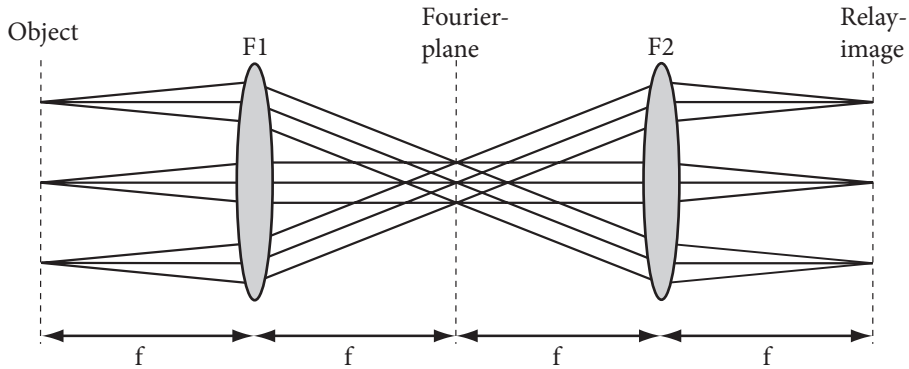


FIGURE 5.13: Relay-imaging setup, consisting of two lenses in a $4f$ -configuration. The transverse field distribution in the Fourier-plane is the spatial Fourier transform of the object beam profile. The second lens transforms this distribution back into the original beam profile at the relay-image plane. Note that an angular deviation in the object-plane (i.e. a nonzero k_x and/or k_y) translates into a spatial separation in the Fourier-plane.

responsible for e.g. the steep edges of a top-hat distribution. An example of the effect of spatial filtering is shown in Fig. 5.14, where the beam profile of the amplifier output is shown with and without spatial filtering between the modules. The unfiltered beam profile suffers from diffraction on the edges of the amplifier Nd:YAG rods, leading to the typical Fresnel diffraction ring pattern in the near-field. When the aperture is placed in the Fourier-plane of the relay-imaging system, these rings are almost completely filtered out. This is because the fast spatial variation of the pattern corresponds to high spatial frequencies, which are not transmitted by the aperture. Note that despite the rigorous change in beam profile, still more than 90% of the incident power is transmitted through the pinhole. Such a spatial filtering setup has been used to improve the beam profile in the flashlamp-pumped post-amp setups described in the two previous sections (see Figs. 5.9 and 5.12).

The $4f$ -system described here also forms the basis for the adaptive phase shaping setup from section 5.1.4. In that particular setup, the grating at $z = 0$ introduces a transverse spatial frequency k_x , which is a function of frequency ω . The separation of the various spatial frequencies k_x in the Fourier-plane therefore also leads to a separation of the temporal frequencies ω , allowing the manipulation of individual frequency components in a way similar to the spatial filtering described in this section.

5.3 NOPCPA amplifier geometry

While a thorough description of various NOPCPA implementations is given in the next three chapters, a more detailed layout of the optical setup and its design are presented in this section. The particular setup that is shown in Fig. 5.15 is the latest version, which produces the highest power in the shortest pulse, and it has been used to obtain the

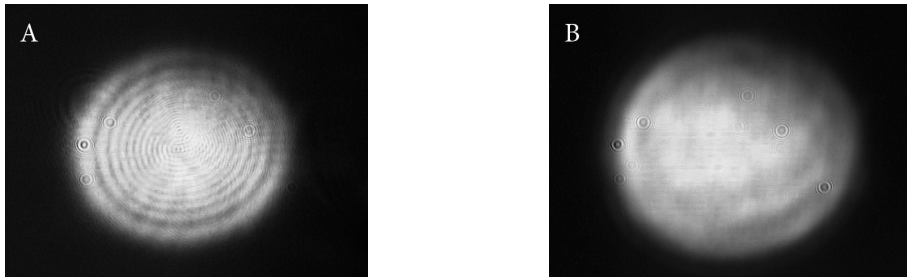


FIGURE 5.14: Effects of spatial filtering on the beam profile. (A) The beam profile at the amplifier output without spatial filtering. Clear diffraction rings can be seen which are caused by the edges of the Nd:YAG rods. (B) The beam profile with spatial filtering, where the diffraction rings have been filtered out almost completely. In both (A) and (B) some small diffraction features are seen, which are due to dust particles on the CCD camera.

results presented in chapters 7 and 8. It consists of a double-pass pre-amplifier and a single-pass power-amplifier stage.

After passing through the stretcher, the seed pulses are downcollimated to a 1 mm diameter using a telescope, and passed through the OPA pre-amplifier. In front of the pre-amplifier, a translation stage is placed to optimize the pump-seed timing inside the amplifier crystal. This BBO crystal (type-I, $\theta = 23.8^\circ$) is 5.5 mm long, and has an aperture of 5 mm \times 5 mm. This first amplification pass is pumped by 10 mJ pulses at 532 nm, which have been produced by frequency doubling a fraction of the light from the pump laser in a type-II KDP crystal. The light from the pump laser has been relay-imaged from the last Nd:YAG amplifier module onto the KDP crystal, using a telescope consisting of an $f = 50$ cm and an $f = 20$ cm lens. The focus in the Fourier-plane of the relay-imaging telescope is placed inside a vacuum tube to prevent self-phase-modulation and optical breakdown in air, and the final beam diameter in the KDP crystal is 4.5 mm. After frequency-doubling, the 532 nm light is relay-imaged onto the first OPA amplifier crystal using another downcollimating telescope. The final pump beam diameter in this first pass is then 1.7 mm, leading to an intensity of about 7 GW/cm², and the gain in this first pass is found to be $\sim 4 \times 10^3$. At this intensity, a subtle fluorescence cone can be observed with an apex angle of about 3.7° (external angle, i.e. outside the crystal) when looking through an infrared viewer. For optimal broadband amplification, we overlap the seed beam with this fluorescence cone, leading to a noncollinear angle around 2.3° inside the crystal.

To pump the second amplification pass, we recycle the light from the first pass by reflecting it back using a curved mirror. The radius of curvature of this mirror (R7) is equal to its distance from the OPA crystal. As a result, the beam profile is relay-imaged from the first pass onto the second, although the beam is not collimated anymore; the initially collimated beam focuses at 25 cm before the crystal, while the beam diameter inside the crystal regains its original value of 1.7 mm. After the first pass, the amplified seed beam slightly diverges due to the already diverging input beam as well as natural diffraction. Instead of compensating this divergence with a curved mirror, the

tween. With a single pass through the crystal, the seed pulse is amplified from 0.5 mJ to a maximum energy of 30 mJ per pulse. As will be discussed in more detail in the later chapters (especially chapter 8), the spectral bandwidth can extend from 720 nm to about 1050 nm, which allows the amplification of pulses with a Fourier-limit of 7 fs.

5.4 Characterization of ultrafast laser pulses

As the amplified laser pulses produced by the NOPCPA system described in the previous section can in principle be compressed to a duration of only 7 fs, the measurement of the actual pulse duration presents quite a technical challenge. For a single-shot measurement of such a pulse in the time domain, a detection system with a response time of much less than one femtosecond would be needed, far beyond the reach of conventional electronics. As a result, the measurement of ultrashort laser pulses is an active research field by itself. In this section, we describe the principle and design of the pulse characterization system that has been used in the course of the present work.

5.4.1 Autocorrelation

The duration of an ultrashort pulse can be measured by time gating the pulse with itself (see e.g. [121]), as depicted in Fig. 5.16A. The incoming pulse is split into two identical replicas with an interferometer. These replicas are subsequently recombined, and reach a detector with a nonlinear intensity response, such as a frequency doubling crystal. By measuring the intensity of the generated second harmonic radiation while scanning one of the arms of the interferometer, a signal as shown in Fig. 5.16B is obtained. This interferogram can be explained by considering the instantaneous peak intensity of the combined pulse replicas as a function of the applied time delay, which is proportional to the second-order correlation function:

$$\begin{aligned}
 I_{\text{SHG}}(t) &= \int_{-\infty}^{\infty} (|E(t) + E(t-T)|^2)^2 dt \\
 &= \int_{-\infty}^{\infty} |A(t)|^4 + |A(t-T)|^4 + 4|A(t)|^2|A(t-T)|^2 \\
 &\quad + 4A(t)A(t-T)(|A(t)|^2 + |A(t-T)|^2) \cos \omega T \\
 &\quad + 2|A(t)|^2|A(t-T)|^2 \cos 2\omega T dt
 \end{aligned} \tag{5.9}$$

where we have written the electric field in terms of a carrier-wave and an envelope function: $E(t) = A(t)e^{-i\omega t}$. When the pulses are completely separated in time ($T \rightarrow \infty$) only the first two terms in equation (5.9) contribute, while for $T = 0$ we have $\cos \omega T = \cos 2\omega T = 1$. The intensity ratio between the peak and the background will therefore be 8 : 1. By scanning T from $-\infty$ to ∞ (in practice somewhat less), a signal similar to Fig. 5.16B is obtained, from which the pulse duration can be reconstructed.

One drawback of this type of measurement is that it requires scanning a time delay, which has to be done slowly compared to the pulse repetition rate in order to obtain sufficient data points per fringe. This limits its usefulness for low repetition rate

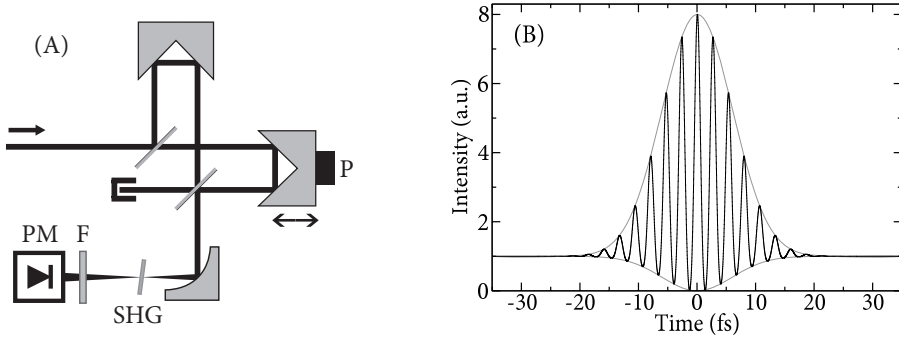


FIGURE 5.16: (A) Dispersion-balanced second-order autocorrelator setup. PM: photomultiplier, F: filter for the second harmonic, SHG: second-harmonic generation, P: Piezo-transducer. (B) Simulated autocorrelation measurement of a 10 fs FWHM Gaussian pulse.

amplifier systems, although single-shot autocorrelators have been developed for longer pulse durations [194].

A much more serious problem with autocorrelation is its insensitivity to phase distortions on the input pulse. Although a small, linear chirp on the input pulse can still be identified from the interferogram, more complicated high-order phase deviations are very difficult to detect using an autocorrelator. Such phase distortions lead to a complex envelope function $A(t)$ in equation (5.9), causing a distorted shape of the measured autocorrelation signal. In principle it is possible to reconstruct the complete pulse shape from an autocorrelation trace, but this requires fitting the interferogram to a model pulse shape. This can only be done reliably when the form of the pulse envelope (e.g. Gaussian, sech^2 , etc.) is known in advance.

5.4.2 Spectral phase interferometry for direct electric field reconstruction

A more sophisticated method for ultrashort pulse characterization is based on spectral interferometry and is known as SPIDER (Spectral Phase Interferometry for Direct Electric field Reconstruction [195]).

In a SPIDER-scheme (see Fig. 5.17), the pulse under consideration is first split in two: One pulse is passed through a strongly dispersive delay line (such as a grating pair or a glass block), while the other pulse is sent into an interferometer to generate two identical pulse replicas with a fixed delay τ between them. These replicas are overlapped with the chirped pulse inside a nonlinear crystal, producing the sum frequency of the respective ultrashort pulse replicas with a narrow-bandwidth spectral slice of the chirped pulse. This results in two UV pulses with an identical spectral phase evolution, but at slightly different central wavelengths. Sending the upconverted pulse pair into a spectrometer leads to a spectral interferogram:

$$I(\omega) = |E(\omega)|^2 + |E(\omega + \Omega)|^2 + 2|E(\omega)E(\omega + \Omega)| \cos[\varphi(\omega + \Omega) - \varphi(\omega) + \omega\tau] \quad (5.10)$$

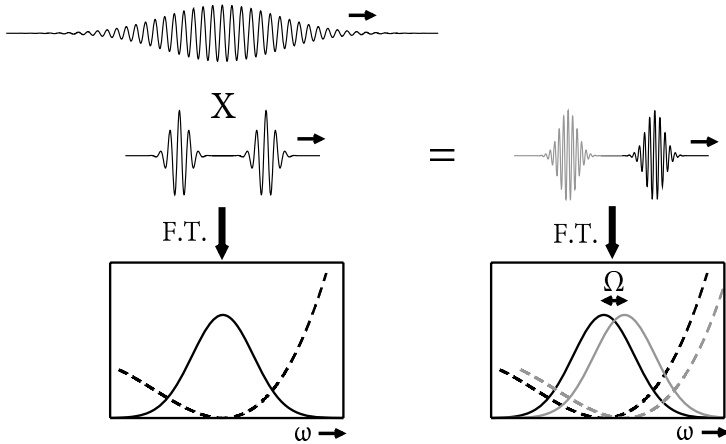


FIGURE 5.17: The principle of spectral phase interferometry for direct electric field reconstruction (SPIDER): Two time-delayed replicas are generated of the pulse to be measured, which are upconverted by sum-frequency-mixing with a strongly chirped pulse. As each replica mixes with a different (narrow-band) spectral part of the chirped pulse, a spectral shear Ω is introduced after upconversion. Using spectral interference, the phase of the pulses can be measured.

Due to the spectral shear Ω that results from the difference in upconversion wavelength between the two pulses, the phase difference $\varphi(\omega + \Omega) - \varphi(\omega)$ is still observable in the interferogram. When both Ω and τ are properly calibrated, the spectral phase $\varphi(\omega)$ can be extracted. Combining the obtained phase information with a measurement of the spectral intensity, the full electric field in the time domain can be reconstructed [195].

In addition, the SPIDER technique has the advantage of single-shot operation, making it suitable for characterization of low repetition rate chirped-pulse amplifier systems [196]. Provided that the bandwidth of the upconversion process is sufficiently large and care is taken to avoid pulse distortion in the SPIDER apparatus itself, pulses with a duration of only a few femtoseconds, i.e. approaching the single-cycle regime, can be fully characterized [197, 198].

5.4.3 Experimental implementation of SPIDER

A schematic of our particular SPIDER implementation is shown in Fig. 5.18. The incoming pulse to be measured is first split by a 10% beamsplitter. The reflection passes through a dispersion-balanced Michelson interferometer, to create two identical pulse replicas separated by $\tau \sim 300$ fs. The pulse transmitted through the beamsplitter is stretched to 2 ps by double-passing a pair of F2-glass prisms. The ultrashort replicas and the stretched pulse are focused in a $30 \mu\text{m}$ thick type-II BBO crystal ($\theta = 41^\circ$) with a small noncollinear angle between them, to allow the beams to be spatially separated after upconversion. A type-II configuration in BBO was chosen for the sum-frequency generation, as this allows phase-matching over the entire bandwidth of the

pulses [197]. The resulting sum-frequency signal is sent into a spectrometer, consisting of a 1200 lines/mm silver-coated grating and an $R = -200$ mm concave mirror in a $2f$ -configuration, and a UV-sensitive CMOS camera. About $50 \mu\text{J}$ per pulse is required for single-shot operation.

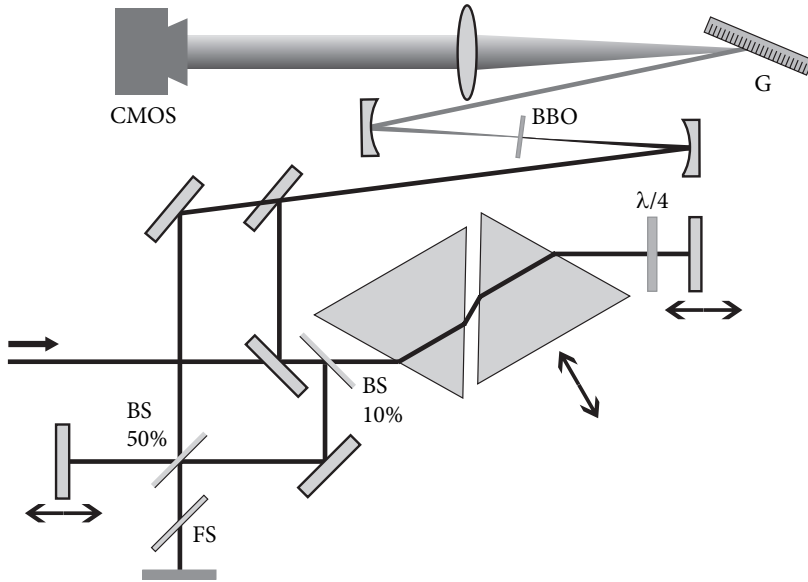


FIGURE 5.18: Schematic of the SPIDER-setup. BD: beamsplitter, FS: 1 mm thick fused silica plate, CMOS: UV-sensitive CMOS camera, G: 1200 lines/mm grating, BBO: $30 \mu\text{m}$ type-II BBO crystal ($\theta = 41^\circ$) for sum-frequency generation.

5.4.4 SPIDER calibration

Calibration of the SPIDER is essential for reliable pulse reconstruction. Especially the time delay τ between the pulse replicas needs to be accurately measured, and preferably monitored continuously during measurements. To this end, we slightly rotate the BBO crystal, such that the polarization of the pulse replicas is partially projected onto the e -axis of the crystal. As a result, the second harmonic of the ultrashort pulse replicas is also generated in the crystal. This SHG signal can be sent into the spectrometer instead of the SPIDER signal, leading to an interferogram on the camera with a phase corresponding to $\cos \omega\tau$. This signal is used for calibration of the time delay τ . Instead of calculating the time delay from this interferogram, the extracted $\omega\tau$ phase trace is directly subtracted from the measured SPIDER traces, yielding the $\varphi(\omega + \Omega) - \varphi(\omega)$ phase difference. For measurements of ultra-broadband (sub-10 fs) pulses, the camera needs to be aligned accurately in the Fourier-plane of the spectrometer. The calibration of τ is performed right before the start of a SPIDER measurement by blocking the

sheared reference pulse and recording only the calibration interferogram. During the actual SPIDER measurements, the calibration interferogram is prevented from reaching the camera by blocking the SHG signal before it reaches the spectrometer (this is made possible by the noncollinear geometry for sum-frequency generation).

The spectrometer wavelength axis and the shear Ω are calibrated simultaneously, by exploiting the pulse stretcher/shaper in the NOPCPA amplifier system (see section 5.1.4). As all the spectral components in the pulse are spatially separated in the Fourier-plane of the stretcher, we can block a single frequency in the fundamental spectrum, and measure the position on the camera where a dip is produced in the SPIDER spectrum (only one pulse replica is upconverted, by blocking one arm of the Michelson interferometer). For a certain frequency, the entire SPIDER spectrum disappears: This particular frequency corresponds to the narrow-band frequency slice in the stretched pulse with which the pulse replica is upconverted. By repeating this process for both pulse replicas we can identify both narrow-band upconversion wavelengths (from which Ω can be calculated directly), and the spectrometer wavelength axis.

5.4.5 Reconstruction of the pulse shape

Besides the single-shot capability, the SPIDER can even be operated in real-time [196, 199, 200], as the phase reconstruction algorithm [201] does not require a large computational effort. The reconstruction steps are shown in Fig 5.19. First, the measured interferogram is curve-fitted using cubic splines and resampled on a grid of evenly spaced frequencies, since the spectrometer pixels are evenly spaced in wavelength. This frequency-sampled interferogram is Fourier-transformed into the time domain yielding a DC-signal with two sidebands at $\pm\omega\tau$. These sidebands are explained by expanding the cosine term in Eq. (5.10) as:

$$\cos [\varphi(\omega + \Omega) - \varphi(\omega) + \omega\tau] = \frac{1}{2} \left(e^{+i[\varphi(\omega+\Omega)-\varphi(\omega)+\omega\tau]} + e^{-i[\varphi(\omega+\Omega)-\varphi(\omega)+\omega\tau]} \right)$$

The $e^{+i[\dots]}$ -sideband is filtered out by multiplication with a super-Gaussian function centered at the sideband position, and the signal is Fourier-transformed back into the wavelength domain. The result is an array of complex numbers, of which the argument is the phase term $\varphi(\omega + \Omega) - \varphi(\omega) + \omega\tau$. This argument can be extracted by calculating the logarithm and taking the imaginary part. This procedure is performed for both the SPIDER-interferogram and the calibration trace: The extracted argument of the calibration trace simply yields $\omega\tau$. Subtracting this calibration from the argument of the SPIDER trace then gives the phase difference $\theta(\omega) = \varphi(\omega + \Omega) - \varphi(\omega)$.

As the absolute phase cannot be measured using SPIDER, we define the phase at the pulse central frequency $\varphi(\omega_c) = 0$. By employing a concatenation procedure, we obtain the spectral phase $\varphi(\omega)$ at a discrete set of frequencies $\omega \pm n\Omega$. Data points that are evenly spaced in the frequency domain are obtained by interpolation of the wavelength axis using cubic splines. When this first phase point $\varphi(\omega_c)$ is defined, the

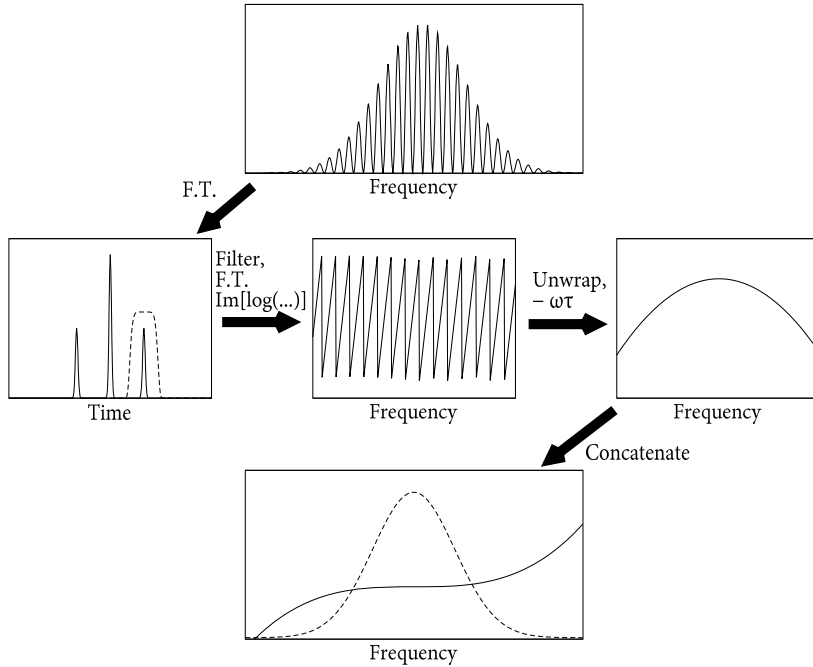


FIGURE 5.19: Steps taken in the reconstruction of the spectral phase using SPIDER: The measured interferogram is Fourier transformed (F.T.) to the time domain, where the sideband is filtered out. This sideband is then transformed back to the frequency domain, and the phase is extracted. Next, the phase is unwrapped, and the time delay calibration $\omega\tau$ is subtracted. After concatenation, the spectral phase of the pulse is retrieved.

rest of the spectral phase curve can be reconstructed as:

$$\begin{aligned}
 \varphi(\omega_c - \Omega) &= \theta(\omega_c - \Omega), \\
 \varphi(\omega_c) &= 0, \\
 \varphi(\omega_c + \Omega) &= -\theta(\omega_c), \\
 \varphi(\omega_c + 2\Omega) &= -\theta(\omega_c + \Omega),
 \end{aligned} \tag{5.11}$$

It should be noted that the spectral phase is only reconstructed on a discrete set of points spaced by Ω . Even though the initial SPIDER measurement contains much more data points, the spectral resolution is limited by the choice of Ω , and phase variations on a smaller frequency scale will mostly be averaged out. This strong oversampling of the SPIDER measurement can be exploited, however, for data averaging: by choosing a different starting pixel for the concatenation procedure (5.11), a new spectral phase reconstruction is obtained that should in principle contain the same information, although on a different grid of sampling frequencies.

The obtained phase information can be combined with a spectral intensity measurement, and Fourier-transformed to the time domain to yield the temporal electric field:

$$E(t) = \frac{1}{2\pi} \int_{-\infty}^{\infty} \left(\sqrt{I(\omega)} e^{i\varphi(\omega)} \right) e^{i\omega t} d\omega \quad (5.12)$$

Although the reconstructed spectral E -field from a SPIDER measurement uniquely defines the pulse shape in time, a more intuitive picture is obtained when the spectral E -field data is padded with zeros at the edges to increase the spectral width $\Delta\omega$. As the time resolution after Fourier transformation scales with $\Delta t = 1/\Delta\omega$, a smoother curve is produced, which contains exactly the same information.

In this way, SPIDER provides a full characterization of the duration and shape of an ultrashort pulse. A typical example of SPIDER in action can be seen in Fig. 5.20. Figure 5.20A shows the measured interferogram of a compressed 10 mJ pulse (of which only about 100 μ J is used as SPIDER input) from a parametric amplifier system running at 30 Hz repetition rate. After Fourier-transformation, the time-trace plotted in Fig. 5.20B is obtained, from which one sideband is filtered out for the required analysis. The reconstructed spectral phase is displayed in Fig. 5.20C, along with the measured spectral intensity. Figure 5.20D contains the corresponding time domain picture revealing an 8.6 fs FWHM pulse width, along with some residual pre- and post-pulse structures. This particular example highlights the added benefit of SPIDER compared to e.g. autocorrelation, especially for the characterization of such ultrashort pulses, which usually have a complicated pulse shape.

5.4.6 SPIDER design considerations

The design of a SPIDER setup mostly depends on the spectral bandwidth that needs to be characterized. Additional care has to be taken when the input power is low, or when large spectral phase deviations need to be measured.

The pulses that we want to characterize have a bandwidth ranging from ~ 710 nm to about 1050 nm. After upconversion with a wavelength around 820 nm, the generated UV spectrum will span from 380 nm to 460 nm. The spectrometer should of course be capable of resolving this entire spectrum. We constructed a spectrometer to meet these criteria, consisting of a 1200 lines/mm grating, an $R = -200$ mm silver coated mirror, and a 1280 \times 1024 pixel CMOS camera (Prosilica CV1280, IEEE-1394a connection, 16.9 mm sensor size, 6.7 \times 6.7 μ m pixel size, 10-bits bit depth).

Since the phase deviations in a SPIDER interferogram show up as variations of the fringe spacing, the time delay τ between the pulse replicas should be chosen such that a sufficient number of fringes is recorded without violating the Nyquist criterion [202] (which states that a minimum of two points per fringe is required for reconstruction of the interferogram). Typically our SPIDER operates with a time delay around $\tau = 250$ -350 fs, so that an interferogram contains about 25-35 fringes and always has more than 30 pixels per fringe.

Another important design parameter is the magnitude of the shear Ω . At this point the Whittaker-Shannon sampling theorem needs to be considered, which states that for a certain frequency stepsize Ω , only temporal structures that fall within a time window

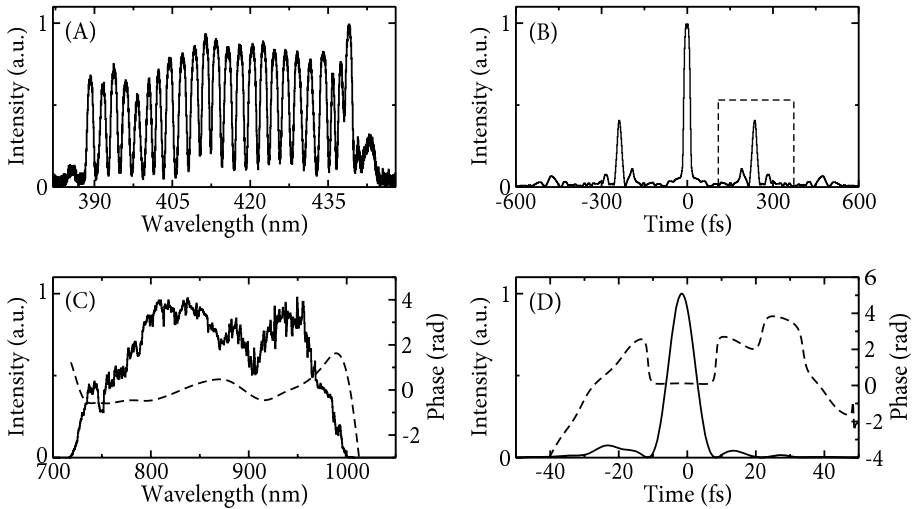


FIGURE 5.20: Experimental demonstration of SPIDER. (A) A measured SPIDER interferogram. (B) The Fourier-transform of the interferogram showing the desired sidebands, of which one is filtered out (dashed lines indicate the position and width of the filter). (C) The extracted spectral phase (dashed curve), together with an independently measured spectrum (solid curve). (D) The reconstructed pulse shape and phase in the time domain. The measured pulse width (FWHM) in this particular example is 8.6 fs.

$T \leq 2\pi/2\Omega$ can be accurately reconstructed; any spectral phase variation that is too fast to be sampled properly at intervals of Ω will undergo aliasing, causing errors in the pulse reconstruction. Since such fast phase fluctuations in the frequency domain correspond to slow temporal modulation, this places an upper limit on the duration of chirped pulses that can reliably be measured. Therefore, Ω should be chosen such that T is sufficiently long compared to the Fourier limit τ_{\min} of the pulse to be measured, i.e. $T \sim 10\tau_{\min}$.

On the other hand, however, Ω should not be chosen too small either, to prevent the measured phase difference $\varphi(\omega + \Omega) - \varphi(\omega)$ from becoming too small. Because the phase retrieval is based on a comparison of the SPIDER fringe pattern with a calibration interferogram, the sensitivity to small spectral phase variations is limited by the accuracy with which $\varphi(\omega + \Omega) - \varphi(\omega)$ can be determined in the presence of noise. When $\Omega \rightarrow 0$ this phase difference tends to zero, which inhibits a reliable phase reconstruction. Therefore Ω should be at least a few percent of the spectral bandwidth of the measured pulse [202]; it is good practice to choose Ω on the order of (or somewhat larger than) the fringe spacing $1/\tau$. For our SPIDER apparatus we typically use a shear of $\Omega/2\pi = 6 - 9$ THz, which is 4-6% of the pulse spectral bandwidth, and allows the reconstruction of pulses with a duration up to about 110 fs. This shear is achieved by chirping the ultrashort pulse with a pair of F2 prisms (see the setup in Fig. 5.18). The required group velocity dispersion to produce a certain shear at a given

delay is $k^{(2)} = \tau/\Omega$. To achieve typical SPIDER operating conditions of $\tau = 261$ fs and $\Omega = 7.0$ THz, the group velocity dispersion should therefore be set to $k^{(2)} = 5.9 \times 10^3$ fs², corresponding to a total path length inside the prisms of 6.3 cm.

5.5 High-harmonic generation

Because of the combination of high intensity and ultrashort pulse duration, the NOPCPA system described in section 5.3 is ideally suited for the generation of high harmonics. While the quantum interference metrology experiments described in chapter 3 have been carried out on a deep-UV two-photon transition, a combination of these frequency comb pulsed excitation techniques with the high-harmonics generated using this NOPCPA system could enable precision measurements at much shorter wavelengths. As an initial experiment, we used single pulses amplified by the NOPCPA system to generate high harmonics in a gas jet.

5.5.1 XUV generation and detection setup

A schematic overview of the setup used for harmonic generation and detection is shown in Fig. 5.21. The compressed NOPCPA output pulses are focused with a combination of two spherical concave mirrors. This two-mirror setup is used to avoid the astigmatism which is usually introduced by focusing a beam with a curved mirror at a nonzero angle. By using two mirrors at an identical angle but in perpendicular planes, the net focal length will be identical in both of these planes. The pulses are focused in the gas jet with a focal length of about 30 cm, leading to an estimated peak intensity of a few times 10^{15} W/cm², which is powerful enough to saturate the harmonic generation process in virtually any gas. The gas jet is produced using a pulsed (30 Hz repetition rate) piezo-valve synchronized to the amplified laser pulses.

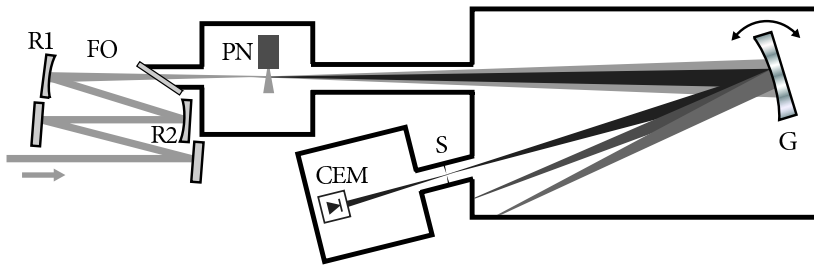


FIGURE 5.21: Setup for generation and detection of high-order harmonics. FO: Focusing optics for astigmatism compensation (see text), R1 and R2 are both concave mirrors with -150 cm radius of curvature. PN: Pulsed nozzle for the generation of a 30 Hz pulsed atomic beam, G: 1200 lines/mm gold-coated curved grating ($R = -100$ cm), S: Slit, CEM: Channel electron multiplier for detection of XUV radiation. The distance from PN to G is 125 cm, and the distance from G to S is 83 cm.

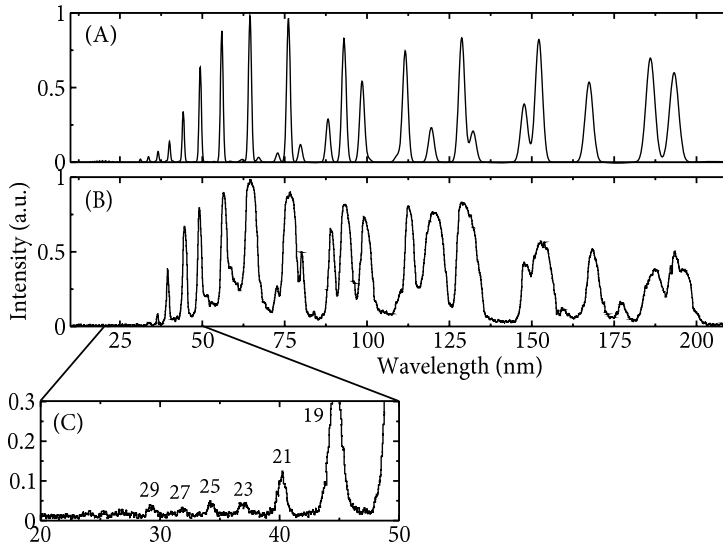


FIGURE 5.22: (A) Simulated harmonic spectrum, taking the monochromator grating and detector efficiency into account. (B) Experimentally observed harmonic spectrum in argon. (C) Higher resolution scan of the 20-50 nm wavelength range showing harmonics up to the 29th order, limited by the short-wavelength cutoff of the monochromator grating.

The generated harmonics propagate collinearly with the fundamental pulses, until after 1 m the beam is dispersed on a gold-coated normal incidence grating with 1200 lines/mm. This grating is curved with a -100 cm radius of curvature, such that the entire setup acts as a monochromator in a $2f$ -configuration. The -1st order of the grating is imaged onto a slit, transmitting only a single wavelength component. It should be noted that the distance from the focus inside gas jet to the grating is set at 125 cm, so that the curved grating refocuses the beam after only 83 cm. This asymmetry ensures easy optical access to the gas jet from the side of the vacuum setup (see Fig. 5.21), which can be useful for future experiments. The transmitted radiation is detected using a channel electron multiplier connected to an oscilloscope, which is read out by a computer. A measurement of the generated harmonic spectrum as a function of wavelength is obtained by scanning the grating angle using a stepper motor, which is calibrated using a position-sensitive resistance.

5.5.2 Measured spectra

A typical spectrum of the generated high harmonic radiation is displayed in Fig. 5.22B. This particular spectrum has been obtained using a gas jet of argon atoms as the non-linear medium for harmonic generation. Argon is a good candidate for high-harmonic generation experiments since it has a high ionization potential and still a reasonable

nonlinear susceptibility, so that it combines relatively low ionization rates and a high harmonic spectral cutoff with a significant harmonic yield.

To understand the complicated structure of the observed harmonic spectrum, we performed a simulation of the expected signal, taking into account the higher orders of the grating, as well as the wavelength-dependent efficiency of the grating and detector. The central wavelength of the fundamental pulse is taken to be 850 nm, which is consistent with the experimental situation. The result of this simulation is shown in Fig. 5.22A, and it immediately clarifies the observed harmonic spectrum in Fig. 5.22B: The measured peak positions show good agreement, and also the relative peak intensities correspond well to the simulations. Only a few discrepancies in the peak intensities occur, which can largely be attributed to uncertainties in the grating efficiency calibration at short wavelengths. The inset (Fig. 5.22C) shows an additional scan of the 20-50 nm wavelength region at a higher resolution (i.e. slower scan speed and a longer averaging time). In this scan, harmonic structure up to the 29th harmonic is clearly observed. Especially for the longer wavelengths, a significant broadening of the harmonic peaks is observed, mainly caused by saturation of the electron channel multiplier.

As is clear from the simulations, the presently observed short-wavelength cutoff is completely determined by the grating diffraction efficiency; while the theoretical curve actually predicts a steeper descent at the short wavelength side of the spectrum, no intensity or phase-matching-induced decrease in harmonic intensity is observed. This is consistent with expectations for such intense few-cycle pulses, for which harmonic wavelengths well below 1 nm may be expected. However, the present monochromator setup with its gold-coated grating and normal-incidence geometry prohibit the detection of such high harmonics. For more sophisticated high-harmonic generation experiments, a grazing-incidence monochromator equipped with e.g. a platinum-coated grating is required. Aside from these limitations in short-wavelength detection capability, the present setup is well-suited for experiments where intense, short-pulse radiation in the 40-100 nm wavelength range is required.

CHAPTER 6

HIGH POWER PARAMETRIC AMPLIFICATION OF 11.8 FS LASER PULSES WITH CARRIER-ENVELOPE PHASE CONTROL

In this chapter, we demonstrate phase-stable noncollinear optical parametric chirped pulse amplification of few-cycle laser pulses. Starting out with \sim nJ energy pulses from a carrier-envelope phase-stabilized modelocked Ti:Sapphire oscillator, the NOPCPA system amplifies these pulses to 0.25 mJ at 1 kHz repetition rate. Pulse compression with a grating compressor and an LCD spatial light modulator yields near Fourier-limited 11.8 fs pulses with an energy of 0.12 mJ. As a pump source, the second harmonic of a synchronized modelocked laser – Nd:YAG amplifier system is employed. Quantitative measurements of the amplifier-induced phase noise are performed using Fourier-transform spectral interferometry, and the compressed pulses are characterized using SPIDER. Our NOPCPA approach is shown to be promising for the next generation of ultrafast amplifiers, aimed at producing terawatt-level phase-controlled few-cycle laser pulses.

6.1 Introduction

Generation of high-power ultrashort laser pulses has become a matter of routine in recent years [117], but for many applications stabilization and control of the phase φ_{ce} between the carrier wave and field envelope is required as well. This control has been demonstrated already several years ago in the field of frequency metrology, with low-power oscillator pulses [105, 106], and recent experiments using multipass Ti:Sapphire amplifiers have shown that it is possible to produce φ_{ce} -stabilized few-cycle pulses at the mJ level [141, 203]. However, increasing the power to terawatt (TW) intensity using Ti:Sapphire-based amplifiers is challenging already without control of φ_{ce} [141, 204, 205], let alone when φ_{ce} -control is required.

A promising alternative to obtain powerful ultrashort laser pulses with φ_{ce} -control is offered by non-collinear optical parametric chirped-pulse amplification (NOPCPA)

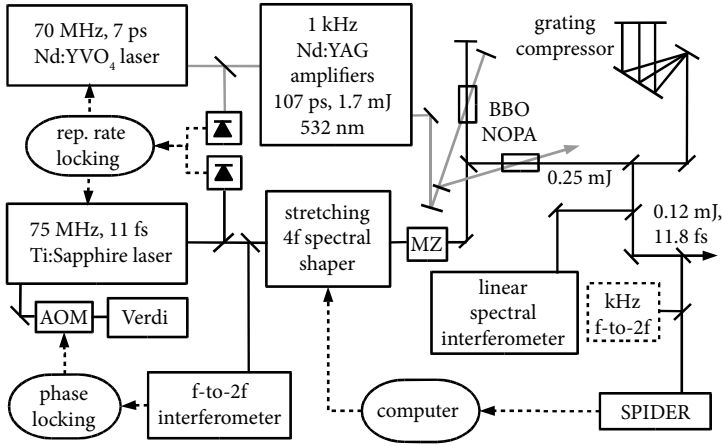


FIGURE 6.1: The setup used for parametric amplification of phase-controlled few-cycle laser pulses. The various blocks in the diagram have already been discussed in detail in the previous chapter. MZ=small Mach-Zehnder pulse replica generator used for the phase measurements, see text.

based on LBO or BBO crystals pumped by 532 nm. Using this technique, multi-TW peak powers have been demonstrated with Nd:Glass laser systems, albeit with pulse lengths of about 155 fs [75] and 300 fs [73] and without phase control. Recently, Hauri et al.[206] reported on phase-preserving NOPCPA with the pump derived from the seed beam by regenerative amplification. They obtained 85 μ J, 17.3 fs pulses and demonstrated phase stability qualitatively. Here we report, to the best of our knowledge, on the first realization of 532 nm pumped parametric amplification of ultrashort laser pulses from a Ti:Sapphire laser, quantitatively demonstrating φ_{ce} -phase-stable ultra-broadband parametric amplification to the mJ level. The pump laser for this approach is based on a Nd:YAG amplified modelocked laser system, which can easily be scaled up with standard Nd:YAG technology so that parametric amplification of few-cycle pulses to TW peak power becomes feasible with a relatively simple system. Moreover, it is demonstrated that grating-based stretching and compression of pulses can maintain carrier-envelope phase stability, in contrast to what is often assumed [166, 207].

Several design studies have been published about systems that in principle should be able to generate TW- and possibly even petawatt peak power few-cycle laser pulses [71, 72]. The main advantages of NOPCPA compared to Ti:Sapphire amplification are the much broader gain bandwidth, the insignificant power dissipation in the amplifier medium, and the low stretching- and compression factor required.

6.2 Phase-stable ultra-broadband NOPCPA setup

A schematic of our setup is shown in Fig. 6.1. The seed pulses stem from a Kerr-lens modelocked Ti:Sapphire oscillator laser (FemtoLaser Scientific Pro), which delivers

~ 7 nJ, 11.0 fs pulses at a repetition rate of 75 MHz. The carrier-envelope phase-slip is locked with a precision of rms $\sim 1/40^{\text{th}}$ of an optical cycle (150 mrad) to $1/5^{\text{th}}$ of a cycle per pulse using the standard f -to- $2f$ technique (see ref. [146] and section 2.2.6). The repetition rate of the Ti:Sapphire laser is stabilized using a dual locking scheme, at 75 MHz for coarse adjustment, and at the 140^{th} harmonic to a 10.4 GHz reference oscillator for fine adjustments and tight synchronization with the picosecond pump laser system. All frequencies are referenced to a GPS-disciplined Rubidium clock.

The Ti:Sapphire laser pulses are stretched to approximately 10 ps in a combined LCD shaper-grating stretcher setup. It consists of two gold-coated cylindrical mirrors (ROC = 0.5 m), two 600 lines/mm gold-coated gratings and a 640 pixel LCD phase-only shaper (Jenoptik SLM-S 640/12). The shaper is traversed twice, and the gratings are displaced from the $4f$ -configuration to generate a group velocity dispersion of 4×10^4 fs². Due to the high damage threshold of BBO, only a small stretching and compression factor ($\sim 1000\times$) is required for the seed pulses. Ray-tracing calculations show that this results in negligible φ_{ce} noise (less than 20 mrad) due to the stretcher and compressor, which was verified by a measurement of the phase noise from these devices by use of a Fourier-transform spectral interferometer.

A home-built cw diode-pumped Nd:YAG amplifier system produces the pump pulses for the OPA. It is seeded by a Nd:YVO₄ modelocked laser (High-Q Laser GmbH) whose 70 MHz repetition rate is asynchronously locked to the same 10.4 GHz oscillator that is used for locking the Ti:Sapphire oscillator laser. To prevent optical damage during amplification, the spectrum of the picosecond laser is clipped in a $4f$ -system to ensure a pulse length of about 100 ps. A combination of a regenerative amplifier and two post-amplifiers boosts the power to 2.8 mJ at 1 kHz. After frequency-doubling in a KTP crystal 1.7 mJ pulses at 532 nm with a duration of 107 ps (measured with a streak camera) are available to pump the OPA.

The stretched pulses from the oscillator laser and the pump beam are both loosely focused into a 10 mm long BBO crystal ($\theta = 22.5^\circ$, $\phi = 0^\circ$, type-I phase matching) and overlapped in time for parametric amplification. The timing jitter between the pump and seed pulses is less than 100 fs. The pump beam has a power density of about 10 GW/cm^2 in the first crystal, and produces only a weak superfluorescence cone without the seed beam present. At an internal angle of the seed beam to the pump beam of 2.38° , phase matching is possible between 740 and 1000 nm [161]. The seed pulses make two passes through the first crystal and one more pass in a second, identical crystal, yielding respectively 3–4 μJ , 0.15 mJ, and 0.25 mJ per pulse, respectively, after each pass, with a pulse-to-pulse power fluctuation of approximately 5%. The unusually high ratio of about 1:10 for the seed to pump pulse duration facilitates an ultra-broad bandwidth. A high energy conversion efficiency of over 20% (signal+idler) is still obtained by saturation of the gain and the possibility to shift the pump and seed pulse in time relative to each other in the second and third pass. In this way the frequencies at the edges of the chirped seed pulse can also profit from the full gain at the center of the pump pulse.

The output pulses are compressed by a grating compressor (1200 lines/mm, separation of ~ 40 mm), after which an output power of 0.12 mJ per pulse is obtained. Dispersion compensation to the third order is achieved by choosing different angles

and grating constants for the stretcher and compressor. Fine tuning of higher-order dispersion is performed with the LCD shaper in the stretcher.

6.3 Pulse characterization

For pulse characterization we have a home-built SPIDER setup [195], which has already been described in the previous chapter. Figure 6.2 shows the fundamental and amplified spectra, together with the spectral phase retrieved from a SPIDER measurement. The combination of the grating-based stretcher and compressor together with the LCD shaper allows us to compensate the spectral phase within ~ 1 rad over the entire amplified bandwidth. Figure 6.3 contains the reconstructed pulse in the time domain, which has a FWHM duration of 11.8 ± 0.3 fs, which is within 5% of the Fourier limit of 11.4 fs.

The amplified spectrum is very different in shape from the input seed spectrum, mainly because of phase-matching effects (preventing the amplification of light below 740 nm) and OPA gain saturation. This spectral shape corresponds quite well to what may be expected from a theoretical point of view (see chapter 4). Note the large gain factor at the long-wavelength side of the spectrum: The oscillator spectrum in Fig. 6.2 has been enlarged for clarity, to demonstrate that there is actually seed light available for the NOPCPA. This small amount of seed light is then amplified to a level comparable to the rest of the spectrum. Even though the differences in spectral shape are substantial, the pulse length of seed and amplified pulses is almost equal. The strong amplitude variations around 900 nm are the result of the dispersion characteristics of the chirped mirrors employed in the seed oscillator. These have little influence on the SPIDER measurements, since this modulation is filtered out in the course of the phase retrieval algorithm.

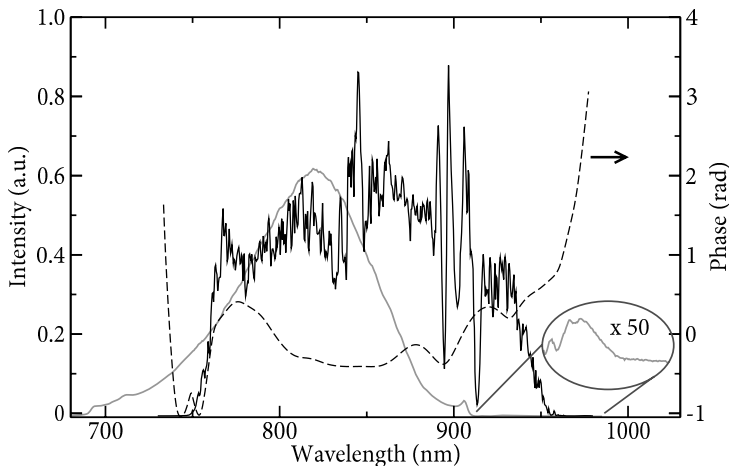


FIGURE 6.2: Measured spectrum of the amplified pulses (black solid line), input seed spectrum (grey line) and the spectral phase (dashed line) that was measured using SPIDER.

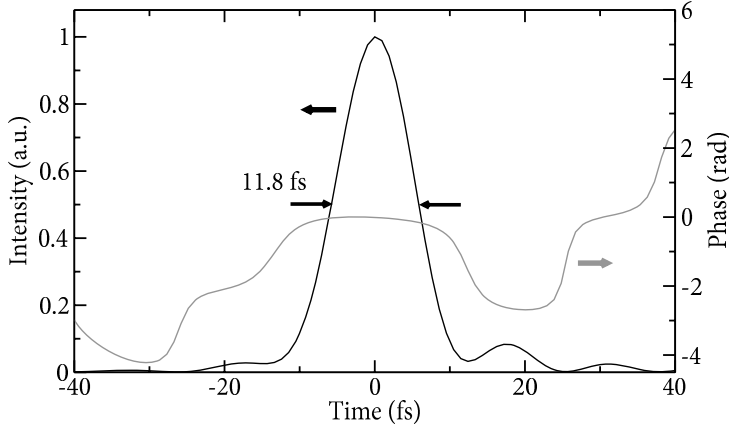


FIGURE 6.3: The pulse shape in the time domain (black line) and the temporal phase (grey line), reconstructed from the spectral intensity and phase shown in Fig. 6.2.

6.4 Phase measurements

6.4.1 Single-shot f -to- $2f$ interferometry

Besides being the method of choice for φ_{ce} -characterization of high repetition rate oscillators, the f -to- $2f$ interferometer can be employed in a single-shot measurement scheme as well [208]. In such a scheme, the input pulse is focused in a 1-3 mm long sapphire plate to generate the required octave-wide spectrum. The use of photonic fibers is not required in this case, since the peak intensity of amplified pulses is orders of magnitude higher than that of oscillator pulses. The infrared part is then frequency-doubled, using a thin (typically 0.1 mm) BBO crystal to upconvert a 10-20 nm wide bandwidth. These pulses are then overlapped with the high-frequency continuum light in space, but a small time delay τ between the pulses is maintained. This delayed pulse pair is then sent into a spectrometer, where spectral interference is observed, according to:

$$\begin{aligned} I(\omega) &= \left| E_1(\omega)e^{i[\omega t + \varphi_{ce}]} + E_2(\omega)e^{i[\omega(t-\tau) + 2\varphi_{ce}]} \right|^2 \\ &= |E_1(\omega)|^2 + |E_2(\omega)|^2 + 2|E_1(\omega)||E_2(\omega)| \cos(\omega\tau + \varphi_{ce}) \end{aligned} \quad (6.1)$$

This method implements the f -to- $2f$ technique in the time domain, using φ_{ce} directly instead of f_{ceo} , and only a single pulse is needed to produce a spectral interferogram. Any variation of φ_{ce} causes the fringe pattern to shift, so that changes of the carrier-envelope phase can be measured by monitoring the position of the fringes for every pulse [208, 209].

Carrier-envelope phase detectors based on this technique have found widespread application, and can also be used in a feedback loop to stabilize the carrier-envelope phase at the output of chirped pulse amplifier systems [141]. However, the reliability of

this type of measurement strongly depends on the pulse-to-pulse intensity stability of the amplifier output. If intensity fluctuations exceed a few percent, amplitude-to-phase coupling effects in the continuum generation induce detrimental phase fluctuations of the produced continuum, compromising the φ_{ce} -measurement. We have constructed various implementations of the single-shot f -to- $2f$ interferometer scheme, but only a weak effect of the phase stabilization has been observed. Additional measurements using two independently generated continua confirmed that in our present NOPCPA system, the output power fluctuations of 5% already introduced ~ 0.8 rad spurious phase noise in the continuum generation process. Therefore, another phase-measurement approach is required to avoid this amplitude-to-phase coupling. A solution is given by Fourier-transform spectral interferometry, which is discussed in the next section.

6.4.2 Fourier-transform spectral interferometry

Instead of using the f -to- $2f$ approach to carrier-envelope phase measurement, an entirely different technique can be used based on linear interferometry. Such a linear measurement relies on a comparison of the pulse under investigation with a reference pulse [210, 211]. Of course, this reference pulse should then have a stable φ_{ce} . Alternatively, to characterize the phase fluctuations induced by an amplifier system, the reference pulse can be derived from the measurement pulse by putting the amplifier in one arm of a Mach-Zehnder interferometer. The input pulse is split in two pulses at the interferometer entrance: One pulse is amplified, while the other simply propagates an equal path length through free space. When these pulses are recombined and made to interfere, any phase fluctuation from the amplifier will cause a shift in the fringe pattern of the interferogram. This method can be employed with both temporal [203] and spectral interferometry [211], although the spectral variant is much easier to align and does not require scanning like the temporal interference version. This spectrally resolved method has been named Fourier-transform spectral interferometry (FTSI); the generated interferogram for this case is given by:

$$I(\omega) = |E_1(\omega)|^2 + |E_2(\omega)|^2 + 2|E_1(\omega)||E_2(\omega)| \cos(\omega\tau + \Delta\varphi_{\text{amp}} + \Delta\varphi_{\text{noise}}) \quad (6.2)$$

where τ is again the time delay between the pulses, $\Delta\varphi_{\text{amp}}$ are the phase fluctuations of introduced by the amplifier, and $\Delta\varphi_{\text{noise}}$ is the ambient phase noise caused by optical path length variations of the interferometer arms. It should be stressed that although FTSI does not provide information on the φ_{ce} -stability of the incoming pulses, it does allow a quantitative measurement of any possible phase noise introduced by any object in the measurement arm of the interferometer (which in this case is the amplifier). To get a better understanding of FTSI interferograms and φ_{ce} , a simple model is shown in Fig 6.4. Since a change in the carrier-envelope phase can be caused by a either a carrier-phase shift or an envelope shift, both possibilities need to be considered. In Fig. 6.4A it can be seen that a phase-variation between pulses induces a shift of the fringe positions in the interferogram. Fig. 6.4B demonstrates the effect of a change in group delay between the pulses while keeping the phase of the carrier wave fixed, which leads to a change of the spectral interferogram's oscillation period. In principle, both

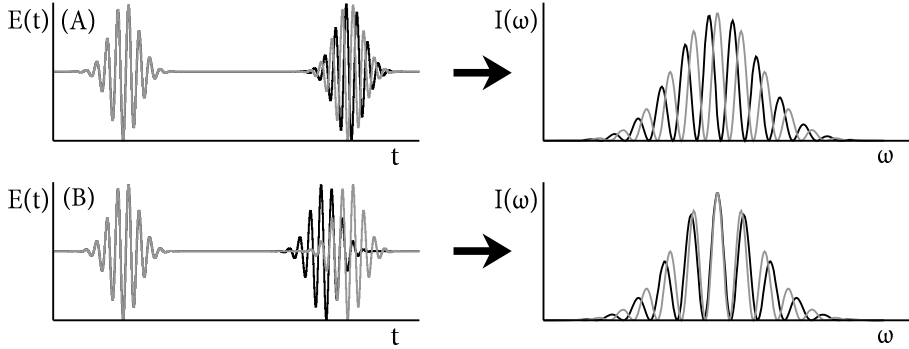


FIGURE 6.4: The effect of carrier-envelope phase variations on an FTSI interferogram. **(A)** Phase-variations between the pulses cause a shift of the fringe positions. **(B)** Group-delay-variations give rise to changes in the fringe period. In principle, a measurement of both these effects is needed for characterization of φ_{ce} (see text for details).

effects need to be measured to properly characterize φ_{ce} . However, the group velocity can be expressed in terms of the phase velocity as:

$$\begin{aligned}
 v_g &= \frac{v_\varphi}{1 - \frac{\omega}{v_\varphi} \frac{\partial v_\varphi}{\partial \omega}} \\
 &\approx v_\varphi + \omega \frac{\partial v_\varphi}{\partial \omega} + \dots
 \end{aligned} \tag{6.3}$$

From this relation it is clear that a change in group velocity is virtually impossible without an accompanying change in phase velocity: The group velocity mostly fluctuates in the same way as the phase velocity, with only small higher-order corrections. Therefore, an accurate measurement of the phase shifts by monitoring the fringe positions already suffices to characterize carrier-envelope phase fluctuations.

Obviously, to get an accurate measurement of the amplifier-induced phase noise $\Delta\varphi_{\text{amp}}$, the $\Delta\varphi_{\text{noise}}$ -term in Eq. (6.2) should be kept as stable as possible. This is not trivial, considering that the typical path length through an amplifier system can be many metres. To measure the possible phase changes of an NOPCPA system at 1 kHz repetition rate, we developed the setup shown in Fig. 6.5. In this design, a small, slightly misaligned Mach-Zehnder interferometer is used to separate the reference and measurement pulses by only a few millimetres in space, and about ~ 100 ps in time. By keeping the pulses so close together, the influence of air flow and acoustic noise will be virtually identical for both pulses, leading to a large degree of common-mode rejection. As a result, the phase noise $\Delta\varphi_{\text{noise}}$ induced between them due to such ambient noise is strongly suppressed. While such an approach would probably not work properly in standard Ti:Sapphire amplifiers it is well suited for phase measurements on NOPCPA systems, as the gain of an OPA is zero when the pump pulse does not overlap with the seed, and because collimated beams are used in the nonlinear interaction. Therefore, the slight separation between the two replica pulses already suffices to keep the refer-

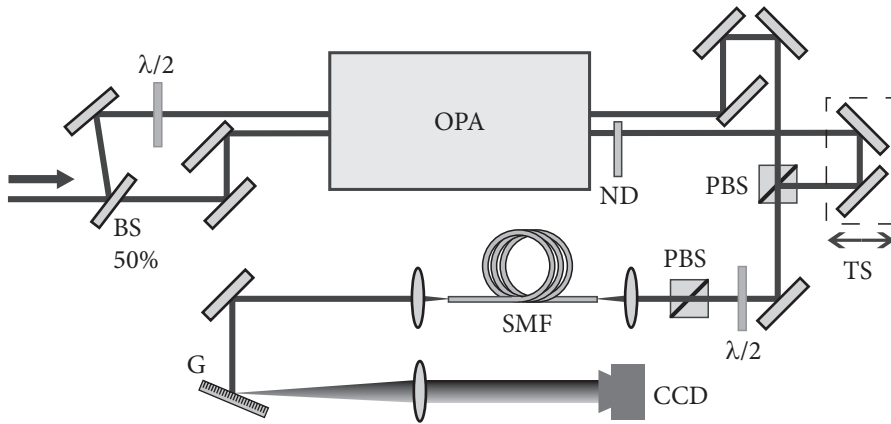


FIGURE 6.5: Fourier-transform spectral interferometry setup to measure the phase noise induced by an optical parametric amplifier (OPA). BS: beamsplitter, PBS: polarizing beamsplitter, ND: neutral-density filter, TS: translation stage, SMF: single-mode fiber, G: grating. Distances are not to scale, in reality the separation between the interferometer arms is only a few millimetres.

ence pulse from being amplified. To be even more thorough, the polarization of the reference pulse is also rotated by 90° to inhibit the phase matching that is required for amplification. Behind the amplifier, the amplified pulse and the reference are recombined, while keeping a time delay τ between them to generate the spectral interference. The relative intensities are set equal using neutral-density filters. A good spatial overlap is ensured by sending the pulses through a single-mode fiber, after which they are coupled into a simple spectrometer consisting of a grating and a curved mirror in a $2f$ -geometry, with a CCD camera in the Fourier plane.

6.4.3 Results of FTSI phase measurements

Using the setup described in the previous section and displayed in Fig. 6.5, the phase-stability of the amplification process has been investigated. Both the amplified- and the reference pulse are sent into the spectrometer, generating bright spectral fringes from which the phase jitter between the two pulses can be deduced. A typical measured interferogram with the amplifier turned on is displayed in Fig. 6.6A, while Fig. 6.6B shows an interferogram that was recorded at maximum amplification. The interferograms are averaged over 30 pulses (~ 30 ms). They have a contrast exceeding 90%, and no significant deterioration is seen when the amplifier is turned on. From this, we can conclude that on timescales shorter than 30 ms, phase jitter added by the OPA is less than 0.1 rad. Tracking the interferogram over a timescale of approximately two minutes results in traces like the one shown in Fig. 6.6C. The slow variations and drift of the signals are attributed to mechanical vibrations and environmental instabilities. From

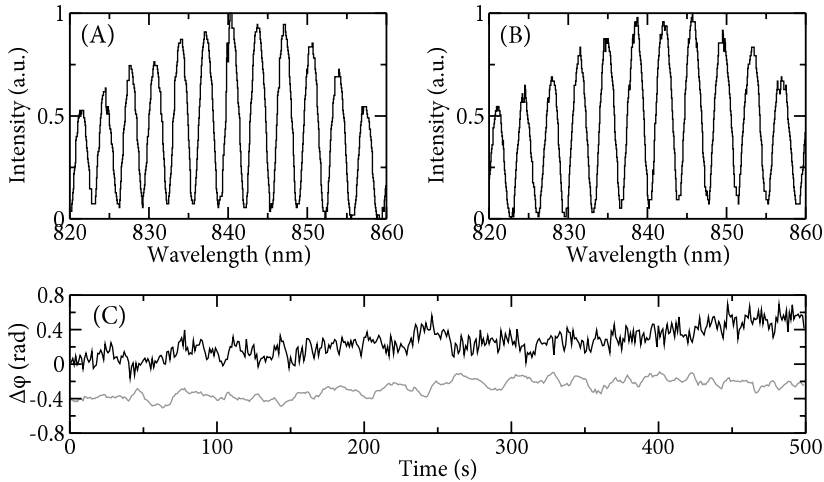


FIGURE 6.6: Phase deviations measured using a linear Fourier-transform spectral interferometer. (A) FTSI interferogram without amplification. (B) FTSI interferogram at full amplification. In both cases, the fringe contrast reaches $\sim 95\%$. (C) Measured phase variations of the interferograms in A and B as a function of time, with (black trace) and without (grey trace) amplification.

a comparison of the phase stability with and without amplification, the phase noise added by the OPA process on a timescale of seconds is found to be about ~ 0.1 rad, or $\sim 1/60^{\text{th}}$ of an optical cycle.

This phase jitter can most likely be attributed to amplitude-to-phase coupling in the OPA process. We have investigated this in more detail by introducing a modulation on the pump pulse intensity, as shown in Fig. 6.7A, while monitoring the phase using the FTSI technique. The resulting phase deviations can readily be observed in the measured signal, which is depicted in Fig. 6.7B. From these graphs we derive that a pump pulse energy modulation of 0.2 mJ induces a phase shift of about 0.7 rad. This indicates that the B-integral (see e.g. [21]) of our amplifier is relatively high, i.e. on the order of π , which corresponds fairly well with the calculated value. A NOPCPA design with a lower B-integral will therefore exhibit even better phase stability. Ross et al. suggest that the spectral phase, and hence φ_{ce} , is gain-dependent [72], which could also induce phase shifts. Calculations using the theory presented in [72] and in section 4.1.3 show that this effect is orders of magnitude smaller than the amplitude-to-phase coupling in our case.

Aside from the optical parametric amplification, an additional issue in maintaining carrier-envelope phase stability through the entire system is the pulse stretching and compression, as mentioned earlier. Recently, there has been some debate in the literature on the issue of phase-noise caused by beam-pointing fluctuations in a grating-based pulse stretching [166, 207]. Our own ray-tracing calculations predict that such effects cause less than 20 mrad of φ_{ce} -noise, but experimental confirmation is of course required. To measure the stretcher-induced phase noise, the pulse stretcher and compres-

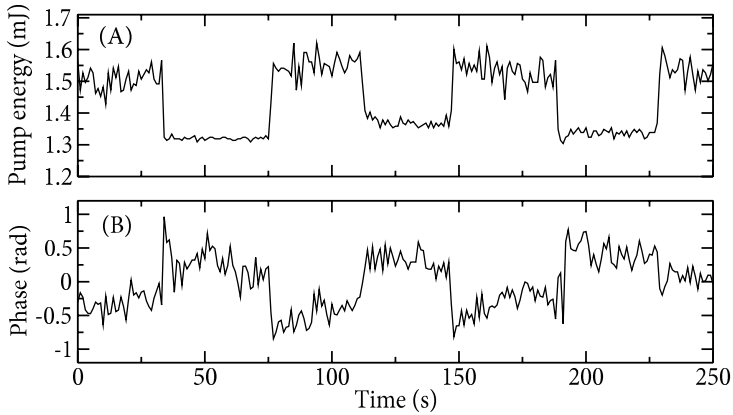


FIGURE 6.7: Amplitude-to-phase coupling in the amplification process. (A) Modulation of the pump pulse energy. (B) Resulting phase variations introduced by the amplifier, measured using FTSI.

sor are placed in one arm of a Mach-Zehnder interferometer while the reference pulse in the other arm is not chirped. The measurement setup is similar to that shown in Fig. 6.5, although the arm separation is much larger in this case, and therefore careful shielding against environmental noise is required. Also in this case, stable high-contrast spectral interference fringes are obtained. When measuring the position of these fringes while changing the input beam pointing angle, no shift was observed within the measurement sensitivity of ~ 40 mrad. Therefore, the grating-based stretching and compression system is confirmed to preserve the stability of φ_{ce} , and these findings have been confirmed by other groups [167, 168].

6.5 Conclusions

In conclusion, we have demonstrated phase-stable amplification of ultrashort laser pulses up to 0.25 mJ per pulse using an NOPCPA laser system with a Nd:YAG pump source. The amplified spectrum spans more than 174 nm FWHM, yielding an output pulse after compression of 11.8 fs and an energy of 0.12 mJ at a 1 kHz repetition rate. We have confirmed that the optical parametric amplification process preserves the carrier-envelope phase stability of the seed pulses, and only ~ 100 mrad of amplifier-induced phase noise has been observed. In addition, the grating-based pulse stretcher and compressor are found to maintain carrier-envelope phase stability.

The combination of a Nd:YAG-based pump laser for the NOPCPA and grating-based stretching and compression shows great potential to replace traditional Ti:Sapphire-based systems to obtain phase-stable terawatt peak power pulses with a duration of 10 fs or less.

CHAPTER 7

GENERATION OF FEW-CYCLE TERAWATT LIGHT PULSES USING OPTICAL PARAMETRIC CHIRPED PULSE AMPLIFICATION

We demonstrate the generation of 9.8 ± 0.3 fs laser pulses with a peak power exceeding one terawatt at 30 Hz repetition rate, using optical parametric chirped pulse amplification. The amplifier is pumped by 140 mJ, 60 ps pulses at 532 nm, and amplifies seed pulses from a Ti:Sapphire oscillator to 23 mJ per pulse, resulting in 10.5 mJ per pulse after compression while amplified fluorescence is kept below 1%. We employ grating-based stretching and compression in combination with an LCD phase-shaper, allowing compression close to the Fourier limit of 9.3 fs.

7.1 Introduction

The study of strong-field laser-matter interactions is a rapidly advancing branch of physics [117]. Progress in topics such as high-harmonic generation and quantum coherent control have led, for example, to the rise of attosecond science [212], laser-based particle acceleration, and laser-assisted nuclear fusion [35]. Since some of these applications require extreme peak power delivered in as short a time span as possible, considerable effort is spent to push the limits in attainable pulse duration and peak intensity.

The current state-of-the-art in peak power consists of huge Nd:Glass-based facilities capable of generating petawatt pulses of ~ 400 fs duration [27–29], and Ti:Sapphire systems which have been demonstrated to produce 0.85 PW in 33 fs pulses [30]. The shortest pulses to date have been generated using noncollinear optical parametric amplifiers (NOPAs) pumped by frequency-doubled Ti:Sapphire amplifiers [67], and through self-phase-modulation of amplified Ti:Sapphire pulses in gas-filled hollow fibers [204]. Both techniques have produced 4 fs pulses at a peak intensity of ~ 1 GW for NOPAs, and up to ~ 100 GW for hollow fibers. However, scaling to higher power is very complicated with such systems.

Present-day high power table-top laser systems mostly rely on Ti:Sapphire as an amplifier medium, and several terawatt-class laser systems have been demonstrated [213–

216]. However, these systems become increasingly complex when aiming for shorter and more intense pulses, as the thermal load on the amplifiers causes wavefront distortions and thermal lensing. Compensation of such effects is only possible with carefully designed optical systems, or cryogenic cooling of the Ti:Sapphire crystals. Also, powerful Ti:Sapphire systems usually require multiple amplification stages (typically a regenerative amplifier and one or more multipass amplifiers), as many passes through the amplification medium are necessary.

In addition, the production of few-cycle pulses is very difficult with Ti:Sapphire amplifiers due to spectral gain narrowing. Elaborate techniques are required to maintain a large bandwidth after amplification, such as spectral broadening in gas-filled hollow fibers between consecutive stages of a Ti:Sapphire amplifier chain [205].

7.2 Optical parametric chirped pulse amplification

An alternative to Ti:Sapphire amplification that is very promising for the production of high power few-cycle laser pulses is optical parametric chirped pulse amplification (OPCPA) [70]. Multi-TW OPCPA systems producing pulses much longer than 100 fs have been demonstrated using Nd:Glass pump lasers [73, 75], and progress towards petawatt powers and beyond is already quite far [71, 72]. At the same time, noncollinear OPCPA (NOPCPA) can have this large gain over a bandwidth supporting sub-10-fs laser pulses [72, 161]. Combined with the absence of significant thermal aberrations, this paves the way for few-cycle pulses with multi-TW peak power.

In the previous chapter, we showed the feasibility of this concept by demonstrating phase-controlled amplification of 11.8 fs pulses to 0.1 mJ energy at a repetition rate of 1 kHz, using a Ti:Sapphire seed laser and a frequency-doubled Nd:YAG pump laser [113]. Ishii et al. [217] performed parametric amplification of 10 fs pulses to 5 mJ at 20 Hz rep. rate. In this chapter we report on the amplification of pulses to 23 mJ at 30 Hz, resulting in 9.8 fs pulses with a peak power exceeding 1.0 TW after compression. These pulses contain little amplified superfluorescence, and have been compressed to within 6% of the Fourier limit using adaptive spectral phase shaping.

7.3 NOPCPA setup

A schematic of our amplifier system is shown in Fig. 7.1. The seed source is a Kerr-lens modelocked Ti:Sapphire oscillator (Femtosource Scientific Pro), delivering 11 fs, 8 nJ pulses at 75 MHz repetition rate. These pulses are stretched to 10 ps full width at half-maximum (FWHM) in a grating-based pulse stretcher (600 lines/mm gold coated gratings), in which a 640-element LCD phase-only spectral shaper (Jenoptik) is incorporated for high-resolution spectral phase control.

As a pump laser source for the NOPCPA, we have constructed a Nd:YAG laser system capable of producing 220 mJ, 60 ps pulses at 1064 nm, with a repetition rate of 30 Hz. It is seeded by a SESAM modelocked 7 ps Nd:YVO₄ laser (High-Q Laser GmbH), synchronized to the Ti:Sapphire laser with a timing jitter of <100 fs. The delay between pump and seed pulses can be adjusted roughly using an electronic phase

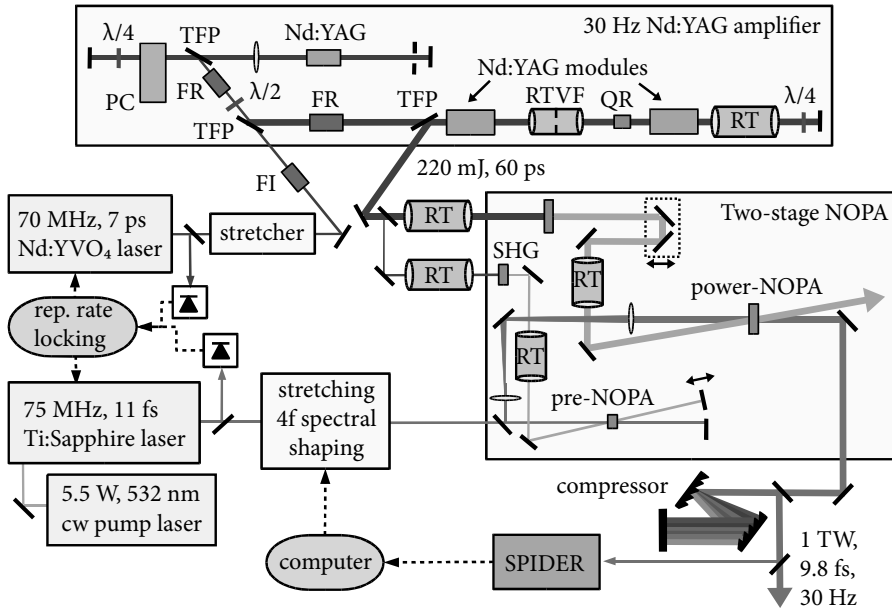


FIGURE 7.1: The terawatt 10 fs NOPCPA setup. Relay imaging is employed from the Nd:YAG amplifier to the SHG crystals, and from there to the OPA-stages (RT, relay imaging telescope; RTVF, relay imaging telescope with vacuum spatial filter). The various parts of the setup are explained in detail in the text. NOPA, noncollinear optical parametric amplifier; FI, Faraday isolator; TFP, thin-film polarizer; QR, quartz rotator; PC, Pockels cell; FR, Faraday rotator. In the two-stage NOPA setup, only reflective optics are used; the lenses drawn represent mirrors.

shifter in the feedback loop of the Ti:Sapphire laser, and fine-tuned with a translation stage in the seed beam [113].

This Nd:YVO₄ laser emits 50 nJ pulses, which are first stretched in time by clipping the spectrum in a zero-dispersion 4f-setup to ensure a pulse duration larger than 60 ps. These pulses are amplified to 1.5 mJ in a diode-pumped Nd:YAG regenerative amplifier. The regenerative amplifier output beam is expanded to 11 mm, and is further amplified to 220 mJ per pulse in a double-pass post-amplifier, based on two flashlamp-pumped 12 mm diameter Nd:YAG rods (EKSPILA Ltd.). These rods are relay imaged onto each other, and the polarization state is rotated between the rods by a 90° quartz rotator to compensate for thermally induced birefringence. The relay image telescope contains a vacuum spatial filter to preserve beam quality. The seed pulses are stretched to only 1/6th of the pump pulse duration, to ensure that the low intensity outer edges of the spectrum still experience a high gain. Gain saturation is then expected to result in a 30 ps flat-top temporal profile, thereby increasing the energy extraction efficiency.

A small part of the 1064 nm light is split off to a SHG crystal (KTP, type-II), where 10 mJ of 532 nm light is generated to pump the first stage of the NOPCPA. It consists of a 5 mm long BBO crystal ($\theta = 22.5^\circ$, $\phi = 0^\circ$, type-I phase matching). Both pump and

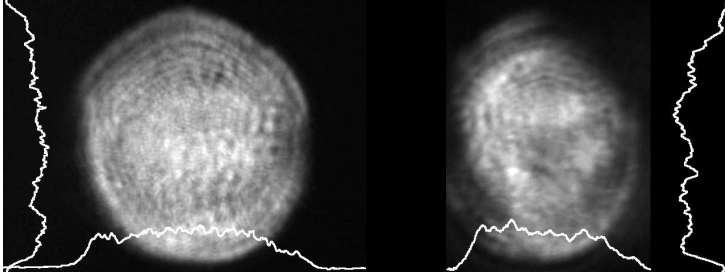


FIGURE 7.2: Beam profile images of the relay-imaged 140 mJ pump beam at the power amplifier (left) and the 10.5 mJ OPA output beam (right). The latter is slightly cut off on the left due to spatial constraints in setting up the relay imaging, without excluding any important features.

seed beam have a diameter of 1.5 mm inside the crystal, with an internal noncollinear angle between them of around 2.38° . The beams are reflected back through the crystal for a second amplification pass. As the gain is highest in this pre-amplifier ($10^3 - 10^4$ small-signal gain per pass), any residual phase mismatch may lead to narrowing of the spectral gain bandwidth. Therefore, the second pass is aligned at a slightly different angle to broaden the amplified spectrum. This pre-amplifier stage increases the pulse energy from 1.5 nJ to a few tenths of a mJ.

The main part of the 1064 nm pump light is passed to another SHG crystal (BBO type-I, 3 mm long, 14 mm diameter), where 140 mJ per pulse at 532 nm is generated. The output of the pre-amplifier is expanded to match the 10 mm diameter pump beam and overlapped with it in a second BBO crystal (5 mm long, 14 mm diameter, same angles as the first NOPCPA crystal). This power-amplifier stage boosts the pulse energy to typically 23 mJ per pulse at 140 mJ pump energy, with less than 1% amplified superfluorescence. A maximum energy of 30 mJ per pulse has been generated with this system, but only with increased amounts of superfluorescence (estimated 6% at 30 mJ), and reduced stability.

After the post-amplifier, the transverse beam profile resembles a top-hat distribution. Relay-imaging has therefore been applied from the post-amplifier to the respective SHG stages, and from there to the OPA crystals. CCD camera images of the pump and amplified signal beam profiles at the power amplifier stage are shown in Fig. 7.2. Due to gain saturation, the beam profile of the amplified signal resembles that of the pump beam. A check for the presence of angular chirp has been performed by scanning a fiber-coupled optical spectrum analyzer across the far-field beam profile, and no position-dependent spectral distribution was detected.

The amount of amplified superfluorescence has been determined by monitoring the fluorescence power in a spectral region around 1000 nm, where the seed pulse has zero spectral intensity. At this wavelength the fluorescence intensity is seen to decrease when seed light is added, as the pump power density is lowered due to gain depletion by the amplified seed pulses. In combination with a measurement of the NOPCPA output

power with and without seeding, the remaining amount of superfluorescence in the presence of seed light can be estimated to be less than $\sim 1\%$ of the total output power.

After amplification the beam is expanded to 13 mm diameter and the pulses are compressed by a grating compressor (1200 lines/mm, 18 mm grating separation). The angles and grating constants of the stretcher and compressor are chosen such that dispersion compensation is achieved up to third order. The compressor has an efficiency of 46%, resulting in recompressed pulses with an energy of 10.5 mJ. To characterize the compressed output pulse, we employ spectral phase interferometry for direct electric field reconstruction (SPIDER) [195]. The measured spectral phase is used as a feedback signal in an optimization loop with the LCD shaper, yielding pulses with a FWHM duration of 9.8 ± 0.3 fs, which is within 6% of the Fourier limit of 9.3 fs. The peak power of the pulses then exceeds 1 TW. The spectra of the input seed and amplified output and the compensated spectral phase, as well as the temporal pulse structure and phase are shown in Fig. 7.3. Considerable reshaping of the spectrum in the amplifier is immediately apparent. Phase mismatching suppresses amplification below 720 nm, while the high gain towards longer wavelengths amplifies even the very weak edge of the spectrum to a sizeable intensity. The spectral phase shows the effects of residual higher order dispersion at the long wavelength side of the spectrum, which could not be completely compensated due to an insufficient shaper resolution (Nyquist limitation). The measured pulse-to-pulse output power fluctuations are about 5% for the NOPCPA, and 3% for the pump laser. An upper limit for possible beam pointing variations is determined to be $50 \mu\text{rad}$ half-angle.

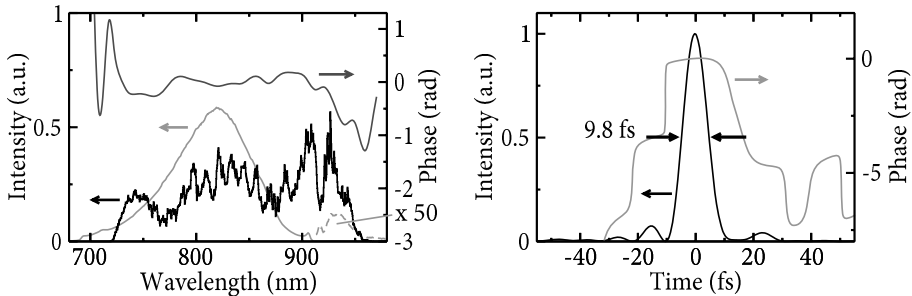


FIGURE 7.3: Left: Spectra of the input seed pulses (grey curve), and the OPCPA output pulses after compression (black curve). The slow modulation results from phase-matching effects in the power-amplifier, while the faster modulation is presumably caused by a synchronization artefact of the scanning spectrum analyzer used for this measurement. Dashed grey curve: seed spectrum 50 times enlarged for clarity. Dark grey curve: spectral phase of the compressed output pulses measured using SPIDER. The deviation from zero at wavelengths longer than 900 nm is caused by limitations of the shaper, see text. Right: Temporal profile of the compressed output pulse (black curve) and temporal phase (grey curve).

7.4 Discussion and outlook

The NOPCPA system described here displays several interesting features. For example, the setup is remarkably compact: the total path length from the Ti:Sapphire seed oscillator to the compressor output can be kept well below 10 metres, and the pulses only pass through 2 cm of material in total. This is mostly due to the high single-pass gain of the NOPCPA stages. Also, the modest stretching ratio employed ($\sim 10^3$) allows the stretcher and compressor to be compact, especially considering that the shaper is integrated in the stretcher. Hence, the seed beam is minimally disturbed (the B-integral of the entire NOPCPA system is calculated to be less than 1), which is beneficial for applications where carrier-envelope phase stability of the amplified pulses is required [141]. The parametric amplification process has already been demonstrated to preserve the phase of the seed pulses [113, 206], and the grating-based stretching and compression is known to be phase-stable as well [113, 167]. Furthermore, the broad gain bandwidth facilitates amplification of sub-10 fs pulses without the need for spectral broadening through self-phase-modulation in gas-filled hollow fibers, making the system more robust, less sensitive to alignment, and better scalable to higher power.

The system described here can be upgraded to deliver >2 TW just by employing negative dispersion stretching and high-throughput bulk glass compression [172, 217]. When using a seed oscillator with a broader spectral bandwidth, pulses shorter than 7 fs should be feasible [72, 161]. Therefore, although the pump laser requires more effort compared to Ti:Sapphire amplifiers due to the high peak power and the need for careful synchronization, a NOPCPA system like the one presented in this paper is very well suited for the amplification of few-cycle laser pulses with a stabilized carrier-envelope phase to the terawatt level and beyond.

7.5 Conclusion

In conclusion, we have demonstrated the production of sub-10 fs pulses with a peak power exceeding one terawatt. The system is remarkably compact due to the high parametric gain and the small stretching-ratio, and produces only low levels of amplified superfluorescence. The pulses are compressed to within 6% of the Fourier limit with good spatial quality. Thermal effects in the amplifier medium are negligible, and do not limit the achievable peak power and repetition rate. With a suitable pump laser, the amplification of few-cycle pulses to multi-terawatt or even petawatt peak powers using NOPCPA seems feasible.

CHAPTER 8

A SOURCE OF 2 TERAWATT, 2.7 CYCLE LASER PULSES BASED ON NONCOLLINEAR OPTICAL PARAMETRIC CHIRPED PULSE AMPLIFICATION

We demonstrate a noncollinear optical parametric chirped pulse amplifier system that produces 7.6 fs pulses with a peak power of 2 terawatt at 30 Hz repetition rate. Using an ultra-broadband Ti:Sapphire seed oscillator and grating-based stretching and compression combined with an LCD phase-shaper, we amplify a 310 nm wide spectrum with a total gain of 3×10^7 , and compress it within 5% of its Fourier limit. The total integrated parametric fluorescence is kept below 0.2%, leading to a pre-pulse contrast of 2×10^{-8} on picosecond timescales.

This system represents a fully operational amplifier system that has been designed to test the limits of NOPCPA. We approach the theoretically predicted spectral bandwidths very closely, and also the energy extraction efficiency corresponds to the expected value. In addition, adaptive spectral phase compensation, pulse contrast and beam profile are of high quality, while the total amplifier system is kept very compact compared to traditional Ti:Sapphire amplifier systems.

8.1 Introduction

The generation of high-intensity few-cycle laser pulses is a subject of great interest [117], as experimental progress in fields such as attosecond science [218] and quantum control [219] is for a large part dependent on the availability of suitable laser sources. In recent years, optical parametric chirped pulse amplification (OPCPA) [70, 71] has been demonstrated to be a very promising technique for the production of ultrashort, high-intensity laser pulses [73, 78]. Especially the development of OPCPA in a noncollinear geometry (NOPCPA) has facilitated the amplification of ultra-broadband spectra both in the Ti:Sapphire wavelength range [79, 113, 217] and at longer wavelengths [220, 221].

In this paper we present an NOPCPA system that produces 2 terawatt (TW) peak intensity laser pulses with a duration of 2.7 optical cycles (7.6 fs). The system utilizes

the full >300 nm gain bandwidth that has been theoretically predicted for a 532 nm pumped NOPCPA system [72, 161] based on BBO crystals, while maintaining spectral phase control over this entire bandwidth. State-of-the-art few-cycle laser sources can deliver sub-3-cycle pulses with an intensity reaching 0.2 TW [222–224]; therefore, our system represents an order of magnitude increase in peak intensity in sub-3-cycle pulse generation, with excellent prospects for further power scaling.

8.2 Ultra-broadband two terawatt NOPCPA system

As parametric amplification is an instantaneous nonlinear optical process, efficient amplification can only be achieved by matching the duration of pump and seed pulses. In OPCPA, an ultrashort, broadband seed pulse is stretched to match its duration to a long, high-energy pump pulse from e.g. a Nd:YAG laser system. Energy transfer and subsequent recompression of the amplified seed pulse then leads to the production of ultrashort high-energy pulses. Specifically, a combination of BBO as the nonlinear medium, a pump wavelength around 532 nm, and a small noncollinear angle ($\sim 2.4^\circ$) leads to an extremely broad gain bandwidth in the near-infrared, potentially supporting the amplification of 7 fs pulses from a Ti:Sapphire laser [71]. An additional advantage of optical parametric amplification is that the single-pass gain can exceed 10^3 , allowing large amplification factors to be achieved in a very compact setup.

We have designed a laser amplifier system that exploits these benefits of NOPCPA to generate terawatt-level few-cycle pulses. Key elements of this system are: 1) A compact, three-pass amplifier with a gain of 3×10^7 ; 2) A stretcher-compressor combination capable of accurate spectral phase compensation over a >300 nm bandwidth; 3) A pump pulse duration in the 10–100 ps range and hence a moderate stretching ratio ($\sim 10^3$); 4) Pump-seed synchronization with sub-picosecond accuracy. All these features are implemented in the setup shown in Fig. 8.1.

The seed laser is a home-built ultra-broadband Ti:Sapphire oscillator, which produces 5.5 nJ pulses at 75 MHz repetition rate, with a spectrum that has a Fourier limit of 6.2 fs. All cavity mirrors have a broadband multilayer coating (Layertec) with negative GVD ranging from -50 to -70 fs². In combination with the dispersion due to a 1 mm fused silica plate, two thin fused silica wedges and the 2.5 mm optical path length Ti:Sapphire crystal, this yields compensation of the dispersion from roughly 670 to 950 nm. The repetition rate of this oscillator is locked to the signal of a 75 MHz RF generator using a piezo-mounted mirror in the laser cavity. For increased stability, we employ an additional lock at the 140th harmonic (10.5 GHz) of the repetition rate, which is generated in a fast photodiode. The seed pulses are stretched to about 13 ps using a grating-based pulse stretcher, in which a 640-element LCD phase-only spatial light modulator (Jenoptik) is incorporated for high-resolution spectral phase control. From the available seed light, 4 nJ pulses are sent into the stretcher, which has a transmission of 25%. A more detailed discussion of pulse stretching and compression is given in section 8.3.

The pump laser source is based on amplification of pulses from a SESAM mode-locked 70 MHz Nd:YVO₄ oscillator (High-Q Laser GmbH). This laser is synchronized

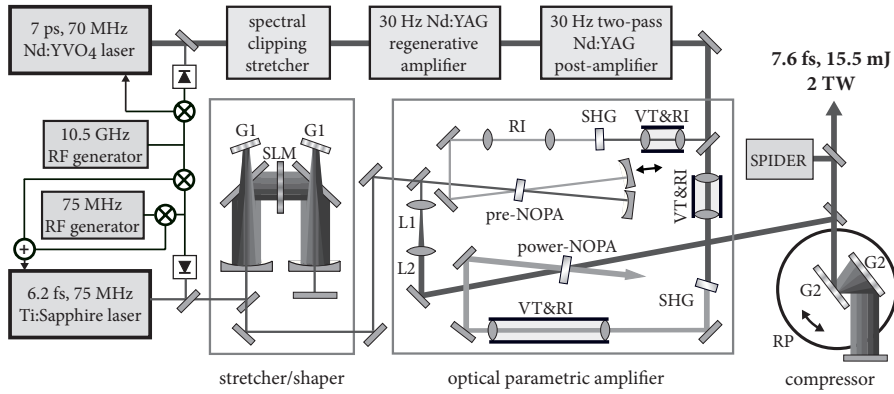


FIGURE 8.1: Schematic of the 2 TW, 7.6 fs NOPCPA system. NOPA: noncollinear optical parametric amplifier, G1: 600 lines/mm grating, G2: 1200 lines/mm grating, SLM: 640-element LCD spatial light modulator, VT: vacuum tube, RI: relay-imaging, RP: rotatable platform, SHG: crystal for second harmonic generation. The lenses L1 and L2 are drawn for simplicity, in practice only reflective optics are used in the seed beam path. See text for further details.

to the Ti:Sapphire oscillator by locking the 150th harmonic of its repetition frequency to the same 10.5 GHz RF generator that is used for the Ti:Sapphire laser stabilization. Such a locking scheme ensures that every 14th pulse from the Nd:YVO₄ laser (corresponding to a 200 ns delay) overlaps with every 15th Ti:Sapphire laser pulse. At the lower repetition rate of an amplifier system (30 Hz in the present case) this then leads to properly synchronized pulses, provided the amplifier pulse repetition period is an integer multiple of the aforementioned 200 ns time delay.

The pulses from the Nd:YVO₄ oscillator are first stretched to 60 ps in time to allow amplification to higher energy without damaging optics. This is done by dispersing the spectrum of the pulses in a $4f$ -setup and cutting away a large part of the spectrum with a slit in the Fourier plane. The 60 ps pulses are then amplified to the mJ level in a diode-pumped Nd:YAG regenerative amplifier. The regenerative amplifier causes some reshaping of the pump pulse, as it operates at a power level where the effects of self-phase-modulation and self-compression start to become appreciable. To limit the influence of these effects the regenerative amplifier is not operated at full saturation (see section 5.2.2). From an autocorrelation measurement, we confirmed that the pump pulse has a smooth shape without significant pre- or postpulses. Further amplification up to 250 mJ per pulse at 30 Hz repetition rate is achieved with a double-pass post-amplifier containing two flashlamp-pumped Nd:YAG modules (EKSPLA Ltd.) in a ring geometry. After second harmonic generation (SHG), up to 160 mJ per pulse is produced at 532 nm. This pump laser system will be explained in detail in a future paper. The difference in pulse duration between pump and seed (60 ps vs. 13 ps) is chosen such that the pump intensity variation is relatively small across the entire chirped seed pulse. Consequently, all spectral components in the seed pulse experience similar gain,

which improves the width of the amplified spectrum. As the wings of the seed spectrum extend considerably beyond the 13 ps FWHM duration of the stretched seed pulse, saturation in the last pass still ensures a good energy extraction efficiency [79].

The actual NOPCPA system consists of only three amplification passes: two in a pre-amplifier pumped by 10 mJ 532 nm pulses, and a final pass through a power-amplifier crystal pumped by 150 mJ of pump light. The pre-amplifier contains a 5.5 mm long BBO crystal ($\theta = 22.5^\circ$, $\phi = 0^\circ$, type-I phase matching) as the gain medium. Both pump and seed beam are collimated to a 1.5 mm diameter, and intersect with a non-collinear angle of about 2.4° inside the crystal. The noncollinear angles in the two passes through the pre-amplifier are aligned slightly differently to optimize the output spectral bandwidth. The pre-amplifier increases the energy of the seed pulses from 1 nJ to about 0.5 mJ.

After the pre-amplifier, the beam is expanded to 10 mm diameter by a telescope, and amplified to 30 mJ per pulse in a single pass through the power-amplifier stage. This power-amplifier has a 5 mm long, 14 mm \times 14 mm BBO crystal (phase-matching angles identical to the pre-amplifier crystal) as the gain medium. Similar to the pre-amplifier, the noncollinear angle is near 2.4° , and optimized by maximizing the amplified bandwidth.

As the transverse beam profile of the pump laser has a top-hat distribution, relay-imaging is applied between the final Nd:YAG amplifier rod in the pump laser and the SHG crystals, as well as between the SHG crystals and the respective OPA amplifier stages. The relay-imaging ensures a good-quality pump beam profile in the OPA crystals. This is of paramount importance for proper NOPCPA operation as gain, pulse

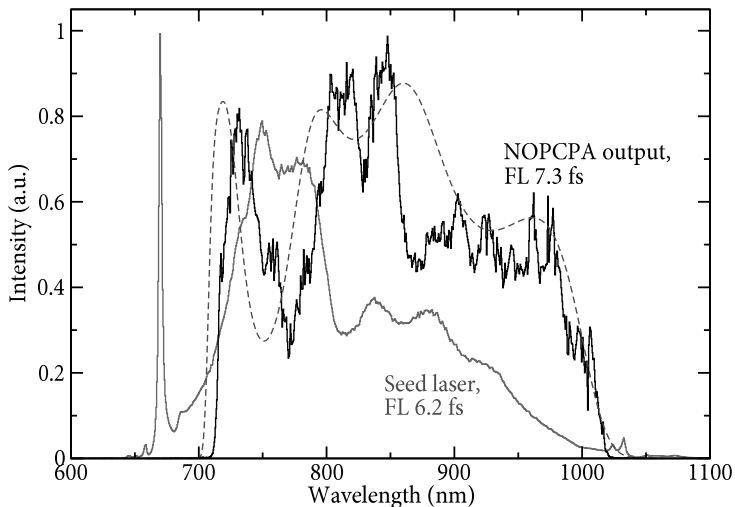


FIGURE 8.2: The oscillator spectrum (black curve), and the NOPCPA output after amplification to 30 mJ per pulse and subsequent pulse compression (grey curve). The dashed grey line is the result of a numerical simulation (see chapter 4 for details). FL: Fourier limit.

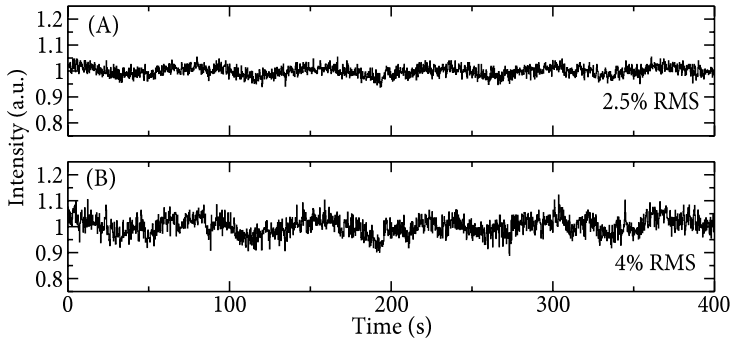


FIGURE 8.3: (A) Measured intensity stability of the pump laser. (B) Simultaneously measured intensity stability of the NOPCPA output pulses.

contrast and beam profile of the amplified seed beam are all strongly affected by the pump beam profile. Where needed, the focus that occurs in the Fourier plane of the relay-imaging systems has been placed in a vacuum tube to prevent optical breakdown and self-phase-modulation in air.

Fig. 8.2 displays a typical spectrum of the oscillator output, and one of the amplified and recompressed pulses after the full NOPCPA system. The part of the oscillator spectrum below 700 nm is actually not transmitted by the stretcher; as the phase mismatch of the parametric amplification process becomes too high for wavelengths below 710 nm to have any significant gain, the stretcher has been designed for spectra between 700 nm and 1100 nm. Fig. 8.2 clearly shows the rectangular spectral shape characteristic of a saturated NOPCPA, and the amplified spectrum extends from about 710 nm to 1020 nm. The width of the generated spectrum is very close to the theoretically predicted limit for an NOPCPA system based on 5 mm long BBO crystals and a pump wavelength of 532 nm [71, 72, 161]. The Fourier limit of the NOPCPA output is 7.3 fs FWHM, which corresponds to a 2.5 cycle pulse at a carrier wavelength of 850 nm. The dashed grey line in Fig. 8.2 is the amplified bandwidth predicted by the numerical model discussed in chapter 4, when using typical experimental parameters of this particular NOPCPA setup as input (the noncollinear angle is taken to be 2.31° in all three passes). This model pulse has a Fourier limit of 7.1 fs, and the experimental observations is in good agreement with this numerically predicted spectrum (see section 4.2 for a more detailed discussion on the numerical modeling).

The intensity stability of the OPA output is measured to be 4% RMS, which is mainly the result of the 2.5% RMS fluctuations of the pump intensity. A typical intensity measurement is shown in Fig. 8.3, showing the intensity variation over several minutes. In this graph a slow oscillation can be seen, which is due to temperature fluctuations in the cooling water of the regenerative amplifier. This influences the efficiency of the laser diodes, which in turn has an effect on the pump laser output power since the regenerative amplifier is not operated in saturation.

While the initial beam profile of the Ti:Sapphire oscillator output is Gaussian, the

beam profile of the amplified NOPCPA output (Fig. 8.4B) adopts the top-hat shape of the pump laser (Fig. 8.4A) due to saturation. To investigate the possibility of spatial chirp in the amplified beam, we measured the spectrum in various parts of the beam using a fiber-coupled spectrometer. Although some spectral variations across the beam have been observed, no systematic spatial chirp is detected. Additional information has been obtained by recording the beam profile with various interference filters in the beam (see Fig. 8.4C). These pictures show some variations, mostly in the regions of low spectral amplitude. This structure is attributed to the wavelength dependent phase matching and sensitivity to perturbations in the pump beam wavefront, leading to some differences in gain and saturation. As was noted in chapter 4, the saturation in NOPCPA can be wavelength-dependent due to the instantaneous nature of the process. The beam profiles depicted in Fig. 8.4 provide evidence that this is indeed the case: For instance, note that the beam profile at the highest intensity regions bears the profile at the highest intensity regions bears the most resemblance to the pump beam, while at spectral regions of lower intensity the beam profile still has a more Gaussian shape. In addition, the low-intensity parts of the spectrum have a more irregular, structured beam profile, which corresponds to a situation where the gain is still large. In any case, the total beam profile that results from the coherent addition of all these spectral components is of good quality (Fig. 8.4B), and is suitable for the production of extremely high power densities in a small focal spot.

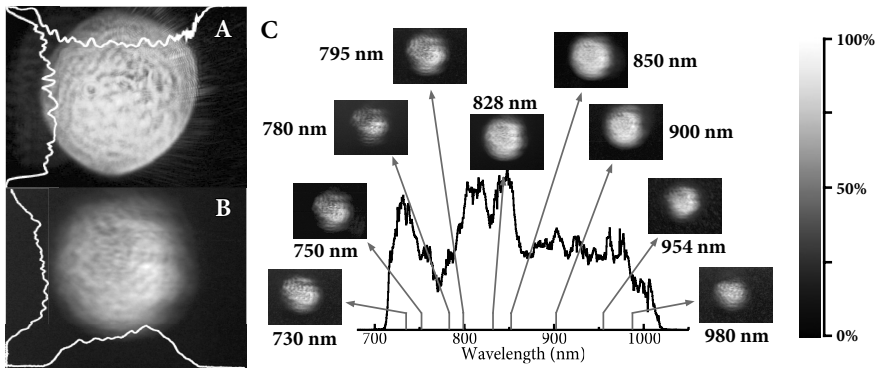


FIGURE 8.4: (A) Beam profile of the pump laser in the power-amplifier stage. (B) Beam profile of the amplified OPA output beam in the power-amplifier stage. (C) Measured beam profile of the OPA output for various parts of the spectrum. All pictures were taken by relay-imaging the beam in the power-amplifier crystal onto a CCD camera. The white traces in A and B represent the beam profile across the center of the respective beams, averaged over 10 rows (or columns) of pixels.

8.3 Spectral phase shaping and few-cycle pulse compression

The stretching and recompression needed for chirped pulse amplification can present serious problems when few-cycle pulses are involved, due to the large bandwidth over which the dispersion needs to be compensated with high accuracy. To date, mJ-level

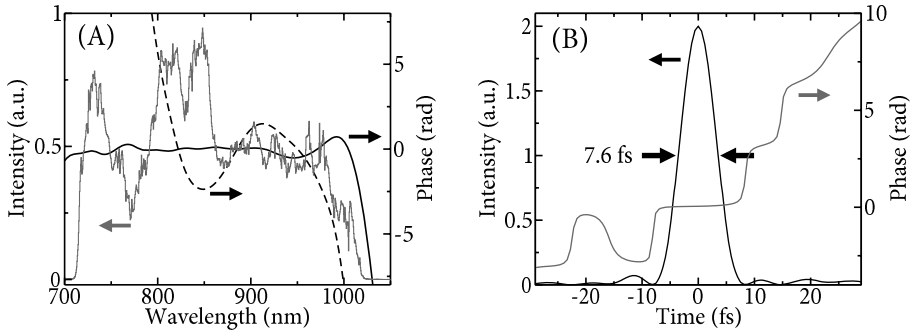


FIGURE 8.5: (A) The spectral intensity (grey curve), and spectral phase before (dashed black curve) and after (straight black curve) adaptive pulse compression with the spatial light modulator. These spectral phase curves have been measured using SPIDER. (B) The reconstructed pulse intensity (black) and phase (grey) in the time domain.

few-cycle pulse sources all employ the output pulses of a relatively narrow-band chirped pulse amplifier, which are spectrally broadened in a nonlinear medium [222–224]. Such pulses require only a minor amount of chirp compensation that can readily be provided by chirped mirrors. Full chirped pulse amplification and recompression for a broad bandwidth with a large stretching ratio has - to the best of our knowledge - not been demonstrated so far for sub-10 fs pulses, although Takada et al. have reported on a stretcher-compressor system for 8 fs pulses, which they employed in the compression of terawatt-level pulses to 12 fs [225].

The options for broadband stretching and compression are limited. For instance, prism compressors would become impractically large for such broad spectra, even when multiple prism sequences are used. Negative dispersion stretching and subsequent bulk glass compression may be applicable to few-cycle pulses [217], and has the advantage of a high compressor efficiency. However, the extreme power densities of a terawatt-class amplifier can easily lead to self-phase-modulation in the bulk material, or distortion of the wavefront due to glass inhomogeneities when larger beam diameters are used. Instead, we have implemented a grating-based stretcher and compressor system. Although the throughput is typically limited to $\sim 50\%$ (after four grating bounces), such a system can be realized in a much smaller setup with only reflective optics.

We have designed a grating stretcher and compressor combination for 400 nm wide spectra that can compensate dispersion up to third order. This is facilitated by different groove densities (600 lines/mm in the stretcher, 1200 lines/mm in the compressor), and by putting the compressor grating pair on a rotatable platform, such that the input angle on the gratings can be tuned (thereby varying the ratio between the different dispersion orders) without affecting the overall alignment. The latter is possible due to the small stretching ratio required for NOPCPA, leading to a very compact compressor with a grating separation of only ~ 20 mm. To counteract higher-order dispersion, a 640-element LCD spatial light modulator (SLM) is incorporated in the Fourier plane of the pulse stretcher, allowing adaptive control over the spectral phase.

The stretcher and BBO crystals together yield a dispersion of $6.3 \times 10^4 \text{ fs}^2$, $-9.54 \times 10^4 \text{ fs}^3$ and $1.88 \times 10^5 \text{ fs}^4$ for the second, third and fourth order dispersion, respectively. Throughout the entire setup we have only used gold-coated mirrors, which have a negligible contribution to the dispersion. The dispersion of air is not taken into account, as the total beam path from oscillator to compressor output is only 13 meters. The compressor can be tuned to compensate the second and third order dispersion, so that a residual fourth order dispersion of about $4.0 \times 10^4 \text{ fs}^4$ remains. Considering the spectral bandwidth of the pulses and the Nyquist limit of the SLM, we calculate that up to $5.34 \times 10^4 \text{ fs}^4$ can be compensated by adaptive phase-shaping. In practice, the requirements on the SLM are eased by partially canceling the excess higher-order phase deviations through over-compensation of the lower-order phase terms. This is done by aligning the compressor while monitoring the spectral phase in real-time using SPIDER [195] such that the residual phase excursions are well within the range of the SLM across the entire spectrum.

The results of the adaptive pulse compression are shown in Fig. 8.5A. Initially, the spectral phase after compression shows deviations ranging from 55 rad at 710 nm to -20 rad at 1020 nm. After adaptive phase shaping with the SLM, the measured residual spectral phase remains within 0.6 rad between 710 and 930 nm, while only above 1000 nm it exceeds 1 rad. The resulting intensity and phase in the time domain are depicted in Fig. 8.5B. The FWHM pulse duration is 7.6 fs, which is within 5% of the 7.3 fs Fourier limit. Some minor pre- and postpulses around ± 11 fs are observed, which are caused by a combination of the residual spectral phase and the rectangular shape of the spectrum. Due to the 52% compressor efficiency, the pulse energy after compression is reduced to 15.5 mJ. This corresponds to pulses with a duration of only 2.7 optical cycles and a peak intensity of 2 TW.

8.4 Pulse contrast measurements

An important issue in NOPCPA is the amount of parametric fluorescence that is generated in the various amplifier stages. To perform experiments on laser-matter interaction at high field strengths, the contrast between the pulse and this fluorescence background becomes an important factor. As an example, note that a typical atomic gas can be significantly ionized by a pulse with an intensity of $\sim 10^{10} \text{ W/cm}^2$. Therefore, if one wants to perform reliable experiments at 10^{18} W/cm^2 , any prepulse or fluorescence pedestal should be suppressed by $> 10^8$ to prevent this prepulse from influencing the system under study. Especially fluorescence from the first pass (where the gain is highest) can be amplified in subsequent passes to form a significant fraction of the total OPA output, limiting the attainable pulse contrast. In our present amplifier system, we made an initial measurement of the amplified fluorescence by blocking the seed light, in which case 0.3% of the total amplified pulse energy remains. However, as the presence of the seed beam will decrease the gain for the fluorescence, the total integrated fluorescence will be less under normal operating conditions. This difference can be determined by cutting away part of the seed spectrum in the grating stretcher, and monitoring the idler wavelength that corresponds to this “missing” signal spec-

trum. An increase in the intensity of this particular idler wavelength is then observed when the seed beam is blocked. From these combined measurements, a total integrated fluorescence of 0.2% in the presence of seed light is deduced.

More detailed information on the parametric fluorescence background can be obtained from a high-dynamic-range autocorrelation measurement. However, such a measurement of the pulse contrast is not trivial when compressed few-cycle pulses are involved, due to the large spectral bandwidth and the sensitivity to chirp. Pulse characterization methods like second-order autocorrelation and SPIDER are not capable of measuring the pulse contrast properly: The SPIDER-technique can not cover such a large dynamic range and time delay, while second-order autocorrelators can not distinguish between pre- and postpulses. Therefore, a high-dynamic-range pulse contrast measurement usually requires two cascaded second-order processes, such as SHG and subsequent sum-frequency generation to obtain the third harmonic.

For a reliable measurement, these upconversion processes should induce no spectral modulation or significant pulse stretching, as any such distortions would immediately appear as a reduced pulse contrast. Third-harmonic generation (THG) is very sensitive to a properly matched pulse duration of the fundamental and second harmonic in the process of sum frequency generation, while the fluorescence background is hardly affected by such a chirp. In addition, THG can induce strong spectral narrowing due to the limited phase-matching bandwidth, and the efficiency is so low that the required dynamic range can only be achieved using single-photon detection techniques and careful suppression of stray light. For this reason, we constructed a high-dynamic-range autocorrelator based on optical parametric amplification [226], which allows for a larger spectral bandwidth than conventional third-order autocorrelation. In this scheme, the second harmonic of the input pulse is used to pump an OPA, seeded by another part of the input pulse. The contrast can then be measured by monitoring the intensity of the produced idler while scanning the pump-seed delay. The larger bandwidth allows for a more reliable characterization of ultrashort pulses, as well as of any possible fluorescence or satellite pulses with a spectrum that differs from the main pulse spectrum. An additional advantage of this method compared to THG is the much higher efficiency, which allows detection using a standard photodiode.

This type of pulse contrast measurement with an OPA correlator (OPAC) is described in detail in [226], although the characterization of few-cycle pulses requires some modifications, as discussed by Tavella et al. [227] for the case of third-harmonic autocorrelation. The OPA correlator (OPAC) setup that we have constructed is shown in Fig. 8.6. Pulses with an energy of about $500 \mu\text{J}$ are split off from the main beam and sent into the OPAC. A small part of the pulse is split off using a wedge to prevent reflections from the back surface from propagating through the correlator. The main part of the pulse is efficiently frequency-doubled by focusing it 10 mm behind a 0.2 mm BBO crystal (type-I, $\theta = 29^\circ$) using an $R = -300$ mm curved mirror. A relatively thin crystal is chosen to minimize chirp and spectral narrowing, which is beneficial for keeping the SHG pulses short, as well as for the amplification of a broad spectrum in the OPA stage. The obtained second harmonic pulses are used to pump the OPA, which employs a 1 mm BBO crystal (type-I, $\theta = 28^\circ$) as the gain medium. The small reflection from the wedge is used to seed the OPA, after passing through a tunable delay line. A

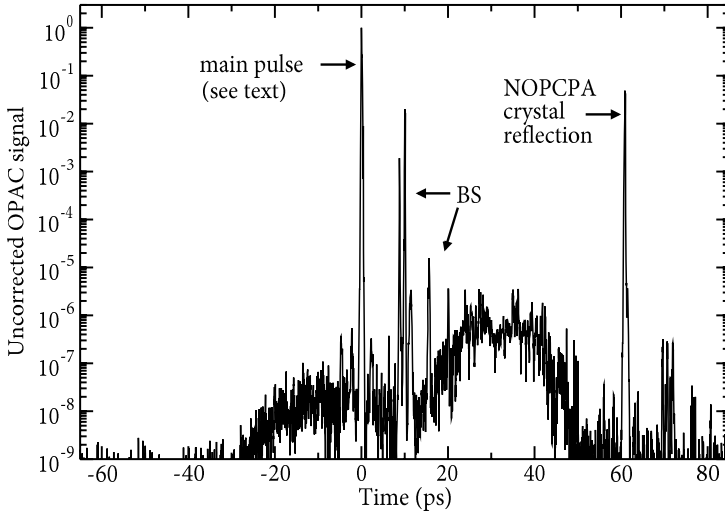


FIGURE 8.7: Uncorrected measurement (raw data) of the pulse contrast using an OPA correlator (OPAC). A few spurious post-pulses can be seen (BS), caused by beamsplitters in the NOPCPA setup. The peak at 60 ps results from a double internal reflection in the first NOPCPA crystal. The fluorescence background peaks at the 10^{-6} level, but stays below 10^{-7} on the leading edge of the pulse. At times when there is no pump light present, the pulse contrast exceeds the detection limit. The height of the main pulse still needs to be corrected for the effects of pulse broadening in the OPAC: by taking this effect into account, the actual pre-pulse contrast is found to be better than 2×10^{-8} .

ple internal reflections of the pump beam inside the 0.2 mm SHG crystal in the OPAC (note that a post-pulse in the pump beam will show up as an artificial pre-pulse in the measurement when scanning the pump-seed time delay); fourth, a significant post-pulse at 60 ps delay arises from a double internal reflection of the signal pulse in the first NOPCPA crystal.

Before attaching any significance to the relative intensities of these features, it should be realized that contrast measurements of few-cycle pulses are easily distorted by various systematic effects. For instance, the SHG used in the OPAC causes spectral narrowing and therefore a longer pulse. In our case, this SHG pulse is estimated to be ~ 40 fs. The effect of such a pulse duration mismatch on the measured OPAC signal is depicted in Fig. 8.8. A schematic of a contrast measurement with fundamental seed and SHG pump pulses of equal duration is shown in Fig. 8.8A, while in Fig. 8.8B the pump pulse is significantly longer than the seed. Comparing these two figures, one can see that a stretched pump pulse not only leads to broader peaks, but also to a decrease of the measured contrast between main pulse and fluorescence background. A quantitative analysis of this effect is performed by calculating convolutions of model pulses with varying pulse duration mismatch. We find that the pulse contrast decreases by a factor approximately equal to the ratio of pump and seed pulse durations, assuming an unchirped seed pulse. A chirp in the seed pulse has negligible effect provided that the

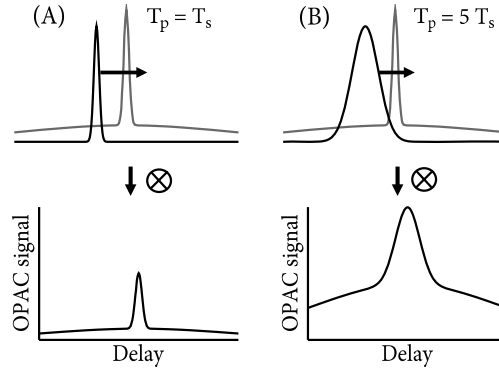


FIGURE 8.8: The influence of a pulse duration mismatch in the OPA correlator. Pump pulse duration T_p is (A) equal to the seed pulse duration T_s ; (B) longer than the seed pulse duration. In both A and B the grey trace represents a short seed pulse on top of a long fluorescence background, while the black trace represents the pump pulse. A comparison of A and B reveals that the use of a pump pulse which is longer than the seed pulse leads to a decrease of the measured contrast ratio between the main pulse and the fluorescence (note that all graphs have a linear scale).

seed pulse remains shorter than the pump pulse. Therefore, to correct for the spectral narrowing of the SHG pulse in the present system, the measured pulse contrast from Fig. 8.7 needs to be increased by an estimated factor of about 5.

The peak at 60 ps also requires careful analysis. This peak can be identified as a double internal reflection (DIR) in the 5.5 mm long NOPCPA crystal, which is amplified by the tail of the pump pulse. Since this pulse is chirped to a duration of 13 ps, its spectral content varies in time and only the longer wavelengths (which are ahead) will be amplified by the tail of the pump pulse. To estimate the spectrum of the DIR pulse after the amplifier, we delayed the seed pulse by 60 ps with respect to the pump. The measured output spectrum has a FWHM of 32 nm centered at 965 nm, which corresponds to a Fourier limit of 43 fs. Because this pulse travels through an additional 11 mm of BBO compared to the main pulse, it will be chirped to about 55 fs when the main pulse is properly compressed. As this pulse is longer than the SHG pump pulse of the OPAC, the contrast of the DIR peak compared to the fluorescence background is realistic, i.e. no correction factor is required in this case. This implies that the present DIR pulse has a peak intensity of less than 1% of the main pulse. However, since it is longer than the main pulse, the total energy content of this DIR pulse is estimated to be about 5%. This DIR pulse energy can be decreased by delaying the seed pulse with respect to the pump, but the present configuration in which the seed pulse timing is set more towards the front of the pump pulse is highly beneficial for the pre-pulse contrast. In Fig. 8.7, a small pre-pulse might also be expected due to the cross-correlation of the SHG of this DIR pulse with the fundamental of the main peak. However, since the spectrum around 965 nm of the DIR pulse is not phase-matched for frequency doubling in the OPAC SHG crystal, such a pre-pulse is not detected.

Taking the aforementioned correction factor of 5 into account, the observed fluorescence background reaches a maximum value of about 4×10^{-7} , but only after the main pulse. The fluorescence level preceding the pulse reaches 2×10^{-8} , and stays below the detection limit of 2×10^{-10} until the onset of the pump pulse at -28 ps. As the shape of the amplified spectrum (see Fig. 8.2) displays the steep edges that are typical for a saturated NOPCPA system, the corresponding pulse in the time domain has some sidebands that rapidly decay in intensity [228]. Therefore, the measured pre-pulse contrast of 2×10^{-8} will only be reached at times >600 fs before the main pulse. This is illustrated in Fig. 8.9, which shows a logarithmic plot of the Fourier-limited pulse shape corresponding to the amplified spectrum, compared to a perfectly Gaussian model pulse shape with the same FWHM pulse duration. Even in the absence of fluorescence, the pulse contrast on short timescales exhibits sidebands caused by the shape of the amplified spectrum.

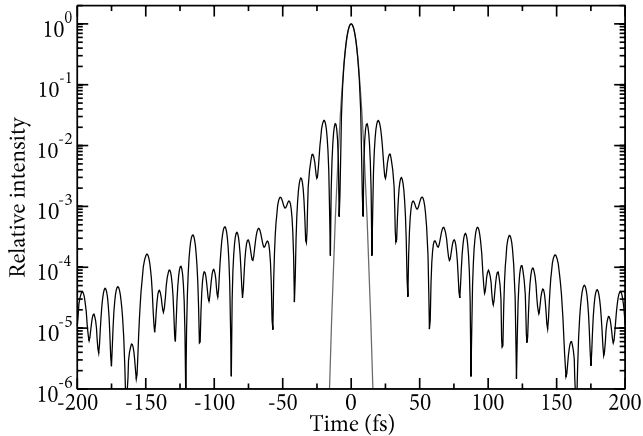


FIGURE 8.9: Maximum achievable pulse contrast on short timescales: Due to the square-shaped amplified spectrum, the temporal pulse shape exhibits sidebands that limit the contrast. The grey trace represents the temporal shape of a pulse that has the same FWHM duration, but with a Gaussian spectrum.

Due to the measurement uncertainty and the required correction factor, the accuracy of the present pulse contrast determination is estimated to be about a factor of 2. The integrated fluorescence background from the measurement shown in Fig. 8.7 is found to be $\sim 0.1\%$ of the main pulse energy, which is in fair agreement with the measured value of 0.2% total integrated fluorescence deduced earlier. The presently achieved pulse contrast constitutes an improvement of more than 3 orders of magnitude over previously published results on the pulse contrast of a short-pulse NOPCPA system [227]. It is interesting to note that even though the measured contrast is comparable to typical Ti:Sapphire multipass amplifiers, in an NOPCPA system the fluorescence is only present for the duration of the pump pulse, which is orders of magnitude

shorter than the inversion lifetime of Ti:Sapphire. Therefore, the total integrated fluorescence energy can be small in comparison.

The possibility of replica pulses produced by the SLM [229] has also been investigated by repeating the contrast measurement with a large linear phase pattern applied to the pulse shaper. No additional peak structure related to the SLM could be observed within the measurement sensitivity. This can be explained by the large spectral bandwidth of the pulses, leading to a significant “nonlinear spectral dispersion” [229] as the frequency components are not linearly spread across the SLM pixels. Any replica pulse generated by pixelation and phase-wrapping errors of the SLM will therefore be chirped to a duration of several picoseconds, leading to a strong decrease in the replica pulse intensity. In addition, the SLM is used in a double-pass configuration. This means that the phase mask steps are halved compared to single-pass implementations, and also that subtle alignment variations between the two passes through the device induce smoothing of the diffracted spectrum, leading to a decrease in the intensity of possible replica pulses.

8.5 Conclusions

In conclusion, we have demonstrated the generation of 7.6 fs laser pulses (2.7 optical cycles) with a 2 terawatt peak intensity at 30 Hz repetition rate, based on noncollinear optical parametric chirped pulse amplification. By using an ultra-broadband Ti:Sapphire oscillator as the seed source, the full spectral gain bandwidth of the 532 nm pumped BBO-based NOPCPA could be utilized, leading to the direct amplification of 310 nm wide spectra to 30 mJ pulse energy. Stretching by a factor of $\sim 2 \times 10^3$ and near-Fourier-limited recompression of these ultra-broadband spectra is performed using a grating-based pulse stretcher with an LCD phase-shaper, and a grating-pair pulse compressor. Important system characteristics such as beam profile, intensity stability and pulse contrast have been investigated, and are found to be of good quality. The pre-pulse contrast reaches 2×10^{-8} on short timescales, and exceeds the 2×10^{-10} detection limit of our contrast measurement setup on timescales > 28 ps.

Due to the compactness of the setup, the absence of thermal effects, and the existing Nd:YAG laser technology, scaling of the intensity by orders of magnitude looks promising, which might allow the generation of sub-3-cycle pulses with an intensity approaching the 100 TW level.

CHAPTER 9

OUTLOOK

9.1 Optimization of the pump pulse shape for NOPCPA

In section 4.2, simulations were presented on the optimum ratio between pump and seed pulse durations in an NOPCPA system, to find a compromise between bandwidth and conversion efficiency. Such a compromise is needed when the pump pulse has a Gaussian temporal profile, as various parts of the chirped seed pulse then experience a different pump intensity. Ideally, the pump pulse should have a perfectly square shape in time: This would lead to a constant gain across the entire seed spectrum, while the amplifier efficiency can be maximized simultaneously. However, such a square pulse shape is difficult to produce in the picosecond range, since e.g. acousto-optic modulators can not be switched at the required speed to actively control the pulse shape. Instead, passive pulse shaping techniques could be employed.

One possible method is time-multiplexing the pump pulse, as schematically drawn in Fig. 9.1. In this scheme, an initially Gaussian pulse is split into various replicas using a multiple beamsplitter setup, which are then recombined after sending them through delay lines of various lengths. By phase-coherently stitching these pulses together, an approximately square shape can be obtained. However, this method is difficult to implement, since the various paths need to be interferometrically stable. Any path length fluctuation on the order of a wavelength will lead to destructive interference between the pulses, causing strong amplitude modulations on the pump pulse shape.

Another method could be amplitude or phase shaping of the pump pulse using a $4f$ -system as introduced in section 5.1.4. For example, one could construct a setup that

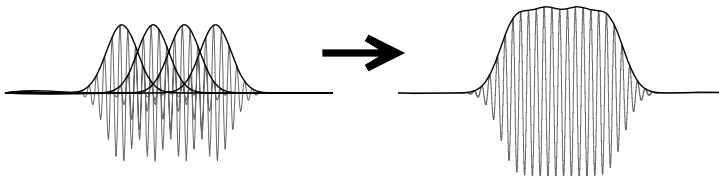


FIGURE 9.1: Time-multiplexing of a Gaussian laser pulse. By creating several pulse replicas with slightly different delays, a longer, square-like total pulse shape can be obtained.

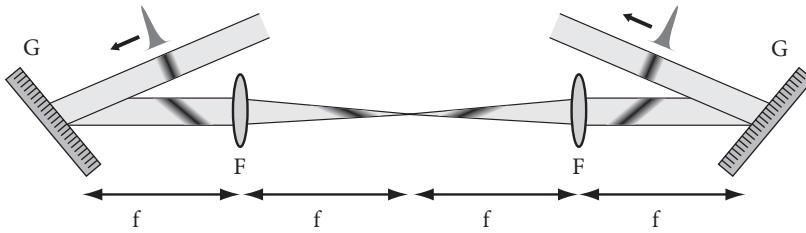


FIGURE 9.2: Principle of pulse front tilting with diffraction gratings (G): In the Fourier-plane of a $4f$ -setup, the pulse front can be made parallel to the propagation direction, effectively interchanging the transverse beam profile and the temporal pulse shape.

introduces e.g. a sinc-function-shaped amplitude modulation in the Fourier-plane of the $4f$ -system. The resulting output pulse shape in the time domain would then be the Fourier-transform of a sinc-function, which is a square. While this method does not have the alignment issues of the time multiplexing technique, a specially tailored amplitude or phase mask is required. While a spatial light modulator as discussed in section 5.1.4 could perform this task, it is a rather bulky and expensive solution.

An interesting possibility to generate square pump pulses would be to perform pulse front tilting on a pump pulse with a top-hat transverse beam profile. Such a setup would also consist of a $4f$ -system, but this time the amplifier would be placed directly in the Fourier-plane. The principle of pulse shaping through pulse front tilting is explained by Fig. 9.2, which shows the diffraction of an ultrashort pulse by a grating. When the pulse is diffracted into the -1^{st} order, one side of the pulse will have traveled a longer path than the other side. While the phase front is perpendicular to the direction of propagation (due to the 2π phase shift between rays diffracted by adjacent grooves of the grating), the pulse front will be tilted after diffraction. When such a tilted pulse is then focused, the tilt will become steeper. In the focus the pulse front becomes parallel to the propagation direction, effectively interchanging the spatial and temporal pulse shapes: A Gaussian pulse with a top-hat beam profile then turns into a square pulse with a Gaussian beam profile. By placing the OPA crystal in the Fourier-plane of such a setup, the nonlinear interaction could then be performed using such a square pump pulse.

An apparent problem with this method is that the pump pulse focuses in the Fourier-plane, which would lead to extreme intensities inside the amplifier crystal. Of course, the focusing needs to be done only in one dimension, since the pulse front tilt is one-dimensional as well. The focusing in this one dimension does not need to present a problem either, since the grating diffraction is also accompanied by spatial dispersion: All frequency components of the diffracted pulse will therefore be focused next to each other. By choosing the right combination of input beam size, grating constant, grating incidence angle and focusing distance, the beam diameter in the Fourier-plane can be adjusted to a suitable size. In addition, the exact duration of the square pulse can also be controlled with these parameters.

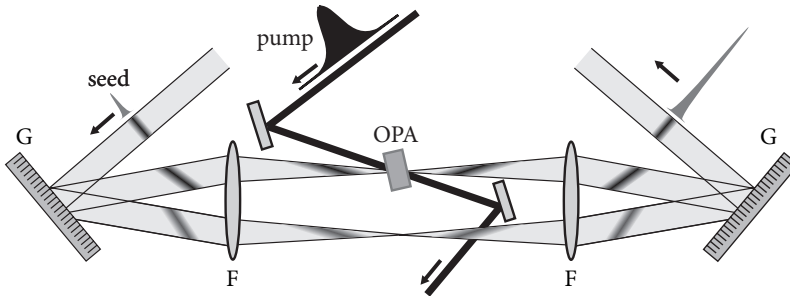


FIGURE 9.3: Principle of optical parametric tilted pulse amplification (OPTPA). Instead of the conventional way of pulse stretching using dispersion, the seed pulse is tilted in a $4f$ -setup. The pulse duration in the Fourier-plane is determined by the diameter of the initial beam, its wavelength, and the grating angle. Note that the spectral bandwidth does not influence the pulse duration, but only the beam diameter in the Fourier-plane as different spectral components are diffracted in different directions. G: grating, F: cylindrical lens or mirror, OPA: nonlinear crystal for optical parametric amplification.

One issue that remains is that the beam profile in the Fourier-plane will resemble the initial temporal pulse shape in one dimension only. For an input pulse with a top-hat beam profile and a Gaussian pulse shape, this would lead to a beam profile which is Gaussian in one dimension and square in the other. Since saturation in an NOPCPA system causes the signal beam to adopt the pump beam profile, the amplified pulse would have the same nonsymmetric shape.

9.2 Optical parametric tilted pulse amplification

A source of high power, narrow-band picosecond pulses can be useful for quantum interference metrology, as it combines high peak intensity with sufficient spectral selectivity to excite only one specific atomic transition. For example, the measurements described in chapter 3 have been performed using ~ 1 ps pulses with μJ -energy. To obtain higher pulse energies, chirped pulse amplification is needed, and especially NOPCPA is a promising candidate for providing such pulses. However, while an NOPCPA system can be designed relatively compactly for ultrashort (and therefore ultra-broadband) laser pulses, the amplification of more narrowband spectra actually requires a larger setup. Although this may seem paradoxical, the stretcher and compressor that are needed to stretch a 10 fs pulse to 10 ps duration are much smaller than the system required to stretch a 1 ps pulse to 10 ps (this can be seen directly from Eq. (2.29)).

A much more compact way of matching pump and seed pulse durations when the initial seed pulse duration becomes longer is the use of pulse front tilting instead of chirped pulse amplification. As was already discussed in section 9.1, a combination of gratings and focusing optics in a $4f$ -geometry can be used to interchange beam profile and pulse duration in the Fourier-plane. While section 9.1 discussed the possibility of

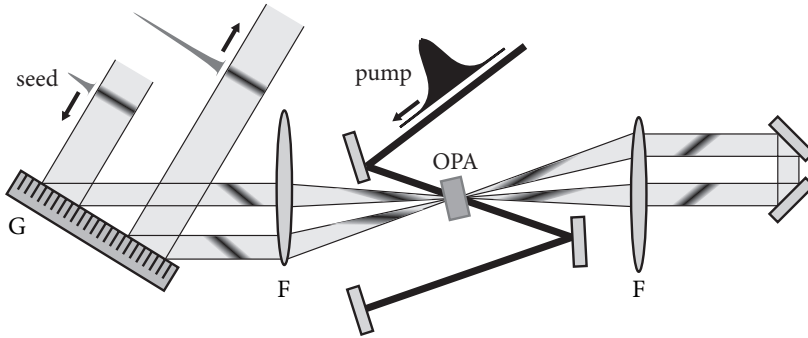


FIGURE 9.4: A flexible double-pass OPTPA setup. The single grating design simplifies the alignment considerably. The amplified wavelength can be tuned either by moving the crystal and pump beam or by rotating the grating, although the latter causes the output beam to shift laterally.

shaping the pump pulse in this way, this method can also be applied as an alternative for chirped pulse amplification by using it to stretch and recompress the seed pulse, as shown in Fig. 9.3. This tilted-pulse amplification (TPA) technique has already been demonstrated with conventional amplifiers (based on Nd:YAG) to improve the energy extraction efficiency in the picosecond regime [230], but can also be applied to the case of optical parametric amplification. Such an OPTPA scheme (optical parametric tilted pulse amplification) combines the high gain and phase stability of a parametric amplifier with the compact pulse duration control achieved by pulse front tilting.

The major advantage of TPA is that the pulse duration in the Fourier-plane is independent of the initial pulse duration: It is completely determined by the initial beam diameter, the central wavelength and the grating angle. In a Littrow configuration, the FWHM pulse duration τ in the Fourier-plane is found to be:

$$\tau = \frac{\sqrt{2 \ln 2} d}{c} \tan \theta_{\text{Litt}} \quad (9.1)$$

where d is the initial beam diameter (defined as the full-width at $1/e^2$ intensity) and θ_{Litt} is the Littrow angle of the grating, which depends on the groove spacing and the wavelength of the light. According to Eq. (9.1), a 1 ps pulse with center wavelength $\lambda = 800$ nm can be stretched to 40 ps duration with a 10 mm beam diameter and an 1800 lines/mm grating ($\theta_{\text{Litt}} = 46.1^\circ$). By comparison, when using chirped pulse amplification such a stretching factor would require a group velocity dispersion of 4×10^7 fs², which is the equivalent of 1.1 km fused silica.

When using a broadband oscillator as a seed source, one can envisage a flexible setup as shown in Fig. 9.4. By rotating the grating, the wavelength of the amplified pulses can easily be tuned over a large bandwidth (although at the expense of a slight translation of the output beam). In addition, by using multiple stages or even separate pump beams and crystals in one stage, multicolor pulses can be produced. The width

of the amplified spectral bandwidth is determined by the spatial overlap between the pump and the seed beam in the Fourier-plane. Because different spectral components are focused at different positions in the Fourier-plane, the OPTPA approach does not seem very suitable for the amplification of few-cycle pulses. However, it can be a very compact and flexible technique for the production of tunable high-power pulses in the picosecond range.

9.3 Towards precision spectroscopy in the XUV

Up to this page, this thesis seems to be separable into two main parts: Chapters 2 and 3 are about precision spectroscopy, while chapters 4–8 deal with few-cycle pulse amplification and NOPCPA). In fact, these two subjects can be combined very well: The NOPCPA systems that have been developed in the course of this work are well suitable for the amplification of pulse pairs to extreme intensities, while maintaining the phase stability from pulse to pulse. By splitting the pump pulse in two and sending one of these replicas into a delay line, two separate pump pulses at a slightly lower power can be produced. The delay line can be adjusted to overlap the pump pulses in the NOPCPA crystals with two consecutive pulses from a frequency comb laser. In principle, the phase stability should be even better for an NOPCPA than for the Ti:Sapphire multi-pass amplifier that was used in chapter 3, since the first pulse does not influence the gain of the second pulse in the instantaneous parametric amplification process. Note that the delay line for the second pump pulse does not need to be interferometrically stable, since the phase of the pump pulse will only be imprinted on the idler, and not on the amplified seed pulse.

From the results obtained in chapter 8, we can infer that with such a scheme it should be possible to generate a pair of phase-locked 7.6 fs pulses, each with an intensity exceeding one terawatt. These pulses have been demonstrated to produce bright high harmonics down to a wavelength of 30 nm (limited by the detection setup), and may be expected to produce photons with keV energy [33]. Therefore, the combination of double-pulse NOPCPA and quantum interference metrology seems ideally suited to extend frequency comb spectroscopy to extremely short wavelength ranges, such as the XUV and even the soft X-ray regimes.

Of course, this is only true if the harmonic generation preserves the phase coherence of the fundamental pulses. Several experiments have already been performed on this matter, with encouraging results but at a low resolution [143, 231, 232]. More recently, two groups have reported on high-harmonic generation using frequency comb pulses inside an external enhancement resonator [233, 234]. With this approach, the peak intensity becomes high enough for harmonic generation without the use of an additional amplifier, and it allows high-harmonic generation at the full oscillator repetition rate. The full comb structure of the fundamental pulses could be preserved in this way, again provided that the harmonic generation does not introduce excessive phase noise. A high phase stability was confirmed for the third harmonic at 266 nm, but measurements on higher harmonics have not yet been reported.

To investigate such phase shifts at high resolution in the vacuum-ultraviolet (VUV),

we performed quantum interference spectroscopy on xenon atoms using 125 nm radiation, which was generated by third-harmonic generation of amplified pulse pairs in a gas cell. By using the xenon atoms as VUV phase detectors, we could confirm that the third-harmonic generation process preserves the phase between the pulses to better than $1/30^{\text{th}}$ of a VUV cycle [235] (200 mrad, which was the detection limit in this particular experiment). These results confirm that frequency comb spectroscopy can be performed with sub-MHz accuracy in the VUV, and that the phase coherence can be expected to remain very good at shorter wavelengths as well. With this data, it seems feasible to measure e.g. the $1s^2\ ^1S_0 \rightarrow 1s6p\ ^1P_1$ transition in helium with ~ 500 kHz accuracy, even though the required excitation wavelength is 51 nm. Such a measurement would improve the knowledge of the ground state Lamb shift in helium by two orders of magnitude, and would constitute a stringent test of two-electron quantum electrodynamics.

APPENDIX A

PROPAGATION IN ABSORBING MEDIA

Equation (2.17) has been derived assuming that the medium is completely free of losses, i.e. $1 + \chi_e = n^2$. In reality, any material will have some degree of absorption. This can be incorporated in the propagation equation by recalling the definition of the refractive index and absorption coefficients from section 2.1.1: $n = \text{Re}\sqrt{1 + \chi_e}$ and $\alpha = (c/\omega)\text{Im}\sqrt{1 + \chi_e}$. Assuming that the absorption parameter α is relatively small, we can make the approximation:

$$1 + \chi_e = (n + i\alpha)^2 \approx n^2 + 2i\frac{nc}{\omega}\alpha \quad (\text{A.1})$$

More formally, this approximation is justified if the absorption losses are small on the length scale of a wavelength:

$$n^2 \gg \frac{c^2}{\omega^2}\alpha^2 \Rightarrow \alpha \ll \frac{n\omega}{c} = k \quad (\text{A.2})$$

Relation (A.1) can then be inserted in the wave equation (2.13), resulting in:

$$\frac{\partial A(z, \omega)}{\partial z} - \frac{i}{2k_0}(k^2 - k_0^2 + 2i\alpha k)A(z, \omega) = 0 \quad (\text{A.3})$$

Making the same approximations and expansion for k as was done in deriving Eq. (2.15), we now find:

$$\frac{\partial A(z, \omega)}{\partial z} + \alpha A(z, \omega) - i \sum_{n=1}^{\infty} \frac{1}{n!} k^{(n)} (\omega - \omega_0)^n A(z, \omega) = 0 \quad (\text{A.4})$$

In a similar way as equation (2.15), we can Fourier-transform this equation to the time-domain to obtain the parabolic equation for the pulse envelope including losses:

$$\frac{\partial A(z, t)}{\partial z} + k^{(1)} \frac{\partial A(z, t)}{\partial t} - \frac{ik^{(2)}}{2} \frac{\partial^2 A(z, t)}{\partial t^2} + \alpha A(z, t) = 0 \quad (\text{A.5})$$

APPENDIX B

PULSES IN TIME AND FREQUENCY

The exact relation between the duration of a pulse and its spectral width can be a considerable source of confusion, due to the many different possible definitions of pulse durations. The notation used throughout this thesis may therefore also be somewhat ambiguous on various occasions. This appendix gives a short overview of the numbers that are normally used to define pulse duration and spectral width, and of the relations between them.

Usually, a Gaussian (optical) electric field pulse in the time domain is written as:

$$E(t) = e^{-(t^2/2\tau^2)} e^{-i\omega_c t} \quad (\text{B.1})$$

The intensity of such a pulse is then written as:

$$I(t) = |E(t)|^2 = e^{-(t/\tau)^2} \quad (\text{B.2})$$

In these equations τ is half of the $1/e$ -pulse duration of the intensity, while half the $1/e$ -pulse duration of the electric field is given by $\tau\sqrt{2}$. However, defining the pulse duration in terms of a $1/e$ -width is not very convenient when non-Gaussian pulse shapes are involved. A more general measure of the pulse duration is the full-width at half maximum (FWHM), as this can be defined for any pulse shape. Usually, when one speaks about “the pulse duration”, this refers to the FWHM width of the pulse intensity Δt , which is related to τ through:

$$\Delta t = 2\sqrt{\ln 2} \tau \quad (\text{B.3})$$

The Fourier transform of a Gaussian pulse in the time domain will lead to a spectrum which is Gaussian in shape as well. The exact Fourier transformation is given by:

$$e^{-at^2} \xleftrightarrow{\mathcal{FT}} e^{-(\omega^2/4a)} \quad (\text{B.4})$$

where it should be noted that these Fourier transformations apply to the electric fields, not to the intensities of the pulse. From this equation one can derive that the spectrum corresponding to a pulse with an intensity FWHM duration Δt is given by:

$$I(\omega) = e^{-\frac{(\omega-\omega_c)^2}{\Delta\omega^2}} = e^{-(\tau^2/4 \ln 2)(\omega-\omega_c)^2} \quad (\text{B.5})$$

and the FWHM spectral intensity is then given by:

$$\Delta\omega_{\text{FWHM}} = \Delta\omega 2\sqrt{\ln 2} = \frac{4 \ln 2}{\Delta t} \quad (\text{B.6})$$

The spectral width is inversely proportional to the pulse duration, and therefore the product of these two quantities is a constant:

$$\Delta\omega_{\text{FWHM}}\Delta t = 4 \ln 2 = 2\pi \times 0.441 \quad (\text{B.7})$$

This equation states that a given spectral bandwidth $\Delta\omega_{\text{FWHM}}$ can only be compressed to a certain minimum pulse duration Δt , which is called the *Fourier-limited pulse duration*. Of course, the pulse duration can be longer than Δt if there is a chirp on the spectrum. From this equation it can be seen that the production of 10 fs pulses requires a spectral bandwidth of 44.1 THz. The number 0.441 is known as the Fourier-limited time-bandwidth product for a Gaussian pulse. This number depends on the shape of the pulse, differing slightly if the pulse is not Gaussian but e.g. sech^2 or top-hat. Every pulse shape has a such a time-bandwidth product, which is a useful reference to compare how well a given pulse has been compressed.

APPENDIX C

SOME MATHEMATICAL BACKGROUND TO THE OPA THEORY

C.1 Integration of the normalized coupled wave equations

In the analytical theory of optical parametric amplification given in section 4.1.2, some steps in the derivations may be a bit too large. Especially the solution of the differential equation (4.6d) for the combined phase θ , which is given by expression (4.8), is not straightforward to derive. As this step is rather crucial in the rest of the discussion, we give its full derivation in this appendix. We start out with the normalized coupled wave equations (C.1), which we recall to be:

$$\frac{\partial u_s}{\partial \xi} = -u_i u_p \sin \theta \quad (\text{C.1a})$$

$$\frac{\partial u_i}{\partial \xi} = -u_s u_p \sin \theta \quad (\text{C.1b})$$

$$\frac{\partial u_p}{\partial \xi} = +u_s u_i \sin \theta \quad (\text{C.1c})$$

$$\frac{\partial \theta}{\partial \xi} = \frac{\Delta k z}{\xi} + \left(\frac{u_s u_i}{u_p} - \frac{u_i u_p}{u_s} - \frac{u_s u_p}{u_i} \right) \cos \theta \quad (\text{C.1d})$$

Since the right-hand side of Eq. (C.1d) is written in terms of $\cos \theta$, it is convenient to rewrite the entire differential equation as:

$$\frac{\partial \cos \theta}{\partial \xi} = -\sin \theta \frac{\Delta k z}{\xi} - \left(\frac{u_s u_i}{u_p} - \frac{u_i u_p}{u_s} - \frac{u_s u_p}{u_i} \right) \sin \theta \cos \theta \quad (\text{C.2})$$

Using Eqs. (C.1) to eliminate the $\sin \theta$ -terms then results in:

$$\frac{\partial \cos \theta}{\partial \xi} = -\frac{\Delta k z}{\xi} \frac{1}{u_s u_i} \frac{\partial u_p}{\partial \xi} - \left(\frac{1}{u_s} \frac{\partial u_s}{\partial \xi} + \frac{1}{u_i} \frac{\partial u_i}{\partial \xi} + \frac{1}{u_p} \frac{\partial u_p}{\partial \xi} \right) \cos \theta \quad (\text{C.3})$$

Although it may not seem obvious at first, it is convenient to perform the following manipulations on the resulting expression:

$$\begin{aligned} \frac{\partial \cos \theta}{\partial \xi} &= -\frac{1}{u_s u_i u_p} \left[\frac{\Delta k z}{\xi} u_p \frac{\partial u_p}{\partial \xi} + \left(u_i u_p \frac{\partial u_s}{\partial \xi} + u_s u_p \frac{\partial u_i}{\partial \xi} + u_s u_i \frac{\partial u_p}{\partial \xi} \right) \cos \theta \right] \\ &= -\frac{1}{u_s u_i u_p} \left[\frac{1}{2} \frac{\Delta k z}{\xi} \frac{\partial u_p^2}{\partial \xi} + \cos \theta \frac{\partial u_s u_i u_p}{\partial \xi} \right] \end{aligned} \quad (\text{C.4})$$

And now this last step can be written in a more insightful way by moving the last term on the right-hand to the left and multiplying both sides with $u_s u_i u_p$. This gives:

$$u_s u_i u_p \frac{\partial \cos \theta}{\partial \xi} + \cos \theta \frac{\partial u_s u_i u_p}{\partial \xi} = -\frac{1}{2} \frac{\Delta k z}{\xi} \frac{\partial u_p^2}{\partial \xi} \quad (\text{C.5})$$

This left-hand side can be identified as a product rule of differentiation, which was applied to:

$$\frac{\partial u_s u_i u_p \cos \theta}{\partial \xi} = -\frac{1}{2} \frac{\Delta k z}{\xi} \frac{\partial u_p^2}{\partial \xi} \quad (\text{C.6})$$

Recall that the ratio z/ξ is a constant, so that Eq. (C.6) can readily be integrated to yield:

$$\cos \theta = \frac{\Gamma - \frac{1}{2} \frac{\Delta k z}{\xi} u_p^2}{u_s u_i u_p} \quad (\text{C.7})$$

which exactly corresponds to Eq. (4.8). From this integration, it also becomes clear that the integration constant Γ is given by:

$$\Gamma = u_s(0)u_i(0)u_p(0) \cos \theta(0) + \frac{1}{2} \frac{\Delta k z}{\xi} u_p^2(0) \quad (\text{C.8})$$

C.2 Elliptic integral manipulations

The exact properties of elliptic integrals and Jacobi elliptic functions are rather complex, and algebraic manipulations with these functions are not always transparent. As the analytical solutions of the coupled wave equations are found to be such elliptic functions, we have simply given the appropriate form without much further analysis of its properties. A thorough overview of the properties and transformation algebra of Jacobi elliptic integrals and functions is given by several mathematical textbooks, such as Abramowitz and Stegun [151].

To make it at least somewhat more insightful how the $\cosh gz$ -behaviour of the small-signal gain (see Eq. (4.16)) can be derived from the more general Jacobi elliptic function sn solution of Eq. (4.15), we give some of the intermediate steps of this derivation here. These steps should enable the reader to confirm the validity of this derivation, by checking the separate steps using e.g. Ref. [151].

We start out from Eq. (4.15), which is expressed as:

$$u_s^2(\xi) = u_s^2(0) \left(1 + \frac{\gamma^2}{1-\gamma^2} (1 - \text{sn}^2[\sqrt{u_p^2(0) + u_s^2(0) - \left(\frac{\Delta kz}{2\xi}\right)^2} \xi + K(\gamma^2)], \gamma^2] \right) \quad (\text{C.9})$$

In this expression, the function $K(\gamma^2)$ is a complete elliptic integral of the first kind: Its presence in the first term of the argument introduces a quarter-wave phase shift of the sn-function, which leads to the correct initial condition $\text{sn}^2 = 1$ at $\xi = 0$, as Eq. (C.9) then simply states that $u_s^2(\xi) = u_s^2(0)$ at $\xi = 0$. The constant γ^2 is given by Eq. (4.14), and depends only on the initial pump and seed intensities and the phase mismatch Δk :

$$\gamma^2 = \frac{u_p^2(0) - \left(\frac{\Delta kz}{2\xi}\right)^2}{u_p^2(0) + u_s^2(0) - \left(\frac{\Delta kz}{2\xi}\right)^2} \quad (\text{C.10})$$

From the properties of elliptic functions it follows that the sn-function with such a quarter-wave phase shift can be expressed as the different elliptic function cd. With an additional transformation, Eq. (C.9) then simplifies to:

$$\begin{aligned} u_s^2(\xi) &= u_s^2(0) \left(1 + \frac{\gamma^2}{1-\gamma^2} (1 - \text{cd}^2[\sqrt{u_p^2(0) + u_s^2(0) - \left(\frac{\Delta kz}{2\xi}\right)^2} \xi, \gamma^2]) \right) \\ &= u_s^2(0) \left(1 + \gamma^2 \text{sd}^2[\sqrt{u_p^2(0) + u_s^2(0) - \left(\frac{\Delta kz}{2\xi}\right)^2} \xi, \gamma^2] \right) \end{aligned} \quad (\text{C.11})$$

Although this last expression probably looks just as bad as Eq. (C.9), one interesting property of this sd-function is that in the limit of $\gamma^2 \rightarrow 1$ it takes the form of the hyperbolic sine-function \sinh . As a result, Eq. (C.11) then simplifies to:

$$I_s(z) = I_s(0) \cosh^2 gz \quad (\text{C.12})$$

which is the familiar form for the small-signal gain of an optical parametric amplifier, as given by Eq. (4.16).

BIBLIOGRAPHY

- [1] T. H. Maiman, *Stimulated optical radiation in ruby*, Nature **187**, 493 (1960).
- [2] W. E. Lamb, W. P. Schleich, M. O. Scully, and C. H. Townes, *Laser physics: Quantum controversy in action*, Rev. Mod. Phys. **71**, S263 (1999).
- [3] W. Gordy, *Microwave spectroscopy*, Rev. Mod. Phys. **20**, 668 (1948).
- [4] P. Forman, "Swords into ploughshares": *Breaking new ground with radar hardware and technique in physical research after World War II*, Rev. Mod. Phys. **67**, 397 (1995).
- [5] J. P. Gordon, H. J. Zeiger, and C. H. Townes, *The maser – new type of microwave amplifier, frequency standard, and spectrometer*, Phys. Rev. **99**, 1264 (1955).
- [6] C. E. Cleeton and N. H. Williams, *Electromagnetic waves of 1.1 cm wavelength and the absorption spectrum of ammonia*, Phys. Rev. **45**, 234 (1934).
- [7] N. G. Basov and A. M. Prokhorov, *Possible methods of obtaining active molecules for a molecular oscillator*, Sov. Phys. JETP **1**, 184 (1955).
- [8] A. L. Schawlow and C. H. Townes, *Infrared and optical masers*, Phys. Rev. **112**, 1940 (1958).
- [9] N. G. Basov, B. M. Vul, and Y. M. Popov, *Quantum-mechanical semiconductor generators and amplifiers of electromagnetic oscillations*, Sov. Phys. JETP **10**, 416 (1959).
- [10] A. M. Prokhorov, *Molecular amplifier and generator for submillimeter waves*, Sov. Phys. JETP **7**, 1140 (1958).
- [11] A. Javan, W. R. Bennett, and D. R. Herriott, *Population inversion and continuous optical maser oscillation in a gas discharge containing a He-Ne mixture*, Phys. Rev. Lett. **6**, 106 (1961).
- [12] R. N. Hall, G. E. Fenner, J. D. Kingsley, T. J. Soltys, and R. O. Carlson, *Coherent light emission from GaAs junctions*, Phys. Rev. Lett. **9**, 366 (1962).
- [13] P. P. Sorokin and M. J. Stevenson, *Stimulated infrared emission from trivalent Uranium*, Phys. Rev. Lett. **5**, 557 (1960).
- [14] E. Snitzer, *Optical maser action of Nd^{3+} in a Barium crown glass*, Phys. Rev. Lett. **7**, 444 (1961).
- [15] P. P. Sorokin, J. R. Lankard, E. C. Hammond, and V. L. Moruzzi, *Laser-pumped stimulated emission from organic dyes: experimental studies and analytical comparisons*, IBM J. Res. Devel. **11**, 130 (1967).

- [16] P. P. Sorokin, J. R. Lankard, V. L. Moruzzi, and E. C. Hammond, *Flashlamp-pumped organic-dye lasers*, J. Chem. Phys. **48**, 4726 (1968).
- [17] J. A. Myer, C. L. Johnson, E. Kierstead, R. D. Sharma, and I. Itzkan, *Dye laser stimulation with a pulsed N_2 laser line at 3371 Å*, Appl. Phys. Lett. **16**, 3 (1970).
- [18] P. F. Moulton, *Spectroscopic and laser characteristics of $Ti:Al_2O_3$* , J. Opt. Soc. Am. B **3**, 125 (1986).
- [19] P. A. Schulz, *Single-frequency $Ti:Al_2O_3$ ring laser*, IEEE J. Quantum Electron. **24**, 1039 (1988).
- [20] A. Sanchez, A. J. Strauss, R. L. Aggarwal, and R. E. Fahey, *Crystal growth, spectroscopy, and laser characteristics of $Ti:Al_2O_3$* , IEEE J. Quantum Electron. **24**, 995 (1988).
- [21] A. E. Siegman, *Lasers* (University Science Books, 1986).
- [22] A. Yariv, *Quantum electronics* (John Wiley & Sons, 1989), 3rd ed.
- [23] S. Naumov, A. Fernandez, R. Graf, P. Dombi, F. Krausz, and A. Apolonski, *Approaching the microjoule frontier with femtosecond laser oscillators*, New J. Phys. **7**, 216 (2005).
- [24] X. Zhou, H. Kapteyn, and M. Murnane, *Positive-dispersion cavity-dumped Ti :sapphire laser oscillator and its application to white light generation*, Opt. Express **14**, 9750 (2006).
- [25] C. Bibeau et al., *Power, energy, and temporal performance of the Nova laser facility with recent improvements to the amplifier system*, Appl. Opt. **31**, 5799 (1992).
- [26] D. Strickland and G. Mourou, *Compression of amplified chirped optical pulses*, Opt. Commun. **56**, 219 (1985).
- [27] M. D. Perry et al., *Petawatt laser pulses*, Opt. Lett. **24**, 160 (1999).
- [28] Y. Kitagawa et al., *Prepulse-free petawatt laser for a fast ignitor*, IEEE J. Quantum Electron. **40**, 281 (2004).
- [29] C. N. Danson et al., *Vulcan Petawatt - an ultra-high-intensity interaction facility*, Nucl. Fusion **44**, S239 (2004).
- [30] M. Aoyama, K. Yamakawa, Y. Akahane, J. Ma, N. Inoue, H. Ueda, and H. Kiriyama, *0.85-PW, 33-fs Ti :Sapphire laser*, Opt. Lett. **28**, 1594 (2003).
- [31] P. B. Corkum, *Plasma perspective on strong field multiphoton ionization*, Phys. Rev. Lett. **71**, 1994 (1993).
- [32] M. Lewenstein, P. Balcou, M. Y. Ivanov, A. L'Huillier, and P. B. Corkum, *Theory of high-harmonic generation by low-frequency laser fields*, Phys. Rev. A **49**, 2117 (1994).
- [33] J. Seres et al., *Source of coherent kiloelectronvolt X-rays*, Nature **433**, 596 (2005).

-
- [34] C. Spielmann et al., *Generation of coherent X-rays in the water window using 5-femtosecond laser pulses*, *Science* **278**, 661 (1997).
- [35] K. W. D. Ledingham, P. McKenna, and R. P. Singhal, *Applications for nuclear phenomena generated by ultra-intense lasers*, *Science* **300**, 1107 (2003).
- [36] W. P. Leemans et al., *GeV electron beams from a centimetre-scale accelerator*, *Nature Physics* **2**, 696 (2006).
- [37] R. A. Snavely et al., *Intense high-energy proton beams from petawatt-laser irradiation of solids*, *Phys. Rev. Lett.* **85**, 2945 (2000).
- [38] V. Malka et al., *Practicability of protontherapy using compact laser systems*, *Med. Phys.* **31**, 1587 (2004).
- [39] J. Magill, H. Schwoerer, F. Ewald, J. Galy, R. Schenkel, and R. Sauerbrey, *Laser transmutation of Iodine-129*, *Appl. Phys. B* **77**, 387 (2003).
- [40] K. W. D. Ledingham et al., *High power laser production of short-lived isotopes for positron emission tomography*, *J. Phys. D* **37**, 2341 (2004).
- [41] S. Nakai and K. Mima, *Laser driven inertial fusion energy: present and prospective*, *Rep. Prog. Phys.* **67**, 321 (2004).
- [42] M. Tabak et al., *Ignition and high gain with ultrapowerful lasers*, *Phys. Plasmas* **1**, 1626 (1994).
- [43] P. A. Franken, A. E. Hill, C. W. Peters, and G. Weinreich, *Generation of optical harmonics*, *Phys. Rev. Lett.* **7**, 118 (1961).
- [44] M. Bass, P. A. Franken, A. E. Hill, C. W. Peters, and G. Weinreich, *Optical mixing*, *Phys. Rev. Lett.* **8**, 18 (1962).
- [45] P. D. Maker, R. W. Terhune, M. Nisenoff, and C. M. Savage, *Effects of dispersion and focusing on the production of optical harmonics*, *Phys. Rev. Lett.* **8**, 21 (1962).
- [46] J. A. Giordmaine, *Mixing of light beams in crystals*, *Phys. Rev. Lett.* **8**, 19 (1962).
- [47] C. C. Wang and G. W. Racette, *Measurement of parametric gain accompanying optical difference frequency generation*, *Appl. Phys. Lett.* **6**, 169 (1965).
- [48] R. H. Kingston, *Parametric amplification and oscillation at optical frequencies*, *Proc. IRE* **50**, 472 (1962).
- [49] N. M. Kroll, *Parametric amplification in spatially extended media and application to the design of tuneable oscillators at optical frequencies*, *Phys. Rev.* **127**, 1207 (1962).
- [50] S. A. Akhmanov and R. V. Khokhlov, *Concerning one possibility of amplification of light waves*, *Sov. Phys. JETP* **16**, 252 (1963).
- [51] J. A. Armstrong, N. Bloembergen, J. Ducuing, and P. S. Pershan, *Interactions between light waves in a nonlinear dielectric*, *Phys. Rev.* **127**, 1918 (1962).

- [52] J. A. Giordmaine and R. C. Miller, *Tunable coherent parametric oscillation in LiNbO₃ at optical frequencies*, Phys. Rev. Lett. **14**, 973 (1965).
- [53] W. H. Louisell, A. Yariv, and A. E. Siegman, *Quantum fluctuations and noise in parametric processes. I*, Phys. Rev. **124**, 1646 (1961).
- [54] B. R. Mollow and R. J. Glauber, *Quantum theory of parametric amplification. I*, Phys. Rev. **160**, 1076 (1967).
- [55] T. G. Giallorenzi and C. L. Tang, *Quantum theory of spontaneous parametric scattering of intense light*, Phys. Rev. **166**, 225 (1968).
- [56] D. A. Kleinman, *Theory of optical parametric noise*, Phys. Rev. **174**, 1027 (1968).
- [57] S. E. Harris, M. K. Oshman, and R. L. Byer, *Observation of tunable optical parametric fluorescence*, Phys. Rev. Lett. **18**, 732 (1967).
- [58] D. Magde and H. Mahr, *Study in ammonium dihydrogen phosphate of spontaneous parametric interaction tunable from 4400 to 16 000 Å*, Phys. Rev. Lett. **18**, 905 (1967).
- [59] R. L. Byer and S. E. Harris, *Power and bandwidth of spontaneous parametric emission*, Phys. Rev. **168**, 1064 (1968).
- [60] G. M. Gale, M. Cavallari, T. J. Driscoll, and F. Hache, *Sub-20-fs tunable pulses in the visible from an 82-MHz optical parametric oscillator*, Opt. Lett. **20**, 1562 (1995).
- [61] P. di Trapani et al., *Group-velocity self-matching of femtosecond pulses in noncollinear parametric generation*, Phys. Rev. A **51**, 3164 (1995).
- [62] T. Wilhelm, J. Piel, and E. Riedle, *Sub-20-fs pulses tunable across the visible from a blue-pumped single-pass noncollinear parametric converter*, Opt. Lett. **22**, 1494 (1997).
- [63] A. Shirakawa, I. Sakane, and T. Kobayashi, *Pulse-front-matched optical parametric amplification for sub-10-fs pulse generation tunable in the visible and near infrared*, Opt. Lett. **23**, 1292 (1998).
- [64] G. Cerullo and S. de Silvestri, *Ultrafast optical parametric amplifiers*, Rev. Sci. Instrum. **74**, 1 (2003).
- [65] E. Riedle, M. Beutter, S. Lochbrunner, J. Piel, S. Schenkl, S. Spörlein, and W. Zinth, *Generation of 10 to 50 fs pulses tunable through all of the visible and the NIR*, Appl. Phys. B **71**, 457 (2000).
- [66] A. Baltuška and T. Kobayashi, *Adaptive shaping of two-cycle visible pulses using a flexible mirror*, Appl. Phys. B **75**, 427 (2002).
- [67] A. Baltuška, T. Fuji, and T. Kobayashi, *Visible pulse compression to 4 fs by optical parametric amplification and programmable dispersion control*, Opt. Lett. **27**, 306 (2002).

-
- [68] M. Vengris, *Biological photoreactions explored by multi-pulse ultrafast spectroscopy*, Ph.D. thesis, Vrije Universiteit (2005).
- [69] A. Gambetta et al., *Real-time observation of nonlinear coherent phonon dynamics in single-walled carbon nanotubes*, *Nature Physics* **2**, 515 (2006).
- [70] A. Dubietis, G. Jonušauskas, and A. Piskarskas, *Powerful femtosecond pulse generation by chirped and stretched pulse parametric amplification in BBO crystal*, *Opt. Commun.* **88**, 437 (1992).
- [71] I. N. Ross, P. Matousek, M. Towrie, A. J. Langley, and J. L. Collier, *The prospects for ultrashort pulse duration and ultrahigh intensity using optical parametric chirped pulse amplifiers*, *Opt. Commun.* **144**, 125 (1997).
- [72] I. N. Ross, P. Matousek, G. H. C. New, and K. Osvay, *Analysis and optimization of optical parametric chirped pulse amplification*, *J. Opt. Soc. Am. B* **19**, 2945 (2002).
- [73] I. N. Ross et al., *Generation of terawatt pulses by use of optical parametric chirped pulse amplification*, *Appl. Opt.* **39**, 2422 (2000).
- [74] I. Jovanovic, C. A. Ebberts, and C. P. J. Barty, *Hybrid chirped-pulse amplification*, *Opt. Lett.* **27**, 1622 (2002).
- [75] X. Yang et al., *Multiterawatt laser system based on optical parametric chirped pulse amplification*, *Opt. Lett.* **27**, 1135 (2002).
- [76] I. Jovanovic, B. J. Comaskey, C. A. Ebberts, R. A. Bonner, D. M. Pennington, and E. C. Morse, *Optical parametric chirped-pulse amplifier as an alternative to Ti:sapphire regenerative amplifiers*, *Appl. Opt.* **41**, 2923 (2002).
- [77] L. J. Waxer, V. Bagnoud, I. A. Begishev, M. J. Guardalben, J. Puth, and J. D. Zuegel, *High-conversion-efficiency optical parametric chirped-pulse amplification system using spatiotemporally shaped pump pulses*, *Opt. Lett.* **28**, 1245 (2003).
- [78] V. V. Lozhkarev et al., *200 TW 45 fs laser based on optical parametric chirped pulse amplification*, *Opt. Express* **14**, 446 (2006).
- [79] S. Witte, R. T. Zinkstok, W. Hogervorst, and K. S. E. Eikema, *Generation of few-cycle terawatt light pulses using optical parametric chirped pulse amplification*, *Opt. Express* **13**, 4903 (2005).
- [80] S. Witte, R. T. Zinkstok, A. L. Wolf, W. Hogervorst, W. Ubachs, and K. S. E. Eikema, *A source of 2 terawatt, 2.7 cycle laser pulses based on noncollinear optical parametric chirped pulse amplification*, *Opt. Express* **14**, 8168 (2006).
- [81] A. L. Schawlow, *Spectroscopy in a new light*, *Rev. Mod. Phys.* **54**, 697 (1982).
- [82] T. W. Hänsch and H. Walther, *Laser spectroscopy and quantum optics*, *Rev. Mod. Phys.* **71**, S242 (1999).
- [83] T. W. Hänsch, S. A. Lee, R. Wallenstein, and C. Wieman, *Doppler-free two-photon spectroscopy of Hydrogen 1S – 2S*, *Phys. Rev. Lett.* **34**, 307 (1975).

- [84] S. A. Lee, R. Wallenstein, and T. W. Hänsch, *Hydrogen 1S – 2S isotope shift and 1S Lamb shift measured by laser spectroscopy*, Phys. Rev. Lett. **35**, 1262 (1975).
- [85] K. S. E. Eikema, W. Ubachs, W. Vassen, and W. Hogervorst, *Lamb shift measurement in the 1^1S ground state of helium*, Phys. Rev. A **55**, 1866 (1997).
- [86] S. D. Bergeson et al., *Measurement of the He ground state Lamb shift via the two-photon $1^1S - 2^1S$ transition*, Phys. Rev. Lett. **80**, 3475 (1998).
- [87] P. J. Mohr and B. N. Taylor, *CODATA recommended values of the fundamental physical constants: 2002*, Rev. Mod. Phys. **77**, 1 (2005).
- [88] H. S. Margolis, G. P. Barwood, G. Huang, H. A. Klein, S. N. Lea, K. Szymaniec, and P. Gill, *Hertz level measurement of the optical clock frequency in a single $^{88}\text{Sr}^+$ ion*, Science **306**, 1355 (2004).
- [89] W. H. Oskay et al., *Single-atom optical clock with high accuracy*, Phys. Rev. Lett. **97**, 020801 (2006).
- [90] R. le Targat, X. Baillard, M. Fouche, A. Bruschi, O. Tcherbakoff, G. D. Rovera, and P. Lemonde, *Accurate optical lattice clock with ^{87}Sr atoms*, Phys. Rev. Lett. **97**, 130801 (2006).
- [91] T. Udem et al., *Absolute frequency measurements of the Hg^+ and Ca optical clock transitions with a femtosecond laser*, Phys. Rev. Lett. **86**, 4996 (2001).
- [92] M. Fischer et al., *New limits on the drift of fundamental constants from laboratory measurements*, Phys. Rev. Lett. **92**, 230802 (2004).
- [93] E. Peik, B. Lipphardt, H. Schnatz, T. Schneider, C. Tamm, and S. G. Karshenboim, *Limit on the present temporal variation of the fine structure constant*, Phys. Rev. Lett. **93**, 170801 (2004).
- [94] H. Schnatz, B. Lipphardt, J. Helmcke, F. Riehle, and G. Zinner, *First phase-coherent frequency measurement of visible radiation*, Phys. Rev. Lett. **76**, 18 (1996).
- [95] Y. V. Baklanov and V. P. Chebotaev, *Narrow resonances of two-photon absorption of super-narrow pulses in a gas*, Appl. Phys. A **12**, 97 (1977).
- [96] R. Teets, J. Eckstein, and T. W. Hänsch, *Coherent two-photon excitation by multiple light pulses*, Phys. Rev. Lett. **38**, 760 (1977).
- [97] J. N. Eckstein, A. I. Ferguson, and T. W. Hänsch, *High-resolution two-photon spectroscopy with picosecond light pulses*, Phys. Rev. Lett. **40**, 847 (1978).
- [98] M. M. Salour and C. Cohen-Tannoudji, *Observation of Ramsey's interference fringes in the profile of Doppler-free two-photon resonances*, Phys. Rev. Lett. **38**, 757 (1977).
- [99] M. M. Salour, *Quantum interference effects in two-photon spectroscopy*, Rev. Mod. Phys. **50**, 667 (1978).
- [100] N. F. Ramsey, *A new molecular beam resonance method*, Phys. Rev. **76**, 996 (1949).

-
- [101] T. Udem, J. Reichert, R. Holzwarth, and T. W. Hänsch, *Accurate measurement of large optical frequency differences with a mode-locked laser*, Opt. Lett. **24**, 881 (1999).
- [102] T. Udem, J. Reichert, R. Holzwarth, and T. W. Hänsch, *Absolute optical frequency measurement of the Cesium D_1 line with a mode-locked laser*, Phys. Rev. Lett. **82**, 3568 (1999).
- [103] J. Reichert, R. Holzwarth, T. Udem, and T. W. Hänsch, *Measuring the frequency of light with mode-locked lasers*, Opt. Commun. **172**, 59 (1999).
- [104] M. Niering et al., *Measurement of the Hydrogen $1s$ - $2s$ transition frequency by phase coherent comparison with a microwave Cesium fountain clock*, Phys. Rev. Lett. **84**, 5496 (2000).
- [105] D. J. Jones, S. A. Diddams, J. K. Ranka, A. Stentz, R. S. Windeler, J. L. Hall, and S. T. Cundiff, *Carrier-envelope phase control of femtosecond mode-locked lasers and direct optical frequency synthesis*, Science **288**, 635 (2000).
- [106] R. Holzwarth, T. Udem, T. W. Hänsch, J. C. Knight, W. J. Wadsworth, and P. S. J. Russell, *Optical frequency synthesizer for precision spectroscopy*, Phys. Rev. Lett. **85**, 2264 (2000).
- [107] P. Russell, *Photonic crystal fibers*, Science **299**, 358 (2003).
- [108] S. A. Diddams et al., *Direct link between microwave and optical frequencies with a 300 THz femtosecond laser comb*, Phys. Rev. Lett. **84**, 5102 (2000).
- [109] A. Bartels, S. A. Diddams, T. M. Ramond, and L. Hollberg, *Mode-locked laser pulse trains with subfemtosecond timing jitter synchronized to an optical reference oscillator*, Opt. Lett. **28**, 663 (2003).
- [110] A. Bartels, C. W. Oates, L. Hollberg, and S. A. Diddams, *Stabilization of femtosecond laser frequency combs with subhertz residual linewidths*, Opt. Lett. **29**, 1081 (2004).
- [111] L.-S. Ma et al., *Optical frequency synthesis and comparison with uncertainty at the 10^{-19} level*, Science **303**, 1843 (2004).
- [112] B. R. Washburn, S. A. Diddams, N. R. Newbury, J. W. Nicholson, M. F. Yan, and C. G. Jorgensen, *Phase-locked, Erbium-fiber-laser-based frequency comb in the near infrared*, Opt. Lett. **29**, 250 (2004).
- [113] R. T. Zinkstok, S. Witte, W. Hogervorst, and K. S. E. Eikema, *High-power parametric amplification of 11.8-fs laser pulses with carrier-envelope phase control*, Opt. Lett. **30**, 78 (2005).
- [114] G. Tempea, M. Geissler, M. Schnürer, and T. Brabec, *Self-phase-matched high harmonic generation*, Phys. Rev. Lett. **84**, 4329 (2000).
- [115] M. Geissler, G. Tempea, and T. Brabec, *Phase-matched high-order harmonic generation in the nonadiabatic limit*, Phys. Rev. A **62**, 033817 (2000).

- [116] R. Kienberger et al., *Atomic transient recorder*, Nature **427**, 817 (2004).
- [117] T. Brabec and F. Krausz, *Intense few-cycle laser fields: Frontiers of nonlinear optics*, Rev. Mod. Phys. **72**, 545 (2000).
- [118] J. D. Jackson, *Classical electrodynamics* (Academic Press, 1998).
- [119] G. P. Agrawal, *Nonlinear fiber optics* (Academic Press, 1995), 2nd ed.
- [120] S. A. Akhmanov, V. A. Vysloukh, and A. S. Chirkin, *Optics of femtosecond laser pulses* (American Institute of Physics, 1992).
- [121] J.-C. Diels and W. Rudolph, *Ultrafast laser pulse phenomena* (Academic Press, 1996).
- [122] I. A. Walmsley, L. Waxer, and C. Dorrer, *The role of dispersion in ultrafast optics*, Rev. Sci. Instrum. **72**, 1 (2001).
- [123] R. W. Boyd, *Nonlinear optics* (Academic Press, 1992).
- [124] Y. R. Shen, *The principles of nonlinear optics* (John Wiley & Sons, 1984).
- [125] S. T. Cundiff, *Phase stabilization of ultrashort optical pulses*, J. Phys. D **35**, R43 (2002).
- [126] T. Udem, R. Holzwarth, and T. W. Hänsch, *Optical frequency metrology*, Nature **416**, 233 (2002).
- [127] A. D. Ludlow et al., *Systematic study of the ^{87}Sr clock transition in an optical lattice*, Phys. Rev. Lett. **96**, 033003 (2006).
- [128] K. W. Holman, R. J. Jones, A. Marian, S. T. Cundiff, and J. Ye, *Intensity-related dynamics of femtosecond frequency combs*, Optics Letters **28**, 851 (2003).
- [129] R. Ell et al., *Generation of 5-fs pulses and octave-spanning spectra directly from a Ti:sapphire laser*, Opt. Lett. **26**, 373 (2001).
- [130] L. Matos, D. Kleppner, O. Kuzucu, T. R. Schibli, J. Kim, E. P. Ippen, and F. X. Kärtner, *Direct frequency comb generation from an octave-spanning, prismless Ti:sapphire laser*, Opt. Lett. **29**, 1683 (2004).
- [131] T. M. Fortier, A. Bartels, and S. A. Diddams, *Octave-spanning Ti:sapphire laser with a repetition rate > 1 GHz for optical frequency measurements and comparisons*, Opt. Lett. **31**, 1011 (2006).
- [132] J. K. Ranka, R. S. Windeler, and A. J. Stentz, *Visible continuum generation in air silica microstructure optical fibers with anomalous dispersion at 800 nm*, Opt. Lett. **25**, 25 (2000).
- [133] S. Hannemann, E. J. Salumbides, S. Witte, R. T. Zinkstok, E.-J. van Duijn, K. S. E. Eikema, and W. Ubachs, *Frequency metrology on the $\text{Mg } 3s^2\ ^1S \rightarrow 3s4p\ ^1P$ line for comparison with quasar data*, Phys. Rev. A **74**, 012505 (2006).
- [134] E. J. Salumbides, S. Hannemann, K. S. E. Eikema, and W. Ubachs, *Isotopically-*

- resolved calibration of the 285-nm Mg I resonance line for comparison with quasar absorptions*, Mon. Notices Roy. Astron. Soc. **373**, L41 (2006).
- [135] C. Cohen-Tannoudji, B. Diu, and F. Laloë, *Quantum mechanics* (John Wiley & Sons, 1977).
- [136] R. T. Zinkstok, *Precise control of electromagnetic fields and atomic excitation*, Ph.D. thesis, Vrije Universiteit (2007).
- [137] J.-P. Uzan, *The fundamental constants and their variation: observational and theoretical status*, Rev. Mod. Phys. **75**, 403 (2003).
- [138] A. Clairon, C. Salomon, S. Guellati, and W. D. Phillips, *Ramsey resonance in a Zacharias fountain*, Europhys. Lett. **16**, 165 (1991).
- [139] M. J. Snadden, A. S. Bell, E. Riis, and A. I. Ferguson, *Two-photon spectroscopy of laser-cooled Rb using a mode-locked laser*, Opt. Commun. **125**, 70 (1996).
- [140] M. Bellini, A. Bartoli, and T. W. Hänsch, *Two-photon Fourier spectroscopy with femtosecond light pulses*, Opt. Lett. **22**, 540 (1997).
- [141] A. Baltuška et al., *Attosecond control of electronic processes by intense light fields*, Nature **421**, 611 (2003).
- [142] A. Marian, M. C. Stowe, J. R. Lawall, D. Felinto, and J. Ye, *United time-frequency spectroscopy for dynamics and global structure*, Science **306**, 2063 (2004).
- [143] R. Zerne et al., *Phase-locked high-order harmonic sources*, Phys. Rev. Lett. **79**, 1006 (1997).
- [144] S. Cavalieri, R. Eramo, M. Materazzi, C. Corsi, and M. Bellini, *Ramsey-type spectroscopy with high-order harmonics*, Phys. Rev. Lett. **89**, 133002 (2002).
- [145] A. Apolonski et al., *Controlling the phase evolution of few-cycle light pulses*, Phys. Rev. Lett. **85**, 740 (2000).
- [146] S. Witte, R. T. Zinkstok, W. Hogervorst, and K. S. E. Eikema, *Control and precise measurement of carrier-envelope phase dynamics*, Appl. Phys. B **78**, 5 (2004).
- [147] V. Kaufman, *Wavelengths and energy levels of neutral Kr-84 and level shifts in all Kr even isotopes*, J. Res. NIST **98**, 717 (1993).
- [148] F. Brandi, W. Hogervorst, and W. Ubachs, *High-resolution vacuum-ultraviolet and ultraviolet photoionization spectroscopy of Krypton*, J. Phys. B **35**, 1071 (2002).
- [149] R. DeSalvo, D. J. Hagan, M. Sheik-Bahae, G. I. Stegeman, E. W. V. Stryland, and H. Vanherzeele, *Self-focusing and self-defocusing by cascaded second-order effects in KTP*, Opt. Lett. **17**, 28 (1992).
- [150] R. A. Baumgartner and R. L. Byer, *Optical parametric amplification*, IEEE J. Quantum Electron. **15**, 432 (1979).
- [151] M. Abramowitz and I. A. Stegun, *Handbook of mathematical functions with*

- formulas, graphs, and mathematical tables* (Dover, New York, 1964), 9 ed.
- [152] D. Zhang, Y. Kong, and J.-Y. Zhang, *Optical parametric properties of 532-nm-pumped beta-barium-borate near the infrared absorption edge*, Opt. Commun. **184**, 485 (2000).
- [153] E. Zeromskis, A. Dubietis, G. Tamosauskas, and A. Piskarskas, *Gain bandwidth broadening of the continuum-seeded optical parametric amplifier by use of two pump beams*, Opt. Commun. **203**, 435 (2002).
- [154] C. Wang, Y. Leng, B. Zhao, Z. Zhang, and Z. Xu, *Extremely broad gain spectra of two-beam-pumped optical parametric chirped-pulse amplifier*, Opt. Commun. **237**, 169 (2004).
- [155] L. Cardoso and G. Figueira, *Bandwidth increase by controlled angular dispersion of signal beam in optical parametric amplification*, Opt. Express **12**, 3108 (2004).
- [156] G. Arisholm, J. Biegert, P. Schlup, C. P. Hauri, and U. Keller, *Ultra-broadband chirped-pulse optical parametric amplifier with angularly dispersed beams*, Opt. Express **12**, 518 (2004).
- [157] H. Liu, W. Zhao, Y. Yang, H. Wang, Y. Wang, and G. Chen, *Matching of both group-velocity and pulse-front for ultrabroadband three-wave-mixing with noncollinear angularly dispersed geometry*, Appl. Phys. B **82**, 585 (2006).
- [158] J. P. Gordon, W. H. Louisell, and L. R. Walker, *Quantum fluctuations and noise in parametric processes. II*, Phys. Rev. **129**, 481 (1963).
- [159] R. A. Fischer and W. K. Bischel, *Numerical studies of the interplay between self-phase modulation and dispersion for intense plane-wave laser pulses*, J. Appl. Phys. **46**, 4921 (1975).
- [160] W. H. Press, S. A. Teukolsky, W. T. Vetterling, and B. P. Flannery, *Numerical recipes in C* (Cambridge University Press, 1992).
- [161] X. Yang et al., *Dependence of spectrum on pump-signal angle in BBO-I non-collinear optical-parametric chirped-pulse amplification*, Appl. Phys. B **73**, 219 (2001).
- [162] N. Forget et al., *Pump-noise transfer in optical parametric chirped-pulse amplification*, Opt. Lett. **30**, 2921 (2005).
- [163] E. B. Treacy, *Optical pulse compression with diffraction gratings*, IEEE J. Quantum Electron. **5**, 454 (1969).
- [164] S. D. Brorson and H. A. Haus, *Diffraction gratings and geometrical optics*, J. Opt. Soc. Am. B **5**, 247 (1988).
- [165] M. Ware, W. E. Dibble, S. A. Glasgow, and J. Peatross, *Energy flow in angularly dispersive optical systems*, J. Opt. Soc. Am. B **18**, 839 (2001).
- [166] F. W. Helbing, G. Steinmeyer, U. Keller, R. S. Windeler, J. Stenger, and H. R. Telle,

- Carrier-envelope offset dynamics of mode-locked lasers*, Opt. Lett. **27**, 194 (2002).
- [167] I. Thomann et al., *Investigation of a grating-based stretcher/compressor for carrier-envelope phase stabilized fs pulses*, Opt. Express **12**, 3493 (2004).
- [168] M. Kakehata et al., *Carrier-envelope-phase stabilized chirped-pulse amplification system scalable to higher pulse energies*, Opt. Express **12**, 2070 (2004).
- [169] E. Gagnon et al., *Long-term carrier-envelope phase stability from a grating-based, chirped pulse amplifier*, Opt. Lett. **31**, 1866 (2006).
- [170] O. E. Martinez, *3000 times grating compressor with positive group velocity dispersion: Application to fiber compensation in 1.3 – 1.6 μm region*, IEEE J. Quantum Electron. **23**, 59 (1987).
- [171] O. E. Martinez, J. P. Gordon, and R. L. Fork, *Negative group-velocity dispersion using refraction*, J. Opt. Soc. Am. A **1**, 1003 (1984).
- [172] D. M. Gaudiosi, A. L. Lytle, P. Kohl, M. M. Murnane, H. C. Kapteyn, and S. Backus, *11-W average power Ti:sapphire amplifier system using downchirped pulse amplification*, Opt. Lett. **29**, 2665 (2004).
- [173] A. Öffner, *Unit power imaging catoptric anastigmat*, Tech. rep., U. S. Patent 3748015 (1973).
- [174] B. E. Lemoff and C. P. J. Barty, *Quintic-phase-limited, spatially uniform expansion and recompression of ultrashort optical pulses*, Opt. Lett. **18**, 1651 (1993).
- [175] D. Du, J. Squier, S. Kane, G. Korn, G. Mourou, C. Bogusch, and C. T. Cotton, *Terawatt Ti:sapphire laser with a spherical reflective-optic pulse expander*, Opt. Lett. **20**, 2114 (1995).
- [176] G. Cheriaux, P. Rousseau, F. Salin, J. P. Chambaret, B. Walker, and L. F. Dimauro, *Aberration-free stretcher design for ultrashort-pulse amplification*, Opt. Lett. **21**, 414 (1996).
- [177] J. Squier, C. P. J. Barty, F. Salin, C. le Blanc, and S. Kane, *Use of mismatched grating pairs in chirped-pulse amplification systems*, Appl. Opt. **37**, 1638 (1998).
- [178] L.-S. Ma, R. K. Shelton, H. C. Kapteyn, M. M. Murnane, and J. Ye, *Sub-10-femtosecond active synchronization of two passively mode-locked Ti:sapphire oscillators*, Phys. Rev. A **64**, 021802 (2001).
- [179] V. Magni, G. Valentini, and S. de Silvestri, *Recent developments in laser resonator design*, Opt. Quant. Electron. **23**, 1105 (1991).
- [180] V. Magni, *Resonators for solid-state lasers with large-volume fundamental mode and high alignment stability*, Appl. Opt. **25**, 107 (1986).
- [181] S. de Silvestri, P. Laporta, and V. Magni, *Novel stability diagrams for CW solid-state laser resonators*, Opt. Lett. **11**, 513 (1986).
- [182] R. Hua, S. Wada, and H. Tashiro, *Versatile, compact, TEM₀₀-mode resonator for*

- side-pumped single-rod solid-state lasers*, Appl. Opt. **40**, 2468 (2001).
- [183] C. G. Durfee III and H. M. Milchberg, *Pulse compression in a self-filtering Nd:YAG regenerative amplifier*, Opt. Lett. **17**, 37 (1992).
- [184] V. A. Venturo, A. G. Joly, and D. Ray, *Pulse compression with a high-energy Nd:YAG regenerative amplifier system*, Appl. Opt. **36**, 5048 (1997).
- [185] D. F. Voss and L. S. Goldberg, *Simultaneous amplification and compression of CW mode-locked Nd:YAG laser pulses*, Opt. Lett. **11**, 210 (1986).
- [186] J. Sherman, *Thermal compensation of a CW-pumped Nd:YAG laser*, Appl. Opt. **37**, 7789 (1998).
- [187] R. Fluck, M. R. Hermann, and L. A. Hackel, *Energetic and thermal performance of high-gain diode-side-pumped Nd:YAG rods*, Appl. Phys. B **770**, 491 (2000).
- [188] I. Moshe and S. Jackel, *Correction of thermally induced birefringence in double-rod laser resonators – comparison of various methods*, Opt. Commun. **214**, 315 (2002).
- [189] W. A. Clarkson, N. S. Felgate, and D. C. Hanna, *Simple method for reducing the depolarization loss resulting from thermally induced birefringence in solid-state lasers*, Opt. Lett. **24**, 820 (1999).
- [190] Q. Lü, N. Kugler, H. Weber, S. Dong, and N. Müller, *A novel approach for compensation of birefringence in cylindrical Nd:YAG rods*, Opt. and Quant. Electron. **28**, 59 (1996).
- [191] M. Ostermeyer, G. Klemz, P. Kubina, and R. Menzel, *Quasi-CW birefringence-compensated single- and double-rod Nd:YAG lasers*, Appl. Opt. **41**, 7573 (2002).
- [192] N. Kugler, S. Dong, Q. Lü, and H. Weber, *Investigation of the misalignment sensitivity of a birefringence-compensated two-rod Nd:YAG laser system*, Appl. Opt. **36**, 9359 (1997).
- [193] E. Hecht, *Optics* (Addison-Wesley, 1987), 2nd ed.
- [194] F. Salin, P. Georges, G. Roger, and A. Brun, *Single-shot measurement of a 52-fs pulse*, Opt. Lett. **26**, 4528 (1987).
- [195] C. Iaconis and I. A. Walmsley, *Spectral phase interferometry for direct electric-field reconstruction of ultrashort optical pulses*, Opt. Lett. **23**, 792 (1998).
- [196] C. Dorrer et al., *Single-shot real-time characterization of chirped-pulse amplification systems by spectral phase interferometry for direct electric-field reconstruction*, Opt. Lett. **24**, 1644 (1999).
- [197] L. Gallmann, D. H. Sutter, N. Matuschek, G. Steinmeyer, U. Keller, C. Iaconis, and I. A. Walmsley, *Characterization of sub-6-fs optical pulses with spectral phase interferometry for direct electric-field reconstruction*, Opt. Lett. **24**, 1314 (1999).
- [198] M. Zavelani-Rossi, D. Polli, G. Cerullo, S. de Silvestri, L. Gallmann, G. Stein-

-
- meyer, and U. Keller, *Few-optical-cycle laser pulses by OPA: broadband chirped mirror compression and SPIDER characterization*, Appl. Phys. B **74**, S245 (2002).
- [199] T. M. Shuman, M. E. Anderson, J. Bromage, C. Iaconis, L. Waxer, and I. A. Walmsley, *Real-time SPIDER: ultrashort pulse characterization at 20 Hz*, Opt. Express **5**, 134 (1999).
- [200] W. Kornelis et al., *Single-shot kilohertz characterization of ultrashort pulses by spectral phase interferometry for direct electric-field reconstruction*, Opt. Lett. **28**, 281 (2003).
- [201] M. Takeda, H. Ina, and S. Kobayashi, *Fourier-transform method of fringe-pattern analysis for computer-based topography and interferometry*, J. Opt. Soc. Am. **72**, 156 (1982).
- [202] M. E. Anderson, L. E. E. de Araujo, E. M. Kosik, and I. A. Walmsley, *The effects of noise on ultrashort optical pulse measurement using SPIDER*, Appl. Phys. B **70**, S85 (2000).
- [203] C. Corsi and M. Bellini, *Robustness of phase coherence against amplification in a flashlamp-pumped multi-pass femtosecond laser*, Appl. Phys. B **78**, 31 (2004).
- [204] B. Schenkel et al., *Generation of 3.8-fs pulses from adaptive compression of a cascaded hollow fiber supercontinuum*, Opt. Lett. **28**, 1987 (2003).
- [205] J. Seres et al., *Sub-10-fs, terawatt-scale Ti:sapphire laser system*, Opt. Lett. **28**, 1832 (2003).
- [206] C. P. Hauri, P. Schlup, G. Arisholm, J. Biegert, and U. Keller, *Phase-preserving chirped-pulse optical parametric amplification to 17.3 fs directly from a Ti:sapphire oscillator*, Opt. Lett. **29**, 1369 (2004).
- [207] F. W. Helbing, G. Steinmeyer, J. Stenger, H. R. Telle, and U. Keller, *Carrier envelope-offset dynamics and stabilization of femtosecond pulses*, Appl. Phys. B **74**, S35 (2002).
- [208] M. Kakehata, H. Takada, Y. Kobayashi, K. Torizuka, Y. Fujihira, T. Homma, and H. Takahashi, *Single-shot measurement of carrier-envelope phase changes by spectral interferometry*, Opt. Lett. **26**, 1436 (2001).
- [209] M. Kakehata, Y. Fujihira, H. Takada, Y. Kobayashi, K. Torizuka, T. Homma, and H. Takahashi, *Measurements of carrier-envelope phase changes of 100-Hz amplified laser pulses*, Appl. Phys. B **74**, S43 (2002).
- [210] A. Baltuška et al., *Phase-controlled amplification of few-cycle laser pulses*, IEEE J. Sel. Top. Quantum Electron. **9**, 972 (2003).
- [211] L. Lepetit, G. Cheriaux, and M. Joffre, *Linear techniques of phase measurement by femtosecond spectral interferometry for applications in spectroscopy*, J. Opt. Soc. Am. B **12**, 2467 (1995).
- [212] M. Hentschel et al., *Attosecond metrology*, Nature **414**, 509 (2001).

- [213] S. Ito, H. Ishikawa, T. Miura, K. Takasago, A. Endo, and K. Torizuka, *Seven-terawatt Ti:sapphire laser system operating at 50 Hz with high beam quality for laser Compton femtosecond X-ray generation*, Appl. Phys. B **76**, 497 (2003).
- [214] C. P. J. Barty et al., *Generation of 18-fs, multiterawatt pulses by regenerative pulse shaping and chirped-pulse amplification*, Opt. Lett. **21**, 668 (1996).
- [215] V. Bagnoud and F. Salin, *Amplifying laser pulses to the terawatt level at 1-kilohertz repetition rate*, Appl. Phys. B **70**, S165 (2000).
- [216] M. Pittman, S. Ferré, J. P. Rousseau, L. Notebaert, J. P. Chambaret, and G. Chériaux, *Design and characterization of a near-diffraction-limited 100-TW, 10-Hz high-intensity laser*, Appl. Phys. B **74**, 529 (2002).
- [217] N. Ishii et al., *Multimillijoule chirped parametric amplification of few-cycle pulses*, Opt. Lett. **30**, 567 (2005).
- [218] A. Scrinzi, M. Y. Ivanov, R. Kienberger, and D. M. Villeneuve, *Attosecond physics*, J. Phys. B **39**, R1 (2006).
- [219] H. Niikura, D. M. Villeneuve, and P. B. Corkum, *Controlling vibrational wave packets with intense, few-cycle laser pulses*, Phys. Rev. A **73**, 021402 (2006).
- [220] T. Fuji et al., *Parametric amplification of few-cycle carrier-envelope phase-stable pulses at 2.1 μm* , Opt. Lett. **31**, 1103 (2006).
- [221] D. Kraemer, R. Hua, M. L. Cowan, K. Franjic, and R. J. D. Miller, *Ultrafast noncollinear optical parametric chirped pulse amplification in KTiOAsO_4* , Opt. Lett. **31**, 981 (2006).
- [222] A. J. Verhoef, J. Seres, K. Schmid, Y. Nomura, G. Tempea, L. Veisz, and F. Krausz, *Compression of the pulses of a Ti:Sapphire laser system to 5 femtoseconds at 0.2 terawatt level*, Appl. Phys. B **82**, 513 (2006).
- [223] J. H. Sung, J. Y. Park, T. Imran, Y. S. Lee, and C. H. Nam, *Generation of 0.2-TW 5.5-fs optical pulses at 1 kHz using a differentially pumped hollow-fiber chirped-mirror compressor*, Appl. Phys. B **82**, 5 (2006).
- [224] G. Stibenz, N. Zhavoronkov, and G. Steinmeyer, *Self-compression of millijoule pulses to 7.8 fs duration in a white-light filament*, Opt. Lett. **31**, 274 (2006).
- [225] H. Takada and K. Torizuka, *Design and construction of a TW-class 12-fs Ti:Sapphire chirped-pulse amplification system*, IEEE J. Sel. Top. Quantum Electron. **12**, 201 (2006).
- [226] E. J. Divall and I. N. Ross, *High dynamic range contrast measurements by use of an optical parametric amplifier correlator*, Opt. Lett. **29**, 2273 (2004).
- [227] F. Tavella, K. Schmid, N. Ishii, A. Marcinkevičius, L. Veisz, and F. Krausz, *High-dynamic range pulse-contrast measurements of a broadband optical parametric chirped-pulse amplifier*, Appl. Phys. B **81**, 753 (2005).

-
- [228] K. Osvay, M. Csatári, I. N. Ross, A. Persson, and C.-G. Wahlström, *On the temporal contrast of high intensity femtosecond laser pulses*, Laser Part. Beams **23**, 327 (2005).
- [229] J. C. Vaughan, T. Feurer, K. W. Stone, and K. A. Nelson, *Analysis of replica pulses in femtosecond pulse shaping with pixelated devices*, Opt. Express **14**, 1314 (2006).
- [230] L. Giniunas, J. Pocius, and R. Danielius, *Energy extraction improvement in picosecond amplifiers by pulse tilting*, Opt. Lett. **31**, 643 (2006).
- [231] M. Bellini, C. Lyngå, A. Tozzi, M. B. Gaarde, T. W. Hänsch, A. L'Huillier, and C.-G. Wahlström, *Temporal coherence of ultrashort high-order harmonic pulses*, Phys. Rev. Lett. **81**, 297 (1998).
- [232] P. Salières et al., *Frequency-domain interferometry in the XUV with high-order harmonics*, Phys. Rev. Lett. **83**, 5483 (1999).
- [233] C. Gohle et al., *A frequency comb in the extreme ultraviolet*, Nature **436**, 234 (2005).
- [234] R. J. Jones, K. D. Moll, M. J. Thorpe, and J. Ye, *Phase-coherent frequency combs in the vacuum ultraviolet via high-harmonic generation inside a femtosecond enhancement cavity*, Phys. Rev. Lett. **94**, 193201 (2005).
- [235] R. T. Zinkstok, S. Witte, W. Ubachs, W. Hogervorst, and K. S. E. Eikema, *Frequency comb laser spectroscopy in the vacuum-ultraviolet region*, Phys. Rev. A **73**, 061801 (2006).

LIST OF PUBLICATIONS

This thesis is based on the following publications:

CHAPTER 3:

Deep-ultraviolet quantum interference metrology with ultrashort laser pulses

S. Witte, R. Th. Zinkstok, W. Ubachs, W. Hogervorst, K. S. E. Eikema

Science **307**, 400-403 (2005).

CHAPTER 4 (SECTION 4.2):

Numerical simulations for performance optimization of a few-cycle terawatt

NOCPA system

S. Witte, R. Th. Zinkstok, W. Hogervorst, K. S. E. Eikema

Applied Physics B, accepted for publication

CHAPTER 6:

High-power parametric amplification of 11.8-fs laser pulses with carrier-envelope phase control

R. Th. Zinkstok, S. Witte, W. Hogervorst, K. S. E. Eikema

Optics Letters **30**, 78-80 (2005).

CHAPTER 7:

Generation of few-cycle terawatt light pulses using optical parametric chirped pulse amplification

S. Witte, R. Th. Zinkstok, W. Hogervorst, K. S. E. Eikema

Optics Express **13**, 4903-4908 (2005).

CHAPTER 8:

A source of 2 terawatt, 2.7 cycle laser pulses based on noncollinear optical parametric chirped pulse amplification

S. Witte, R. Th. Zinkstok, A. L. Wolf, W. Hogervorst, W. Ubachs, K. S. E. Eikema

Optics Express **14**, 8168-8177 (2006).

Publications that have not been reproduced in this thesis:

- Frequency comb laser spectroscopy in the vacuum-ultraviolet region
R. Th. Zinkstok, S. Witte, W. Ubachs, W. Hogervorst and K. S. E. Eikema
Physical Review A **73**, 061801(R) (2006).
- Frequency metrology on the $EF\ ^1\Sigma_g^+ \leftarrow X\ ^1\Sigma_g^+(0,0)$ transition in H_2 , HD, and D_2
S. Hannemann, E. J. Salumbides, S. Witte, R. T. Zinkstok, E. -J. van Duijn,
K. S. E. Eikema, and W. Ubachs
Physical Review A **74**, 062512 (2006).
- Frequency metrology on the $Mg\ 3s^2\ ^1S \rightarrow 3s4p\ ^1P$ line for comparison
with quasar data
S. Hannemann, E. J. Salumbides, S. Witte, R. T. Zinkstok, E. -J. van Duijn,
K. S. E. Eikema, and W. Ubachs
Physical Review A **74**, 012505 (2006).
- Control and precise measurement of carrier-envelope phase dynamics
S. Witte, R. Th. Zinkstok, W. Hogervorst and K. S. E. Eikema
Applied Physics B **78**, 5 (2004).
- Third-harmonic generation of a continuous-wave Ti:Sapphire laser in external
resonant cavities
J. Mes, E. J. van Duijn, R. Zinkstok, S. Witte and W. Hogervorst
Applied Physics Letters **82**, 4423 (2003).
- High-resolution LIF measurements on hyperfine structure and isotope shifts in var-
ious states of Lu I using the second and third harmonic of a cw Ti:sapphire laser
S. Witte, E. J. van Duijn, R. Zinkstok and W. Hogervorst
European Physical Journal D **20**, 159 (2002).
- Hyperfine structure and isotope shift of transitions in Yb I using UV and deep-UV
cw laser light and the angular distribution of fluorescence radiation
R. Zinkstok, E. J. van Duijn, S. Witte and W. Hogervorst
Journal of Physics B **35**, 2693 (2002).
- Hyperfine structure and isotope shift measurements on $4d^{10}\ ^1S_0 \rightarrow 4d^9\ 5p\ J = 1$
transitions in Pd I using deep-UV cw laser spectroscopy
E. J. van Duijn, S. Witte, R. Zinkstok, and W. Hogervorst
European Physical Journal D **19**, 25 (2002).

SUMMARY

An important topic in laser physics is the ability to control and manipulate the electric field of light, and to generate ever shorter light pulses with a controlled waveform. Such pulses allow the construction of an “ultra-high-speed camera” that can follow the fastest processes in nature. In principle, the shortest pulse that can be produced will contain at least one half-cycle of the electric field. This implies that faster pulses can only be made with light at a shorter wavelength, such as extreme-ultraviolet or soft-X-ray radiation. The production of ultrashort X-ray pulses can be achieved through high-harmonic generation in a gas, using powerful laser pulses with a controlled electric field.

Another challenge in atomic physics is the measurement of absolute transition frequencies in atoms, ions and molecules with ever increasing precision. Such high-precision measurements allow a direct comparison between experimental observations and theoretical predictions about the structure of matter. In addition, they can lead to more accurate atomic clocks, and could be used to detect possible changes of fundamental constants over time. While the invention of the frequency comb has revolutionized precision measurements, its impact has remained limited to the ultraviolet, visible and near-infrared spectral regions where narrow-band continuous-wave lasers are available. One of the goals of this thesis is to develop methods for performing frequency comb spectroscopy at much higher frequencies. This frequency range (known as the extreme-ultraviolet) contains many atomic and ionic transitions that are of fundamental physical interest, but narrow-band continuous-wave lasers are not available at such high frequencies.

To achieve these goals, we have constructed a laser source that can produce ultrashort laser pulses with extreme peak intensity, while maintaining the phase coherence and the frequency comb spectrum of these pulses. Phase-locked pairs of these powerful broadband pulses can then be used for high-resolution frequency measurements. In addition, these intense ultrashort phase-controlled laser pulses are well-suited for the production of coherent ultrashort soft-X-ray pulses with a duration below 1 femtosecond (10^{-15} seconds). A more detailed background and motivation for the work that is presented in this thesis is given in chapter 1, along with an outline of its contents.

Besides providing a theoretical background on the physics and propagation of ultrashort light pulses, chapter 2 introduces all aspects of the frequency comb laser system that we have constructed. This frequency comb forms the basis of our spectroscopy experiments, which will be discussed in chapter 3. The modes of the frequency comb have been stabilized to a GPS-disciplined Rb-clock, allowing a frequency accuracy of 10^{-11} in a 10 second averaging time. The carrier-envelope phase shift between pulses has been stabilized to better than $1/40^{\text{th}}$ (RMS) of an optical cycle using f -to- $2f$ interferometry and fast electronics.

In chapter 3, a proof-of-principle experiment is presented that demonstrates the feasibility of high-resolution frequency metrology with broadband laser pulses. We

show that pairs of phase-locked pulses from our frequency comb oscillator can be amplified and frequency-upconverted without losing pulse-to-pulse phase coherence, and that these pulses can be used for accurate frequency measurements. We exploit the phase coherence between the individual laser pulses to induce quantum interference in krypton atoms, coherently exciting one particular atomic transition under study. From a measurement of the final excited state population as a function of the phase and time delay between the laser pulses, the transition frequency can be deduced. We have performed an absolute frequency calibration of the krypton $4p^6 \rightarrow 4p^5 5p[1/2]_0$ two-photon transition in the deep-ultraviolet spectral range, at a wavelength of 2×212.55 nm. An absolute frequency accuracy of 3.5 MHz (1×10^{-9} relative accuracy) has been achieved, using powerful picosecond laser pulses that have a spectral bandwidth of about 1 THz and a peak intensity of several megawatts. Isotope shifts have been measured with 150 kHz accuracy. This method of measuring transition frequencies combines the high peak intensity of the individual pulses with the high resolution given by the total duration and pulse-to-pulse phase coherence of the full pulse train. Therefore, it enables high-resolution frequency comb spectroscopy in wavelength ranges where narrow-band continuous-wave lasers are not available.

Now that this method of performing frequency metrology has been proven successful, an important next step to advance this technique further is the construction of suitable laser systems that can provide intense and phase-stable laser pulses. A promising candidate for the amplification of ultrashort laser pulses to extreme intensity without the loss of phase coherence is noncollinear optical parametric chirped pulse amplification (NOPCPA). This technique is based on the process of optical parametric amplification (OPA), in which a high energy photon is split into two photons of lower energy inside a nonlinear optical medium. This OPA process can effectively work as an amplifier by seeding the nonlinear interaction with a weak laser pulse containing photons with the right energy. Energy transfer can then take place from a high-power pump pulse to this low-power seed pulse. Optical parametric amplification can be scaled up to produce extremely high-intensity pulses by combining it with the principle of chirped pulse amplification (CPA). In a CPA scheme, an ultrashort pulse is first stretched in time by a dispersive delay line, known as a pulse stretcher, to lower the peak intensity before amplification. This stretched pulse is amplified and subsequently recompressed in a second delay line with dispersion of opposite sign compared to the stretcher. The combination of OPA and CPA in a noncollinear geometry is known as NOPCPA, and this technique has several interesting properties that should allow the phase-stable amplification of extremely broadband laser pulses to high intensity.

The theory of how OPA works is given in the first part of chapter 4. For the second part of this chapter, simulations on a realistic NOPCPA amplifier system have been performed, to find optimal working values for many important parameters in such a system. We have developed a computer simulation program based on the split-step Fourier algorithm, which incorporates both dispersion and nonlinearity during pulse propagation through multiple amplification stages. A good agreement with the experimental situation described in later chapters is found. We find various effects that are specific to NOPCPA (i.e. that do not occur in conventional population-inversion-based

laser amplifiers), such as wavelength-dependent gain saturation and the need for tight synchronization of pump and seed pulses.

To develop the desired amplifier system for few-cycle terawatt laser pulses, several different NOPCPA systems have been constructed and systematically investigated. To allow such an investigation, we constructed various auxiliary optical systems, such as a stretching and compression system for few-cycle laser pulses with a spectral throughput of 400 nm, and an Nd:YAG-based pump laser source that delivers up to 160 mJ per pulse at a wavelength of 532 nm in 60 ps pulses. In addition, the required diagnostic tools have been designed and constructed, such as a SPIDER system to measure the pulse duration with sub-femtosecond resolution, as well as setups for the characterization of pulse contrast and phase stability. Most of these parts of the total NOPCPA system are described in detail in chapter 5.

The three different experimentally realized NOPCPA implementations are then discussed in chapters 6–8. In chapter 6, an NOPCPA system is presented that produces 0.1 mJ, 11.8 fs pulses at 1 kHz repetition rate. Using Fourier-transform spectral interferometry, quantitative measurements on the phase stability of the amplified pulses have been performed. We find that the NOPCPA amplification adds less than 100 mrad phase noise ($<1/60^{\text{th}}$ of an optical cycle) to our pulses, confirming that NOPCPA can indeed be used for the amplification of phase-locked frequency comb pulses.

Chapter 7 presents a system that takes the pulse intensity to a much higher level: Using the NOPCPA technique, we have constructed the first laser system that produces sub-10 fs pulses with an intensity exceeding a terawatt, at a repetition rate of 30 Hz. The total fluorescence is kept well below 1%. Since only three amplification stages are required to reach terawatt intensity, and the required stretching ratio of the pulses is only $\sim 10^3$, the amplifier system can be kept remarkably compact, and currently stands as one of the smallest terawatt amplifiers in the world.

The proof-of-principle terawatt system from chapter 7 has been upgraded to provide even shorter pulses at higher intensity, as explained in chapter 8. By seeding the amplifier with a new, home-built ultrabroadband Ti:Sapphire oscillator capable of producing 6.2 fs pulses, the amplifier output could be pushed to its theoretically predicted limit in terms of spectral bandwidth. In addition, an improved pump laser design is used to boost the power further. This system generates 7.6 fs pulses with an intensity of 2 TW. These pulses are compressed to within 5% of its Fourier-limited pulse duration of 7.3 fs, using grating-based stretching and recompression combined with adaptive spectral phase shaping. With an OPA-based pulse contrast measurement setup suited for few-cycle laser pulses, we found a pre-pulse contrast of 2×10^{-8} between the main pulse and the fluorescence background.

Chapter 9 concludes this thesis. In this chapter, several options are presented to optimize the pump pulse shape for NOPCPA, based on time-multiplexing and pulse-tilting. A new parametric amplification scheme is proposed, which we have named optical parametric tilted pulse amplification. This implementation of parametric amplification may provide a compact and flexible setup for frequency comb spectroscopy with ultrashort laser pulses. Finally, the current status of frequency comb spectroscopy in the extreme-ultraviolet is reviewed, and the prospects of precision measurements using our NOPCPA system are discussed.

SAMENVATTING

Een onderwerp in de laserfysica dat sterk in de belangstelling staat, is de mogelijkheid om het elektrische veld van licht te kunnen controleren en manipuleren, en het produceren van steeds kortere lichtpulsen met een gecontroleerde golfvorm. Met behulp van zulke pulsen kan een “ultra-hoge-snelheids-camera” worden gebouwd, waarmee de snelste processen in de natuur kunnen worden gevolgd. In principe zal de kortste lichtpuls die kan worden gemaakt altijd minimaal een halve oscillatie van het elektrische veld bevatten. Dit betekent dat snellere pulsen alleen kunnen worden gemaakt met licht dat een kortere golflengte heeft, zoals extreem-ultraviolet of zachte Röntgenstraling. De productie van ultrakorte Röntgenpulsen is mogelijk door middel van hoge-harmonische generatie in een gasvormig medium, met behulp van extreem sterke laserpulsen met een gecontroleerd elektrisch veld.

Een andere grote uitdaging in de atoomfysica is het meten van absolute overgangsfrequenties in atomen, ionen en moleculen met een steeds hogere precisie. Zulke zeer nauwkeurige metingen laten een directe vergelijking toe tussen experimentele observaties en theoretische voorspellingen over de structuur van materie. Ook kunnen ze gebruikt worden voor de ontwikkeling van preciezer werkende atoomklokken, en voor het detecteren van mogelijke tijdsafhankelijke variaties van fundamentele constanten. De ontwikkeling van de frequentiekam heeft op dit gebied tot een ware revolutie geleid, maar de impact van deze uitvinding is tot op heden beperkt gebleven tot het ultraviolet, het zichtbare en het nabij-infrarode spectrale gebied, waar smalbandige continue lasers beschikbaar zijn. Een doel van het onderzoek dat wordt beschreven in dit proefschrift is de ontwikkeling van methodes voor frequentiekam-spectroscopie bij veel hogere frequenties. In dit frequentiebereik (dat bekend staat als het extreem-ultraviolet) bevinden zich veel overgangen in atomen en ionen die van fundamentele fysische interesse zijn. Echter, het ontwikkelen van de smalbandige continue lasers, die vooralsnog nodig zijn voor precisie metingen, stuit op grote technologische problemen in dit frequentiegebied.

Voor het verwezenlijken van deze doelen is een lasersysteem ontwikkeld dat in staat is om ultrakorte laserpulsen te genereren met een extreem hoog piekvermogen, terwijl de fase-coherentie en de frequentiekam-structuur van de pulsen behouden blijft. Fase-stabiele paren van deze intense, breedbandige pulsen kunnen vervolgens worden gebruikt voor hoge-resolutie frequentie metingen. Daarnaast zijn zulke krachtige ultrakorte fase-gecontroleerde laserpulsen uitermate geschikt voor de productie van coherente Röntgenstraling met een pulsduur van minder dan een femtoseconde (10^{-15} seconden). Een meer gedetailleerde achtergrond en motivatie van het onderzoek dat wordt gepresenteerd in dit proefschrift is te vinden in hoofdstuk 1, samen met een beschrijving van de indeling.

Naast de theoretische achtergrond van de fysica en de voortbewegingseigenschappen van ultrakorte laserpulsen, bevat hoofdstuk 2 ook een beschrijving van alle as-

pecten van het frequentiekam-lasersysteem dat we hebben gebouwd. Deze frequentiekamlaser vormt de basis van onze spectroscopie-experimenten. De modes van de frequentiekam zijn gestabiliseerd ten opzichte van een GPS-gecontroleerde Rb-klok, waarmee een absolute frequentie-nauwkeurigheid van 10^{-11} (gemiddeld over 10 seconden) gehaald wordt. De faseverschuiving tussen de draaggolf en de omhullende pulsform is gestabiliseerd met een precisie van beter dan $1/40^{\text{ste}}$ (RMS) van een optische periode, met behulp van f -naar- $2f$ interferometrie en snelle electronica.

In hoofdstuk 3 wordt een experiment gepresenteerd dat de praktische haalbaarheid van hoge-resolutie frequentiemetingen met breedbandige laserpulsen aantoonst. We laten zien dat paren van fase-stabiele pulsen uit een frequentiekam oscillator kunnen worden versterkt en in frequentie opgeconverteerd, zonder de onderlinge fase-coherentie tussen de pulsen te verliezen. Deze pulsen kunnen vervolgens worden gebruikt voor nauwkeurige frequentiemetingen. We gebruiken de fase-coherentie tussen de individuele pulsen om quantum-interferentie in krypton atomen te induceren, waarmee een specifieke atomaire overgang coherent wordt geëxciteerd. Door middel van een meting van de hoeveelheid atomen in de aangeslagen toestand als functie van de fase en het tijdsverschil tussen de laserpulsen kan vervolgens de overgangsfrequentie worden bepaald. Wij hebben een absolute frequentiebepaling uitgevoerd van de krypton $4p^6 \rightarrow 4p^5 5p[1/2]_0$ twee-foton overgang in het diep-ultraviolet bij een golflengte van 2×212.55 nm, met een nauwkeurigheid van 3.5 MHz (1×10^{-9} relatieve nauwkeurigheid). Hiervoor gebruikten we intense picoseconde laserpulsen met een spectrale bandbreedte van ongeveer 1 THz en een piekvermogen van enkele megawatts. We hebben isotopieverschuivingen gemeten met een nauwkeurigheid van ~ 150 kHz. Deze methode om overgangsfrequenties te meten combineert de hoge piekintensiteit van de individuele pulsen met de hoge resolutie die wordt bepaald door de totale duur en fase-coherentie van de volledige pulstrein. Hierdoor kan hoge-resolutie frequentiekam-spectroscopie worden toegepast in golflengtegebieden waar smalbandige continue lasers niet beschikbaar zijn.

Nu deze methode voor het meten van frequenties succesvol is gebleken, is een belangrijke volgende stap voor de verdere ontwikkeling van deze technologie het opbouwen van geschikte lasersystemen. Een veelbelovende kandidaat voor het versterken van ultrakorte laserpulsen naar extreme intensiteiten, zonder verlies van fase-coherentie, is niet-collineaire optische parametrische gechirpte puls versterking (in het Engels afgekort tot NOPCPA). Deze techniek is gebaseerd op het proces van optische parametrische versterking (OPA), waarbij een foton van hoge energie uit een zogenaamde pomppuls wordt opgesplitst in twee fotonen met een lagere energie in een niet-lineair optisch medium. Dit OPA-proces kan effectief als een versterker werken door de niet-lineaire interactie te voeden met een zwakke laserpuls die fotonen bevat met de juiste energie. In dat geval zal er energieoverdracht plaatsvinden van de hoog-vermogen pomppuls naar de geïnjecteerde puls met het lage vermogen. Optische parametrische versterking kan worden opgeschaald voor de productie van extreem hoog-vermogen pulsen door de techniek te combineren met het principe van gechirpte puls versterking (CPA). In een CPA schema wordt een ultrakorte puls eerst in de tijd verlengd door middel van een dispersief bundelpad (in het Engels een "pulse stretcher" genaamd), om het piekvermogen te verlagen voordat versterking plaatsvindt. Deze verlengde

puls wordt versterkt, en vervolgens weer in de tijd gecompriemd in een bundelpad met tegengestelde dispersie in vergelijking met de stretcher. De combinatie van OPA en CPA in een niet-collineaire geometrie staat bekend als NOPCPA, en deze techniek heeft verscheidene interessante eigenschappen die fase-stabiele versterking van extreem breedbandige pulsen naar hoog vermogen mogelijk maakt.

De theorie van parametrische versterking wordt uitgelegd in het eerste deel van hoofdstuk 4. Voor het tweede deel van dit hoofdstuk zijn numerieke simulaties uitgevoerd aan een realistisch NOPCPA versterker-systeem, om de optimale waarden te vinden voor de belangrijkste parameters in zo'n systeem. Een computersimulatie-programma is ontwikkeld dat gebaseerd is op het split-step Fourier algoritme, waarmee zowel dispersie als niet-lineaire effecten tijdens pulspropagatie te modelleren zijn in meerdere versterkingsstappen. De simulaties vertonen een goede overeenkomst met de experimentele situaties (die in de latere hoofdstukken beschreven worden). We vinden verscheidene effecten die specifiek zijn voor NOPCPA (m.a.w. die niet voorkomen in conventionele versterkers die werken op basis van populatie-inversie), zoals golflengte-afhankelijke verzadiging en de noodzaak voor nauwkeurige synchronisatie van de pomp-puls met de puls die moet worden versterkt.

Om het gewenste versterkersysteem voor ultrakorte terawatt-laserpulsen te ontwikkelen zijn verschillende NOPCPA systemen opgebouwd en systematisch onderzocht. Als onderdeel van deze ontwikkelingen zijn verscheidene optische deelsystemen opgebouwd, zoals een verlengings- en compressiesysteem voor ultrakorte laserpulsen met een spectrale bandbreedte van 400 nm, en een Nd:YAG pomplaser die tot 160 mJ per puls kan leveren bij een golflengte van 532 nm en een pulsduur van 60 ps. Verder zijn de benodigde diagnostische systemen ontworpen en opgebouwd, zoals een SPIDER-systeem voor het meten van de pulsduur met sub-femtoseconde resolutie, en opstellingen voor het karakteriseren van het puls-contrast en de fase-stabiliteit. De meeste van deze onderdelen van het totale NOPCPA-systeem worden in detail beschreven in hoofdstuk 5.

De drie verschillende experimenteel gerealiseerde NOPCPA-implementaties worden behandeld in hoofdstukken 6–8. In hoofdstuk 6 wordt een NOPCPA-systeem gepresenteerd dat 0.1 mJ, 11.8 fs pulsen op 1 kHz herhalingsfrequentie produceert. Met behulp van spectrale interferometrie zijn kwantitatieve metingen uitgevoerd aan de fase-stabiliteit van de versterkte pulsen. Uit deze metingen blijkt dat het NOPCPA versterkingsproces minder dan 100 mrad faseruis toevoegt ($<1/60^{\text{ste}}$ van een optische periode), wat bevestigt dat NOPCPA inderdaad gebruikt kan worden voor het versterken van fase-stabiele frequentiekam pulsen.

Hoofdstuk 7 presenteert een systeem dat de pulsintensiteit naar een veel hoger niveau tilt: Met behulp van de NOPCPA-techniek hebben wij het eerste lasersysteem gebouwd dat sub-10 fs pulsen produceert met een piekvermogen van meer dan een terawatt, bij een herhalingsfrequentie van 30 Hz. De totale parametrische fluorescentie wordt ruim beneden 1% gehouden. Slechts drie versterkerstappen zijn nodig om het terawatt-vermogen te halen, en de vereiste verlengingsfactor van de pulsen is $\sim 10^3$. Hierdoor kan het versterkersysteem opmerkelijk compact gehouden worden, en is op dit moment een van de kleinste terawatt-versterkers ter wereld.

Het prototype terawatt-systeem uit hoofdstuk 7 is verbeterd en aangepast om nog kortere pulsen te leveren bij nog hoger vermogen, wat wordt beschreven in hoofdstuk 8. Door de versterker te injecteren met pulsen uit een nieuwe, door onszelf ontwikkelde ultra-breedbandige Ti:Saffier laser die 6.2 fs pulsen kan leveren, kan de versterker-output worden opgestuwd naar zijn theoretisch voorspelde maximale spectrale bandbreedte. Verder is een nieuwe pomplaser ontwikkeld, waarmee ook het vermogen verder verhoogd wordt. Dit systeem produceert 7.6 fs pulsen met een piekvermogen van 2 terawatt. Deze pulsen worden gecomprimeerd tot op 5% van hun Fourier-gelimeerde pulsduur van 7.3 fs, door middel van een pulscompressor op basis van tralies en adaptieve spectrale fasecontrole. Het pulscontrast is gekarakteriseerd met behulp van een op parametrische interactie gebaseerde meetopstelling, die geschikt is voor ultrakorte laserpulsen. Uit deze metingen blijkt dat het contrast tussen de hoofdpuls en de fluorescentie-achtergrond 2×10^{-8} is.

Hoofdstuk 9 sluit dit proefschrift af. In dit hoofdstuk worden verschillende mogelijkheden gepresenteerd om de vorm van de pomppuls te optimaliseren voor NOPCPA, gebaseerd op multiplexen van pulsen en het kantelen van het pulsfront. Een nieuwe opstelling voor parametrische versterking wordt voorgesteld, op basis van pulsen met een gekanteld pulsfront in plaats van in de tijd verlengde pulsen. Deze implementatie van parametrische versterking kan gebruikt worden als een compacte en flexibele opstelling voor frequentiekam-spectroscopie met ultrakorte laserpulsen. Tenslotte wordt de huidige status van frequentiekam-spectroscopie in het extreem-ultraviolet uiteengezet, en worden de vooruitzichten voor precisieingen met ons NOPCPA-systeem besproken.

DANKWOORD

Eindelijk heb ik dit proefschrift af. Het was veel werk, teveel en te moeilijk om helemaal alleen voor elkaar te krijgen. Gelukkig zijn er veel mensen geweest die hebben bijgedragen aan het onderzoek waarover ik zojuist een boek heb volgeschreven, en zonder hen was mij dit zeer waarschijnlijk ook niet gelukt. Ik schrijf dus graag nog een extra bladzijde vol om mijn dank te betuigen aan iedereen die aan de totstandkoming van mijn proefschrift heeft bijgedragen.

Als eerste Kjeld Eikema. Kjeld, jouw kennis, inzicht en experimentele vaardigheid zijn ronduit indrukwekkend te noemen. Ik heb ontzettend veel van je geleerd. Je directe stijl van begeleiden werkt voor mij erg prettig, en de goede sfeer die over het algemeen in het lab hangt is voor een groot deel te danken aan de manier waarop jij de boel runt. Bedankt voor alles, en succes met alle nieuwe, ambitieuze experimenten.

Wim Hogervorst, bedankt voor de kans om in jouw groep een promotieonderzoek te doen. De goede faciliteiten in het lasercentrum zijn voor een groot deel aan jouw visie en beleid te danken. Ik heb het ook altijd erg bijzonder gevonden, hoe je precies op het moment dat de metingen net beginnen te werken het lab binnenloopt om te kijken hoe het ervoor staat. Over intuïtie gesproken...

Roel Zinkstok mag in deze lijst uiteraard niet ontbreken. Roel, wat ben ik blij dat we hier samen aan begonnen zijn. Het scheelt zo ontzettend veel als je met z'n tweeën problemen kunt oplossen in plaats van alleen. Bovendien wordt het werk er een stuk leuker van, ik heb een hoop goede herinneringen aan de afgelopen jaren. De dingen die je soms meemaakt als promovendus... Veel succes in de toekomst, en tot ziens!

I would like to thank the entire Atomic Physics group for creating such a relaxed atmosphere. There is always someone around for help, advice or simply to tell jokes. You guys helped a lot in making everyday work fun. While I want to thank all my former and present colleagues, I would like to mention "my generation", the guys that I had the longest time overlap with: John, Sandro, Edcel, and Tom. Thanks also to the next generation of the femtosecond lab, Amandine and Dominik, for keeping the lab running so well. Good luck with all the experiments.

Eric-Jan van Duijn, van jou heb ik in eerste instantie geleerd hebt hoe je met lasers werkt, en wat een leuk werk dat is. Ook aan mijn huidige onderzoek heb je een wezenlijke bijdrage geleverd, met praktische adviezen, maar vooral ook met het uitlenen van eigenlijk alles, van filters tot complete versterkermodule en lasers.

Jacques Bouma wil ik bedanken voor de vele technische bijdragen aan onze opstellingen, en zeker ook voor de grote kasten vol met zo ongeveer alles waarmee je een experiment werkend kunt krijgen.

Petra de Gijsel, bedankt voor de administratieve hulp en het regelen van van alles en nog wat. Bedankt ook voor de vrolijke gesprekken en de gezelligheid die je daarbij meebrengt.

Verder zijn er nog een flink aantal mensen die mij weliswaar niet direct hebben geholpen met het aandraaien van spiegels en het analyseren van meetgegevens, maar die mij wel gesteund hebben met alles daaromheen. "Sorry, ik ben wat later", "Sorry, dan kan ik niet", "Sorry, trainen wordt niks vanavond", en soortgelijke uitspraken heb ik vrij vaak gedaan in de afgelopen jaren. Gelukkig heb ik vrienden en familie met veel geduld en begrip, en dat is erg prettig. Bedankt.

Vooraf mijn ouders en mijn broer wil ik hiervoor bedanken, omdat ze me gesteund hebben bij alles wat ik doe. Anne Lisa, bedankt dat je er voor me bent. Bedankt voor alles.

Stefan